Advancements in bender-element testing - frequency effects

by

Muhammad Irfan

A thesis

presented to the University of Waterloo

in fulfillment of the

thesis requirement for the degree of

Doctor of Philosophy

in

Civil Engineering

Waterloo, Ontario, Canada, 2019

Examining committee membership

The following served on the Examining Committee for this thesis. The decision of the Examining Committee is by majority vote.

External examiner

Dr. Siva Sivathayalan
Professor in Geotechnical Engineering
Department of Civil and Environmental Engineering
Carleton University

Co-Supervisor

Dr. Giovanni Cascante
Professor
Department of Civil and Environmental Engineering
University of Waterloo

Co-supervisor

Dr. Dipanjan Basu
Associate Professor
Department of Civil and Environmental Engineering
University of Waterloo

Internal member

Dr. Sriram Narasimhan
Professor
Department of Civil and Environmental Engineering
University of Waterloo

Internal member

Dr. Shunde Yin
Associate Professor
Department of Civil and Environmental Engineering
University of Waterloo

Internal-external member

Dr. Eihab Abdel-Rahman
Professor
Department of Civil and Environmental Engineering
University of Waterloo

Author’s Declaration

I hereby declare that I am the sole author of this thesis. This is a true copy of the thesis, including any required final revisions, as accepted by my examiners.

I understand that my thesis may be made electronically available to the public.

Abstract

Modern building and bridge codes require seismic design of foundations and structures; for which, the evaluation of the soil's response to dynamic loads is an important requirement in seismic design. The dynamic soil response is governed by its dynamic properties such as shear modulus (wave velocity) and damping ratio. These soil dynamic properties are typically measured in laboratory mostly using a bender element system (BE) or a resonant column (RC) device. However, the operating frequency range of BEs (e.g. 1 to 15 kHz) and the RC (e.g. 20 to 220 Hz) are not representative of typical earthquake loads (e.g. 0.1 to 10 Hz). In addition, there are significant limitations in BE and RC testing which reduce their reliability. Thus, current seismic designs could be either conservative or unsafe.

A major limitation in BE testing is that there is no standard procedure; mostly because the soil-BE interaction is not well understood; and the characterization of BE inside a soil specimen was not possible. On the other hand in RC testing, the soil dynamic properties cannot be evaluated simultaneously as function of frequency and strain. In a typical narrow-band resonant column test (e.g. sine sweep, random noise), the induced shear strains are different at each frequency component. Therefore, the main objectives of this study are to understand better the soil-BE interaction; which will provide the basis for the development of reliable guidelines for BE testing; and to verify the BE test results using the standard RC device.

The main objectives are achieved by testing the BE using a state-of-the-art laser vibrometer and a newly developed transparent soil to measure the actual response of the bender element transmitter (T_x) and receiver (R_x) inside different media such as air, liquids, and sand under different confinements. Then, the dynamic characteristics of the T_x are measured using advanced modal analysis techniques originally developed for structural applications (e.g. Blind Source Separation). The modal analysis is used to investigate if the different BE vibration modes correspond to a cantilever beam, as currently assumed or a cantilever plate. The R_x is also studied to assess the effects of compressional waves, the total damping of the BE system inside the medium on the actual evaluation of the shear wave velocity of the soil. In addition, the dependence of the

output voltage from the R_x and the applied strain is investigated at different confining pressures. The thesis concludes with the dynamic characterization of a sensitive clay (Leda clay) that is present in large areas of Eastern Canada (Leda or Champlain sea clay) BE and RC tests are performed on unique undisturbed samples.

All results presented in this study represent to the averages of multiple tests (more than 10 for RC and more than 500 for BEs). In all cases, the maximum coefficient of variance was 3 % which demonstrates the repeatability of the measurements. Contrary to a common assumption in BE testing, measurements on the transparent soil show that the T_x response inside the specimen is significantly different from the actual input voltage. In addition, BE measurements in soil and oil show that the time delay between input excitation and T_x response is not constant but it decreases with the increase in frequency. Results from the modal analysis of the T_x show a cantilever beam deformation (2D) only for the first mode of the T_x response in air and liquids; however, the response inside the soil specimen (no confinement) shows a cantilever plate behavior (3D). The excitation frequency in BE test should not be constant as commonly done; but it should be increased at each confinement level to match the increase in natural frequency and improve the signal-to-noise ratio.

The overall damping ratio of the T_x increases up to 30% with confinement because of the soil-BE interaction, causing additional challenges in the evaluation of shear wave velocity and damping ratio from BE tests. The measured BE-system response shows a significant *p*-waves interference that affects the evaluation of the shear wave velocity. The *p*-wave interference must be carefully evaluated for the correct interpretation of the results. The *p*-wave interference is clearly observed when the R_x response is measured inside different liquids. This interference increases with the increase in the excitation frequencies. The R_x response in the transparent soil shows that participation of high frequencies and the interference of *p*-waves increases with increase in confinement. The *p*-wave arrivals mask the shear wave arrivals; which can lead to the overestimation of shear waves by more than 25 %. The results from the RC and BE tests on fused quartz and Leda clay specimens confirm the conclusion that high input frequencies enhance the generation of *p*-waves. The theoretical relationship between the maximum BE displacement and maximum input voltage for the T_x or the maximum output voltage for

the R_x is verified for the first time for liquids and sands at no confining pressure. The peak displacements at the tip of the BE increased linearly with the input voltage because the maximum displacement in a piezo-electric transducer is proportional to the applied voltage. RC and BE tests performed on four Leda clay samples showed the effects of shear strain, confinement, and excitation frequency on shear modulus and damping ratio of the Leda clay. The effect of frequency is evaluated using a recently proposed methodology called the 'carrier frequency' (CF) method. The stiffest sample displayed the highest degradation with the increase in shear strain. There is a 15 % difference observed between the shear wave velocity estimates from RC and BE tests. The RC tests at frequencies below 100 Hz showed no effect of loading frequency on shear modulus and damping ratio; however, BE tests at frequencies centred at 12kHz did show a 15% change in wave velocity. This change could be attributed to the loading frequency or to the complex interaction of between *p*-waves and *s*-wave in BE testing. Loading frequency in BE tests does have a significant effect in the results, up to 40% error in the estimation of s-wave velocity, as the interaction between *p*-waves and *s*-waves increases with frequency.

Acknowledgements

First of all, I would like to thank the Almighty for granting me the opportunity and power to work for my PhD. Then, I am very thankful to my supervisors, Dr. Giovanni Cascante and Dr. Dipanjan Basu for allowing me to work with them. Their invaluable support and guidance have been critical in bringing me where I am right now. They have inspired me to think scientifically while dealing with any problem, whether the problem is related to my studies, career, or problems of life in general. My understanding of the fundamentals of maths and engineering has taken a huge leap from where I was when I started my PhD in 2013 because of my supervisors' guidance. On top of that, their moral support has taught me numerous life lessons using which I was able to navigate though these tough PhD years. They never left me alone and were always there to help me, specially during the family problems I went through in the last couple of years.

My dear and extremely supportive parents, loving and caring wife, wonderful kids, Ali Amena and Ahmed, and lovely sisters have been tremendous in their support and assistance during my PhD. Without their support, this PhD would not be possible.

I am thankful to the committee members of my thesis, Dr. Sriram Narasimhan, Dr. Shunde Yin, and Dr. Eihab Abdul-Rahman, for taking time out of their busy schedule to examine my thesis and for providing valuable suggestions and feedback. Special thanks to the external member, Dr. Siva Sivathayalan, who agreed to be the external examiner and travel all the way from Ottawa to attend my defense.

I would like to thank Dr. Ayan Sadhu from University of Western Ontario and Dr. Kamelia Atefi Monfared from the University at Buffalo for their contributions in Chapters 5 and 6 of this thesis respectively.

Heavily indebted to the funding support from the Ministry to Transportation, Ontario (specially Dave Dundas), NSERC, Department of Civil Engineering at UW, and Graduate studies office.

I am very grateful to all my friends in the NDT and geotechnical groups at University of Waterloo for their persistent support and motivation: Dr. Hassan Ali (my first contact at University of Waterloo after the professors), Dr. Maria Jose Rodríguez (wonderful lady),

Fredy Diaz-Duran (a delightful friend and my first office mate), Dr. Sabah Fartosy, Dr. Bijan Mahbaz, Dr. Kamelia Atefi, Dr. Fernando Tallavo, Dr. Wei Zhang, Dr. Bipin Gupta, Piotr Wiciak and his wife Paula, Cristobal Lara, Dr. Ammar Shakir, Dr. Taher Ameen, Faraz Goodarzi, Mehdi Fazaeli, Mathieu Finas.

I don't think I will be able to find a better team of lab technicians than those at the civil engineering labs at University of Waterloo. They have helped me so much that I am not able to thank them enough: Terry Ridgeway, Anne Allen, Mark Sobon, Peter Volcic, Douglas Hirst, Richard Morrison and Jennifer Moll (chemical engineering).

Thank you to the machine shop experts whom I have constantly bugged to get help from them: specially Phil Laycock, Fred Bakker, Mark Kuntz and Jorge Cruz. I would like to also appreciate the help from the administrative staff at the Civil Engineering Department specially Victoria Tolton, Ellie Clark, Nicole Schmidt, Shirley Springall, Chris Peace, Paul Thompson and Kevin Rampersad (IT experts).

Thanks to all the students whom I have TA'd and have shown their appreciation of my efforts, specially the Fall 2016 class of Linear Algebra who nominated me for the Sandford-Fleming award.

I would like thank Dr. Zahid Khan from the American University of Sharjah for his support and guidance and Dr. Richard Bathurst from Royal Military College of Canada for his fused quartz and mineral oil supplies. Thanks to Dr. David Brush and Dr. Leo Rothenberg for their words of encouragement. Thank you to Rob Sibley, Corinne Cory, and Kiyomi Schwartz from Petro-Canada for their free supply of mineral oils.

Finally, thanks to everyone whom I have missed above and who helped me directly and indirectly during my studies. I highly appreciate the financial support from the Canadian government which has greatly helped me survive these years.

Dedication

I dedicate this work to all people around the world who are suffering from hunger, homelessness and life threating situations. May peace be in your lives.

Table of contents

Table of Figures

List of symbols

G – Shear modulus

G_{max} – shear modulus at low strain.

ξ – Damping ratio

V_s – shear wave velocity of soils

ω_n – radial resonance frequency

f_n – resonance frequency

L_b – bender length

b – bender width

h – bender thickness

ρ_b – bender mass density

ρ_L, ρ – mass density of liquid

ρ_s – mass density of the soil sample

μ – viscosity of liquid

E_b – bender Young's modulus

T_x – bender element transmitter

R_x – bender element receiver

f_c – central frequency

1 Introduction

Earthquakes are some of the most devastating natural disasters that cause tremendous damage to the economy. Even low intensity earthquakes have the potential to cause significant damages because the earthquakes impact most the infrastructure (e.g. bridges, buildings, roads etc.) which is typically worth millions of dollars. Earthquake damages can be mitigated if a reliable procedure of seismic design of structures is used. Accurate understanding of soil behavior in response to seismic loads is highly important for a reliable seismic design. Even very low magnitude earthquake waves (Magnitude < 4.0) can be amplified by up to six times by some soils before the earthquake waves reach the surface (Crow et al. 2011; Atkinson and Cassidy 2000). Past occurences (e.g. Mexico City 1985) have shown that site amplified earthquakes waves have caused more damages than the actual earthquake would have caused. Many modern building and bridge codes, such as the National Building Code of Canada (NBCC 2015), now require mandatory seismic design checks for structures depending on site class. The Canadian Highway Bridge Design Code (CHBDC) will be introducing a dedicated section for seismic design in 2020. Therefore, solid understanding of controlling the soil response to seismic loads is critical in seismic design of structures.

The most important dynamic properties governing the soil response to seismic loads are shear modulus (G) and damping ratio (ξ) because they define the soil behavior in geotechnical earthquake engineering problems such as seismic design of foundations, liquefaction, slope stability, etc (Kramer 1996). Shear modulus is a measure of the stiffness of the soil while damping ratio is a measure` of energy dissipation in the soil. Shear modulus at low strain levels (G_{max}) is related to another dynamic property of soils called the shear wave velocity (V_s). Seismic designs in all major codes require sites to be classified into different classes based on the average shear wave velocity of the top 30 m of the soil profile, and different site classes have different seismic design requirements. Knowing that these dynamic properties govern the dynamic soil behavior, accurate estimation of these dynamic properties is critical for a reliable seismic design.

There are only two laboratory tests available to measure these dynamic properties of soils at low shear strains which represents seismic loads ($\gamma < 10^{-3}$); they are bender elements (BE) and resonant column (RC) tests. Field tests such as seismic cone penetration (SCPT) and downhole (DHT) tests are also used to estimate the dynamic properties of soils at low strains; however, errors and inconsistencies are more difficult to control in the field than in laboratory. Therefore, laboratory methods are preferred over field tests to understand the effects of different factors on the dynamic properties of soils at low strains.

BE test is a widely used and simple-to-operate laboratory test for measuring V_s. RC test is an ASTM standard test widely used for measuring G and ξ of the soil at strains between 10^{-4} % and 10^{-2} %.

The loading frequency ranges of BE (1 – 15 kHz) and RC (20 – 220 Hz) tests are different from the loading frequency range of seismic loads (0.1 – 10 Hz). The effects of loading frequency on dynamic properties of soils are not understood well, therefore, the estimated dynamic properties of soils are not representative of seismic loading frequency. In addition, BE and RC tests have their own limitations which limit the reliability of the measured dynamic properties of soils using BE and RC tests. A major limitation in BE test is that the BE test procedure has not been standardized yet because the actual behavior of the benders when inserted in the soil specimen is not well understood. In RC test, the induced shear strain of soil the sample is not the same for all frequencies at which the transfer function is estimated because the shear strain and loading frequency cannot be controlled independently.

1.1 Research Objectives

The main objectives of this study are to understand better the soil-BE interaction; which will provide the basis for the development of reliable guidelines for BE testing; and to verify the BE test results using the standard RC device. Below is a list of sub-objectives and the tasks associated with the sub-objectives:

1. To understand the BE transmitter behavior inside the soil sample. This objective is achieved by evaluating the BE transmitter behavior with different input excitations, in multiple surrounding media, and under varying vertical stresses using time domain data. The time domain data is measured using a state-of-the-art laser vibrometer in air, liquids of different mass densities and in a transparent soil specimen.
2. To evaluate whether the BE behave as a cantilever beam and to investigate BE-soil sample interaction. This objective is achieved by extracting dynamic properties of the transmitter in different media. Resonance frequencies, damping ratios and vibration mode shapes of the BE-transmitter in variable conditions are determined by performing experimental modal analysis of the transmitter. A thoroughly calibrated numerical model of the transmitter is used to advance the understanding of the BE-soil sample interaction.
3. To understand the BE transmitter and receiver system behavior inside the soil specimen. This objective is accomplished by evaluating simultaneously the response of BE transmitter and receiver with different input excitation frequencies and amplitudes and in multiple surrounding media. Again, the measurements are obtained using a laser vibrometer.
4. To evaluate the low-strain behavior of Leda clays which are found in abundance in Easter Canada. The effects of shear strain and confinement on the low-strain dynamic properties of Leda clays are evaluated using the carrier frequency (CF) and equal strain (ES) methods along with the conventional RC method. Effects of loading frequencies are investigated using the CF method and by comparing the RC and BE test results.

1.2 Thesis organization

This thesis is divided into eight chapters with four of them including the work submitted/to be submitted to journal papers. Chapter 1 discusses the motivation, research objectives and thesis organization.

Chapter 2 presents the theoretical background of the concepts used in this study such as the wave propagation and linear-time invariant systems.

Chapter 3 presents the literature review of the dynamic properties of soils. First, the factors affecting the dynamic properties are discussed. Then, the methodologies used for measuring these dynamic properties at different strains and frequencies are presented. Finally, background of the BE and RC tests is discussed.

Chapter 4 presents the evaluation of the frequency response of the BE transmitter. First, the BE transmitter response in air is evaluated using different input excitations. Then, the transmitter is inserted in liquids of different viscosities and densities. Finally, the transmitter responses in transparent soil under different vertical stresses are evaluated.

Chapter 5 is an extension of Chapter 4 in which modal characteristics of the transmitter is discussed using the results of experimental modal analysis of the transmitter in different surrounding media and the effects of these media on the vibration modes of the transmitter is evaluated. A numerical model of the BE-transmitter is developed based on experimental results in air; then, the model properties are changed to match the numerical model responses in different media to the experimental responses.

Chapter 6 presents the study of BE receiver behavior in air, liquids, and in transparent soil sample. BE transmitter and receiver responses are compared in different media. The effects of input voltage amplitude, input excitation frequency and liquid mass density on the receiver behavior are evaluated.

Chapter 7 presents the study of low-strain dynamic properties of leda clays using RC equipment with different interpreting techniques.

Chapter 8 presents the conclusions and future research. Main conclusions of this study related to the advancement of BE and RC tests are summarized. Then, the future work required is described.

2 Theoretical Background

2.1 Wave propagation in a finite elastic medium

Review of wave propagation theory in a bounded medium is essential for understanding the analytical concepts of Resonant Column and Bender Element techniques. In general, wave propagation with laboratory techniques allows the study of soil behavior without significantly affecting the soil specimen. The frequency dependent velocity and attenuation of waves are widely used to estimate material properties. Different types of waves have been studied; this study focuses on shear wave propagation because the governing dynamic stiffness parameter of soils is the shear modulus (*G*). However, equivalent explanations can be presented for Young's modulus (compressional waves) because wave equation is the same for both compressional and shear waves. The one-dimensional (1D) wave equation for torsional vibrations in a rod is derived and solved next, followed by relating the 1D wave equation/solution to BE and RC tests (Richart et al., 1970).

A torque (*T*) is applied on a transverse section of a rod and the response is the twist angle (θ) as shown in Fig. 2-1 below.

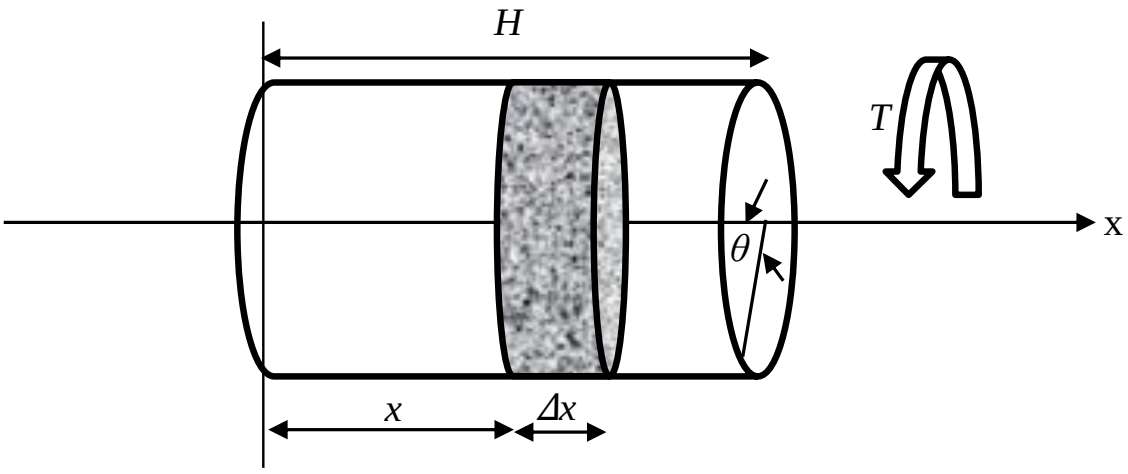

Fig. 2-1: Torsion and twist angle in a rod

T and θ are related through the equation

$$T = GJ\frac{\partial\theta}{dx} \tag{2.1}$$

where J is the polar moment of inertia of the cross-section of the rod, and $\frac{\partial\theta}{dx}$ is the twist angle per unit length.

Furthermore, the rotational inertia in an element of the rod of length Δx is equal to the torque which can be written as

$$T = \rho\Delta xJ\frac{\partial^2\theta}{\partial t^2} \tag{2.2}$$

where ρ is the mass density of the rod and $\frac{\partial^2\theta}{\partial t^2}$ represents the rotational acceleration.

Fig. 2-2 shows the rod of length Δx. Newton's second law is applied to get

$$-T + (T + \frac{\partial T}{\partial x}\Delta x) = \rho\Delta xJ\frac{\partial^2\theta}{\partial t^2} \tag{2.3}$$

which on simplification becomes

$$\frac{\partial T}{\partial x} = \rho J\frac{\partial^2\theta}{\partial t^2} \tag{2.4}$$

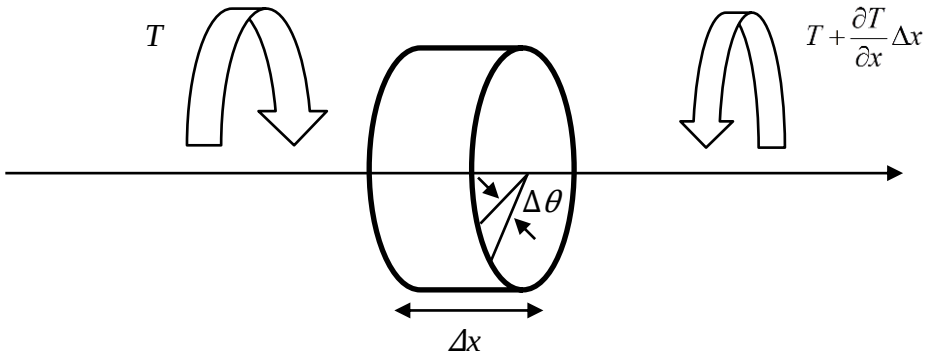

Fig. 2-2: Torsion in a small element

Substituting Eq. 2.1 into Eq. 2.4 gives

$$\frac{\partial}{\partial x}\left(GJ\frac{\partial \theta}{\partial x}\right) = \rho J\frac{\partial^2 \theta}{\partial t^2} \tag{2.5}$$

and simplifying Eq. 2.5 results in

$$\frac{\partial^2 \theta}{\partial t^2} = V_S^2\frac{\partial^2 \theta}{\partial x^2} \tag{2.6}$$

where V_s is the wave velocity of the shear waves in the rod given by

$$V_S^2 = \frac{G}{\rho} \tag{2.7}$$

Eq. 2.6 is the one dimensional wave equation for a finite elastic medium (Richart et al. 1970). This equation is a linear partial differential equation with constant coefficients; hence, superposition of solutions is applicable. For a finite rod, the solution to Eq. can be written as a trigonometric series solution in the form

$$\theta = A(C_1\cos\omega_n t + C_2\sin\omega_n t) \tag{2.8}$$

where θ is the twist angle along the length of the rod, C_1 and C_2 are constants, and ω_n is the natural frequency of nth mode of vibration of the rod.

Eq. 2.8 represents the torsional vibration of the rod in a natural mode which can be substituted in Eq. 2.6 to obtain

$$\frac{d^2A}{dx^2} + \frac{\omega_n^2}{V_S^2}A = 0 \tag{2.9}$$

where

$$A = C_3\cos\left(\frac{\omega_n x}{V_S}\right) + C_4\sin\left(\frac{\omega_n x}{V_S}\right) \tag{2.10}$$

Eq. 2.10 represents the displacement amplitude of the rod and the constants C_3 and C_4 depend on the boundary conditions. The relevant boundary conditions for this study are fixed and free ends. Fig. 2-3 shows the rod with fixed free boundary conditions. At the left end (x = 0), A = 0 and $\partial A/\partial x$ = 0 is zero at the right end (x = H).

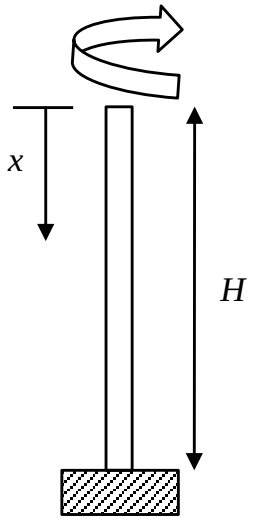

Fig. 2-3: Rod with fixed-free boundary conditions

Substituting $x = 0$ in Eq. 2.10 yields $C_3 = 0$. For C_4, Eq. 2.10 is differentiated with respect to x. The result is

$$\frac{dA}{dx} = \frac{\omega_n}{V_S}\left(-C_3 \sin\frac{\omega_n x}{V_S} + C_4 \cos\frac{\omega_n x}{V_S}\right) \qquad 2.11$$

Substituting $x=H$ in Eq. 2.11 will result in the transcendental equation

$$\cos\left(\frac{\omega_n H}{V_S}\right) = 0 \qquad 2.12$$

Eq. 2.12 represents the mode shape function for a fixed free rod in torsional mode. To satisfy Eq. 2.12, which results in

$$\omega_n = \frac{n\pi V_S}{2H} \text{ for n = 1, 3, 5..} \qquad 2.13$$

Hence, Eq. 2.10 can now be written as

$$A = C_4 \sin\frac{n\pi x}{2H} \qquad 2.14$$

2.1.1 Bender Element (BE) test

The wave propagation theory in BE test is relatively simple; travel time of the elastic shear waves along the length of the rod is used to estimate *G* using Eq. 2.7. If a torsional wave takes the time (*t*) to travel along the rod of length (*H*), then *G* can be estimated as

$$G = \rho \frac{H^2}{t^2} \tag{2.15}$$

where $V_S = H/t$ is substituted in Eq. 2.7 and ρ is the mass density of the rod.

2.1.2 Resonant Column (RC) test

In RC test, the soil specimen is assumed as a continuous, linear elastic, isotropic and homogenous cantilever solid cylinder; therefore, the wave equation (Eq. 2.4) will apply. The driving and motion monitoring instruments are attached at the free end of the soil specimen. Theoretically, the effects of these instruments are combined into a lumped mass (Fig. 2-4); this lumped mass changes the boundary condition at the free end. Therefore, Eqs. 2.12 - 2.14 are not applicable. Following are the modifications corresponding to the boundary conditions in RC test theory.

A torque (*T*) is applied at the free end for inducing the torsional vibrations. This torque is equal to the rotational inertia of the lumped mass

$$T = \frac{\partial \theta}{\partial x} GJ = -I_o \frac{\partial^2 \theta}{\partial t^2} \tag{2.16}$$

where I_o is the mass polar moment of inertia of the lumped mass and *J* is the polar moment of inertia of the rod.

Since $A = 0$ at $x = 0$, $C_3 = 0$ in Eq. 2.10. For $x = H$, we find $\partial\theta/\partial x$ and $\partial^2\theta/\partial t^2$

$$\frac{\partial \theta}{\partial x} = \frac{\partial A}{\partial x}(C_1 \cos \omega_n t + C_2 \sin \omega_n t)$$

and

$$\frac{\partial^2 \theta}{\partial t^2} = -\omega_n^2 A(C_1 \cos \omega_n t + C_2 \sin \omega_n t)$$

Eq. 2.16 is substituted in the above to get

$$GJ\frac{\partial A}{\partial x} = I_o \omega_n^2 A \qquad 2.17$$

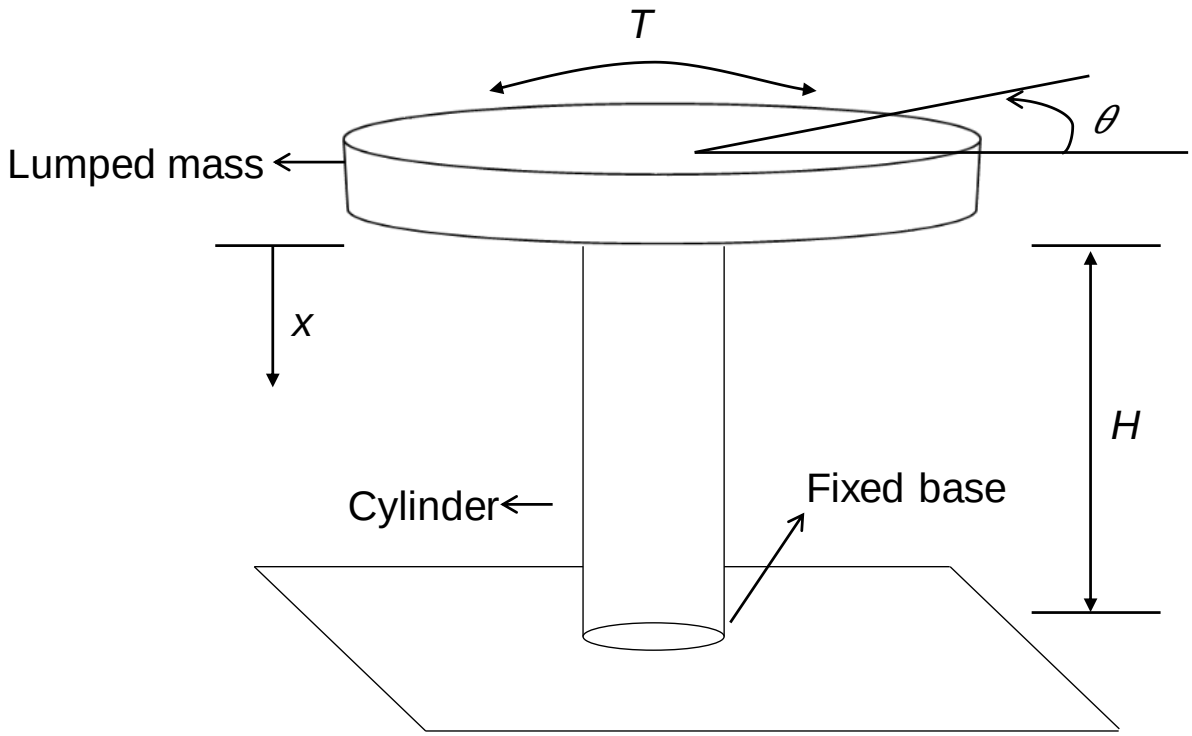

Fig. 2-4: Cantilever cylinder with rigid mass at the free end

Then, Eq. 2.14 and its derivative are substituted in Eq. 2.17 for $x = H$ to obtain

$$GJ\frac{\omega_n}{V_s}\cos\frac{\omega_n H}{V_s} = \omega_n^2 I_o \sin\frac{\omega_n H}{V_s} \qquad 2.18$$

Knowing that $I = J\rho H$ for a uniform rod, Eq. 2.18 can be reduced to

$$\frac{I}{I_o} = \frac{\omega_n H}{V_s}\tan\frac{\omega_n H}{V_s} \qquad 2.19$$

where I is the mass polar moment of inertia of the rod.

The above procedure shows how the 1D wave propagation equation can be used with RC test boundary conditions to estimate V_s of the soil by knowing the resonance frequency (ω_n) of the specimen. Similarly, V_s can be estimated using BE test conditions.

Eq. 2.15 actually represents in the relationship of shear modulus at low strains (G_{max}) with V_S

$$G_{max} = \rho V_S^2 \qquad 2.20$$

BE tests are not typically used for estimating the damping ratio (ξ) of the soil. In RC tests, ξ is determined independently using the phenomenon of attenuation of waves.

2.1.3 Attenuation

Attenuation of waves is the decrease in amplitudes of the waves in space. Main causes of attenuation are geometric spreading, apparent attenuation, and material losses (material damping ratio) (Winkler and Nur 1979). All of these causes are represented by parameters to define attenuation. The focus in this study will be on the parameters of attenuation which represent material losses. Following are the definitions of these parameters:

2.1.3.1 Damping ratio (ξ)

Damping ratio is defined as the ratio between system damping and critical damping. For a single degree of freedom system, the equation of damping ratio is

$$\xi = \frac{c}{c_{cr}} = \frac{c}{2\sqrt{km}} \qquad 2.21$$

where c_{cr} is the critical damping coefficient, c is the system damping coefficient, k and m are the stiffness and mass of the system respectively. c_{cr} is the boundary between oscillatory and non-oscillatory motion. For underdamped system $c < c_{cr}$, for critically damped, $c = c_{cr}$, and for over-damped, $c > c_{cr}$

2.1.3.2 Logarithmic decrement

This parameter is estimated using the method of free vibration; it is defined as the natural log of two successive amplitudes of free vibration of the system. The expression is

$$\delta = \frac{1}{n} \ln \frac{u_i}{u_{i+n}} \qquad 2.22$$

where u_i represents the maximum amplitude of i^{th} cycle and n is the number of cycles between the two amplitudes.

2.1.3.3 Quality factor

For a linear visco-elastic medium, attenuation can be quantified using the complex modulus

$$G^* = G_R + iG_I \qquad 2.23$$

where G_R is the storage modulus (real or elastic component) and G_I is the loss modulus (imaginary or viscous component). Quality factor (Q) is defined as the ratio between G_R and G_I. Q can also be estimated using the half-power bandwidth method (section 3.2.1). The damping ratio and logarithmic decrement are parameters typically used to determine the material damping in conventional RC testing. These parameters are measured using methods such as half-power and free vibration (section 3.2.1). The shear modulus is determined independently even though soil behaves as a visco-elastic medium even at very low strains (Lo Presti et al. 1997).

2.2 Linear time-invariant (LTI) system

The concepts of laboratory methods used in this study for measuring the dynamic properties of soils are based on the assumption that the system of soil specimen and the equipment are LTI because the strain levels in these techniques are in very small to small range.

Analysis of systems which are linear and time-invariant is significantly simpler than that of other systems. The assumption of LTI system facilitates the *system identification* problems (explained below). A time-invariant system is the one which does not change its characteristics over time; a linear system is the one in which the superposition principle

can be applied i.e. sum of time-shifted input is directly related to the sum of time shifted output. Details of LTI systems such as their properties can be reviewed from Santamarina and Fratta (2005).

2.2.1 System identification in time domain

The mass-dashpot system is a single-degree-of-freedom (SDOF) LTI system which is represented by the equation of motion

$$m\ddot{y} + c\dot{y} + ky = f \tag{2.24}$$

where *f* is the input force, *y* is the response, and *m, c,* and *k* represent the SDOF system properties; these properties characterize the LTI system. The problem of identifying these system properties is termed as the 'inverse problem' where an impulse response can be used to determine these properties. An impulse response is the response of the system (for example the mass-dashpot system) when an impulse is applied to that system (*f* in Eq. 2.29 is impulse)

The underdamped impulse response of a SDOF system is given by

$$h(t) = \frac{e^{-\xi\omega_o t}}{m\omega_o\sqrt{1-\xi^2}}\sin(\omega_o\sqrt{1-\xi^2}t) \tag{2.25}$$

where ω_o is the radial resonance frequency, ξ is the damping ratio, and *m* is the mass of the SDOF system.

The advantage of assuming an LTI system is that the impulse response contains all the information about the system. Obtaining impulse response in practice is not possible because the impulse function and its response are mathematical ideologies. The system characteristics are obtained by processing the input and output results in frequency domain (next section). However, if an appropriate analytical model of the system is available, the measured impulse response can be curve-fitted to obtain approximations of the system characteristics.

2.2.2 System identification in frequency domain

Consider again the SDOF system represented by Eq. 2.24. In time domain, an impulse is used as the input force to determine the impulse response. If the input force is replaced by a complex exponential, Eq. 2.24 can be written as

$$m\ddot{y} + c\dot{y} + ky = F_o e^{i\omega t} \tag{2.26}$$

where F_o is the amplitude of the input force. The response of the system then becomes

$$y(t) = H(\omega) F_o e^{i\omega t} \tag{2.27}$$

Substituting *y(t)* in Eq. 2.26 will yield the expression for the transfer function $H(\omega)$ as

$$H(\omega) = \frac{1}{k}\left[\frac{\omega_n^2}{\omega_n^2 + i2\xi\omega\omega_n - \omega^2}\right] \tag{2.28}$$

Eq. 2.28 is a complex function which represents the frequency response function or the transfer function of the SDOF system based on the displacement response (*y*). Similar transfer functions can be obtained for velocity $(\dot{y})$ and acceleration $(\ddot{y})$ responses. They are expressed as

$$H(\omega) = \frac{1}{k}\left[\frac{i\omega\omega_n^2}{\omega_n^2 + i2\xi\omega\omega_n - \omega^2}\right] \qquad \text{for velocity} \tag{2.29}$$

$$H(\omega) = \frac{1}{k}\left[\frac{-\omega^2\omega_n^2}{\omega_n^2 + i2\xi\omega\omega_n - \omega^2}\right] \qquad \text{for acceleration} \tag{2.30}$$

The frequency response functions presented above also completely characterize the system in frequency domain. Although the displacement impulse (Eq. 2.30) and displacement frequency (Eq. 2.33) responses are in different domains, they provide the same system information; therefore, they must be related. Indeed, the frequency response is the Fourier transform of the impulse response expressed as

$$H(\omega) = \int_{-\infty}^{\infty} h(t).e^{-j(\omega t)} \tag{2.31}$$

Similar conclusion can be made for the velocity and acceleration transfer functions.

3 Literature review

3.1 Dynamic characterization of soils

Dynamic response of soils can be studied using either the phenomenological or micromechanical theory (Lai and Rix 1998). Micromechanical theory is a classical approach which is based on the identification of a deformable soil with regions of three-dimensional Euclidean spaces. Soil is modelled as an assembly of interacting rigid or deformable discrete particles. However, in phenomenological theory, soil behavior is studied via causes and effects at a macro level. Micromechanical theory is further divided into the framework of discrete and continuum mechanics which are based on different mathematical models. Neither micromechanical nor phenomenological theories incorporate comprehensive features of soils, particularly of soils under cyclic loads (Lai and Rix 1998). Both theories can provide reasonable results if the problem under consideration satisfies the assumptions of that model. While recognizing the importance of studying soil response at a microscopic level, phenomenological approach has been adopted in this study to model the dynamic behavior of soils.

3.1.1 What are the dynamic properties of soils?

The mechanical behavior of soils in response to dynamic (or cyclic) loading is governed by the dynamic properties of soils. The two most important dynamic properties of soils are shear modulus (G) and damping ratio (ξ). Shear wave velocity of soils (V_s) is another important soil property which is related to G_{max} i.e. shear modulus at low strains. Solution of various problems in soil dynamics such as seismic design of foundations, soil liquefaction assessment and site response analysis rely on the knowledge of these dynamic properties of soils. Moreover, substantial research has been performed during the past 20 to 30 years to study the response of soils to cyclic loads such as earthquakes or machine vibrations (Lai and Rix 1998, Richart et al. 1970). This research suggests that a better understanding of the dynamic properties of soils can be achieved by understanding the factors that affect these dynamic properties. Numerous testing methodologies have been utilized (phenomenological approach) to understand the factors affecting the dynamic behavior of soils. This is similar to the approach used in

defining the strength of soils whereby triaxial tests are adopted to understand the stress strain behavior of soils.

3.1.2 Factors affecting the dynamic properties of soils

Factors affecting *G and ξ* can be divided into external and internal (Lai and Rix 1998). Internal factors include soil properties such as void ratio, soil type, and in-situ effective stress; external factors correspond to the external actions such as applied shear stress/strain magnitude, shear stress/strain rate, and shear stress/strain duration. This study focuses on the effects of the external factors.

Shear stress/strain magnitude is the most important external factor affecting the dynamic behavior of soils. This magnitude is proportional to the level of shear strain induced in the soils when the soil is subjected to dynamic loads (Vucetic 1994). Dynamic soil behavior is categorized according to the level of shear strain induced in the soil (Vucetic 1994). Table 3-1 shows three types of soil behavior based on the strain level limits defined as γ_L, and γ_V. Values of these strain levels depend on the soil type. For example, for a fully saturated clayey soil with plasticity index (PI) ≈ 50, γ_L = 0.001 % and γ_V = 0.01 %.

Table 3-1: Shear strain levels and the corresponding soil behaviors

Shear strain magnitude	Very small strain	Small strain	Medium to large strain
	$0 < \gamma \leq \gamma_L$	$\gamma_L < \gamma \leq \gamma_V$	$\gamma_V < \gamma$
Soil response	Linear viscoelastic	Non-linear viscoelastic	Non-linear elasto-visco-plastic

γ_L – linear threshold strain

γ_V – volumetric threshold strain

Table 3-1 shows that the dynamic soil behavior can never be perfectly elastic because, even at *very small* strains, energy is dissipated in soil (Lo Presti et al. 1997). In the *small* strain region, the soil experiences permanent deformations; whereas, irrecoverable microstructural changes leading to large deformations in the soils occur in the *medium* to *large* strain range.

In this study, dynamic soil behavior in *very small* strain regions will be investigated. The term *small/low* strain is used instead of *very small* strain in this study.

Stress/strain duration is another external factor affecting the dynamic properties. Stress/strain duration of dynamic loads is equivalent to the number of cycles when the dynamic loads are of cyclical nature. The intensity of effects of duration depends on the shear strain range. Increase in the strain duration (or the no. of cycles) causes a decrease in shear modulus of soils; however, this effect is not significant in the small strain region (Shibuya et al. 1995).

Effects of *stress/strain rate (or frequency)* of dynamic loads applied on soils also depends on the level of shear strains given in Table 3-1. Considerable research has been performed for evaluating effects of frequency at strains greater than γ_L (Lo Presti et al. 1997; Shibuya et al. 1995). The results from these studies have shown that, in general, the increase in excitation frequency causes an increase in shear modulus of the soils, especially in the soils with high plasticity. Frequency effects for *small* strain regions have not been characterized well because of the limitations in methods used for measuring dynamic properties at these strain levels. These limitations are described in the following section

3.2 Methods for measuring low-strain dynamic properties of soils

The effects of loading frequency on dynamic properties can be characterized accurately if reliable techniques are available to measure these dynamic properties of soils. Dynamic properties for small strain regions can be measured using laboratory or field techniques. Field techniques provide more representative estimates of dynamic properties; however, field measurements are affected by several factors such as non-homogeneity of soil layers, radiation damping, and geometric effects. Moreover, all field measurements involve the use of wave propagation phenomenon to measure the dynamic properties of

soils. The wave propagation phenomenon can get extremely complex because the field measurements are performed on large soil mass.

On the other hand, lab measurements can be obtained in an environment where parameters affecting the soil behavior can be controlled. The soil specimens used in a laboratory experiment are usually of a regular shape. The laboratory measurements can also be validated using analytical theories with certain assumptions; therefore, the studies on the effects on dynamic properties can be better conducted using lab techniques. However, lab techniques for *small* strain measurements have limitations and assumptions which make it difficult to evaluate the loading frequency effects. Two common lab techniques available to measure dynamic properties at small strains (10^{-7} % to 10^{-1} %) are resonant column (RC) and bender elements (BE). Fig. 3-1 shows the strain levels achieved along with the loading frequencies in RC and BE tests compared to those of cyclic triaxial (CT) and cyclic direct simple shear (CDSS) tests. Significant gaps in loading frequency range can be observed amongst the different techniques in Fig. 3-1. The inherent methodology of these techniques does not allow over lapping shear strains or loading frequencies.

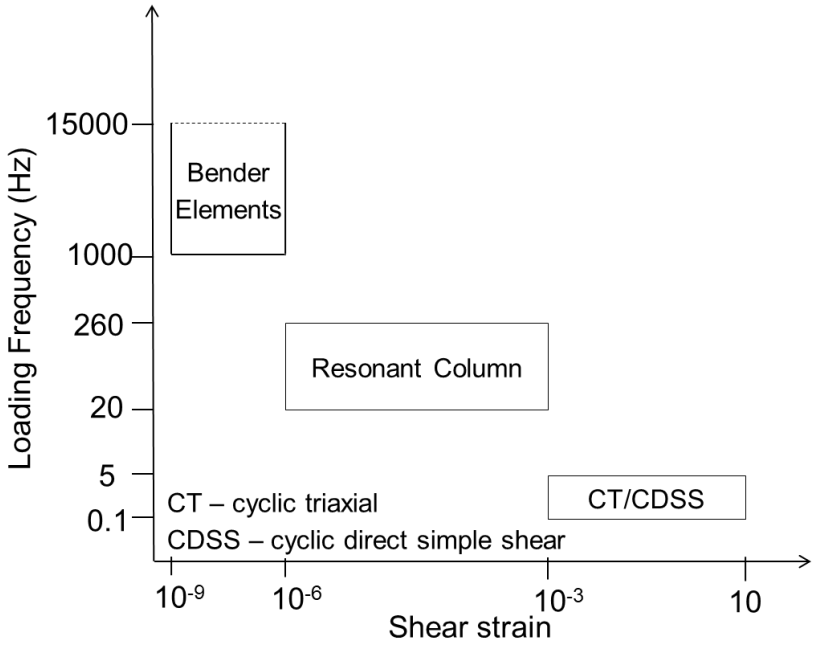

Fig. 3-1: Induced shear strains in common laboratory tests

3.2.1 Resonant Column (RC) test

RC method is an ASTM standardized method used for measuring shear modulus (G) and damping ratio (ξ) at different shear strain levels and confinement stresses. Several types of RC devices have been developed which differ based on the boundary conditions and modes of vibration. Hardin and Richart (1963) developed a device with free-free boundary conditions to measure longitudinal and torsional vibrations; this equipment could only be tested in isotropic conditions. Hardin and Music (1965) added the capability of deviatoric axial loading to the RC equipment which could be operated at strains around 10^{-5}. Then, Drnevich (1967) developed a fixed-free resonant column in which strains up to 10^{-3} could be imposed on the specimen. Several other devices were developed later which combined the torsional shear and resonant column techniques to measure dynamic properties for strains between 10^{-6} to 10^{-1} (Isenhower 1979).

The configuration of RC test with free-free boundary conditions is difficult to simulate because the specimen is never exactly 'free'. Therefore, fixed-free boundary conditions are preferred for RC technique. A solid cylindrical soil specimen is subjected to axi-symmetric loading from an electro-magnetic system with a driving plate attached to the free end; the response is also measured from the free end using accelerometers attached to the driving plate. The driving and response measuring system is accounted in theoretical derivation by a lumped mass (section 2.1.2). The resonance frequency ($\omega_n = 2\pi f_n$) of the soil specimen is measured from the transfer function obtained by performing a sinusoidal frequency sweep of the soil specimen. Random noise has also been used to perform the frequency sweep (Cascante and Santamarina 1997). Theoretical transfer function for the RC test is expressed as (Khan 2007)

$$\frac{T_o(\omega)\mathrm{e}^{-j\omega t}}{\varphi(\omega)} = \left[1 - \left(\frac{\omega}{\omega_n}\right)^2 + j2\xi\left(\frac{\omega}{\omega_n}\right)\right]\omega_n^2\left(I_o + \frac{I}{3}\right) \qquad 3.1$$

where T_o and φ represent the torque (input) and twist angle (output) of the specimen.

Fig. 3-2 shows a typical transfer function from the RC test results. The solution of one-dimensional wave propagation (Eq. 2.37) along with Eq. 3.2 can be used to estimate the value of V_s.

$$\frac{I}{I_o} = \frac{\omega_n H}{V_s} \tan \frac{\omega_n H}{V_s} \qquad 3.2$$

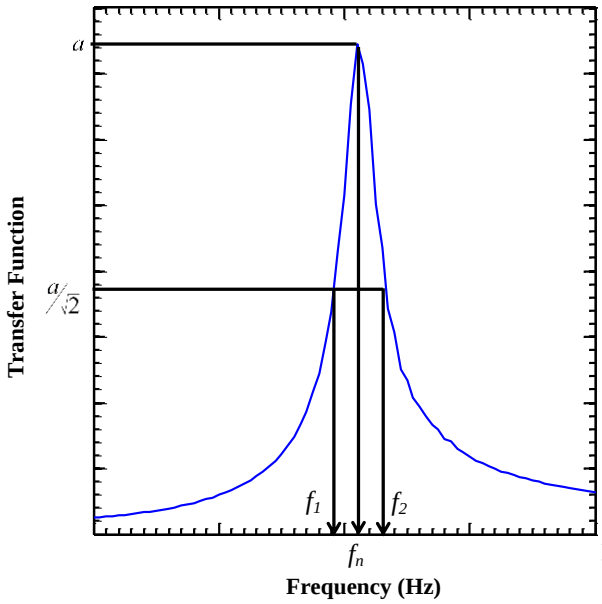

Fig. 3-2: A typical transfer function

The value of I/I_o in Eq. 3.2 is obtained by calibrating the RC system with aluminum or PVC probes of known resonance frequencies (section 7.6.4). Damping ratio (ξ) is typically obtained independently from the half-power bandwidth or free vibration method; these methods are reviewed below.

Half-power bandwidth method: two frequencies (f_1 and f_2) corresponding to the half-power of peak of the transfer function $a/\sqrt{2}$ are measured from the transfer function (Fig. 3-2). Then, the value of ξ is estimated as

$$\xi = \frac{f_2 - f_1}{2f_n} \qquad 3.3$$

Free vibration: In this method, damping ratio is computed using the logarithmic decrement of the free vibration response of the SDOF system (Fig. 3-3); the free vibration response is induced by an initial condition (displacement or velocity). In RC test, the initial

condition is achieved by turning off the driving mechanism which will stop the dynamic excitations. The maximum amplitudes of two cycles are used with Eq. 3.4 below to estimate the logarithmic decrement (δ) (Clough and Penzien 2003)

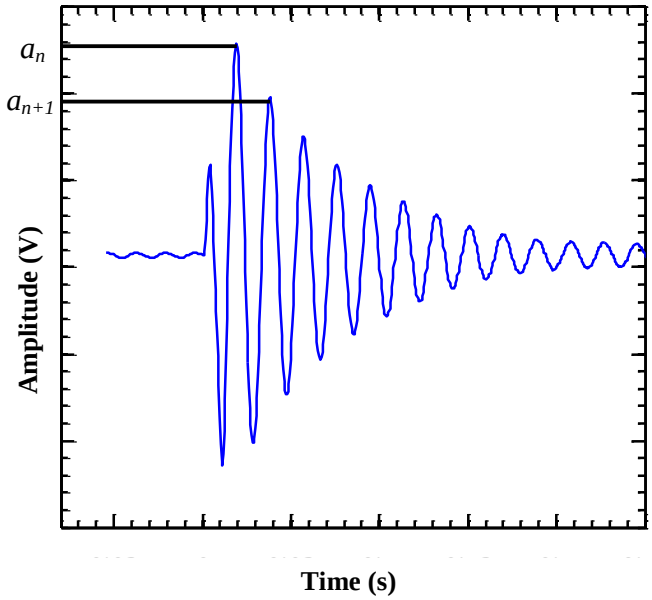

Fig. 3-3: SDOF system response

$$\delta = \ln \frac{a_n}{a_{n+1}} = \frac{2\pi\xi}{\sqrt{1-\xi^2}} \qquad 3.4$$

where a_n and a_{n+1} are obtained from the time domain response (Fig. 3-3).

3.2.2 Bender Element (BE) testing

BE are electro-mechanical transducers capable of converting electrical energy to mechanical and vice versa. A bender element is made up of two thin piezo-ceramic plates bonded together with conducting surfaces in between and outside (Lee and Santamarina 2005). These plates are covered with epoxy material to avoid short-circuiting the transducers. An electrical voltage is applied on to the bender element; due to the polarization of the ceramic material, this voltage elongates one plate and shortens the other. The opposite movement of the plates causes the bender element to bend. On the contrary, when the bender element is mechanically forced to bend, one plate is stretched

while the other is compressed; an electrical voltage is generated as a result of this bending. Fig. 3-4 shows the element in straight and bent positions.

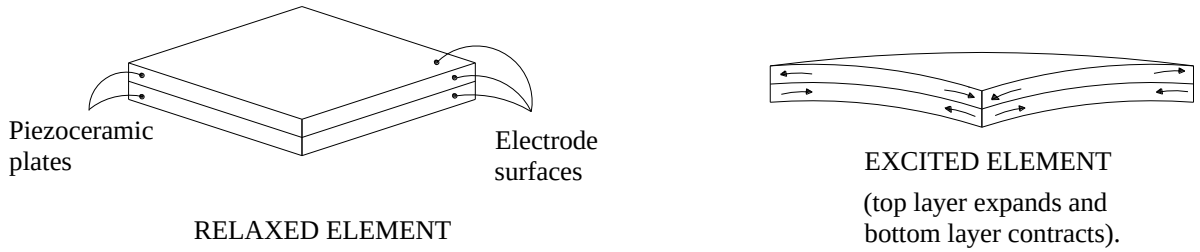

Fig. 3-4: BE in relaxed and excited positions (after Dyvik and Madhsus, 1985)

Bender elements (BE) have been widely used with dynamic geotechnical equipment such as cyclic triaxial and resonant column (Schultheiss 1981); they are attached to the pedestals of these geotechnical equipment and inserted into the soil specimen (Fig. 3-5). BE test method was first proposed by Shirley (1978) and Shirley and Hampton (1978), and has been very popular over the years because of its simple operation. A pair of BE are used where one is the BE transmitter (T_x) and other is the receiver (R_x). The BE transmitter at one end generates a shear wave due to the perturbation caused by the input voltage (Fig. 3-5). This wave propagates along the length of the soil specimen and bends the BE receiver. The electrical voltage generated by the receiver movement is recorded, and the arrival time of the shear wave is determined. The travel time of the shear wave along a known length of specimen gives a direct measure of V_s of the soil specimen (Eq. 2.15). The travel distance of the shear wave is typically the tip-to-tip distance between the BE (Lee and Santamarina 2005).

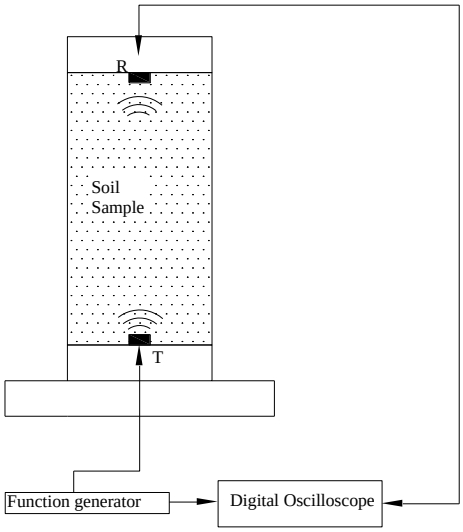

Fig. 3-5: BE with dynamic geotechnical equipment

3.3 Limitations in RC and BE tests

Soil behaves as a visco-elastic medium at small strains for which the dynamic properties should be evaluated simultaneously (Lai et al. 2001). Conventional RC test does not allow simultaneous measurements of G and ξ. Moreover, dynamic properties evaluated using RC test correspond only to the resonance frequency of the specimen; measurements at other loading frequencies are not possible.

The operation of BE test is simple; however, BE testing has not been standardized yet because of difficulty in interpreting BE test results. The difficulty is mainly because, when BE are inserted in the soil specimen, the actual behavior of BE is unknown which makes it challenging to determine accurately the arrival time of the perturbation. Moreover, the frequency of vibration of BE in the soil cannot be determined.

The limitations highlighted above in BE and RC tests make it difficult to evaluate the loading frequency effects on the dynamic properties of soils. An experimental program is proposed in this study to address some of these limitations to allow the evaluation of loading frequency effects on dynamic properties in small strain range. A set of RC tests on Leda clays is performed along with measuring the actual vibrations BE in different media.

4 Novel evaluation of bender element transmitter response

4.1 Introduction

Shear wave velocity of soil (V_s) is an important parameter for seismic characterization of sites and dynamic analysis of structures. The bender element (BE) method is widely used to measure V_s in laboratory specimens (Shirley and Hampton 1978). In this method, two piezo-ceramic transducers (the bender elements) are inserted at the opposite ends of a soil specimen and an input voltage signal is applied to one of the transducers (the transmitter). This signal generates a disturbance in the soil sample, and the mechanical energy from the shear wave propagating through the soil sample is converted to an output voltage signal upon reaching the other transducer (receiver). The distance between the transmitter (T_x) and receiver (R_x), and the shear wave travel time t_s from T_x to R_x are used to estimate V_s (Dyvik and Madshus 1985). Despite its popularity, no standardized procedure is available for the BE method mainly because the response of the BEs inside the soil specimen has not been characterized experimentally.

A few experimental studies have been performed to hypothesize the actual behaviour of BEs inside the soil specimens. Rio (2006) measured, using a laser velocimeter, the response of transmitters in air and under embedded conditions inside a synthetic rubber specimen. Rio (2006) showed that, when bender elements are embedded in synthetic rubber specimens, the natural frequency and damping ratio of transmitter vibration are greater and the amplitude of vibration is less than the corresponding quantities measured when the bender elements are in air. The first mode resonance frequency in air of one of the benders (dimensions 1.5 mm x 6 mm x 8 mm) studied by Rio (2006) is 3.4 kHz. Rio (2006) estimated that the maximum shear strain from the peak BE displacements was of the order of 10^{-3}%, which is inconsistent with the maximum shear strain in BE testing given by previous researchers (Camacho-Tauta et al. 2015; Leong et al. 2005; Pennington et al. 2001). Pallara et al. (2008) used a laser vibrometer to study the response of a transmitter in air and showed that the shape of the transmitter response is different from the shape of the input signal. These studies provide a preliminary insight into the response of BEs inside the soil specimen; however, because of the use of

synthetic rubber specimens in these studies, the response of BEs embedded inside a soil specimen is still not well understood.

A novel experimental program is described in this study in which the actual transmitter vibrations inside a transparent soil specimen are measured using a state-of-the-art laser vibrometer. The transparent soil used in this study has mechanical properties similar to those of granular soils with angular particles (Ezzein and Bathurst 2011). First, the effects of input excitation on transmitter response in air is measured by subjecting the transmitter to sine, step, and square pulse excitations. This exercise is done in two steps: first, measurements are taken at one point located at the centre of the free end of the transmitter surface, and then measurements are taken at several points on the transmitter surface. Then, the effect of voltage amplitude applied on the transmitter response is measured by exciting the transmitter with increasing voltage amplitude of input pulses and measuring the peak displacement using the laser. The effects of mass density and viscosity on the transmitter response are evaluated by measuring the transmitter response in water, sucrose of different concentrations, and mineral oil mixture (liquid used for making the transparent soil). Finally, the transmitter response is measured inside a transparent soil specimen and compared with the input excitation. The effects of applied vertical stress in the transparent soil on transmitter response are also evaluated. The effects on the transmitter responses are characterized using changes in peak displacement amplitude, natural frequencies, and damping ratios, which are obtained from the displacement responses of the transmitter and their frequency spectra. In addition, the effect of input excitation frequency on the relative time shift between input excitation and transmitter responses in air, mineral oil, and soil is studied by analysing the transfer functions between the sine-sweep input excitations and the transmitter responses.

4.2 Background

4.2.1 Estimation of arrival time

In a conventional BE test, the shear waves travel time t_s is computed as the time difference between the input signal $x(t)$ from the transmitter and the output signal $y(t)$ from the receiver (Fig. 4-1). The travel time is associated with the transfer function H_{Soil} which is calculated as the ratio between the frequency spectrum of the output signal $Y(\omega)$ and the input signal $X(\omega)$. However, time delays are introduced at different stages in a BE test because of multiple transfer functions involved (Wang et al. 2007). Fig. 4-1 shows the multiple time delays in a BE test and their associated transfer functions; t_1 is the time delay between the input voltage and the transmitter response with the transfer function H_{Tx}; t_2 is the delay between the transmitter and receiver responses with the transfer function H_{Rx}; and t_3 is the delay between the receiver response and the output voltage with the transfer function H_o. Most of the studies in BE testing have focused on improving the accuracy of t_s because of the difficulty in measuring t_1, t_2, and t_3 and their transfer functions; therefore, the reliability of conventional BE test results has been dependent on the accuracy of the measured t_s. Several factors affect the accuracy of the measured t_s such as quality control in manufacturing of BEs (Lee and Santamarina 2005), coupling and alignment of BEs in the soil specimen (Gohl and Finn 1991), near-field effects (Arroyo et al. 2003), and type of input excitation pulse (Brignoli et al. 1996; Jovicic et al. 1996; Lee and Santamarina 2005).

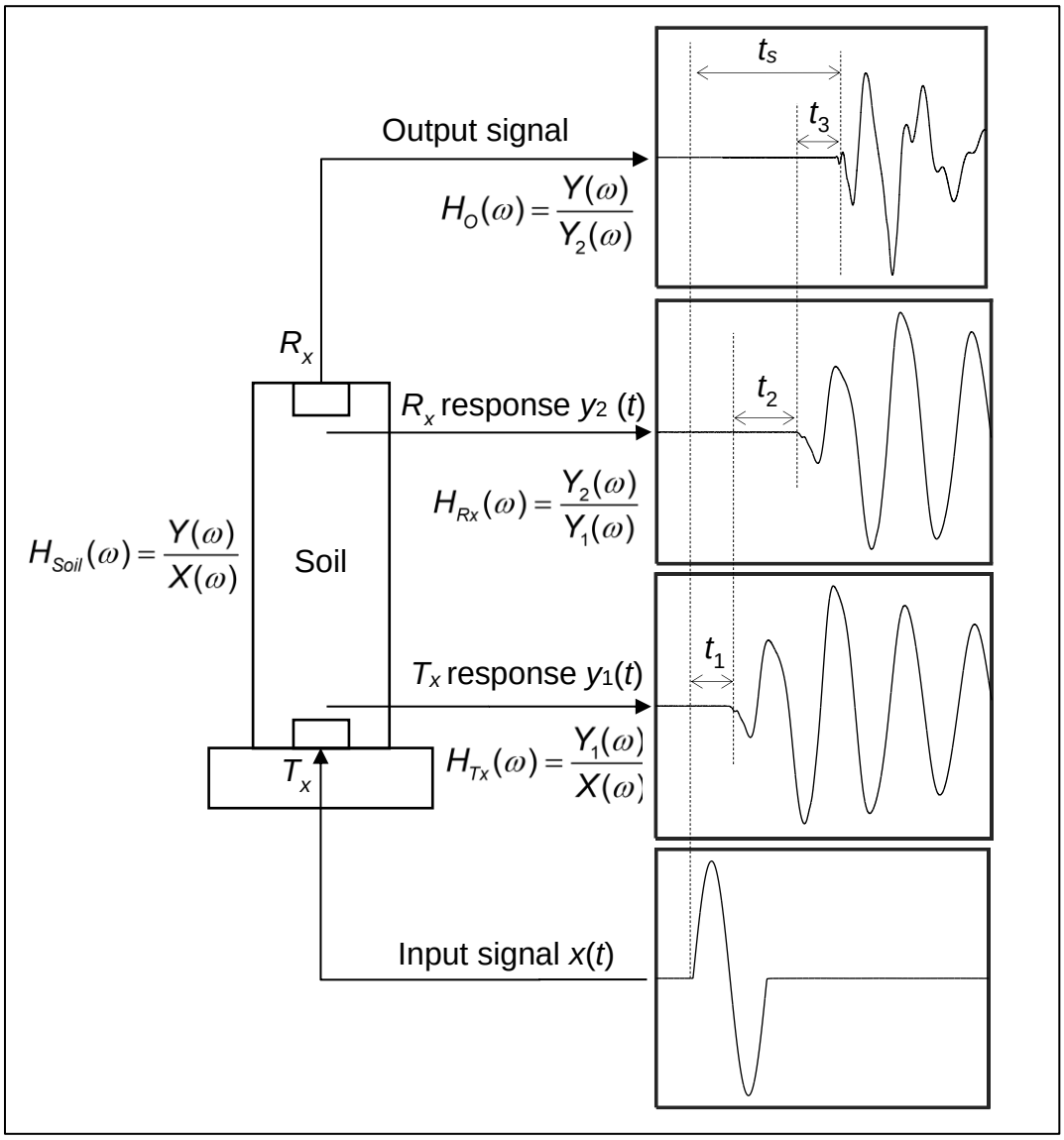

Fig. 4-1: Shear wave arrival times and transfer functions at different stages in a conventional BE test setup

Different time and frequency domain methods have been proposed for accurate measurement of t_s. In the simplest time domain method, the first arrival from the output signal (receiver end) is selected with the assumption that no refracted or reflected waves are present. Individual judgement is used in this method because no agreeable recommendations are available for identification of the first arrival. Measurement of time

difference between characteristic points (such as peaks and troughs) of the input and output signals is also sometimes used in the time domain. An important drawback of this method is the assumption of plane wave propagation without the consideration of reflected or refracted waves. Viggiani and Atkinson (1995) proposed a method of computing cross-correlation between input and output signals. All these methods depend on the assumption that the frequency contents of the input and output signals are the same; however, this assumption is idealistic because input and output signals in soils can never have the same frequency content as the output signal is influenced by the soil and other electronic devices in a BE test. Arulnathan et al. (1998) and Lee and Santamarina (2005) proposed the use of second arrival of the output signal that occurs when the shear wave from the receiver reflects back to the transmitter and then again reflects back to the receiver. However, the second-arrival based methods depend on a particular travel distance and boundary characteristics of the sample; because the boundary conditions and travel distance vary from one BE test setup to another, the second-arrival based methods cannot be generalized to all BE test setups. Further, the second arrival is often very weak to be reliably detected. The existence of different methods for the evaluation of t_s is a direct consequence of the current lack of understanding of the actual response of the BE inside the soil, which the present work addresses.

Several frequency domain methods have been proposed for estimation of t_s because of the limitations of the time domain methods. Discrete π-point identification is a method in which a sinusoidal sweep is performed manually (Sachse and Pao 1978) . The input sine frequencies that result in a perfect phase shift between the signals are picked as the π-point frequencies. Then, Eq. 4.1, which relates input sine frequency f, wave velocity V, wave length λ, travel length of the wave L, and phase angle φ, is used to estimate the phase angle

$$V = f\lambda = 2\pi f \frac{L}{\varphi} \qquad 4.1$$

The plot of phase angle versus frequency is a straight line, and the slope of this line gives an estimate of t_s according to Eq. 4.2:

$$t_s = \frac{1}{2\pi}\frac{d\varphi}{df} \qquad 4.2$$

This frequency domain method is more systematic, but manual sweeping to identify the π-points is time consuming and only a limited number of π-points can be recorded. Greening and Nash (2004) enhanced this method by proposing a setup to perform a continuous and automatic sine sweep rather than discrete and manual; the results from this method include unwrapped phase and coherence plots against the frequency. Viana da Fonseca et al. (2009) used the moving windows algorithm in which the unwrapped phase is plotted for different frequency bandwidths. Alvarado and Coop (2012) used the transfer functions between different voltage inputs and measured voltage outputs to evaluate the performance of the BE system. Camacho-Tauta et al. (2016) estimated V_S using a modified frequency domain method for BE tests and compared the results with those of resonant columns (RC) tests.

Notwithstanding several research studies performed on the estimation of t_s, both the time and frequency domain methods have not provided conclusive recommendations for estimating t_s because the actual behaviour of the BEs inside the soil specimen is not well understood. As the accuracy of all methods depends on the input and output signals, it is important to obtain the actual signal generated by the transmitter and the actual signal received by the receiver for estimation of t_1, t_2, and t_3 (Fig. 4-1). Because the actual signals are not explicitly known, estimation of t_s is approximate even if better methods of estimation are used. Therefore, the actual transmitter and receiver responses must be characterized and estimates of t_1, t_2, and t_3 must be determined along with their transfer functions. This study focuses on characterizing the actual transmitter response under different conditions by putting the transmitter in air, in different liquids, and, especially, in transparent soil, and investigating the variation of the measured time t_1 as function of frequency.

4.2.2 BE vibration

Vibration characteristics of a BE is assumed to be similar to those of a cantilever beam (Lee and Santamarina 2005). The resonance frequency of the n^{th} mode of vibration of a BE in air can be estimated from Eq. 4.3 (Clough and Penzien 2003)

$$f_n = \frac{k_{Ln}^2}{2\pi(\alpha L_b)^2}\sqrt{\frac{E_b I_b}{\rho_b A_b}} \tag{4.3}$$

where k_{Ln} is a characteristic number that depends on n and the boundary conditions; L_b, I_b and ρ_b are the length, area moment of inertia ($I_b = b\ h^3/12$), and mass density of BE, respectively; h, b, and A_b ($A_b = L_b\ h$) are the thickness, width, and cross-sectional area of the BE, respectively; E_b is the Young's modulus of the piezoceramic element; α is the effective length factor with $\alpha = 1$ when the BE is perfectly fixed to the base and $\alpha > 1$ when there is flexibility in connection between the BE and the base.

The resonance frequency of the first mode of vibration of a BE when embedded in soil can be estimated from Eq. 4.4 (Lee and Santamarina 2005)

$$f_1 = \frac{1}{2\pi}\sqrt{\frac{1.875^4\dfrac{E_b I_b}{(\alpha L_b)^3} + \eta E_s L_b}{\rho_b A_b \alpha L_b + (\rho_s b^2 L_b)\beta}} \tag{4.4}$$

where ρ_s and E_s are the mass density and Young's modulus of soil, respectively; β is the experimental factor related to the volume of soil affecting the vibration of BE; and η (≈ 2) is the mean displacement influence factor at the soil-BE interface (Poulos and Davis 1974).

4.3 Materials

Responses of BEs while inserted in multiple liquids including water, sucrose solutions, and mineral oil, and in transparent soil sample made with fused quartz and mineral oil are investigated in this study. These materials in which the BEs are inserted are described in this section.

4.3.1 Sucrose solution

Sucrose solution made with two levels of sugar concentration, 20%, and 40% by weight, are used in this study in addition to pure water (which acted as a base case with 0% sugar concentration). This gives the opportunity to investigate the transmitter response in liquids with different densities and viscosities (different sugar concentrations produced different densities and viscosities) the details of which are presented in Table 4-1. The choice of sucrose is made based on the fact that sucrose can be readily used for making a transparent soil specimen (Guzman and Iskander 2013) and that the effects of different sucrose concentrations on the transmitter response would help in analysing the measurements in transparent soils.

4.3.2 Mineral oil and transparent soil

The mineral oil mixture used in this study is prepared with two mineral oils, namely, Krystol-40 and Puretol-7 (Ezzein and Bathurst 2011; Weast et al. 1981). The mixture is colourless, odourless, and chemically stable. The viscosity and density of this oil mixture are presented in Table 4-1.

Transparent soils have been developed and used in the past for studying many geotechnical problems (Ezzein and Bathurst 2011; Iskander 2010). In this study, the transparent soil developed by Ezzein and Bathurst (2011) is used, and is made up of fused quartz and mineral oil mixture described above. Fused quartz is a noncrystalline form of quartz sand (with silicon dioxide [SiO_2] as the main mineral present), which is widely used in semiconductors, solar cells, and telescopes. The transparency in the soil specimen occurs because of similar refractive indices of fused quartz and the mineral oil mixture. The mechanical properties (such as the shear strength) of this transparent soil are comparable to cohesionless soils of angular shaped particles (Ezzein and Bathurst

2011). The grain size distribution of the fused quartz used in this study is shown in Fig. 4-2.

Table 4-1: Properties of liquids used in this study

Liquid	Viscosity μ (cP)	Density ρ (g/mL)
Mineral Oil	8.2	0.8
Water	1	1
Sucrose – 1 (20% by weight)	1.7	1.1
Sucrose – 2 (40 % by weight)	5.2	1.2

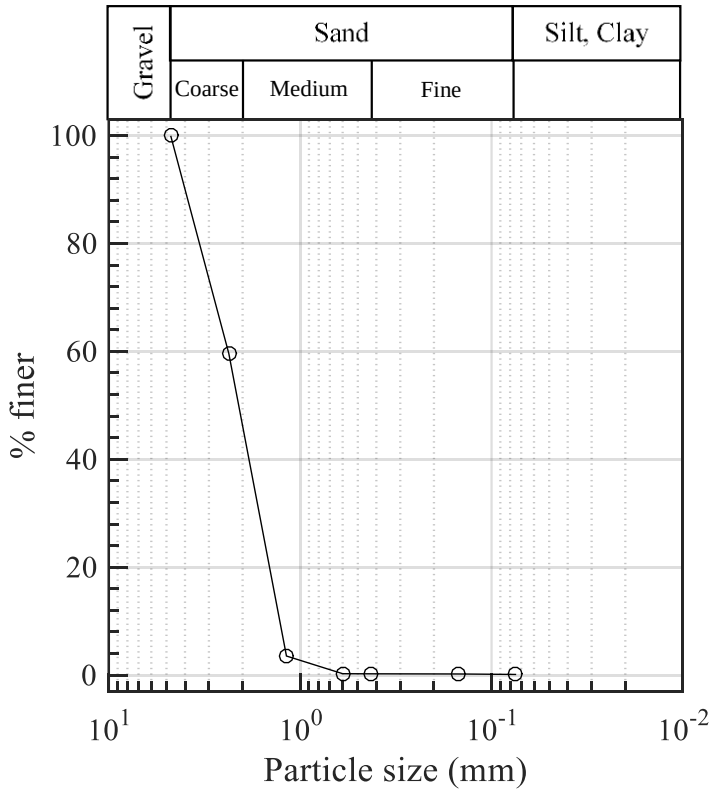

Fig. 4-2: Grain size distribution of fused quartz used to prepare transparent soil specimens

4.4 Experimental setup and specimen preparation

A novel experimental setup consisting of a BE transmitter, peripheral electronics, a laser vibrometer, liquids (as described above), and a transparent soil specimen is used in this study. A typical transmitter is used in this study which is rectangular in shape with surface dimensions of 6 mm $\times$ 14 mm, and a thickness of 1.5 mm, and is attached to a steel base plate. A schematic of the transmitter cross-section and experimental setups in air, in soil without confinement, and in soil under confinement are shown in Fig. 4-3.

The laser vibrometer used in this study is a single point vibrometer developed by Polytec Inc. (Polytec 2013). This device operates on the principle of heterodyne interferometer to obtain the characteristics of the mechanical vibrations (Polytec 2013). The laser beam emanating from the laser head is pointed at the target (transmitter in this case) which reflects back the laser beam. A phase/frequency modulation of the laser light is generated by the displacement/velocity amplitudes of the target because of Doppler effect. Then, the vibration decoder recovers this modulation and converts it into signals that can be displayed on a computer screen. Phase modulation of the Doppler effect is used for displacement information while frequency modulation is used for velocity information. The laser vibrometer is capable of measuring displacements with frequencies up to 24 MHz (Polytec 2013).

A function generator (FG) (model HP33120A) is used to generate an input voltage signal to the transmitter through the steel base; this input signal is monitored on an oscilloscope (HP-54645A) and stored in a computer. The transmitter response to the input voltage is measured by the laser head (LSH) (OFV-5000), which is fixed to an aluminium plate; the laser head measurements are decoded by the vibration controller and the output signal from the vibration controller is also monitored on the oscilloscope and stored in the computer. The steel base is fixed to a positioning stage which allows controlled movements of the steel base along the horizontal plane (moving left/right and into/out of the plane of the paper in Fig. 4-3.). The positioning stage allows transmitter vibrations to be measured at different points on the transmitter surface. The positioning stage can also be moved in the vertical direction manually. The positioning stage and the aluminium plate

are fixed on an isolation table (manufactured by NewPort) to prevent the ambient vibrations from affecting the laser measurements.

The equipment setup for measurements in liquids and transparent soil is similar to that of measurements in air and includes a plexiglass box to hold the liquids and transparent soil in place (Fig. 4-3). A groove in the steel base is used to place an o-ring to prevent the liquid from leaking. The plexiglass box is polished with a polishing liquid to ensure maximum transparency for penetration of laser beam. The liquid is poured in the box gently until the transmitter gets completely submerged. For preparing transparent soil specimen, the mineral oil mixture is poured in the box until the transmitter is fully submerged and then fused quartz particles are placed by wet-pluviation. The application of vertical stress around the transmitter in the transparent soil is made by placing dead weights on top of the transparent soil specimen with the help of a plastic cylinder (Fig. 4-3c).

A reflecting paper is glued on to the transmitter surface to enhance the signal quality of the laser vibrometer, as recommended by Polytec Inc. The distance x between the laser head and transmitter is maintained at 0.5 m for all the tests (Fig. 4-3). All time signals are recorded for a total time of 5 ms with a time interval of 3.2×10^{-5} ms.

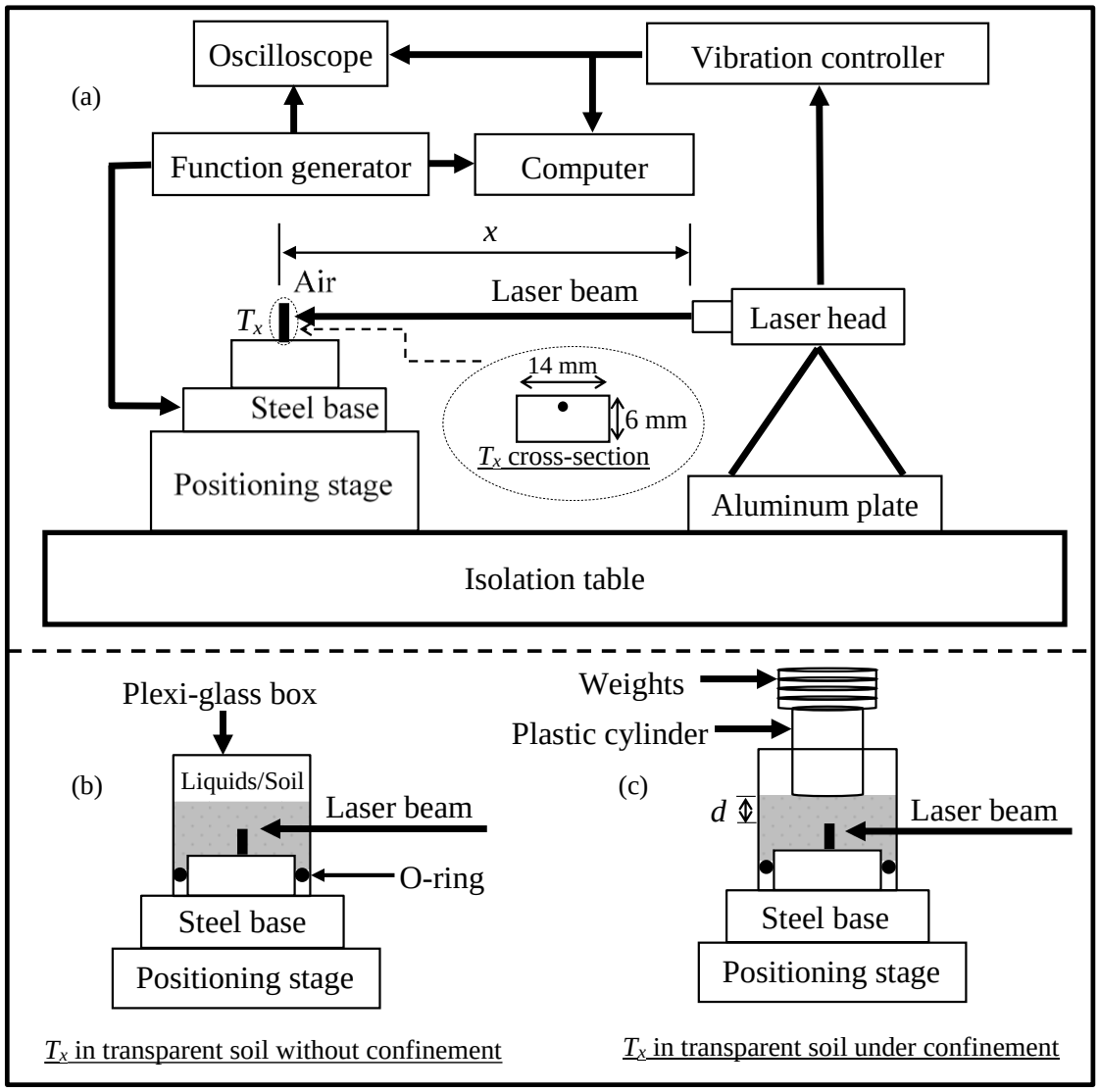

Fig. 4-3: Schematic of measurements (a) in air, (b) in soil without confinement, and (c) in soil with confinement

4.5 Experimental procedure

Actual vibrations of the BE transmitter are measured in different media. For each measurement, an average of 500 time signals is saved as the representative time signal. The standard deviation of the 500 time signals varied from 0.14 to 0.2 for length of the time signals

4.5.1 Measurements in air

Different input excitations have been used in the past in conventional BE testing; the most common excitations are sine, step, and square pulses (Jovicic et al. 1996; Rio 2006). These input excitations are used here to evaluate the effects of different input excitations on the actual transmitter response in air. The central frequency used for the sine and square pulses is 9 kHz because it is close to the first natural frequency of the transmitter used in this study. This first natural frequency is determined from the transmitter response to a frequency sweep (discussed below). First, the effects of input excitations are evaluated at a single point, which is at the centre of the free end of the transmitter (shown in Fig. 4-3 as a solid circle on T_x cross-section). Then, the effects of input voltage amplitude applied on the transmitter response at that single point in air are evaluated. The transmitter is excited with input excitations of different amplitudes and the peak displacements of the transmitter response are measured. Subsequently, the effects of input excitations are evaluated at 102 points on the transmitter surface; thus, for this case, the response of the transmitter is represented by 102 degrees of freedom. The responses of these points are used to simulate the motion of the transmitter, which shows the movement of the transmitter in real time.

4.5.2 Measurements in liquids

Transmitter responses in different transparent liquids are obtained to evaluate the effects of density ρ and dynamic viscosity μ of the liquids on the transmitter response. The effect of plexiglass box is assessed first by measuring the transmitter response with the transmitter placed inside the box without the liquids. Water, sucrose solutions with different concentrations, and the mineral oil mixture are then poured separately to measure the transmitter response at the single location shown in Fig. 4-3 in each of these solutions. After each measurement, the steel plate is unbolted from the positioning stage

to discard the solutions. The box is washed thoroughly before reassembling, and measurements of the response with plexiglass box alone are repeated to ensure repeatability.

4.5.3 Measurements in transparent soil

The transmitter response is measured in the transparent soil specimen (prepared by pluviation of quartz in mineral oil) at the point shown in Fig. 4-3. This measurement represents the case of at rest condition because no weight is placed on the transparent soil. The effect of additional confinement on the transmitter response is evaluated by measuring the transmitter response in the transparent soil after subjecting the soil specimen to different levels of vertical stresses by adding weights on top of the transparent soil specimens in increments of 0.8 kg to generate vertical stresses up to 35 kPa. The applied vertical stress is calculated as the load over the circular area of the plastic cylinder used to transfer the load from the weights to the soil.

4.5.4 Transfer functions in different media

The transfer function of the transmitter is calculated as the ratio of the frequency spectrum of the transmitter response over the frequency spectrum of the input voltage signal. First, the transfer functions of the transmitter responses in air to a sine pulse, a square pulse, and a sine sweep (frequency bandwidth = 0-50 kHz) are calculated. These transfer functions are used to identify the modes of vibration of the transmitter response in air. Then, the transfer function of the transmitter response to a sine sweep in transparent soil is calculated and compared with the transfer function in air. The point on the transmitter where these measurements are made is marked with a solid circle on the transmitter cross-section in Fig. 4-3. The transfer function from the sine sweep is calculated in real time using a dynamic analyser, while the transfer functions from the sine and square pulses are calculated using the frequency spectra of the input and output signals. The frequency spectra of the input and output signals are calculated using MATLAB™.

4.6 Results and discussion

4.6.1 Verification of laser measurements

4.6.1.1 Code test

The reflected laser light from the test object contains the velocity and displacement information. The accuracy of these signals is evaluated here by measuring one set of displacement and velocity response of the bender element in air and compared to displacement and velocity signals using theoretical calculations.

First a set of theoretical displacement and velocity functions are used to verify the MATLAB™ code that is used for evaluating the accuracy of laser measurements. Eq. 4.5 shows the displacement function (x) with two sinusoids which is used for verification.

$$x(t) = A_1 e^{-i\xi_1\omega_1 t}\sin(\omega_1 t) + A_2 e^{-i\xi_2\omega_2 t}\sin(\omega_2 t) \qquad 4.5$$

Where the amplitude of the sinusoids are A_1 = 1 and A_2 = 0.2, the angular frequencies are ω_1 = 2π x 7000 Hz and ω_2 = 2π x 20000 Hz and the damping ratios are ξ_1 = 0.03 and ξ_2 = 0.05. The values for these parameters are arbitrarily selected with the amplitude of the second sinusoid (mode) less than that of the first and the angular frequency and damping ratio of the second mode larger than those of the first. Fig. 4-4 partially shows the plot of Eq. 4.5 against time; although the signal looks like a response of the single-degree-of-freedom system with a single mode, the indications of the second mode are that the maximum amplitude of the signal is less than 1 (maximum amplitude of the first mode is A_1 = 1) and the other indication is circled in Fig. 4-4.

Fig. 4-5 shows the frequency spectrum of the displacement signal *x(t)*. The presence of two sinusoids in *x(t)* is clearly observed from the frequency spectrum. The estimated values of the frequencies (f_1 and f_2) and damping ratios (ξ_1 and ξ_2) are very similar to those that are used to create *x(t)* (Eq. 4.5); however, the relative amplitude of the second sinusoid in the frequency spectrum is significantly less that used in *x* (0.04 compared to 0.2). This difference is because of the loss of energy (leakage) to the higher frequencies because of a sudden increase in the displacement at around time = 1 ms (Fig. 4-4) (Santamarina and Fratta 2005)

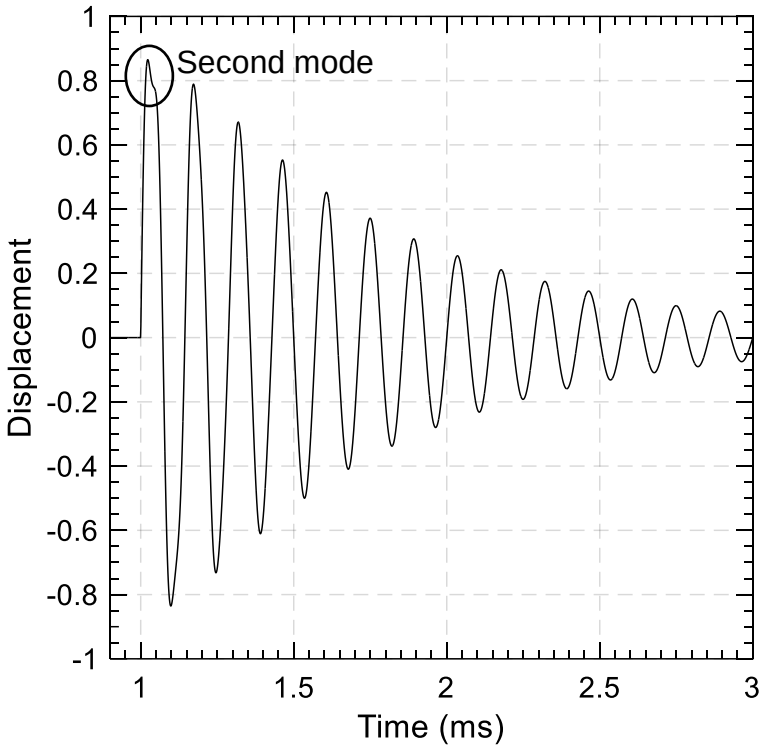

Fig. 4-4: Plot of displacement amplitude vs time of Eq. 4.5

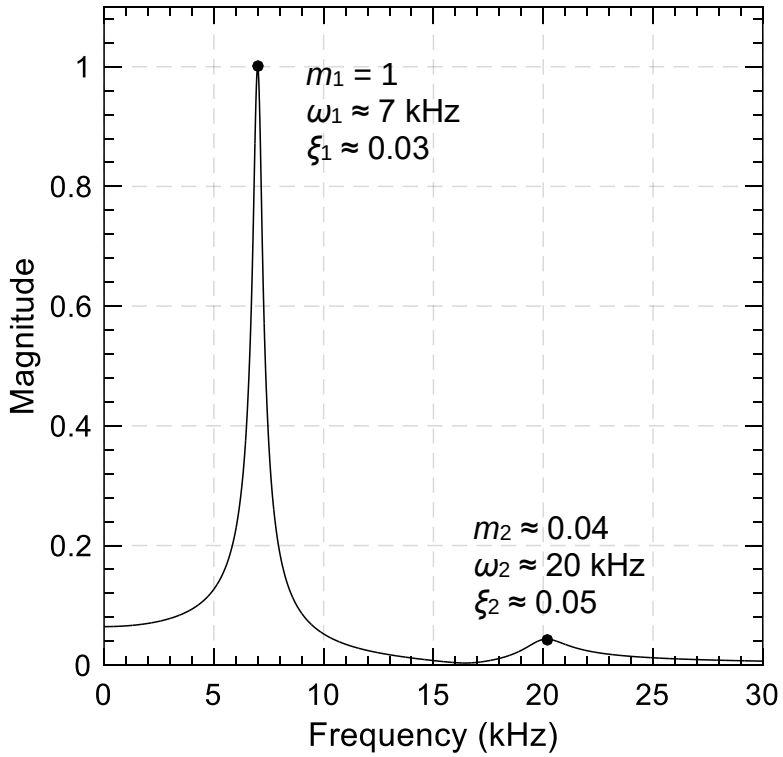

Fig. 4-5: Frequency spectrum of the displacement signal shown in Fig. 4-4

The theoretical velocity of the two sinusoids in Eq. 4.5 obtained by differentiating the displacement function *x* is given in Eq. 4.6 below

$$\dot{x} = A_1\omega_1 e^{-\xi_1\omega_1 t}\cos(\omega_1 t) - A_1\xi_1\omega_1 e^{-\xi_1\omega_1 t}\sin(\omega_1 t) - A_2\xi_2\omega_2 e^{-\xi_2\omega_2 t}\sin(\omega_2 t) + A_2\omega_2 e^{-\xi_2\omega_2 t}\cos(\omega_2 t) \quad 4.6$$

This equation and the estimated velocity obtained by differentiating the function *x(t)* from Eq. 4.5 is presented in Fig. 4-6; the estimated velocity is in excellent agreement with the theoretical velocity.

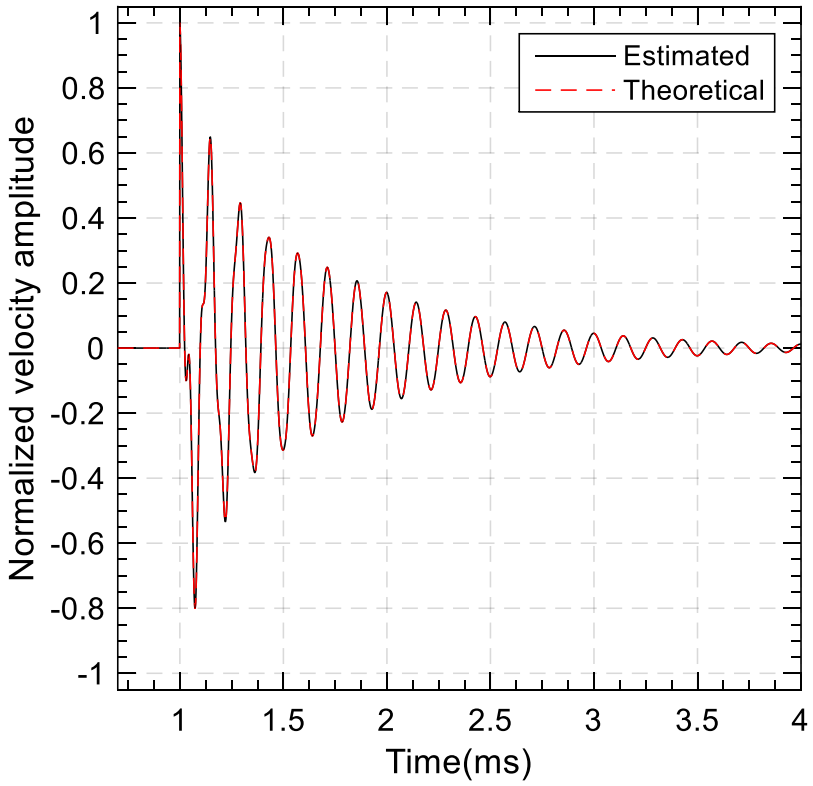

Fig. 4-6: Normalized velocity amplitude against time from Eq. 4.6

The frequency spectra magnitude of the two velocity signals are shown in Fig. 4-7; these figures also corroborate the conclusion that the numerical differentiation performed using MATLAB™ to estimate the velocity signal from the displacement function *x(t)* works well.

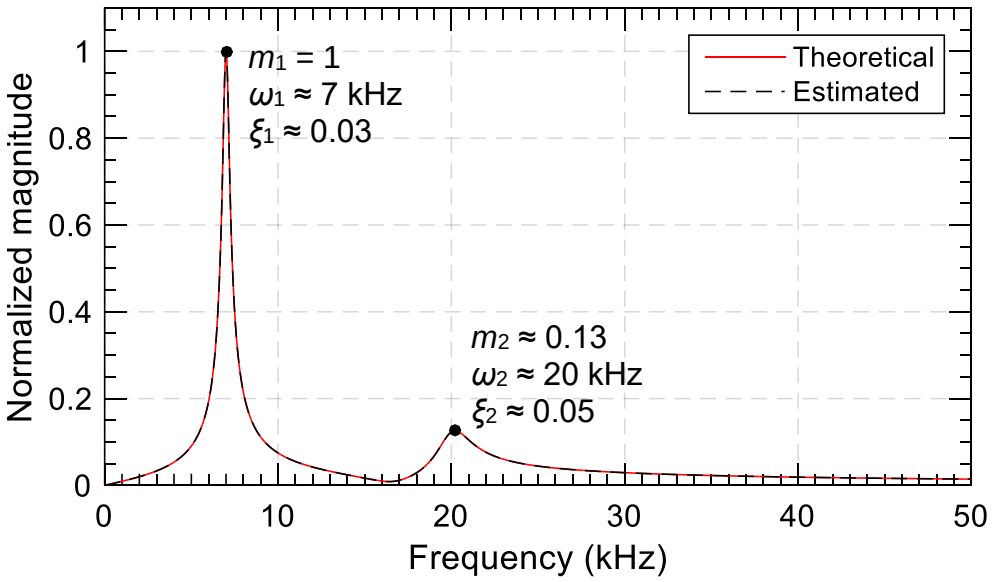

Fig. 4-7: Frequency spectrum magnitude and unwrapped phase of the two velocity signals

The velocity function ($\dot{x}$) in Eq. 4.6 is numerically integrated and compared with the theoretical displacement function (Eq. 4.5); this comparison is shown in Fig. 4-8. This figure also shows that the numerical integration code used in MATLAB™ works well to estimate the displacement from a velocity signal.

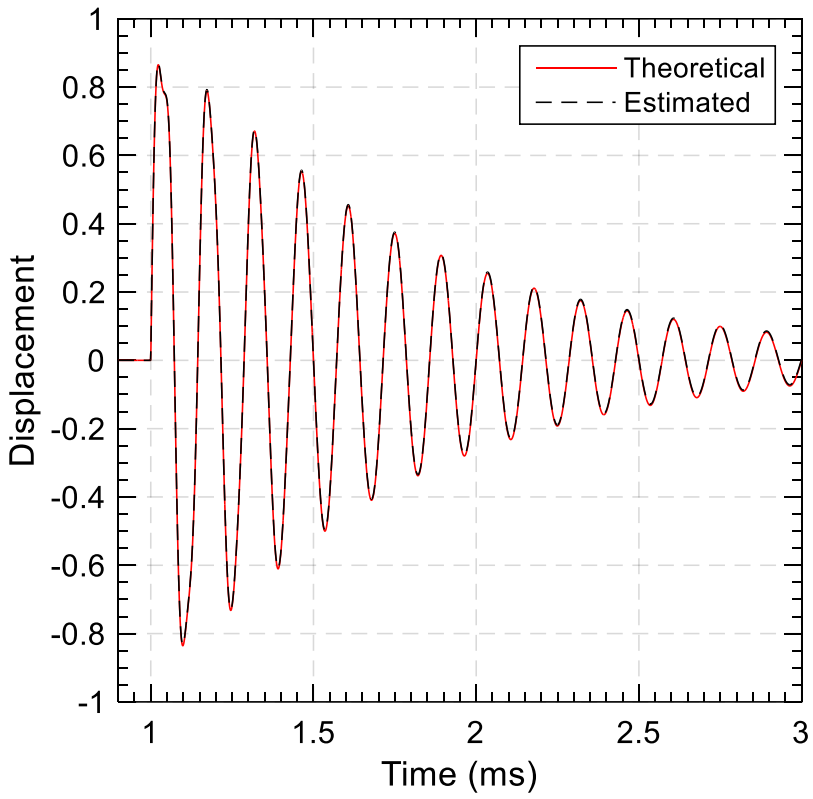

Fig. 4-8: Theoretical and estimated displacement against time

4.6.1.2 Verification of the bender response

A pair of typical bender transmitter displacement and velocity responses (at the same location on transmitter surface) in air to a sine pulse of central frequency (f_c) = 26 kHz are shown in Fig. 4-9 and Fig. 4-10 along with the sine input pulse (10 VPP). Note that f_c = 26 kHz is used because it is close to the second mode of vibration of the transmitter in air. This input pulse results in greater participation of the second mode of the transmitter along with the first mode of vibration. The maximum displacement amplitude is 13 nm and the maximum velocity amplitude is 2.1 mm/s.

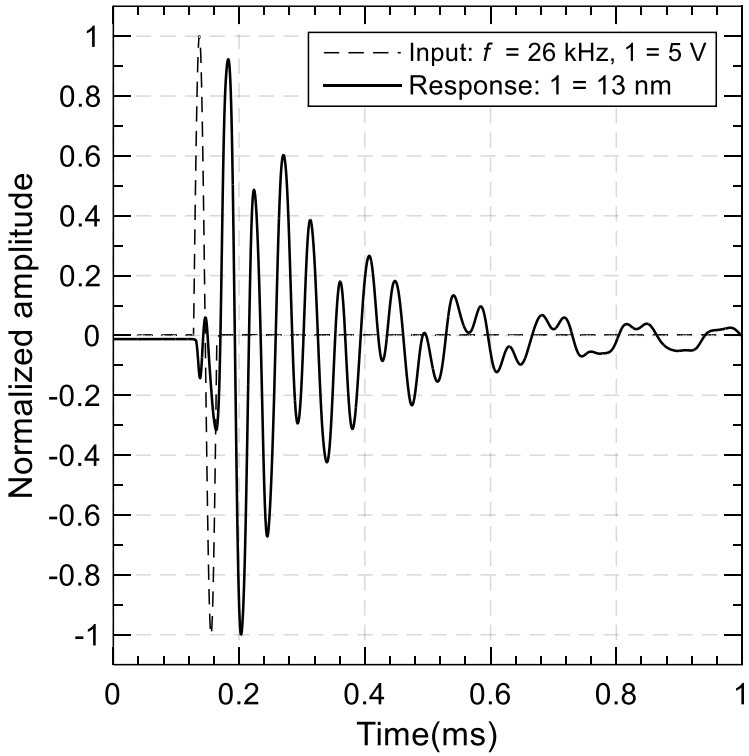

Fig. 4-9: A typical bender transmitter displacement response in air to a sine pulse of 26 kHz central frequency

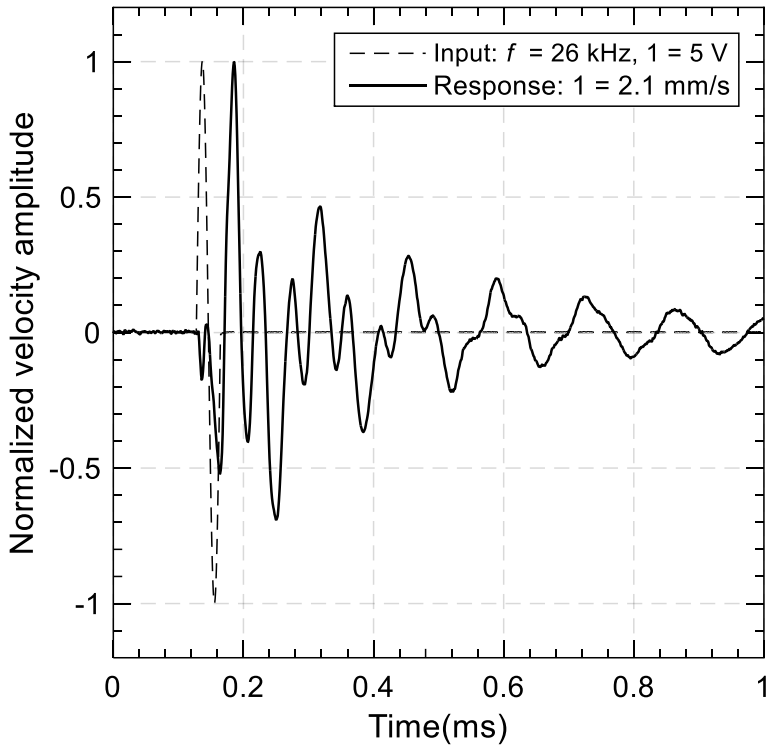

Fig. 4-10: Bender transmitter velocity response in air to a sine pulse of 26 kHz central frequency

Fig. 4-11 shows the frequency spectra of the displacement and velocity responses of the bender transmitter shown in Fig. 4-9 and Fig. 4-10. The resonance frequencies and the damping ratios of the two modes of the transmitter estimated from the two signals are very similar; however, the magnitudes of the two modes are significantly different. The magnitude of the first mode from the displacement response is ≈ 40 % less than that of the velocity response; and the magnitude of the second mode of the displacement response is ≈ 30 % larger than that of the velocity. Note that the central frequency of the input sine pulse is closer to the resonance frequency of the second mode of the transmitter; therefore, the energy in the second mode is expected to be higher than that in the first mode which means that the frequency spectrum of the displacement response is more accurate. Frequency spectra of the velocity response also shows an extra peak at low frequency (around 1 kHz) which is not observed in the frequency spectrum of the displacement response.

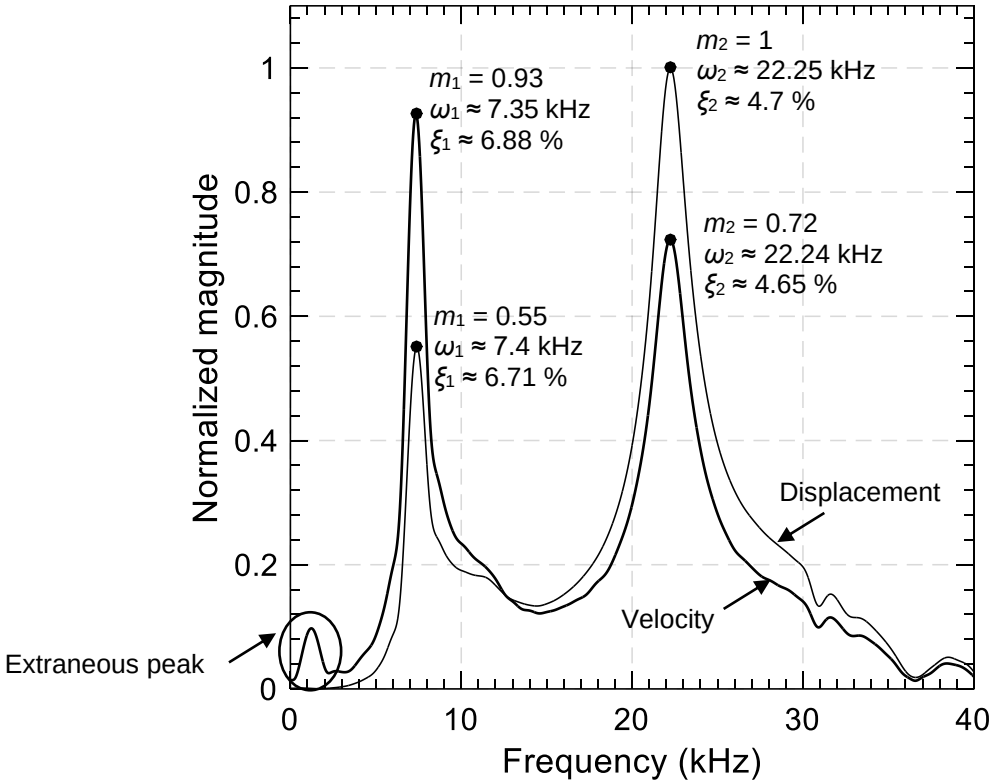

Fig. 4-11: Frequency spectra of the measured displacement and velocity of the transmitter response to a sine pulse of 26 kHz central frequency

Fig. 4-12 shows the velocity response of the transmitter in air measured from the laser and the velocity response estimated from the displacement response by numerical differentiation. The maximum velocity amplitude of the measured laser response is ≈ 14 % more than that of the estimated velocity response; the frequency content of the responses appears to be very different. The displacement response of the transmitter measured from the laser is compared to the estimated displacement response (by numerical integration) in Fig. 4-13. Although the measured displacement amplitude is also higher than the estimated amplitude like the velocity responses, the difference between the maximum amplitudes is greater than the difference between the maximum amplitudes of the velocity responses. The maximum displacement amplitude of the measured response is ≈ 17% greater than that of the estimated displacement response. The frequency content between the measured and estimated displacement responses are also very distinct. In both these comparisons, the measured velocity response from the

laser appears to be incorrect. This conclusion is further investigated by estimating the frequency spectra of the estimated displacement and velocity responses and compared with the frequency spectra of the measured displacement velocity and laser responses.

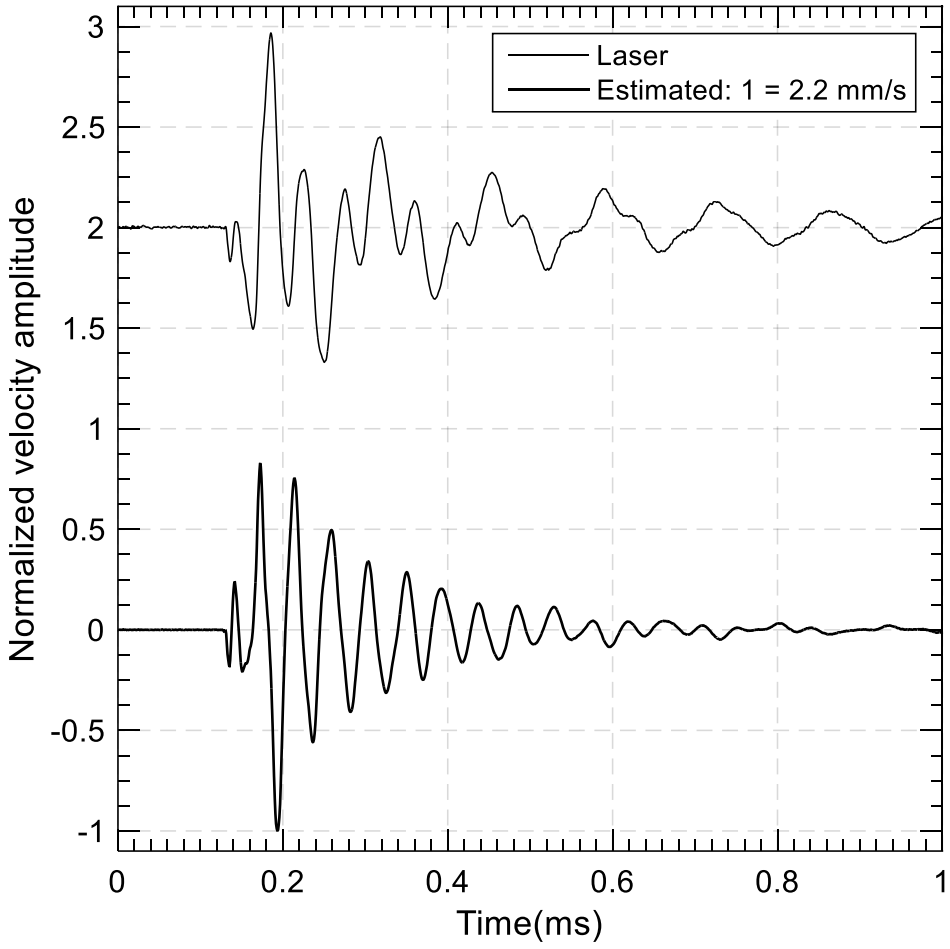

Fig. 4-12: Transmitter velocity response measured from the laser and the velocity estimated from the laser displacement response

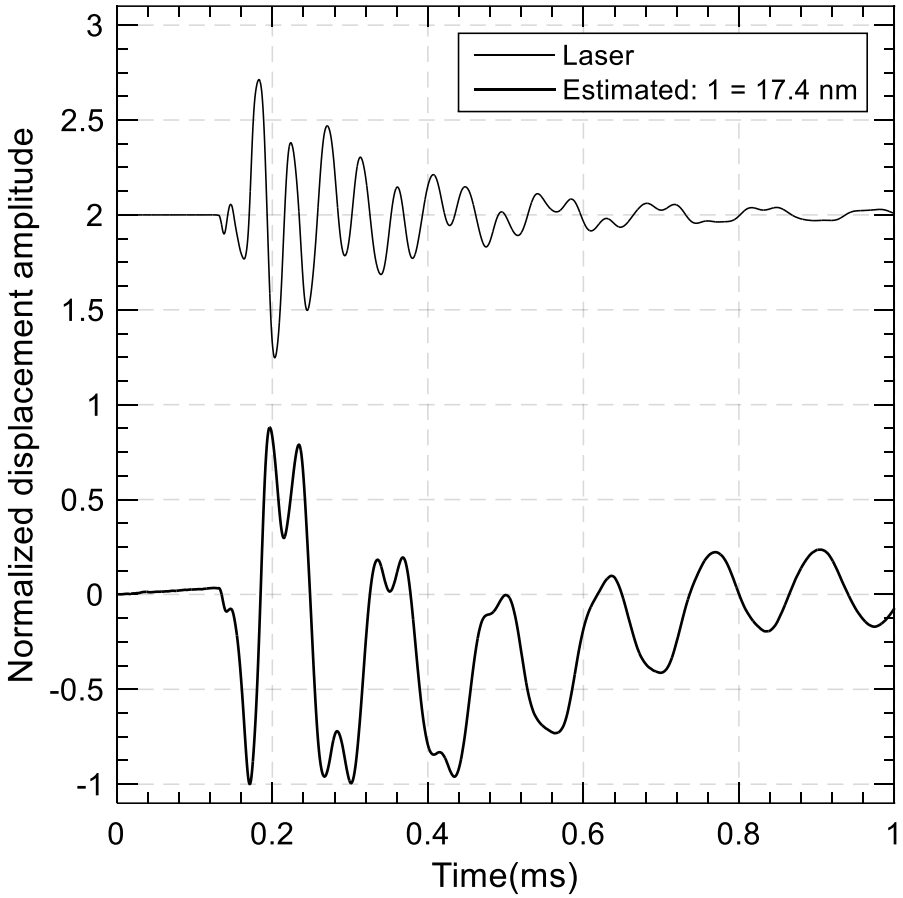

Fig. 4-13: Transmitter displacement response measured from the laser and the displacement response estimated from the laser velocity response

Fig. 4-14 shows the frequency spectra of the estimated displacement and velocity responses. The magnitude of these spectrum are normalized to the magnitude of the second mode of the measured displacement shown in Fig. 4-11. Resonance frequencies and damping ratios of the two modes of the transmitter estimated from both velocity and displacement responses are similar to those of the measured responses shown in Fig. 4-11; however, the magnitudes are different. The frequency spectrum of the velocity estimated from the measured displacement response again shows high energy in second mode of vibration as is shown for measured displacement response in Fig. 4-11. Lastly, the displacement frequency spectrum shows leakage of energy to the lower frequencies which is not observed in the frequency spectrum of the measured displacement response in Fig. 4-11. These results suggest that the velocity measurements from the laser

vibrometer are inaccurate; hence, the focus of the measurements in this study will be on the displacement responses of the transmitter.

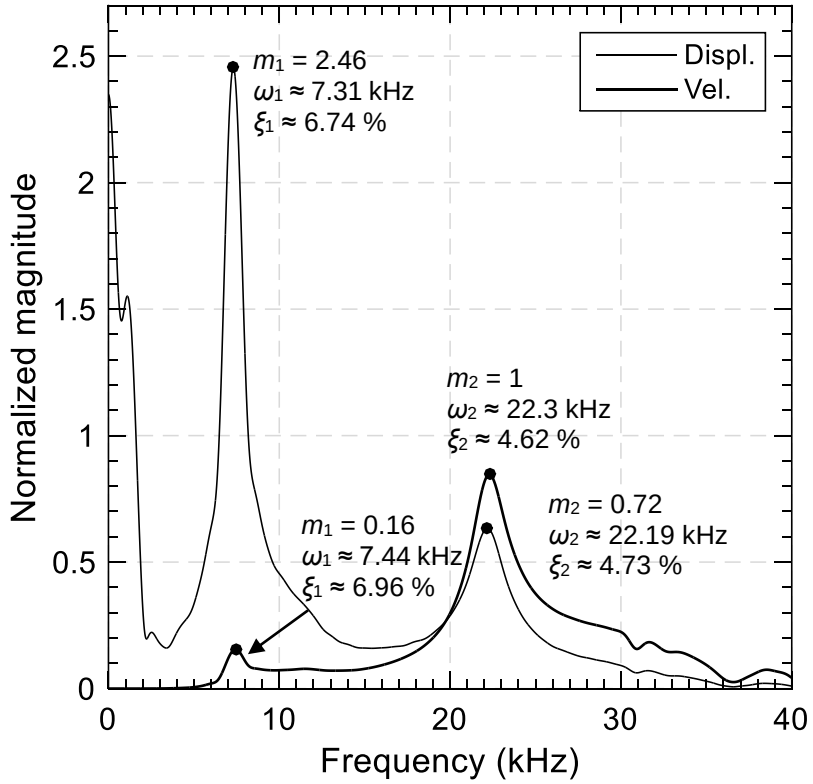

Fig. 4-14: Displacement and velocity responses of the transmitter estimated using numerical integration and differentiation respectively: normalized to the maximum magnitude of the frequency spectrum of the measured displacement response

4.6.2 Measurements in air

Fig. 4-15 shows the transmitter displacement in air as a function of time for different input excitations. The displacements are normalized with respect to the peak displacement of the transmitter response to the square pulse in air. The three input excitations used are 9 kHz sine pulse, step pulse (Heaviside), and the 9 kHz square pulse (half cycle) all with a voltage amplitude of 10 volts peak-to-peak. The transmitter responses to square and step pulses show considerable participation of higher modes during the first 0.3 ms compared with the response of transmitter to the sine pulse. After 0.3 ms, the first mode of vibration dominates in all the three responses. Participation of the higher modes occurs

because of higher energy contents at higher frequencies in step and square pulses. This is corroborated by the analytical power spectra of different pulse types presented in Fig. 4-16, which shows that the energy of the sine pulse (bold line) is less than that of the square pulse. Fig. 4-15 indicates that the first negative peak of the transmitter response to sine pulse, after the excitation pulse, is less than half of that corresponding to the square pulse while the first positive peak of the transmitter response to sine pulse, after the excitation pulse, is close to half of that of the response to the square pulse. The difference in the amplitudes of transmitter response to sine and step pulses is negligible (3% difference in the negative peak amplitudes and 6% difference in the peak amplitudes). The energy in the response to sine pulse is similar to that of the response to step pulse. This similarity is likely because the central frequency of the input sine pulse matches the first mode resonant frequency of the transmitter (f_1). These results show that the type of input excitation does influence the bender behaviour, contrary to that reported by others (Alvarado and Coop 2012).

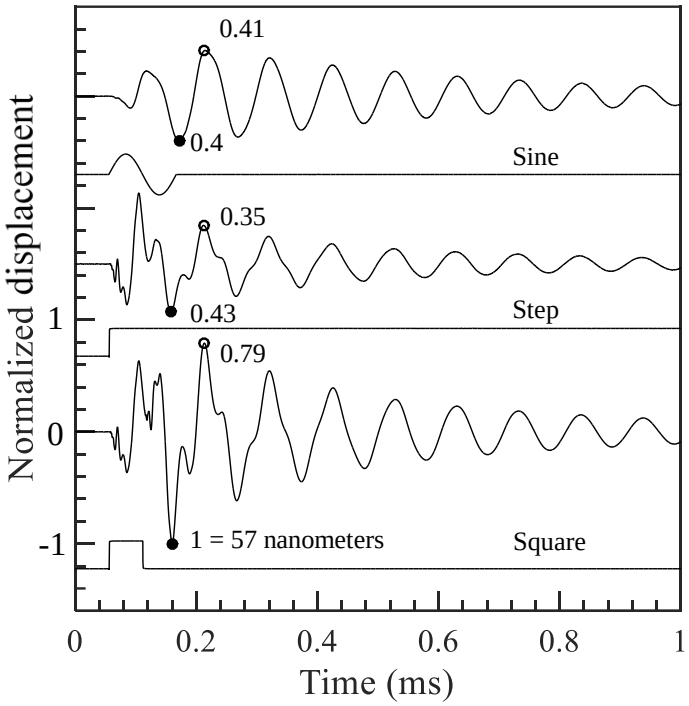

Fig. 4-15: Transmitter input and corresponding output responses in air for three input excitations – sine, step, and square; the first positive and negative peaks after input pulses are marked.

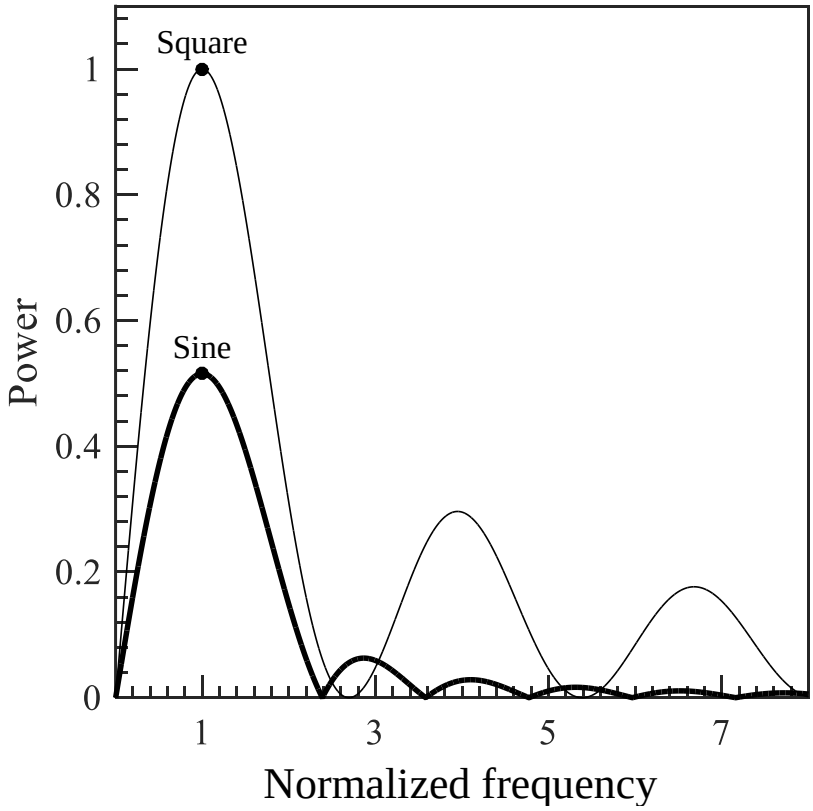

Fig. 4-16: Power spectra of sine and square pulses (after Tallavo et al. 2009)

Fig. 4-17 shows the frequency spectra of the three displacement responses shown in Fig. 4-15 with a focus on the first mode of vibration. The first mode resonance frequency f_1 of the transmitter from all the three responses is the same (≈ 9.7 kHz); however, the peak magnitude of the spectrum of transmitter response to sine pulse is 50% of that of the square pulse. Fig. 4-18 shows the three frequency spectra with a focus on the second mode of vibration of the transmitter responses to the three pulse types. The magnitude of the spectrum of the transmitter response to sine pulse is substantially less than those to square and step pulses. The difference in the second mode frequency f_2 of transmitter responses to square and step pulses is less compared with the difference in the transmitter responses to square and sine pulses. This occurs because the magnitude of f_2 for sine response is very low (0.5 of the magnitude of f_1 of square pulse) to the extent that the Fourier calculations could not distinguish the peak properly (Fig. 4-18). The first

mode resonance frequency of the bender used in this study (f_1 = 9.7 kHz) is about 3 times larger than the corresponding resonance frequency of the bender studied by Rio (2006) (e.g., f_1 = 3.4 kHz). Thus, the maximum displacements measured in this study should be around 3 times smaller than the displacements obtained by Rio (2006) because according to equations (3) and (5), the maximum displacement is inversely proportional to the resonant frequency. However, the change in resonance frequencies does not justify the three orders of magnitude difference in the displacements of the bender used in this study and that of Rio (2006).

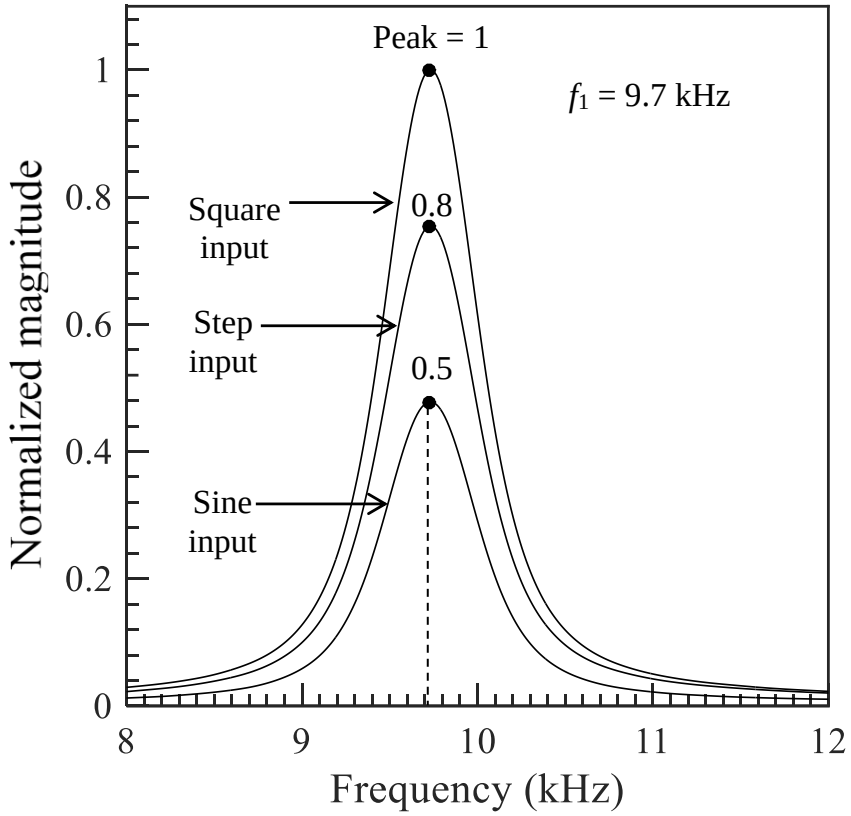

Fig. 4-17: Frequency spectra of the transmitter responses in air to three types of input excitations: 1st mode

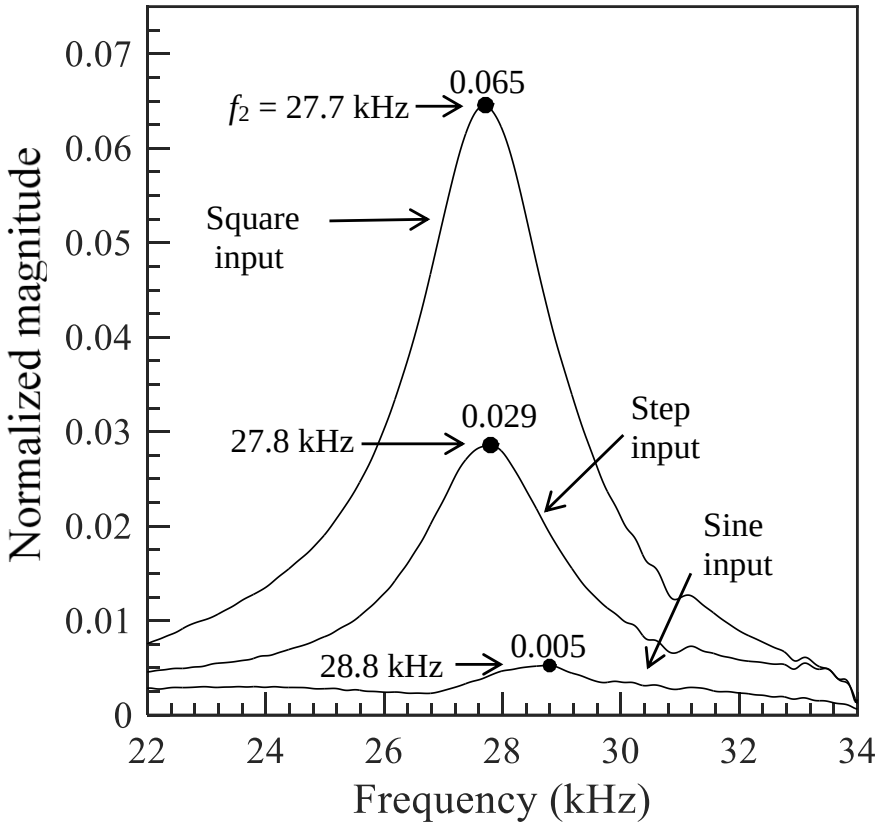

Fig. 4-18: Frequency spectra of the transmitter responses in air to three types of input excitations: 2nd mode

The results above suggest that input pulses of square and step types excite higher modes. An input pulse of sine type can be used if participation of higher modes is not desirable. However, a higher input voltage might be needed for sine pulses to increase the amplitude of the response. Over the years, several uncertainties have arisen in the literature concerning the selection of appropriate input excitation pulse in conventional BE testing. The discussion presented here and the corresponding results in Figs. 4-16 to 4-18 help reduce some of these uncertainties.

Bender elements are small-sized plates and identifying their deformation behaviour is crucial for understanding the actual behaviour of the transmitter inside the soils. Based on the transmitter displacement readings recorded at 102 points on its surface for input sine and square pulses, aggregated responses of the transmitter to the sine and square pulses are simulated using Matlab™. These simulated responses (i.e., deformations of

transmitter) are shown in Fig. 4-19 and Fig. 4-20 at 0.32 ms from the start of the excitation. The peak amplitude of 57 nm of the square pulse response is more than double the peak amplitude of 25 nm of the sine pulse response. Moreover, the square pulse response indicates a larger participation of higher modes than the sine pulse response. This result corroborates the results of Figs. 4-15 and 4-18 where it is shown that the square pulses excite higher modes in the transmitter response. These simulations further show that the transmitter response to a square pulse is similar to that of a cantilever plate (with flexural response in mutually perpendicular directions), which is in contradiction to the typical assumption made in BE tests that the transmitter vibrates as a beam inside the soil (Lee and Santamarina 2005). However, the transmitter response in air to a sine pulse can be considered close to that of a beam because the first mode of vibration dominates the response. The plate behaviour of the transmitter applies to a BE of any typical size as the dimensions affect the resonance frequency of the BE but not significantly the shape of the vibration modes.

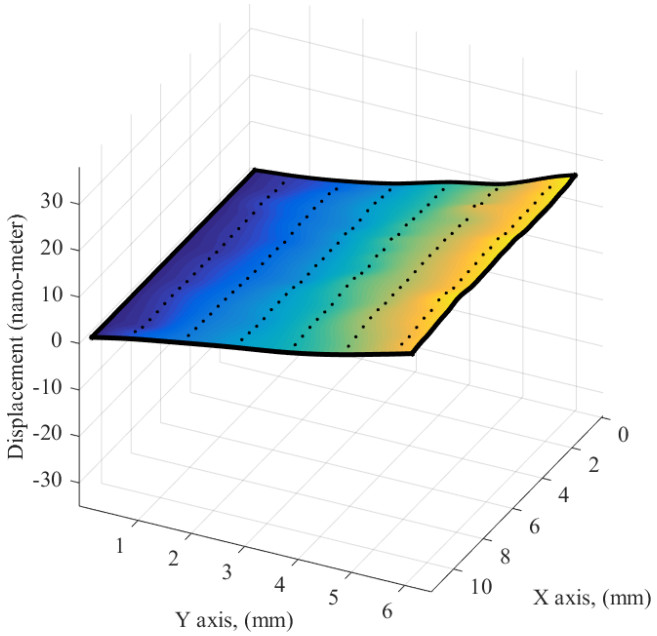

Fig. 4-19: Snapshot of the transmitter response in air to a sine input excitation at 0.32 ms

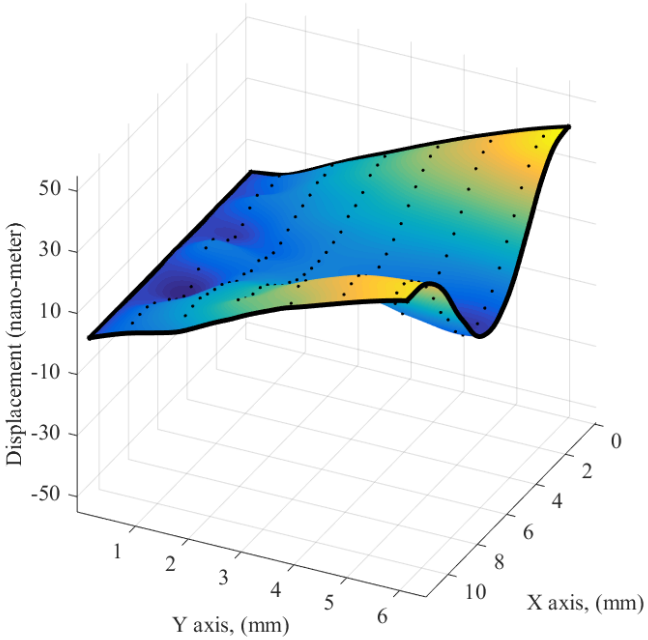

Fig. 4-20: Snapshot of transmitter response in air to a square input excitation at 0.32 ms

Lee and Santamarina (2005) recommend the use of Eq. 4.3 for approximating resonance frequencies of a bender element vibration in air. The measured first mode resonance frequency of the transmitter (f_1 = 9.7 kHz) can be used to determine the accuracy of this recommendation. Properties of the transmitter used in this study are: E_b = 6.3 x 10^{10} Pa, ρ_b = 7700 kg/m^3, L_b = 6 mm, b = 14 mm, and h = 1.5 mm (Camacho-Tauta et al. 2015). Further, the characteristic number k_L for the first and second modes of vibration of a cantilever beam with fixed-free condition are 1.8751 and 4.69, and these values are used in the calculations. Using f_1 = 9.8 kHz, the effective length factor α is estimated to be 1.048. The measured second mode resonance frequency (f_2 = 27.5 kHz) of the transmitter in air is compared with the value of f_2 estimated using Eq. 4.3. The estimated value from equation (3) is 60.68 kHz which is very different from the actual measured f_2 (= 27.5 kHz). This result shows that Eq. 4.3 is not a reliable estimator of the resonance frequency of bender element vibration in air.

4.6.3 Measurements in liquids

This section presents the responses of the transmitter submerged in various liquids listed in Table 4-1. The effect of the presence of plexiglass box on the penetration of laser beam is studied before performing measurements with transmitter in liquids. The effect is quantified by calculating the percent difference between signals of the transmitter responses in air with and without the presence of plexiglass box for a given input excitation. A maximum difference of 2.1% is noted which is rather small and, therefore, it is assumed in this study that the presence of plexiglass box has negligible impact on the observed transmitter response data.

The laser beam of the laser vibrometer used in this study is usually affected by the refractive index of the medium through which the beam penetrates. To evaluate the effects of the refractive indices of different media on the laser measurements, transmitter responses are measured in air with different media present in between the laser head and the transmitter. The effects of the presence of different media on the transmitter response in air were found to be negligible and are not considered further in obtaining the results discussed below.

Fig. 4-21 shows the first 1.1 ms of the displacement responses of the transmitter subjected to 9 kHz sine pulse measured in liquids. All the output signals are normalized with respect to the negative peak displacement of the transmitter response in the mineral oil mixture. The peak displacement of the transmitter response in sucrose-2 is 41% less than that in the mineral oil (the peak displacements are shown by solid circles in Fig. 4-21). In general, a 50% increase in the density ρ of the liquids caused a 40 % decrease in the peak displacement at a rate of about 23 nm-mL/g.

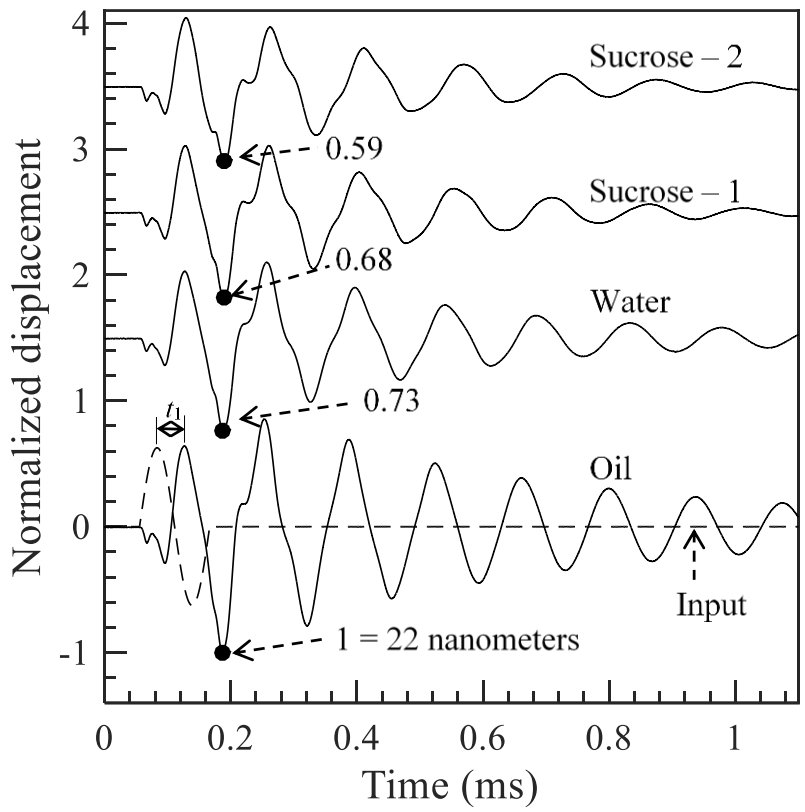

Fig. 4-21: Transmitter responses to 9 kHz sine pulse in various liquids

The time signals shown in Fig. 4-21 are used to compute the damping ratio ξ of the transmitter in different liquids using the logarithmic decrement method. The first mode natural frequencies f_1 of the transmitter in these liquids are obtained from the frequency spectra of these time signals. Fig. 4-22 presents the variations of f_1 and ξ with density ρ of different liquids. Clearly, the presence of liquids has a significant effect on f_1 and ξ of the transmitter. Addition of water alone reduced f_1 by 30% and enhanced ξ by about 120% from their corresponding values in air. Both f_1 and ξ more or less vary linearly with the ρ; with a 50% increase in ρ, f_1 decreases by about 12% at the rate of 1.8 kHz-mL/g and ξ increases by about 95% at the rate of 10.7%-mL/g. This decrease in f_1 and increase in ξ is the result of added liquid mass around the transmitter.

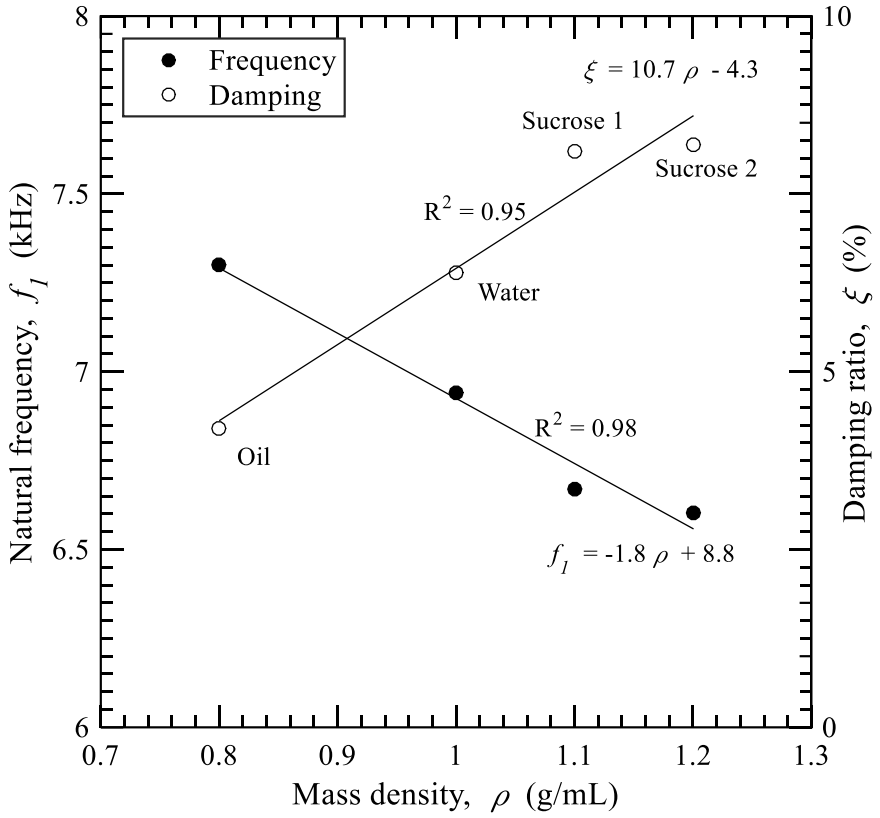

Fig. 4-22: Natural frequency and damping ratio of transmitter response versus mass density of liquids

The effects of fluid viscosity μ on f_1 and ξ are presented in Fig. 4-23. The first natural frequency decreases and damping ratio increases as μ increases from 1 (for water) to 5.2 cP (for sucrose-2). However, the transmitter response in the mineral oil does not follow this trend. This difference occurs possibly because the density of the mineral oil is the least amongst the four liquids. Even though the viscosity of oil is the greatest (8.2 cP), the change in density from sucrose-2 to mineral oil governs the transmitter behaviour more than the change in viscosity. The trend of decreasing f_1 and increasing ξ is expected to continue if a sucrose solution with a concentration greater than 40% is used.

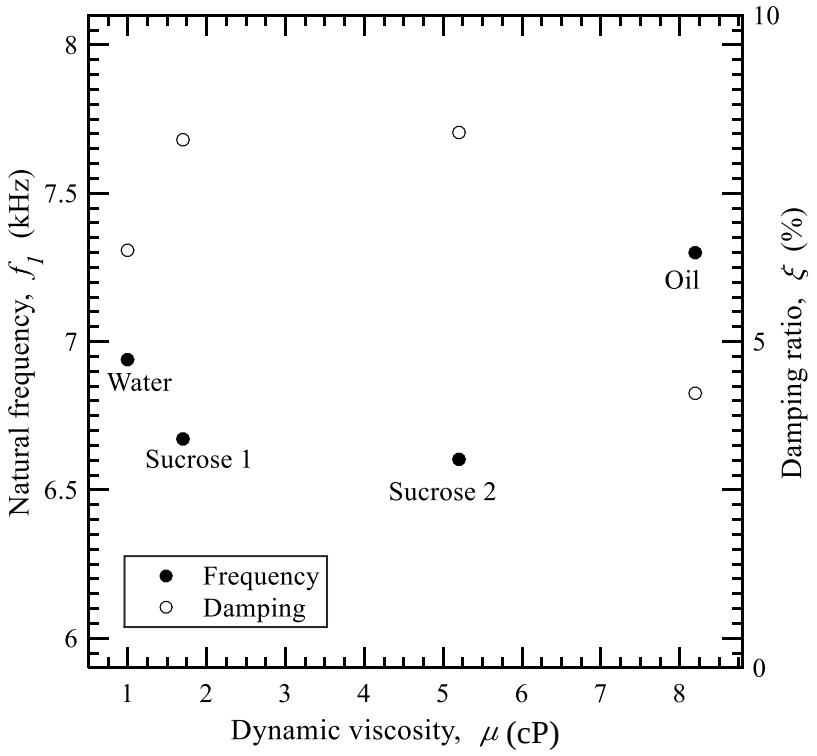

Fig. 4-23: Natural frequencies and damping ratios of the transmitter for different fluids with different viscosities

4.6.4 Measurements in transparent soil

Fig. 4-24 shows the displacement response of the transmitter embedded in transparent soil (with zero applied vertical stress) and subjected to a 9 kHz sine pulse. As expected, the presence of transparent soil significantly reduces the displacement of the transmitter vibration; the peak displacement is reduced by 70% from its value in air. f_1 and ξ of the transmitter in the transparent soil are calculated from the frequency spectrum shown in Fig. 4-25 (the plot corresponding to 0 kPa stress). The addition of fused quartz results in an increase in mass around the transmitter because of which f_1 and ξ of the transmitter response in transparent soil are respectively about 9% less and 300% more than f_1 and ξ of the transmitter response in air. These results confirm that the transmitter response in transparent soil is completely different from the sine pulse input excitation. The reliability of conventional BE test results now becomes highly questionable because the

predominant assumption in BE test is that the transmitter response in soil has the same shape as the shape of the input excitation (Lee and Santamarina 2005).

Eq. 4.4 and the resonance frequency f_1 of the transmitter in soil (8.3 kHz) are used to estimate the coefficient β. Youngs modulus E_s and mass density ρ_s of the transparent soil are 72 GPa and 1310 kg/m^3 respectively (Ezzein and Bathurst 2011), and α = 1.048 is calculated from the measurements in air above. The estimated β, for a fused quartz transparent soil, is ~208 which is about 100 times larger than the values obtained for a sand specimen by Lee and Santamarina (2005) and Camacho-Tauta et al. (2015). This result shows that the experimentally determined value of β depends not only on the volume of the soil mass affected by the bender but also on the soil confinement and geometry of the BE.

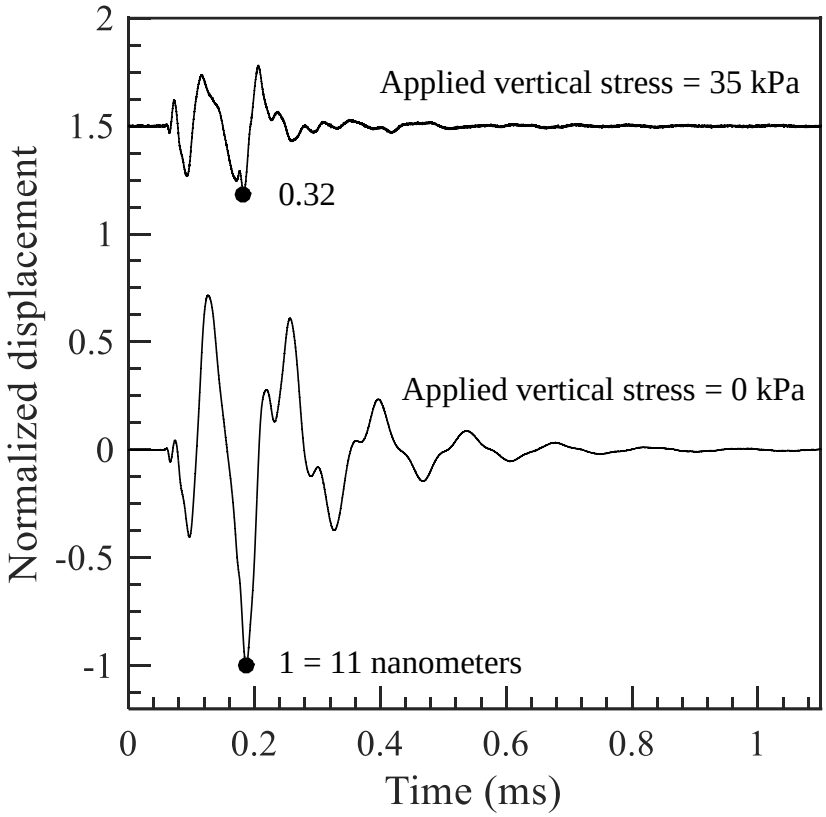

Fig. 4-24: Transmitter responses in transparent soil with no applied stress and with applied vertical stress of 35 kPa

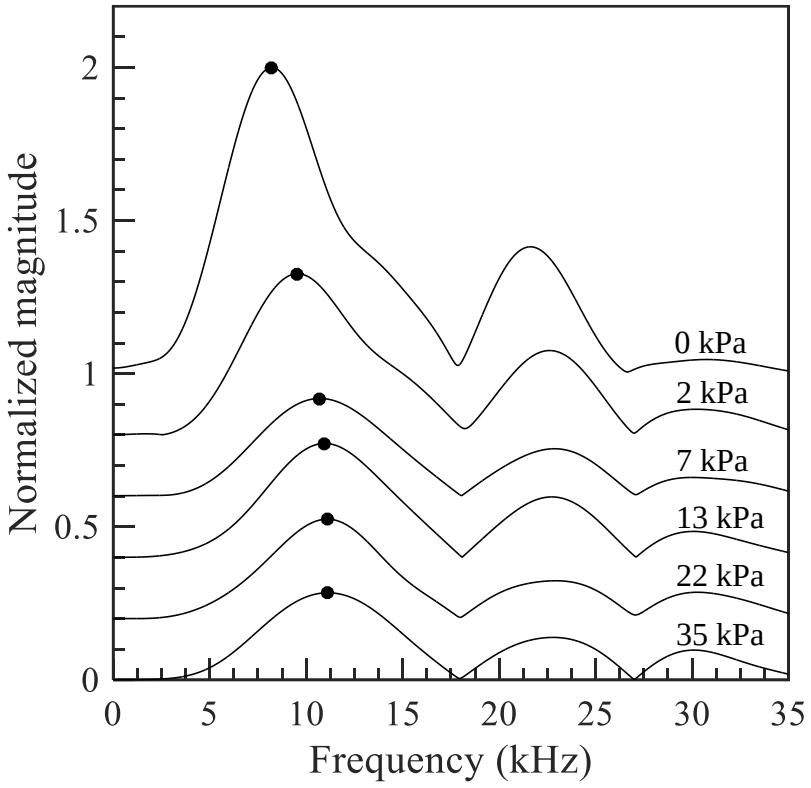

Fig. 4-25: Frequency spectra of the transmitter responses in transparent soil under different vertical stresses

4.6.5 Effects of vertical stress

Fig. 4-24 also shows the normalized displacement signals of the transmitter response for an applied vertical stress σ_v = 35 kPa. The increase in σ_v from 0 to 35 kPa reduces the peak displacement by 67%. The frequency spectra of the signals measured with the transmitter under six different vertical stresses are shown in Fig. 4-25 with the peaks of the spectra indicated by solid circles corresponding to f_1 in each case; these peak magnitudes and f_1 are plotted against vertical stress in Fig. 4-26.. The peak magnitude from the spectra and f_1 show approximately linear relationships with logarithm of the applied vertical stress. The peak magnitude reduces at a rate of 0.21 unit/kPa and f_1 increases at a rate of 0.06 kHz/kPa.

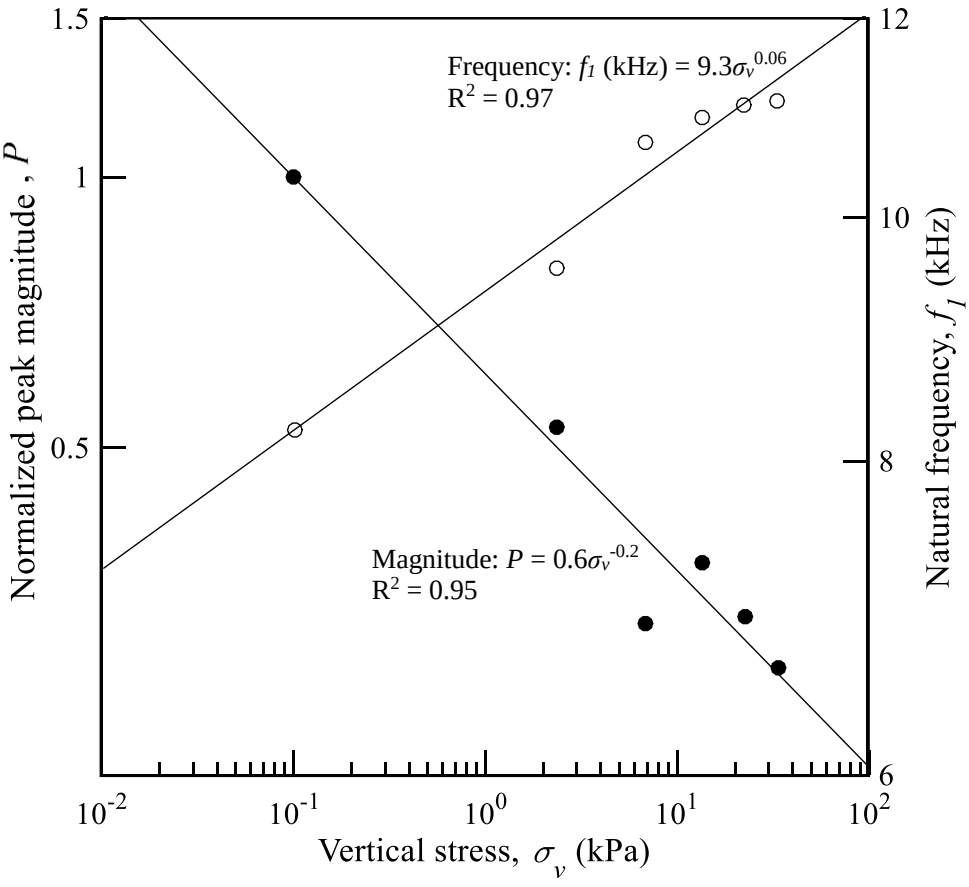

Fig. 4-26: Natural frequency and peak amplitude of the transmitter response versus applied vertical stress

4.6.6 Transfer functions and arrival times

Multiple modes of vibration participate when the transmitter is excited by an input voltage. Identifying these modes of vibration and their levels of participation is important because these modes control the characteristics of the perturbation generated by the transmitter in a BE test and also contribute in delaying the shear wave arrival at the receiver end (Fig. 4-1). Fig. 4-27 shows the transfer functions of the transmitter in air calculated using the response to three excitation signals: sine pulse, square pulse, and a 0-50 kHz bandwidth sine sweep. Properties of the three modes of vibration identified using the sine sweep transfer function are presented on the figure. The natural frequencies of the transmitter are f_1 = 9.8 kHz, f_2 = 27.5 kHz, and f_3 = 47.2 kHz. The corresponding damping ratios of these modes of vibrations are ξ_1 = 2.9%, ξ_2 = 4.1%, and ξ_3 = 5.9%. The third

mode of transmitter vibration cannot be identified from the transfer function of the square pulse while only the first mode of vibration is identifiable from the transfer function of the sine pulse. These results show that the transfer function from the sine sweep excitation is the most appropriate for identifying the various modes of transmitter vibration.

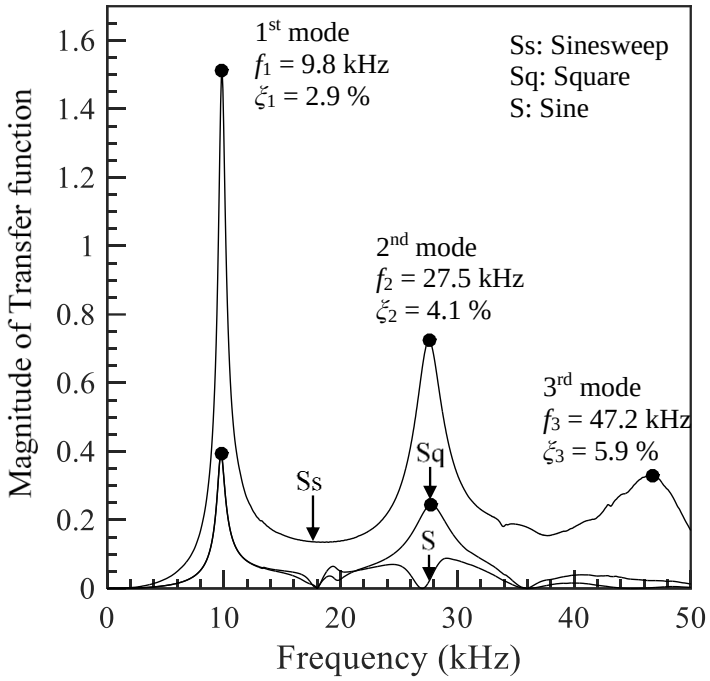

Fig. 4-27: Transfer function of transmitter response in air from sine sweep, sine pulse and square pulse

Fig. 4-28 shows the transfer function of the transmitter vibration in transparent soil from the sine sweep excitation. Also plotted in the figure is the transfer function of the transmitter vibration in air. There is significant difference in the modal properties of the two transfer functions. For example, the peak magnitude corresponding to the first mode reduced by about 90%, the natural frequency reduced by about 25%, and the damping ratio increased by about 400% when the transparent soil is placed around the transmitter.

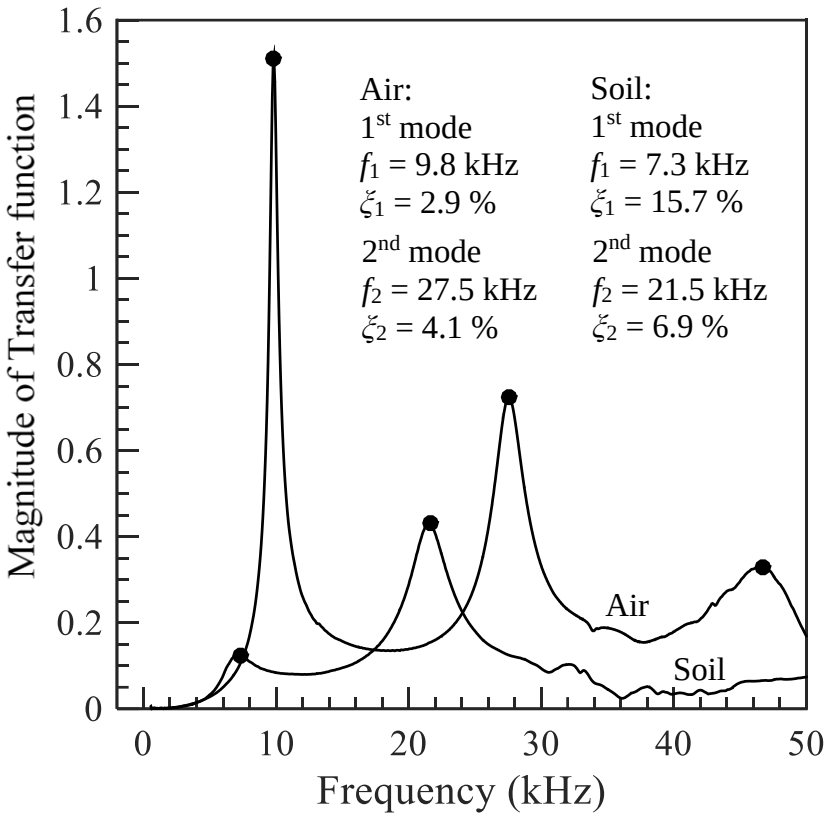

Fig. 4-28: Transfer function of transmitter response in air and soil to using sinusoidal sweep excitation

Unwrapped phase of the transfer functions can be used to calculate the relative time shift between input excitation and transmitter response, and the variation of relative time shift with frequency and the properties of the surrounding medium can also be evaluated. Fig. 4-29 presents the variation of the relative time shift with frequency in air, mineral oil mixture, and in transparent soil. The relative time shift in all three media appears to reach the same constant value (0.05 ms) at higher frequencies. The relative time shift of 0.05 ms is larger than the total time delay of BE systems reported in the literature (Camacho-Tauta et al. 2015; Lee and Santamarina 2005) because it includes the time delay of the laser system which has a more sophisticated electronics that the typical BE system (e.g., velocity decoder). The estimated average time delay of the laser system used by Rio (2006) is in the same order of magnitude (0.04 ms). Fig. 4-29 mainly shows that the relative time shift in the BE system is frequency dependent and is affected by the

properties of the surrounding medium. These results explain why the frequency methods tend to work better at higher frequencies (Camacho-Tauta et al., 2015) when the relative time shift converges to a constant value.

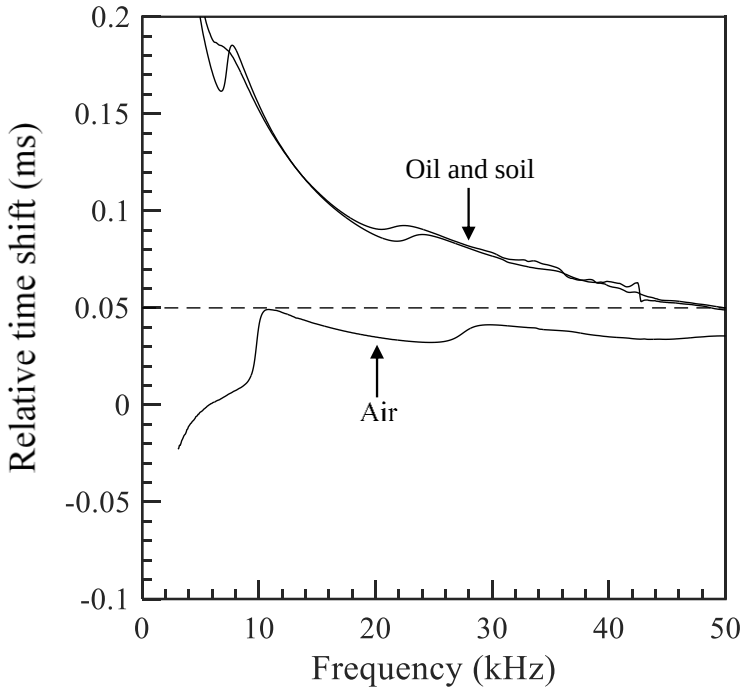

Fig. 4-29: Relative time-shift as function of frequency between input excitation voltage and displacement transmitter response in air, oil, and soil using a sine pulse excitation

The relative time shift is greater in mineral oil mixture and transparent soil than in air because the mineral oil and soil create added mass effect around the transmitter (Sader 1998). The difference in relative time shifts in mineral oil and transparent soil is not significant; this is most likely because no vertical stress is applied on the transparent soil for the measurements presented in Fig. 4-29. The results show that the relative time shift between input voltage excitation and transmitter response is a function of viscosity and density of the medium in which the bender is inserted. Therefore, the commonly used assumption in the frequency-based methods that the input excitation voltage is representative of the transmitter response is incorrect and requires revision.

4.7 Conclusions

Bender elements (BEs) are commonly used to estimate the shear wave velocity of soil samples in laboratories. The BE test remains without a standardized procedure mainly because of a lack of understanding of the actual behaviour of BEs inside the soil specimen. This chapter presents the results of a novel experimental program in which the actual behaviour of a transmitter bender element placed inside a transparent soil is studied for the first time using a state-of-the-art laser vibrometer. The transparent soil has properties (such as shear strength) close to those of granular soils with angular particles. Actual BE vibrations are measured in air, in liquids of different mass densities and viscosities, and in transparent soil specimens under different vertical stresses.

The effects of input excitation pulses in air are assessed by measuring the transmitter response to three input pulses: sine, step, and square. The effect of input voltage amplitude on the BE response is studied by measuring the transmitter responses to sine pulses of different amplitudes. The results clearly show a linear relationship between the input voltage and the peak BE displacement in air, confirming the trend predicted by the theoretical equation. The 3D response of the BE transmitter in air to sine and square input pulses is measured on a grid containing 102 nodes on the surface of transmitter. Natural frequencies and damping ratios of different modes of vibration of the transmitter in air are determined by using a sinusoidal sweep excitation. The effect of liquid density and viscosity on the transmitter response to sine input pulse is examined by measuring the BE displacements in water, sucrose of two different concentrations, and a mineral oil mixture. The effects of vertical stress on the BE response to sine input pulses are investigated by measuring transmitter response in the transparent soil under different applied vertical stresses. Finally, the transfer functions between the BE responses and the input excitation are calculated to understand the effects of input excitations and surrounding media on the relative time shift between input excitation and transmitter response.

This study shows from actual measurements of transmitter vibrations inside a soil that the response of the transmitter embedded in soil is significantly different from the input excitation. These results raise serious questions on the reliability of the analysis of BE

tests using frequency methods because these methods assume that the BE response has the same shape as the input excitation. Novel results of this study show that the square input pulse causes the largest displacement in the transmitter response in air while the smallest transmitter displacement is obtained from the sine pulse. The square and step input pulses cause greater participation of the higher modes in the transmitter response than the sine input pulse. The simulations of the actual transmitter response to sine and square input pulses also corroborate the conclusion that the square pulse excites higher modes more than the sine pulse.

Transmitter responses measured in liquids show that a 50% increase in density causes a decrease in f_1 by about 12% and an increase in ξ_1 by about 95% for the range of liquid density (0.8-1.2 g/mL) considered in this study. The investigation of the effect of viscosity on transmitter response shows that density governs the transmitter response more than the viscosity of liquids.

The results of transmitter response in transparent soil show that f_1 of the transmitter vary linearly with logarithm of vertical stress. In order to determine the vibration modes of the transmitter, transfer functions of the transmitter are calculated using sine pulse, square pulse, and a 0-50 kHz bandwidth sine sweep as the input excitations. Three modes of vibration of the transmitter response in air are identified; their natural frequencies are 9.8 kHz, 27.5 kHz, and 47.2 kHz, and the corresponding damping ratios are 2.9%, 4.1%, and 5.9%. It is found that the sine sweep is most suitable for calculating the transfer function of the transmitter. The transfer function of the transmitter response measured in soil shows that, as expected, the modal properties of the transmitter response change significantly in soil. The relative time shifts between the input excitation and the transmitter responses are the functions of frequency and surrounding media; these differences decrease with increase in frequency and approach a constant value of about 0.05 ms. This result explains why the frequency-based methods tend to work better at higher frequencies. This relative time shift does not represent the actual time delay between the input excitation and the transmitter response because it includes the time delay caused by the laser vibrometer used in this study. The relatively large time delay of the laser system is compatible with reported values in the literature.

5 Evaluation of dynamic response of the bender-element system in different media

5.1 Introduction

This chapter presents the results of experimental modal analysis of a transmitter (T_x) to extract modal properties of the transmitter. The aim of this chapter is to advance the understanding of the frequency response of the T_x inside the soil by performing the experimental modal analysis of the T_x in different media including air, liquids of different mass densities, and transparent soil. The experimental modal analysis is necessary for understanding the frequency response of the T_x because the method of mechanical force exerted by the electrical input voltage on the T_x is unknown. Experimental modal analysis allows the determination of the frequency response of the T_x inside the soil without knowing the actual force (Avitabile 2001). A new T_x with dimensions different from that used in the measurements for Chapter 4 is used. Along with the mode shapes, the study of effects of liquids mass density and induced vertical stress in the soil is enhanced by testing in liquids of greater density and in transparent soil with higher vertical stress.

Laser vibrometer is used to measure the T_x response at different locations on the T_x surface. A system identification algorithm called the Second-order Blind Identification (SOBI) is used for analyzing these laser measurements to determine the frequencies, damping ratio, and mode shapes of the T_x inside different media (Sadhu and Narasimhan 2014; Sadhu et al. 2017).

This chapter also presents the results of a numerical study of the transmitter response to address the lack of understanding of the complicated interactions between the BE and the embedding soil. Robust numerical modeling, and advanced utilization of the laser technology are perhaps the only practical techniques – so far – for accurately characterizing BE-soil interactions.

5.2 Background

5.2.1 Experimental modal analysis

A summary of the SOBI method along with a brief introduction of the experimental modal analysis are presented; more details can be found in Belouchrani et al. (1997) and Sadhu and Narasimhan (2014). SOBI is one of the methods available for solving a class of mathematical models associated with experimental modal analysis.

The process of estimation of the modal parameters of a vibrating system using physical responses of that system is called experimental modal analysis (Avitabile 2001). In a typical modal analysis, the input force used to excite the system must be known for performing the analysis (Ljung 1987). However, advancements in the fields of structural engineering and signal processing have led to the development of an analysis called Blind Source Seperation (BSS) which circumvents the need for knowing the input force (Sadhu et al. 2017); this type of modal analysis is also called output-only modal identification. The input force in BE test is unknown; therefore, BSS is best suited for estimation of the T_x modal parameters.

5.2.2 Second-order blind identification (SOBI)

Blind source separation (BSS) is a signal processing tool that has been abundantly used in OMA (Cardoso 1998). This technique is called ‘blind’ because the input forces, i.e., the sources that cause the system response are unknown. Modal parameters are determined by solving different statistical optimization problems which differ based on the assumptions in the mathematical model (Kerschen et al. 2007). In BSS, the matrix of the measured system responses is equivalent to the modal transformation matrix times the matrix of modal coordinates. This model is analogous to the solution of equation of motion of a multi-degree of freedom system. The motivation of BSS is that the matrix of the modal coordinates is a special case in which the sources are functions of time (Sadhu et al. 2017).

Considering a linear, classically damped, and lumped-mass n-degrees of freedom (*DOFs*) system subjected to an input force $F(t)$, the governing equation of motion is given by

$$M\ddot{x}(t)+C\dot{x}(t)+Kx(t)=F(t) \quad (5.1)$$

where, $x(t)$ is a vector of displacements at the degrees of freedom (*DOFs*), M is the mass matrix, C is the damping matrix, and K is the stiffness matrix. The solution of Eq. 5.1 can be written in matrix form as

$$\mathbf{x}=\Phi\mathbf{Q} \quad (5.2)$$

where $\mathbf{x}$ is an $N \times m$ matrix of measured responses at m locations and N samples of each response, Φ is an N x N modal transformation matrix of the T_x , and $\mathbf{Q}$ is an N x n matrix of n vectors of modal coordinates. The mathematical form of the BSS model which SOBI solves (approximately) is

$$\mathbf{x}=\mathbf{A}\mathbf{s}+\mathbf{b} \quad (5.3)$$

where $\mathbf{b}$ is the matrix of the uncorrelated measurement noise, $\mathbf{s}$ is a matrix (N x n) of unknown source signals, and $\mathbf{A}$ is the mixing matrix (N x N) which contains source contributions. It can be clearly observed that Eqs. 5.2 and 5.3 are analogous with Φ equivalent to $\mathbf{A}$ and $\mathbf{Q}$ equivalent to $\mathbf{s}$. $\mathbf{Q}$ is a special case of $\mathbf{s}$ in which the sources are functions of time. SOBI works for 'over-determined' models in which the measured responses are greater than or equal to the number of *DOFs* (i.e., $m \geq n$) with the assumption that the arrival of source signals is instantaneous and the sources arrive at the same time at the measurement locations ('instantaneous' model). Further, SOBI can be applied only for time-invariant systems for which $\mathbf{A}$ has time-independent coefficients. There are other assumptions associated with SOBI (Belouchrani et al. 1997) that allow utilization of matrix diagonalization procedures to identify the sources and solve Eq. 5.3 to extract the modal parameters of the system. These are:

- The sources are assumed to be stationary,
- The sources are spatially uncorrelated but temporally correlated
- Measurement noise is uncorrelated

SOBI comes under the class called Second-order methods (SOS) because these methods use the auto-correlation matrices (second-order statistics) of the measured responses.

Mathematically, the starting point of the SOBI solution is construction of covariance matrices $\mathbf{R_x}(0)$ and $\mathbf{R_x}(p)$ at time zero and at an arbitrary non-zero time lag p, respectively, using the measured response matrix $\mathbf{x}(k)$ (k is the time sample no.), as shown below:

$$\begin{aligned}\mathbf{R_X}(0) &= E\left\{\mathbf{x}(k)\,\mathbf{x}^T(k)\right\} = \mathbf{A}\,\mathbf{R_S}(0)\,\mathbf{A}^T \\ \mathbf{R_X}(p) &= E\left\{\mathbf{x}(k)\,\mathbf{x}^T(k-p)\right\} = \mathbf{A}\,\mathbf{R_S}(p)\,\mathbf{A}^T\end{aligned} \tag{5.4}$$

Where $\mathbf{R_s}(p) = E\left\{\mathbf{s}(k)\,\mathbf{s}^T(k-p)\right\}$ is the covariance matrix comprising of source vectors.

A numerical procedure called the joint approximate diagonalization along with the use of advanced mathematical tools such as whitening, orthogonalization, and unitary transformation lead to an estimated matrix $\hat{\mathbf{A}}$ of $\mathbf{A}$ (Belouchrani et al. 1997). Subsequently, the source matrix $\mathbf{s}$, through which the modal coordinates matrix $\mathbf{Q}$ are estimated, is obtained using

$$\mathbf{s} = \hat{\mathbf{A}}^{-1}\mathbf{x} \tag{5.5}$$

The source matrix $\mathbf{s}$ is equivalent to the modal coordinates matrix $\mathbf{Q}$. The natural frequency and damping associated with each mode are estimated by applying standard time domain or frequency domain processes on the modal coordinates from $\mathbf{Q}$ (Sadhu et al. 2017).

Despite its relative simplicity, SOBI method has been successfully used in complex applications such as retaining walls (Rainieri et al. 2012), underground structure (Popescu 2010), dam (Popescu 2011), and in a power system (Seppänen et al. 2015). On the other hand, SOBI method has a few limitations which are listed below

- SOBI method cannot be independently applied in an ‘under-determined’ system i.e. where $m < n$ and the inverse of matrix $\mathbf{A}$ does not exist.
- SOBI method cannot be used where the input forces and structural responses are non-stationary such as in earthquakes, traffic loading and human-induced excitations.

- SOBI method cannot be applied where the mixing matrix i.e. **A** has time-dependent coefficients (time-variant system)

The BE test system is typically assumed to be a linear-time invariant system; the input excitation applied to the T_x can be assumed to be instantaneous (instantaneous model). Moreover, the T_x responses at different locations of the T_x surface are equal to the number of *DOFs* of the T_x (i.e., $m = n$). Therefore, the SOBI method is a suitable option for extracting the modal parameters of the T_x.

5.3 Literature review on numerical studies

Numerous numerical attempts have been previously made to improve the understanding of bender element testing, neither of which focus on transmitter-medium interactions. Jovicic et al. (1996) performed two-dimensional (2D) plane-strain finite element (FE) analyses for estimating the shear wave arrival time in which a soil node was forced to oscillate transversely in a single sinusoidal pulse. Arulnathan et al. (1998) presented a 2D plane-strain FE analysis to evaluate the sources of errors in determining the travel time. A sinusoidal wave bending moment uniformly distributed along the length of the transmitter was used as the input excitation (alternative to a displacement at the bender tip). Arroyo et al. (2002; 2006) created a three-dimensional (3D) numerical model using *FLAC*^{3D} in which an input sinusoidal signal was applied at the bender tip; the response displacements were estimated in locations away from the transmitter. Rio (2006) presented numerical simulations using *FLAC*^{3D} in which a partially embedded bender in a half cylindrical sample was simulated; springs were simulated at the nodes of the embedded bender. However, in both the studies of Rio (2006) and Arroyo et al. (2006), the characteristic parameters and the proposed models were not calibrated/verified against experimental data. Cheng and Leong (2018) presented a three-dimensional finite element model to interpret damping ratios from bender element tests. The bender element was replicated by a row of nodes located on the surface of a cylindrical sample, where a sinusoidal horizontal displacement was introduced. A key limitation in current numerical models is the lack of understanding of the relationship between the input voltage and the actual transmitter displacements inside the soil. The excitation wave generated from the transmitter has been replicated in different forms, e.g. displacement

time histories assigned on nodes on the transmitter tip or along the length of the embedded transmitter. Another common method, which ignores bender-soil sample interaction, is to assign displacement time histories directly on the sample surface. The accuracy of these methods has not been established yet in the literature.

The numerical study is aimed at accurately characterizing the interactions of the BE-transmitter with the medium in which it is embedded. Experimental measurements of the transmitter displacements are obtained in different media (air, liquids, and transparent soil) and under different conditions such as in liquids of different mass densities and in transparent soil under different vertical stresses. Numerical model of the transmitter is calibrated using experimental transmitter response in air. Then, the numerical model is customized to match the transmitter response in liquid and transparent soil; the changes needed in the numerical model to match the experimental transmitter response are analyzed to understand the BE-soil sample interaction. Finally, a parametric study is performed to evaluate the effects of different sample properties on the transmitter resonance frequency and damping ratio. The resonance frequency varies linearly with all the elastic parameters studies (*v, G*, *K*) while the damping ratio does not follow the regular trends. (Atefi-Monfared, K. 2019).

5.4 Experimental setup

The experimental setup used for this chapter is similar to the one used for measurements in Chapter 4. However, there is a small difference; the plexi-glass box used for holding the liquids/transparent soil is replaced by a smaller plexi-glass tube of 1.5 inches x 1.5 inches x 3 inches with a wall thickness of 0.125 inches (Fig. 5-1). This tube is used to minimize the quantity of the transparent soil through which the laser penetrates to reach the transmitter and because the transparency of the transparent soil is much better with this smaller tube.

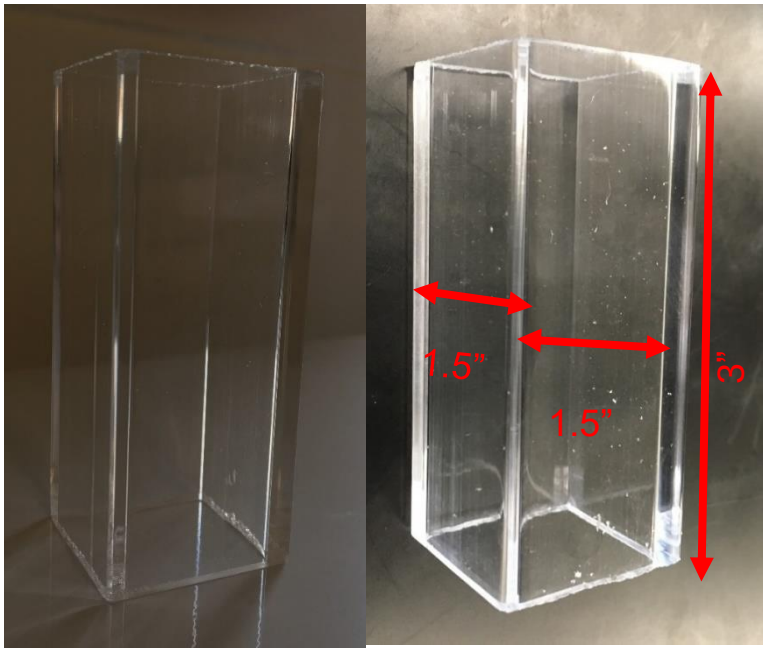

Fig. 5-1: Plexi-glass square tube used for holding the transparent soil

A schematic of the setup with the new plexi-glass tube is shown in Fig. 5-2. Note that the bender transmitter (T_x) used in this study is different from the one used for chapter 4. The dimensions of this new T_x are 13 mm x 5 mm x 0.5 mm. The weights used for inducing the vertical stress in the transparent soil are placed on a steel rod with a rectangular base plate instead of the plastic cylinder (Fig. 5-3). Another difference in this setup is the addition of a piezo-driver to generate higher input voltages to be applied to the T_x. The function generator has a maximum output voltage of 10 VPP; this voltage is insufficient for the T_x to respond at higher vertical stresses. The piezo-driver amplifies the input voltage by 25 before applying the input voltage to the T_x. This amplified signal is higher than the maximum voltage that can be monitored on the computer or the oscilloscope; therefore, the input voltage is reduced within the piezo-driver before the input voltage is monitored/stored on the oscilloscope/computer.

5.4.1 Description of the setup

The function generator generates an input voltage which is amplified by the piezo-driver before applying to the T_x; the amplitude of this input voltage is reduced before monitoring and storing on the oscilloscope and computer. The T_x vibrates in response to the amplified

input voltage; these vibrations are measured by the laser head through the laser beam. Note that the laser setup is capable of measuring vibrations of frequencies of up to 25 MHz. The vibration controller digitizes the laser readings to be monitored/stored in the oscilloscope/computer. This process is followed for all measurements i.e. in air, liquids, and transparent soil with confinements except that the piezo-driver is not used (needed) for measurements in air and liquids because the amplitude of the T_x response in air and liquids is sufficient.

Note that the replacement of the big plexi-glass box with the smaller square tube for holding the liquids and soil means the *o-ring* placed in the groove of the base platen is no longer required. However, the base of the square tube has to be sealed to prevent leakage of liquids through the base of the square tube; for this purpose, silicon sealant is applied at the base of the square tube before placing it around the T_x on the base platen

The reflecting tape used for laser measurements in liquids/soil in chapter 4 is also replaced by a better reflecting tape which is found to give more consistent results; this tape (called reflective sheet targets) is typically used with surveying equipment and is commercially available (SOKKIA^{TM}). The distance between the laser head and T_x (x) is required to be at least 250 mm for sufficient laser focus (Polytec 2013); it was maintained at 610 mm for all the tests (air, liquids, soil). All time signals are recorded for a length of 5 ms with a time step of 3.9×10^{-5} ms. An average of 500 signals is measured and stored for all measurements to reduce noise contamination in laser measurements.

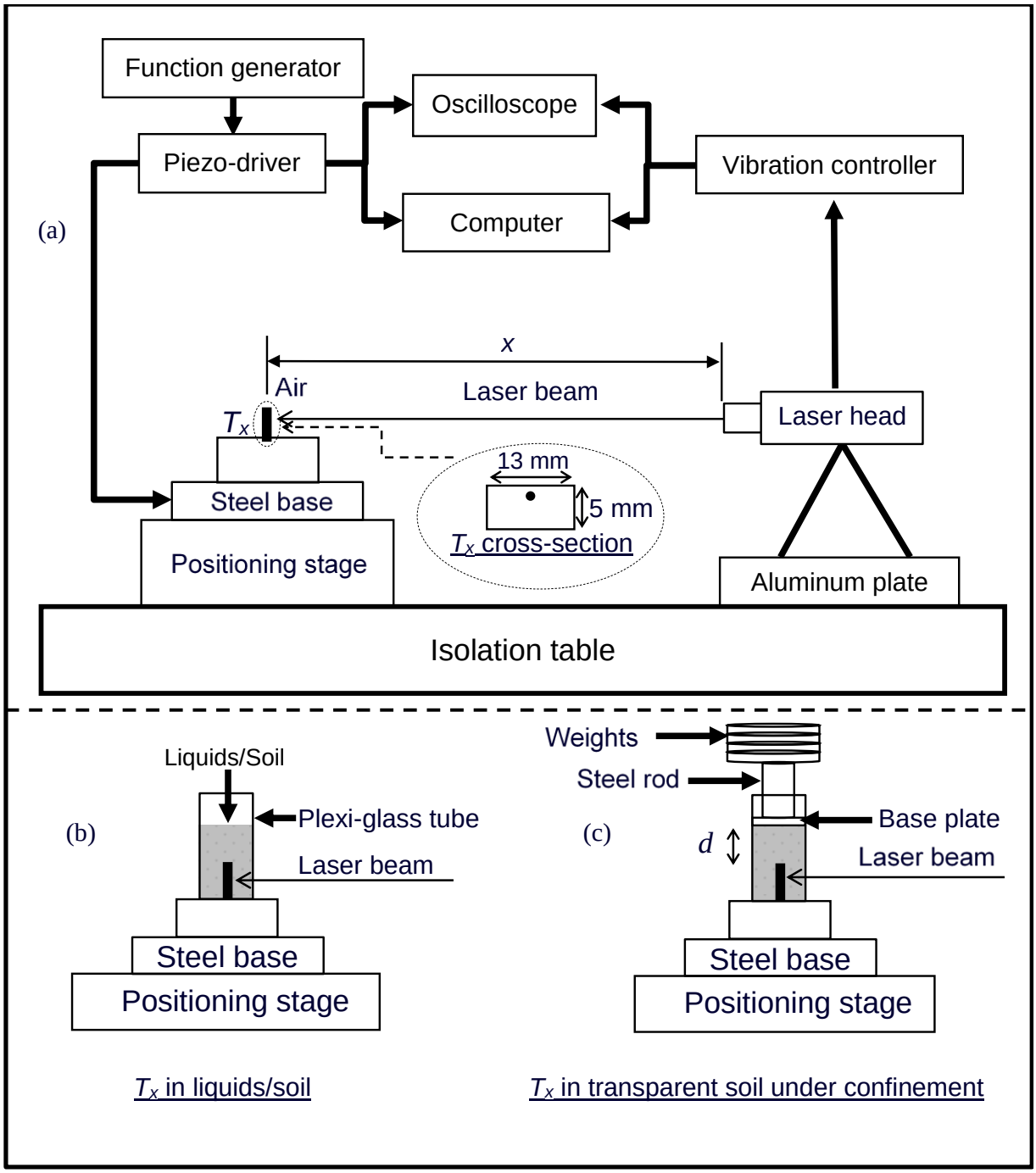

Fig. 5-2: Schematic of the experimental setup for measuring T_x vibrations in liquids and transparent soil

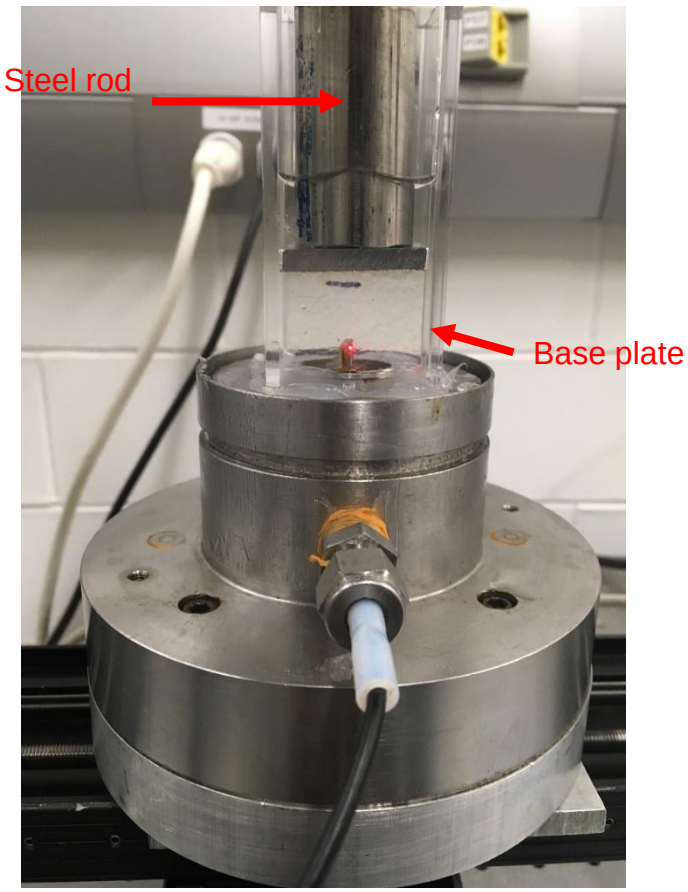

Fig. 5-3: Weights on the steel rod to induce vertical stress in the transparent soil

5.4.2 Calibration of piezo-driver

The piezo-driver is used to amplify the input voltage from the function generator before the input voltage is sent to the transmitter (Fig. 5-2). The electrical circuit of the piezo-driver amplifies the signal by 25 times. The calibration of the piezo-driver is performed to ensure that the piezo-driver is amplifying the signals according to the specifications. This calibration is done by estimating transfer function of the piezo-driver using a spectrum analyzer (HP-35670A). The built-in source of the spectrum analyzer is used to generate random noise signals of different voltage levels (from 0.6 VPP to 12 VPP) and input into the piezo driver; simultaneously, the input signal is sent to the input channel of the spectrum analyzer. The output from the piezo-driver is sent to the output channel of the analyzer and the transfer function is estimated. Fig. 5-4 shows the magnitude plots of the transfer functions of the piezo-driver in response to lowest and highest voltage levels

tested. The magnitude plot of higher voltage level is offset by 1 for clarity. Fig. 5-4 shows that the piezo-driver amplifies the signal by 25 times as expected; and the magnitude is constant across the frequency range of 3-25 kHz. The DC-component noise in frequency range of 0 to 3 kHz does not affect the results of this study because the relevant frequency range is from 7 kHz to 25 kHz. These results show that the piezo-driver is suitable for use with the experimental setup in this study.

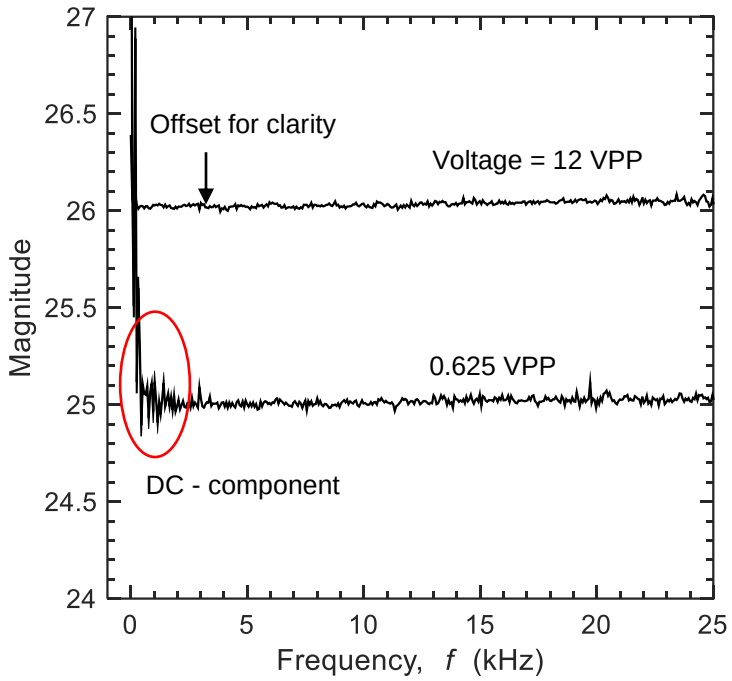

Fig. 5-4: Transfer functions of the piezo-driver with different input voltages (offset by 0.5)

5.5 Experimental methodology

5.5.1 Measurements in air

The T_x responses at different locations on the T_x surface are required to form the operating data for performing the BSS of the T_x. The positioning stage is utilized to move the T_x (target) such that the laser is pointed at different locations on the T_x surface and the time signals of the T_x response are measured. This set of signals is processed with the SOBI algorithm to extract the T_x modal parameters. Fig. 5-5 shows the locations on the T_x surface at which the vibrations are measured. The spacing between the locations on the T_x is 0.5 mm along the length of the transmitter and 1 mm along the width. An average of a total of 500 measurements at each point on T_x surface is used for further processing.

Sine pulse is a suitable input signal for analyzing the T_x response in different media (Section 4.5.1). A sine-pulse of 10 volts peak-to-peak (VPP) is used as the input signal V_{app} to measure the T_x response in air. The first resonance frequency f_1 of the T_x response in air is selected as the central frequency f_c of this sine pulse to maximize the energy in the first mode of the T_x response (Section 4.6.2). The resonance frequency f_1 is picked from the transfer function of the T_x which was experimentally determined using a spectrum analyzer (HP-35670A). The input excitation given to the T_x for determining the transfer function is a sine-sweep applied from the built-in source of the analyzer; and the response of the T_x to the sine-sweep is measured using the laser at the center of the free end of the T_x (point 5 in Fig. 5-5, also shown as a dot in Fig. 4-3).

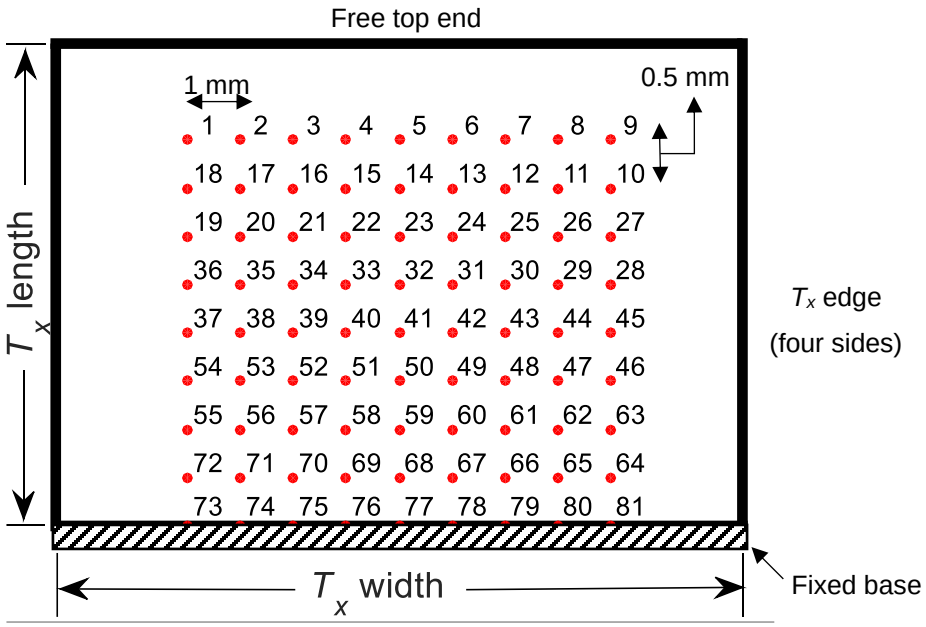

Fig. 5-5: Locations of laser measurements on the T_x

5.5.2 Measurements in liquids

The locations for measurements with T_x in liquids are the same as that for measurements in air (Fig. 5-5). The liquids used for this study are the same as those used for chapter 4 i.e. mineral oil mixture (least dense), water, sucrose of 20 % and 40 %; however, a sucrose of 60 % concentration (ρ_L = 1.287 g/mL) is added to the list of liquids in which T_x response is measured. Densities of the liquids are measured in the lab. The procedure followed for measurements in liquids is similar to that of air except that now the square-tube is placed around the T_x and sealed with the silicon sealant. Silicon sealant is left for it be cured for three hours before gently pouring the liquids in the square tube up to 1 inch (25.4 mm) level. The silicon sealant is broken and the square tube and T_x with the base platen are thoroughly washed in between measurements for different liquids. The effect of plexi-glass presence around the T_x has already been discussed to have negligible effect in chapter 4; this exercise is repeated (but not presented to avoid repeatability) to ensure that the square tube effect can be neglected in the analysis of the measurements in liquids. The displacement time signals in liquids are gathered and processed using the SOBI algorithms to assess the effects of density on the modal shapes of the T_x. The frequency spectra of the transmitter responses in these liquids are used to estimate the

resonance frequency and damping ratio of the transmitter in these liquids. The input signal used is again the sine pulse signals with a 10 VPP amplitude.

5.5.3 Measurements in transparent soil

The measurement locations on the T_x surface for responses in transparent soil are the same as those for air and liquids (Fig. 5-5). Fused quartz are air-pluviated in the tube after the measurements in the oil are completed to make a soil sample of plan dimensions 32 mm $\times$ 32 mm (which are the same as the internal dimensions of the tube) and height 25 mm. Fig. 5-6 shows a picture of the soil sample around the T_x placed on the base platen. The time signals of the T_x responses to a sine pulse input excitation (with V_{app} = 25 VPP and $f_c = f_1$) at different locations are processed using the SOBI algorithm to estimate the T_x modal parameters in soil.

The vertical stress σ_v in the soil is induced by placing dead weights on a steel rod which is placed on the soil for transferring the load from the weights to the soil. A rectangular base plate with dimensions equal to the internal area of the square tube (32 mm $\times$ 32 mm) is glued to the base of the steel rod to ensure uniform load distribution on the soil. Then, the vertical stress σ_v at the top of the transmitter is estimated from the weight and internal area of the square tube (load / area).

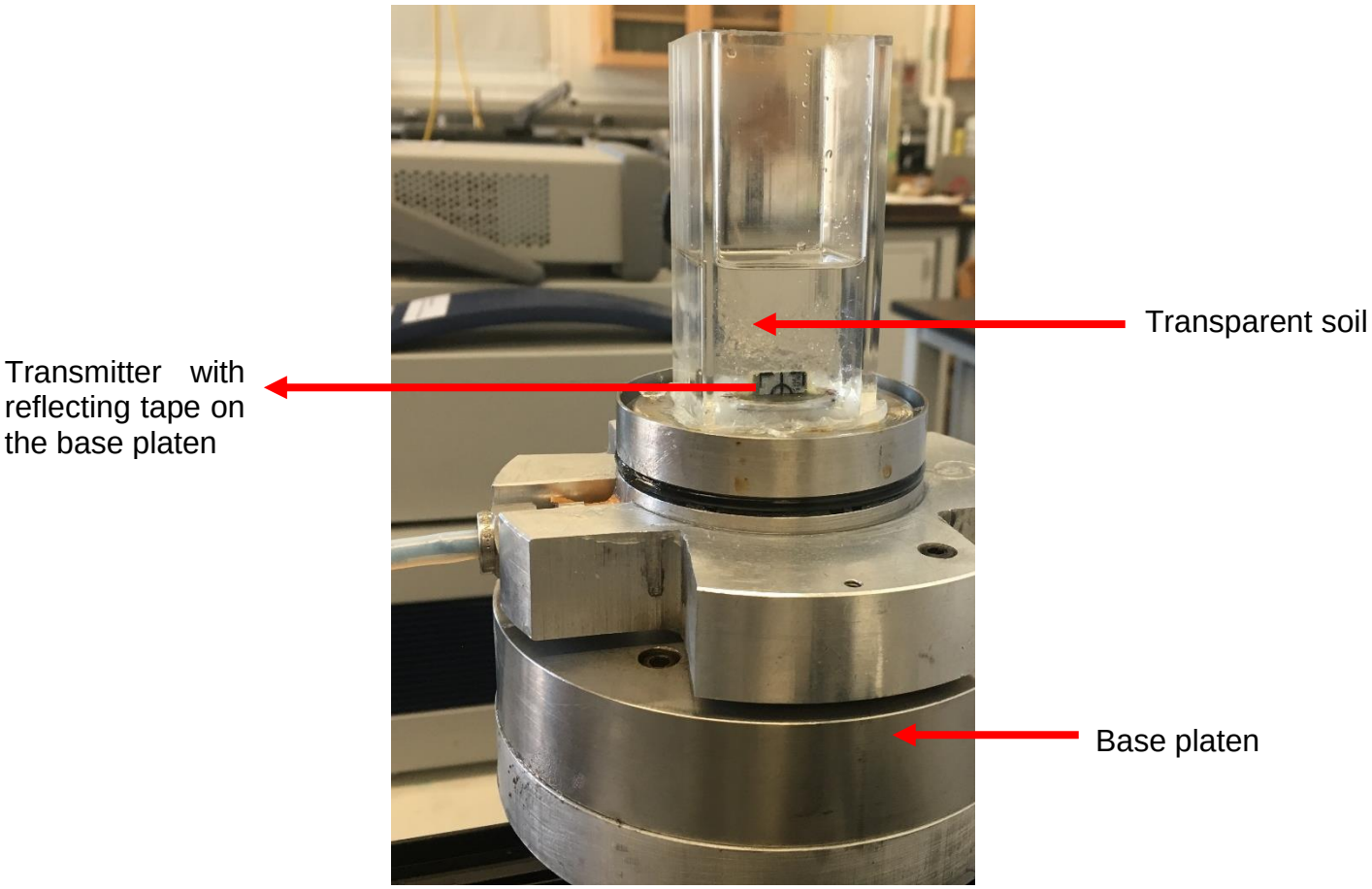

Fig. 5-6: Transparent soil sample around the T_x in the square tube on the base platen

5.6 Numerical analysis

The commercial software FLAC^{3D} based on explicit finite difference method, is used to simulate the BE-transmitter response while embedded in the different materials described above (Atefi-Monfared, K. 2019). The sample size and bender element dimensions are those of the experimental setup. The material properties of the bender element and the surrounding medium are determined through rigorous calibration with the laser displacement readings obtained from laboratory experiments. The mesh geometry – which has been identified to have a notable effect on a systems' dynamic response (Hardy, 2002 & 2003; Arroyo et al., 2002 & 2006; Rio, 2006) – as well as the manner of employing the excitation wave are determined through a rigorous calibration of the numerical model with the laser displacement readings obtained from laboratory experiments. The primary step for a fundamental assessment of bender-medium interaction is to calibrate the bender element. This is achieved through modeling the bender element response to a pulse loading in air (free-vibration). The calibrated bender element model is subsequently implemented to assess the effects of various materials on the dynamic response of the bender.

For accurate representation of wave transmission through the model in all simulations, we assure the spatial element size $\triangle L$ to satisfy the criteria that $\Delta L \leq \lambda/10$ (Kuhlmeier and Lysmer, 1973) where ΔL is the spatial element size and λ is the wavelength associated with the highest frequency component.

In FLAC3D, material damping may be specified in various forms: *Rayleigh damping*, which is frequency dependent; *hysteretic damping*, where damping allows strain-dependent modulus; and *local damping*, an approximate method to include hysteretic damping. The local damping has been commonly employed for dynamic simulations, also adopted by Arroyo et al. (2002 & 2006) and Rio (2006). Local damping enters the dynamic equilibrium calculations as a force proportional to the out-of-balance nodal forces and not to the nodal velocity. This technique was borrowed from DEM methods (Cundall, 1987). Local damping (α_L) can be estimated based on the critical damping ratio (D) $\alpha_L = \pi D$. D varies between 1 % and 5 % for most soils at shear strains mainly induced in pulse tests (Santamarina et al. 2001). In this study, both the local Rayleigh damping and the local

damping is adopted for simulations. The damping coefficient in different media is estimated through calibration of the model with the experimental displacement data set. Simulations suggest that both the Rayleigh and local damping give similar results, the former however reduced the run time of the model notably.

Consistent with the experimental setup, the bender is subjected to a horizontal sinusoidal velocity pulse, after which it is allowed to vibrate within the given sample. The excitation wave in the numerical model is defined such to replicate zero displacements and zero velocities on the bender at time t = 0. The horizontal displacement pulse used in the analysis is given by:

$$u = A\left[1-\cos\left(\frac{2\pi ft}{10}\right)\right]\sin\left(2\pi ft\right) \qquad 5.6$$

where A is a displacement coefficient obtained from the laser recording of the input pulse at the bender tip. The best replication of the bender response recorded in the laboratory was achieved where the excitation pulse was assigned at the center node of the embedded bender element tip.

5.7 Results and discussion

5.7.1 Transmitter transfer function in air

Transfer function of the T_x is important to estimate the first mode resonance frequency f_1 of the T_x because f_1 is used as the central frequency f_c of the sine pulse for T_x responses in different media (unless noted otherwise). The spectrum analyzer calculates the transfer function in real time; time domain data of this transfer function is monitored and stored in an oscilloscope. A sine sweep of frequency range 0.1-50 kHz (spanning over the spectrum analyzer range limit) with V_{app} = 0.5 VPP is used and the T_x response to this sine sweep is measured using the laser vibrometer. A typical pair of input and output time signals corresponding to the transfer function of the T_x in air is shown in Fig. 5-7. The spectrum analyzer calculates the power spectra of these input and output signals; then, the transfer function is calculated by dividing the cross-power spectrum over the input power spectrum. The change in wavelengths of the sine waves in the input signal shows the change in input frequencies with a constant voltage amplitude. The rise and fall of the

output signal amplitude indicates the resonance region. Resonance frequency f_o and damping ratio ξ of this resonance region can be roughly estimated by this time signal; however, a more accurate method to estimate the f_o and ξ is to use the frequency domain data of these signals (transfer function).

Fig. 5-8 shows the magnitude of the T_x transfer function in air; two modes of vibration are identified in the frequency range of 0.1 to 50 kHz with their corresponding resonance frequencies f_1 and f_2, and damping ratios ξ_1 and ξ_2. The magnitude of the transfer function (TF) shows that the energy in the first mode of vibration is 50% more than that of the second mode of vibration, f_2 (= 33.9 kHz) is more than double of f_1 (= 15.28 kHz), but $\xi_1 \approx \xi_2$. f_1 = 15.28 kHz is used as the central frequency f_c of the sine pulse to measure the T_x response in different media (unless noted otherwise). Note that the resonance frequencies and damping ratios of this transmitter are higher than those of the transmitter used in chapter 4. The transmitter used in this chapter has smaller dimensions than that of chapter 4 which aligns with this result of higher resonance frequencies and damping ratios.

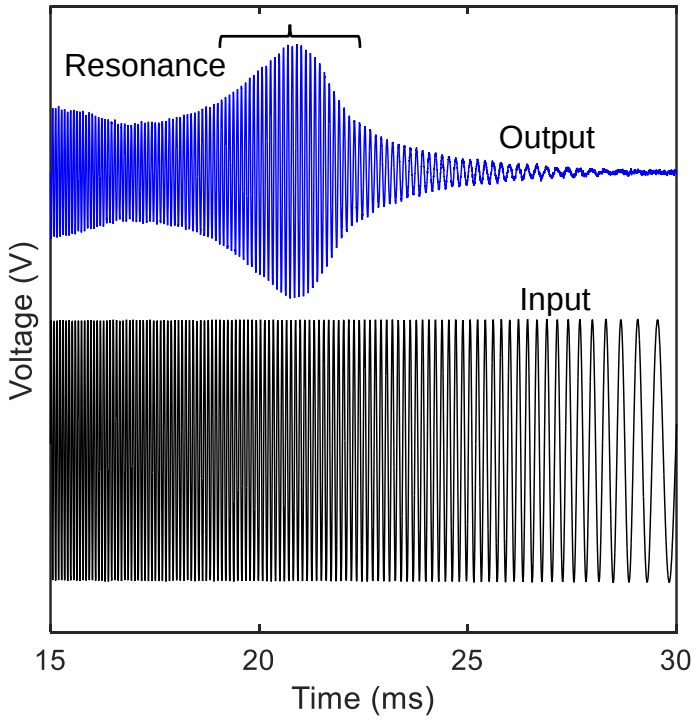

Fig. 5-7: Typical pair of time signals used for calculating the transfer function of the T_x in air

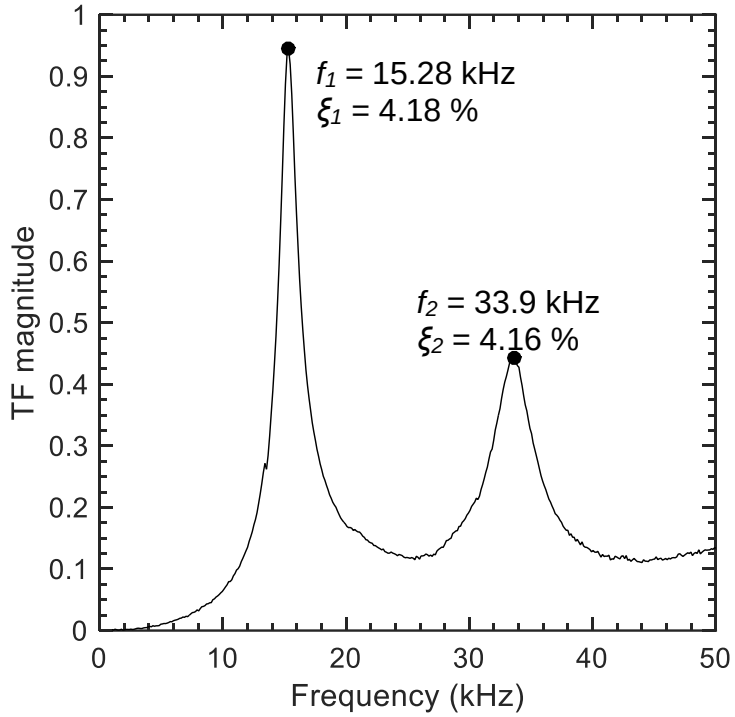

Fig. 5-8: Transfer function of the transmitter in air

5.7.2 Mode shapes in air

The T_x responses in air to a sine-pulse (V_{app} = 10 VPP, f_c = 15.3 kHz) measured using the laser at different locations (Fig. 5-5) are processed using the SOBI algorithm to extract the first three mode shapes of the T_x in air (Fig. 5-9). The modal coordinates of the mode shapes are estimated using the SOBI procedure described in the background section. The peak modal coordinate of each mode shape and the maximum displacement u_{max} of the T_x in air corresponding to the peak modal coordinate of the first mode are shown in Fig. 5-9. These mode shapes are close to those of a cantilever plate vibration (Leissa 1969); the first mode shape is a bending mode, the second mode is a plate mode (twisting), and the third mode is the second beam bending mode. This result shows that the typical model of a cantilever beam used in BE test is not valid (Lee and Santamarina 2005). The first bending mode is the dominant mode as expected; the peak values corresponding to the second and third modes are only 5 % and 1 % of the peak value of the first mode, respectively. This result is in agreement with the results of Irfan et al. (2019) that the first mode is the dominant mode because the input excitation (sine pulse

in this case) frequency $f_c \approx f_1$ of the T_x in air. The minor contribution of the second and third modes also corroborates the findings of Chapter 4 that the sine pulse input excitation introduces lesser energy in higher modes than a square pulse.

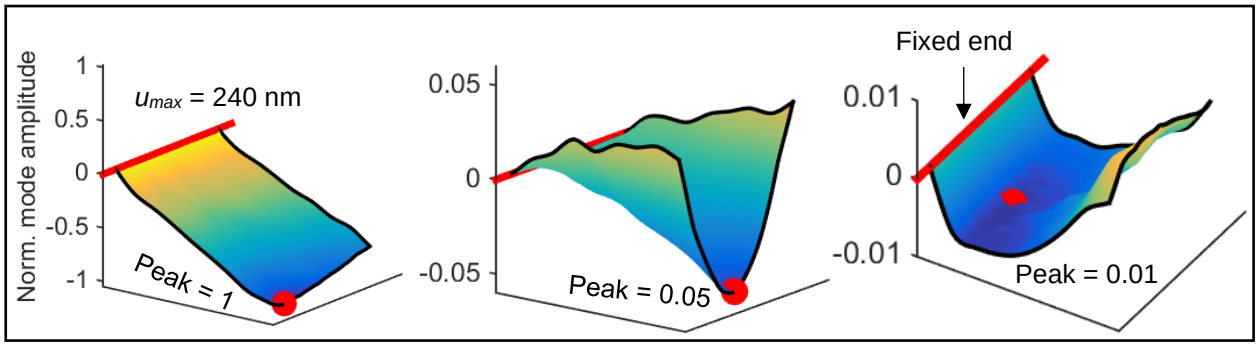

Fig. 5-9: First three mode shapes of the transmitter vibration in air normalized with respect to the peak coordinate value of the first mode (red dot marks the peak amplitude; BE base (width = 13 mm) marked by the red line)

5.7.3 Effects of input voltage amplitude

Generally, the voltage of the input signal applied to the T_x in BE tests is arbitrarily selected. The effect of the input voltage on the T_x behaviour has not been studied because the actual T_x displacements cannot be measured in BE test. Leong et al. (2005) proposed an equation for estimating the peak-to-peak displacement $x_{p\text{-}p}$ of a T_x of length L_b and thickness h when the T_x is subjected to an input voltage V_{app}:

$$x_{p-p} = \frac{3L_b^2 V_{app} d_{31} \beta}{2h^2} \qquad 5.7$$

where d_{31} is the piezoelectric strain constant and β is a constant added in this study to represent the effects of liquids ($\beta = 1$ in air).

The actual displacements of the T_x is measured and checked against Eq. 5.7. The $x_{p\text{-}p}$ of the T_x in air and in oil are measured in response to a sine pulse (f_c = 15.28 kHz) with different peak-to-peak input voltages (V_{app}); these measurements are plotted with Eq. 5.7 in Fig. 5-10. The values of the constants to evaluate Eq. 5.7 are: d_{31} = 390 $\times$ 10^{-12} m/V

(Piezo 2005), L_b = 0.005 m (measured), and h = 0.0005 m (measured). A very good agreement is observed between Eq. 5.7 (theoretical) and the experimental displacements in air with only a 2% difference in the slopes. The estimated $\beta = 0.4$ in oil shows that the slope of the experimental transmitter displacements in liquid is 60 % smaller than that in air. The effects of liquids other than oil on the transmitter displacements are discussed in Chapter 6.

Rio (2006) also measured the transmitter displacements using a laser vibrometer and compared his experimental results with the results obtained using Eq. 5.7; the $x_{p\text{-}p}$ in air of two T_x tested by Rio (2006) in response to an input voltage with V_{app} = 20 V are estimated to be 36 μm and 12 μm. These displacements are three orders of magnitude higher than those predicted by Eq. 5.7. The corresponding maximum shear strain along the BE height based on these peak displacements is of the order of 10^{-3}%; which is inconsistent with the results from previous researchers (Pennington et al., 2001; Leong et al., 2005; Camacho-Tauta et al., 2015).

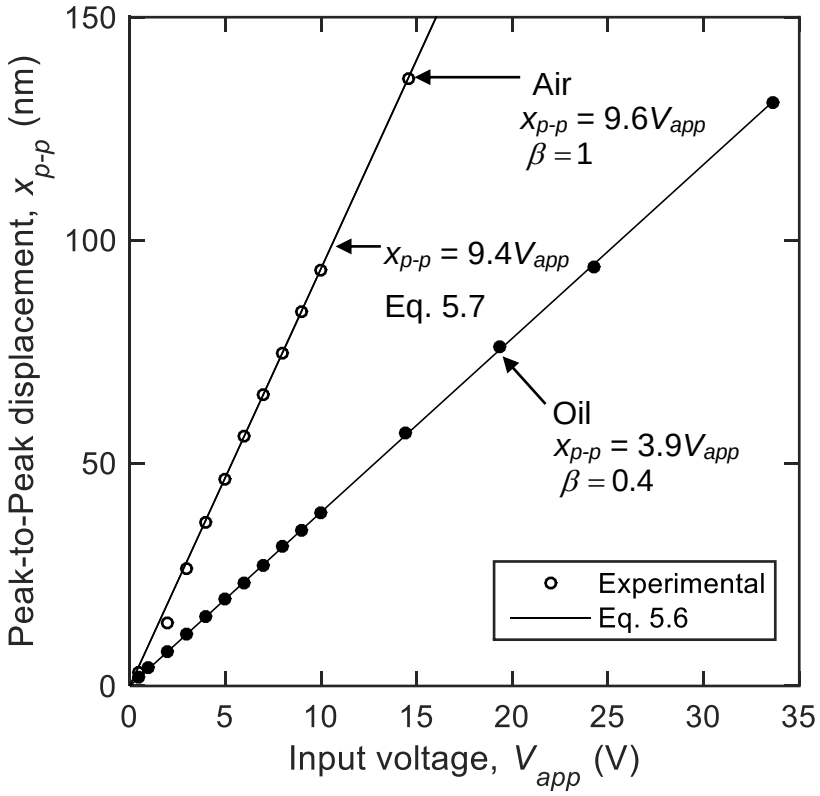

Fig. 5-10: Peak displacement vs peak-to-peak input voltage amplitude in air and liquid along with the equation

5.7.4 Transmitter displacement response in oil

The T_x displacement response to a sine pulse (f_c = 15.28, V_{app} = 10 VPP) measured inside the oil (point 5, Fig. 5-5) is presented in Fig. 5-11. The figure shows that, even inside a liquid, the T_x response is similar to the free vibration response of a single-degree-of-freedom system. The estimated values of f_o and ξ of the T_x exponential decay are 11.58 kHz and 4.40 % respectively. A small mismatch between the displacement response and the theoretical decay in the time range < 0.3 ms indicates a minor presence of higher modes of vibration in the T_x response. This higher mode presence is also observed in the frequency spectra of this time signal (next section).

The effects of volume of the oil around the T_x inside the tube on the T_x behavior are investigated to ensure the measurements are not affected if the liquid volumes change. T_x responses in three volumes (20 mL, 50 mL, and 80 mL) are measured (point 5, Fig. 5-5). Increasing the volume four times (from 20 mL to 80 mL) resulted in no significant

changes in the T_x response shown in Fig. 5-11; the only change was that the peak displacement of the T_x response reduced by 0.02 %.

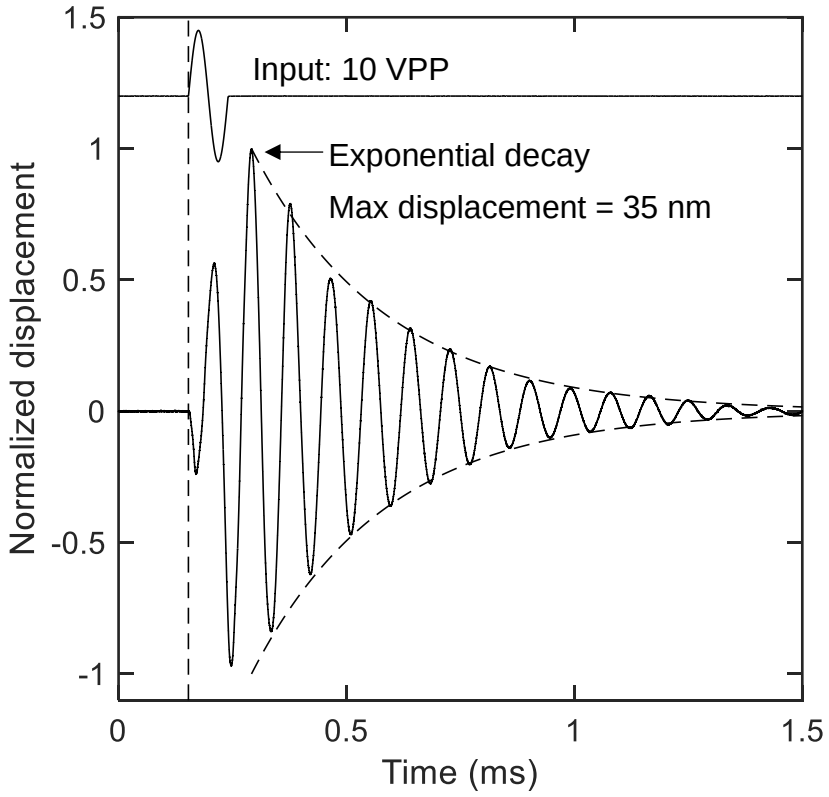

Fig. 5-11: Normalized transmitter response to a sine pulse input excitation inside the mineral oil mixture

5.7.5 Effects of liquid mass density on transmitter

T_x responses to a sine pulse in five liquids with different densities ρ_L are measured using the laser vibrometer (at point 5, Fig. 5-5). The frequency spectra of these T_x responses are shown in Fig. 5-12 with the first and second mode peaks marked with solid circles. With increase of ρ_L by 50% the magnitude of the first mode decreases by 15% but f_1 decreases only by 5%. The average ratio of the maximum spectral magnitude of the first mode over the second mode of vibration (magnitude of f_1 over magnitude of f_2) of the T_x in liquids is about 22, while this ratio in air is about 38. Therefore, the added mass of the liquids reduces the relative participation of the second mode in the T_x response by 44%.

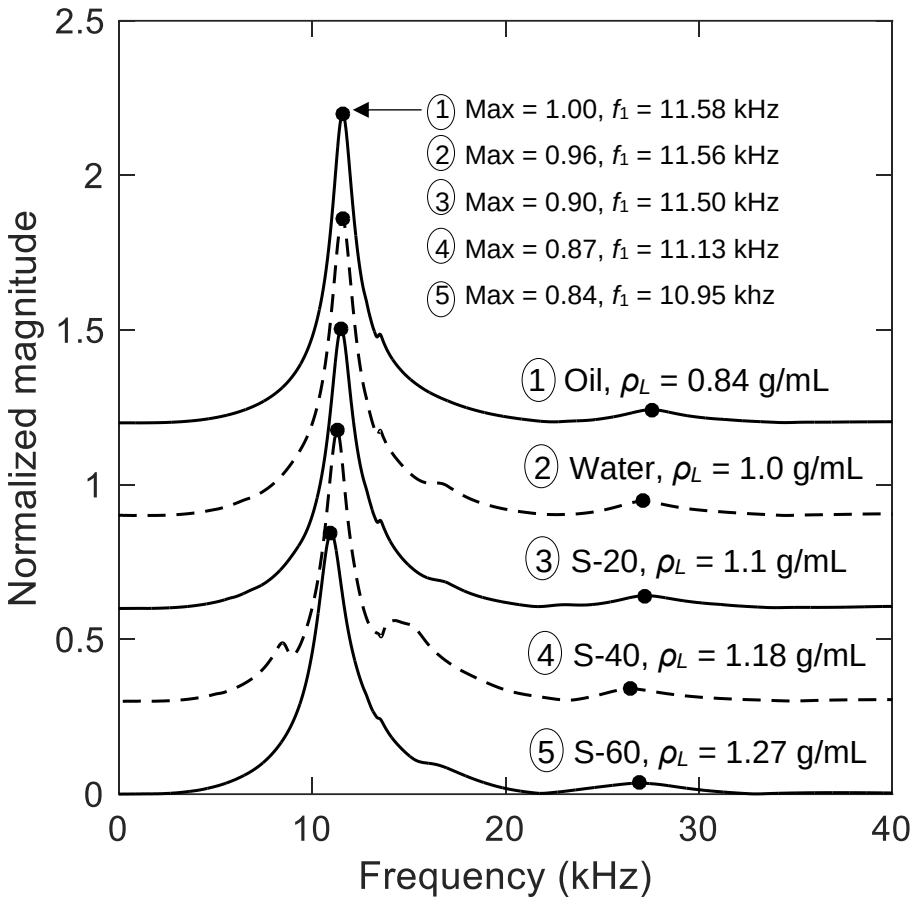

Fig. 5-12: Normalized frequency spectra magnitudes of transmitter vibration inside different liquids

Chu (1963) proposed the following equation for estimating the ratio between the radial resonance frequency of a cantilever beam in an inviscid fluid (ω_{fluid}) and in vacuum (ω_{vac}):

$$\frac{\omega_{fluid}}{\omega_{vac}} = \sqrt{1+\frac{\pi\rho_L b}{\alpha\rho_b h}} \qquad 5.8$$

where ρ_L and ρ_b are the densities of the fluid and beam respectively, b and h are the width and the thickness of the beam, and the constant α represents the mode number. Eq. 5.8 is used to estimate the theoretical f_1 of the T_x inside the five liquids using the values ω_{vac} = 2π × 15.28 kHz (radial resonance frequency in air), ρ_b = 7700 kg/m^3, b = 0.013 m, h = 0.0005 m, $\alpha = 4$ along with liquid densities. The resonance frequency in vacuum is assumed to be the resonance frequency in air because less than 1 % has been reported

in the literature (e.g. Chon et al. 2000). The theoretical frequencies and the experimental resonance frequencies f_1 and f_2 are plotted in Fig. 5-13 against ρ_L.

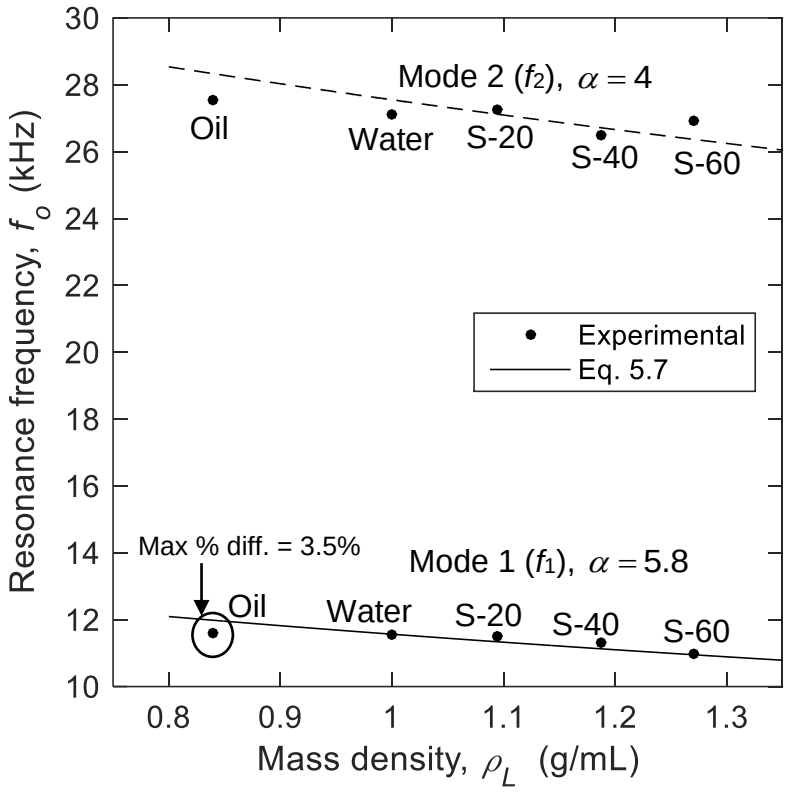

Fig. 5-13: Experimental and theoretical (Eq. 5.8) f_1 and f_2 of the transmitter in different liquids as functions of the liquid density

The experimental first mode resonance frequencies f_1 match very well with the theoretical frequencies calculated using Eq. 5.8. The maximum percentage difference between the theoretical and the experimental f_1 is 3.5% which corresponds to the f_1 in oil; the theoretical resonance frequency in oil is greater than the corresponding experimental frequency. This result is consistent with the reduction in the resonance frequency with fluid viscosity μ proposed by Sader (1998) because Eq. 5.8 does not consider the effects of fluid viscosity on the resonance frequency. Secondly, the effect of ρ_L are stronger than the effects of μ as has been shown by previous studies (Sader 1998; Atkinson and Lara 2007).

The theoretical f_2 (estimated with the f_2 in air and $\alpha = 4$) did not match very well with the experimental f_2. However, by increasing the constant α from 4 to 5.8, a reasonably good match between the theoretical and the experimental f_2 is achieved (dashed line in Fig. 5-13). Therefore, Eq. 5.8 can be used for estimating f_2 of a cantilever beam in inviscid liquids with $\alpha = 5.8$.

Fig. 5-14 shows the damping ratios ξ_1 and ξ_2 (calculated using the half-power bandwidth method) for the first and second modes of vibration, respectively, of the T_x inside the liquids along with the results of Vazquez et al. (2009) for an atomic force microscope (AFM) probe. The T_x results are compared with these AFM probes because: (i) there are no other BEs studies which present the results of a T_x response in liquids and (ii) AFM probes are piezo-electric microcantilevers (used in the aerospace industry), which are expected to have a behavior similar to a T_x. The values estimated by Vazquez et al. (2009) have been normalized so that the ξ of the AFM probe in water (7.96%) matches the ξ of the T_x in water (4.63%); this difference in ξ is because f_0 of AFM probe is an order of magnitude higher than that of the T_x. Moreover, the dimensions of the AFM probe are 10 times smaller than the dimensions of T_x which implies that the estimated ξ would be higher as shown in previous studies (Atkinson and de Lara 2007; Sader 1998)

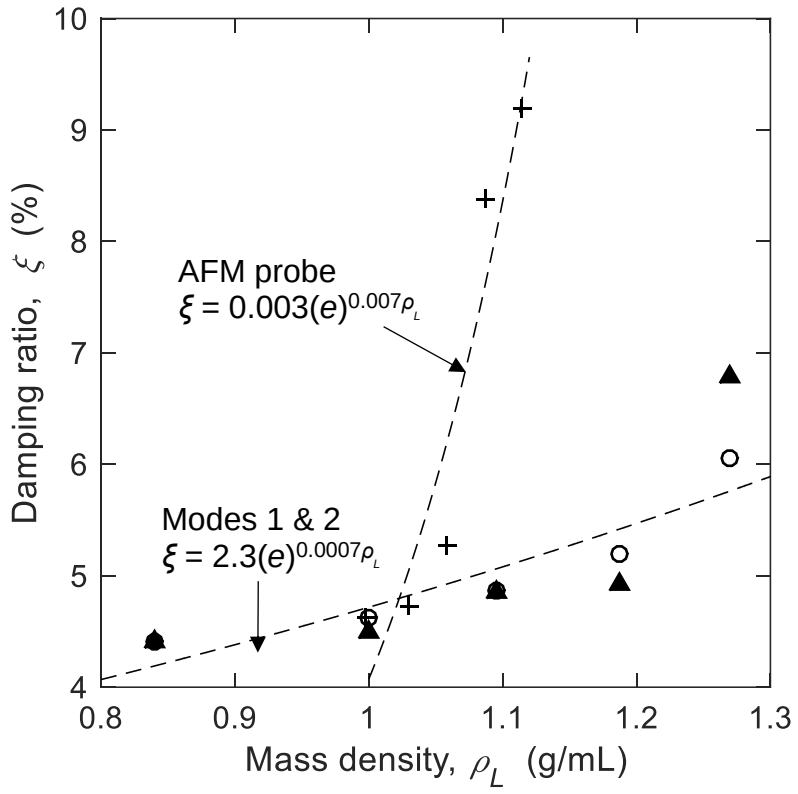

Fig. 5-14: Damping ratio of the first two modes of the transmitter inside the liquids vs the mass density of the liquids

The results in Fig. 5-14 are in agreement with the findings of Faria and Inman (2014) in that the equivalent damping of a system comprising of a cantilever beam submerged in a fluid increases with increase in ρ_L — a 50% increase in ρ_L results in a 56% increase in the first mode damping ratio ξ_1. However, the trend (e.g. linear or exponential) of this increase has not been established yet in the literature. This study shows an approximately exponential increase in both ξ_1 and ξ_2 of the T_x with ρ_L. The estimated ξ_1 and ξ_2 of the T_x are very similar in oil, water, and S-20; whereas, a difference of 5% and 12% is observed between ξ_1 and ξ_2 of the T_x in S-40 and S-60 respectively. The results of Vazquez et al. (2009) also show an exponential increase; however, the rate of increase is much greater than the rate of increase in ξ_1 and ξ_2 of this study. One possible reason for this difference is because of the difference in geometry of the AFM probe and the T_x; the dimensions of the T_x used by Vazquez et al. (2009) are 0.241 mm × 0.364 mm compared with 5 mm ×

13 mm of the T_x. This interpretation is investigated further in the next section and is also in agreement with the results of Chon et al. (2000) and Atkinson and de Lara (2007).

5.7.6 Effects of transmitter dimensions

The T_x used in this study has dimensions 13 mm $\times$ 5 mm $\times$ 0.5 mm (T1), and the T_x used in Chapter 4 with a similar experimental setup is of dimensions 14 mm $\times$ 6 mm $\times$ 1.9 mm (T2). The estimated theoretical frequencies of the transmitters T1 and T2 calculated using Eq. 5.8 are plotted with the experimental frequencies against ρ_L in Fig. 5-15. This figure clearly shows the effect of T_x dimensions on f_1 of T_x inside liquid; the ratio b/h (Eq. 5.8) of T2 is ≈72% smaller than that of T1 and the f_1 of T2 in water (e.g.) is 40% smaller than that of T1. The maximum difference between the theoretical and experimental values of f_1 of T1 in liquid is about 3.5%, while it is about 6.6% for T2. A review of the actual displacements of T1 and T2 showed that the T2 base is more flexible that the T1 base (manufacturing fault); this greater flexibility is the reason for the larger % difference between the T2 experimental and theoretical f_1. The differences in theoretical and experimental displacements are due to the fact that Eq. 5.8 assumes the fixed end of the beam to be completely restrained (i.e., completely rigid). Nevertheless, a good agreement between the theoretical and experimental f_1 is observed for both T1 and T2.

Further investigation of the effect of the T_x dimensions on the T_x behavior is done by comparing the ξ_1 of T-1 and T-2. The estimated ξ_1 of T-1 and T-2 are 4.18% (Fig. 5-8) and 2.9% (Chapter 4) respectively. This result corroborates the finding in the previous section that the damping ratio of a T_x with smaller dimensions is higher than that of a T_x with larger dimensions because the resonance frequency of the T_x with smaller dimensions is larger than the frequency of a T_x with larger dimensions.

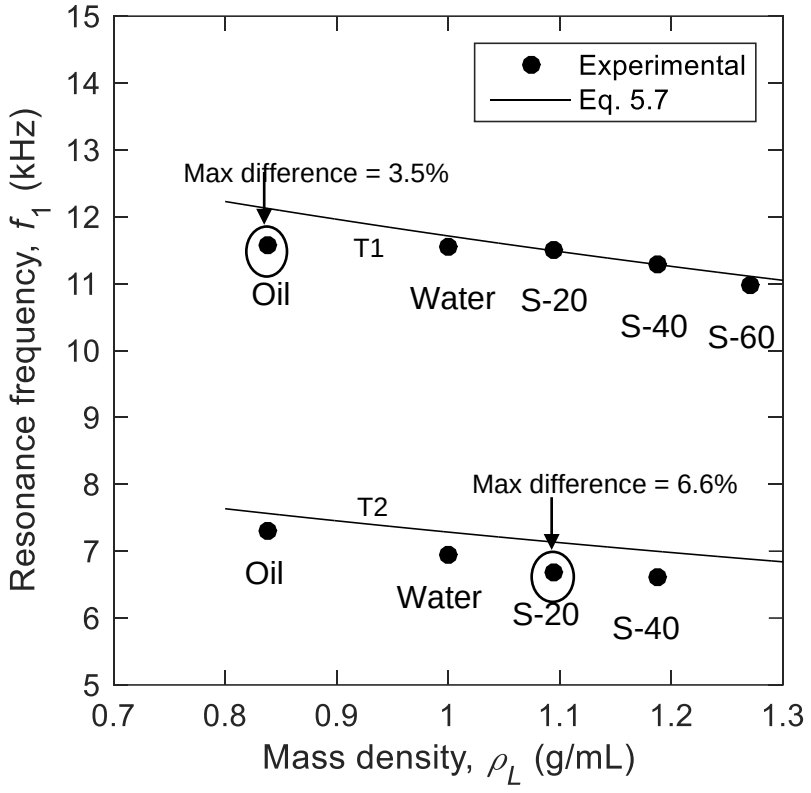

Fig. 5-15: Experimental and theoretical (Eq. 5.7) f_1 of two transmitters with different dimensions as functions of liquid density ρ_L (T1: 13 x 5 x 0.5 mm, T2: 14 x 6 x 1.9 mm)

5.7.7 Effects of Reynolds number

The typical Reynolds number is a dimensionless quantity used in fluid mechanics to help predict the fluid flow patterns (high *Re* → turbulent, low *Re* → laminar). Sader (1998) proposed a modified Reynolds number (*Re*) definition (Eq. 5.9) for liquids in which a cantilever beam of width b vibrates with a radial resonance frequency (ω).

$$Re = \frac{\rho_L \omega_L b^2}{4\mu} \qquad 5.9$$

Re is a dimensionless parameter that combines ρ_L and μ of fluids, and therefore, the use of *Re* helps investigate the combined effects of ρ_L and μ. Fig. 5-16 shows f_1 of T_x plotted against *Re* of different liquids estimated using Eq. 5.9. A power law relationship is found to fit the experimental data well (R^2 = 0.98). An outlier in this curve-fit is the f_1 in oil. *Re* of the oil is the least amongst the five liquids because its μ is ≈ 10.22 cP whereas its ρ_L is ≈

0.84 g/mL such that its density is less than and viscosity is greater than those of water; this combination of ρ_L and μ is in contrast with combination of other liquids used in this study. The power law curve-fit matches very well for f_1 of the T_x in liquids whose ρ_L increases proportionally with the μ (unlike the oil). Fig. 5-16 shows that the *Re* estimated using Eq. 5.9 increases as the μ decreases; the largest estimated *Re* is of water which has the least μ amongst the liquids used in this study.

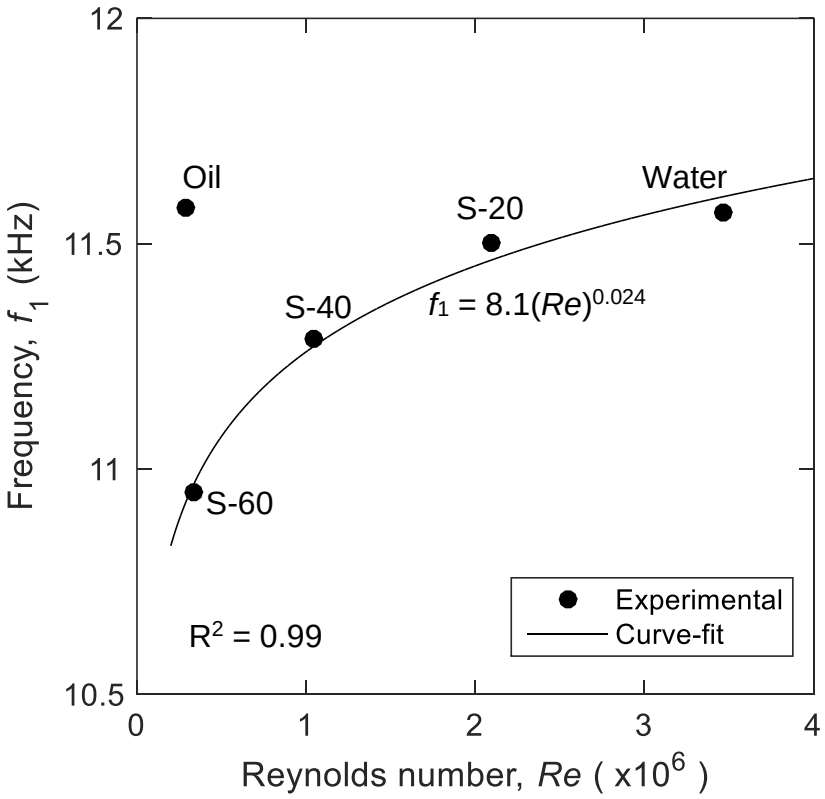

Fig. 5-16: Resonance frequency of the first mode of vibration of the transmitter in different liquids versus the Reynold's number of the liquids

Fig. 5-17 shows the variation of ξ_1 of T_x with *Re* with an excellent power-law curve fit without the damping ratio of the T_x inside the mineral oil (R^2 = 0.99). This result is in agreement with the findings of Chon et al. (2000) in that the equivalent damping of a system (represented by the quality factor in Chon et al. 2000) with a cantilever beam immersed in a fluid decreases as *Re* increases. Figs. 5-16 and 5-17 also show that the ρ_L controls the T_x behavior inside the oil rather than its μ. This finding is deduced from the

fact that f_1 of the T_x in oil is higher than that in water (f_1 decreases with increase in ρ_L) and the ξ_1 is lower (ξ_1 increases with increase in ρ_L). The ρ_L of the oil is 0.84 g/mL and ρ_L of water is 1.0 g/mL; whereas the μ of the oil (10 cP) is 10 times higher than that of water (1 cP).

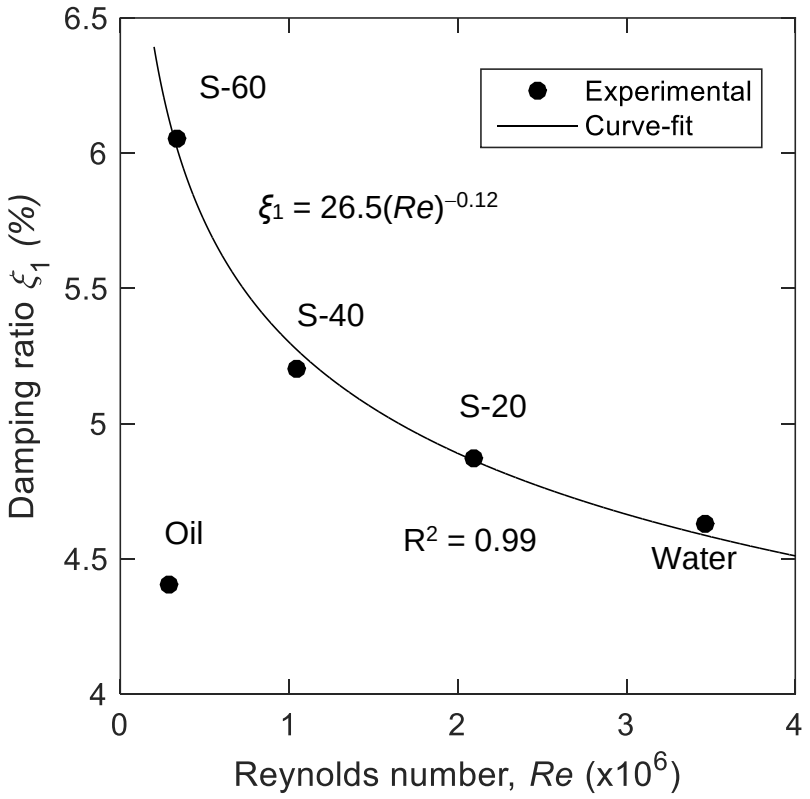

Fig. 5-17: Damping ratio for first mode of vibration of the transmitter in different liquids versus the Reynold's number of the liquids

5.7.8 Mode shapes in liquids

The T_x responses in five liquids at different locations on the T_x surface (Fig. 5-5) are processed using the SOBI algorithm to extract the mode shapes of the T_x in these liquids. The first three mode shapes of the T_x in liquids are shown in Fig. 5-18 presented in the order of increasing ρ_L (e.g. Fariah and Inman 2014). The T_x mode shapes in S-60 are not shown because of inaccurate results. The maximum displacement u_{max} of the T_x response in the liquids are shown in nanometers. The mode shapes are normalized with respect to the peak values of the first mode shape in each liquid. These results show that u_{max} of the

T_x decreases as the ρ_L increases because of the added mass effect on the T_x. All three mode shapes in all the liquids are similar to the mode shapes in air. This result is in agreement with the findings of Fario and Inman (2014) in that the presence of the added mass does not affect the first three mode shapes.

The peak modal coordinate of the second mode shape in oil is different from the peaks of the second mode in all other liquids. The peak coordinate in oil is 10% more than the first mode peak coordinate, which shows that the second mode participation of the T_x response in oil is higher than the first mode. In contrast, the second and third mode participation in the T_x response in water, S-20, and S-40 is significantly less compared with the first mode participation. The second mode peak coordinates in water, S-20, and S-40 are in the range 2-7% of the first mode peak coordinate, and the third mode peak coordinates are in the range 0.5-1% of the first mode peak coordinate. These results show that the first mode controls the T_x response despite the added mass effect of the liquids except in the case of oil. The T_x mode shapes in oil require further investigation to understand the reason for greater participation of the second mode.

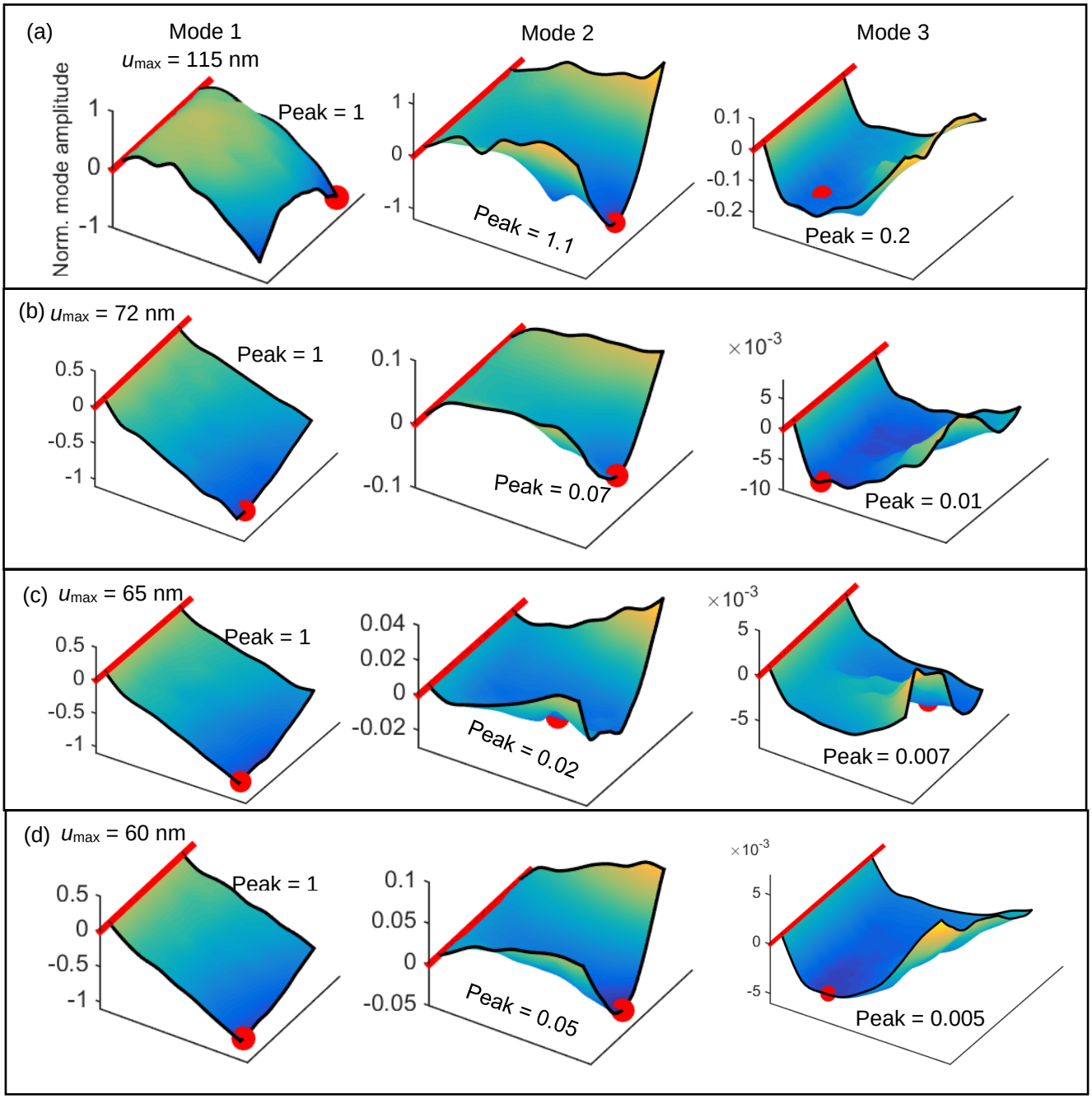

Fig. 5-18: First three mode shapes of the transmitter in different liquids: (a) oil, (b) water, (c) S-20, and (d) S-40 normalized with respect to the max displacement of the first mode of vibration (red markers indicate highest amplitude; red line indicates BE base (b = 13 mm)).

5.7.9 Transmitter response in transparent soil with different vertical stresses

The results of measurements in transparent soil in Chapter 4 are limited to a vertical stress (σ_v) of 35 kPa; in this chapter, the vertical stress (σ_v) reached is up to 400 kPa. The T_x response to a sine pulse (f_c = 15 kHz, V_{app} = 25 VPP) are measured in the transparent soil specimen under different confinements (represented by the applied vertical stress σ_v). Fig. 5-19 shows the displacement responses with u_{max} of the T_x under five vertical stresses. The u_{max} decreases with increase in σ_v as expected; the reduction in the number of cycles in the time signals also shows that the damping ratio of the T_x increases with increase in σ_v. Moreover, the higher frequencies start to dominate the T_x response as σ_v increases indicating that higher modes participate with greater energy at greater values of σ_v.

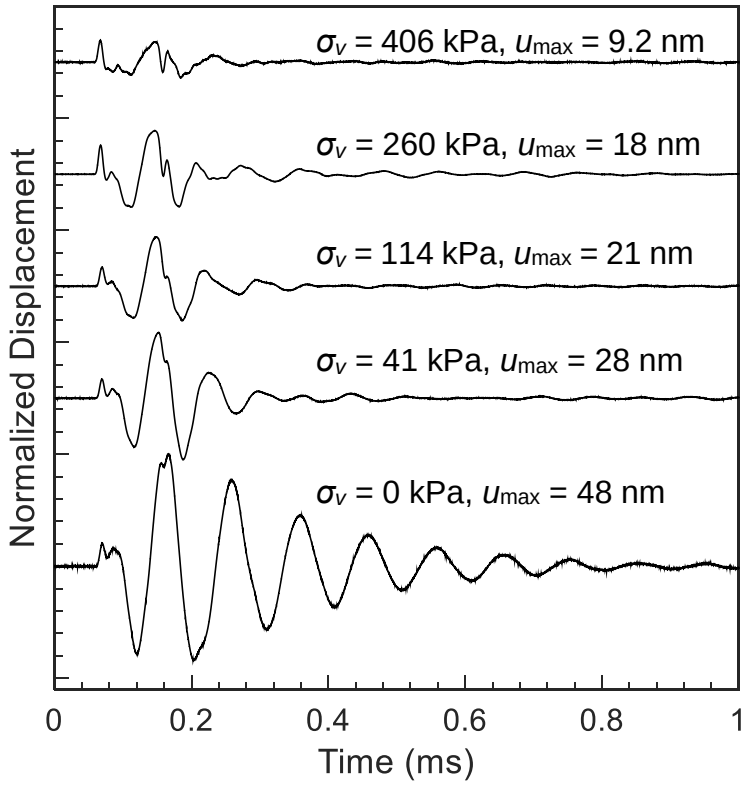

Fig. 5-19: Transmitter response to a sine pulse inside transparent soil under different vertical stresses

The frequency spectra of the displacement responses of the T_x inside the soil with vertical stresses are shown in Fig. 5-20. Fig. 5-20 corroborates the results of the displacement responses; the magnitude of the first mode of vibration is decreasing with increase in vertical stress. Moreover, the resonance frequency of the first and second modes of vibration of the T_x are increasing with increase in vertical stress. Note that the energy in higher modes of vibration is also increasing as the vertical stress is increasing which shows that higher modes become increasingly important as vertical stress increases.

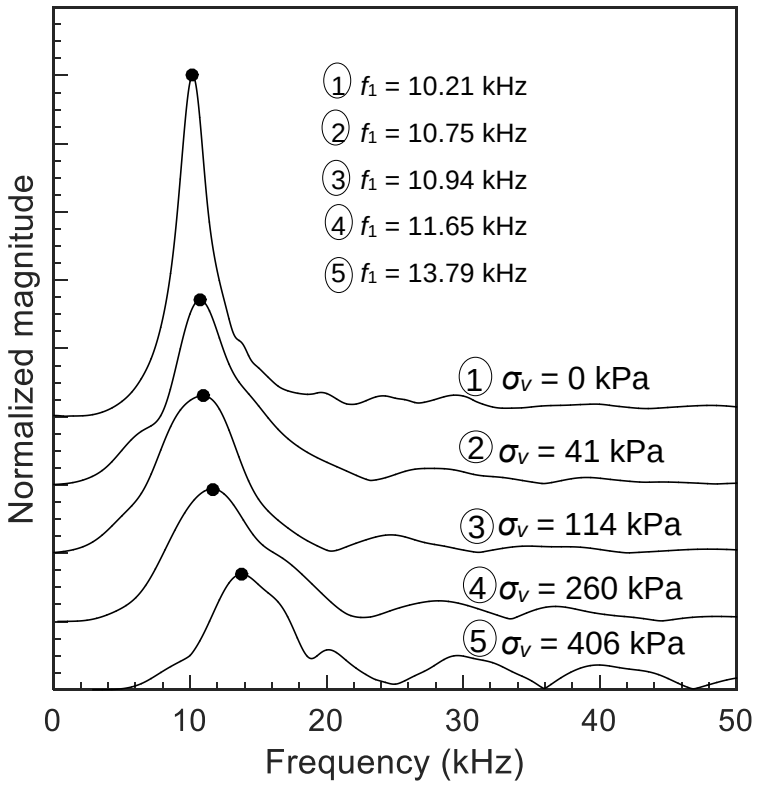

Fig. 5-20: Frequency spectra of the displacement response of the transmitter inside the soil at different vertical stresses

The f_o a soil sample is proportional to the V_s, which has a power-law relationship with the isotropic confining stress in soil (Santamarina et al. 2001). The logarithm of f_1 is plotted against the logarithm of σ_v in Fig. 5-21 and there is a good linear fit (R^2 = 0.92), which implies that f_1 is related with σ_v through a power-law relationship with the parameters α = 2.1 and β = 0.1 (Santamarina et al. 2001). This estimate of β is lower than the typical β (= 0.25) generally obtained for sands; a possible reason for this difference is that the

fused quartz with angular particles is three times stiffer than sands (Ezzein and Bathurst 2011) and the β-exponent decreases with increase in the stiffness of the material (Santamarina et al. 2001; Weast et al. 1981).

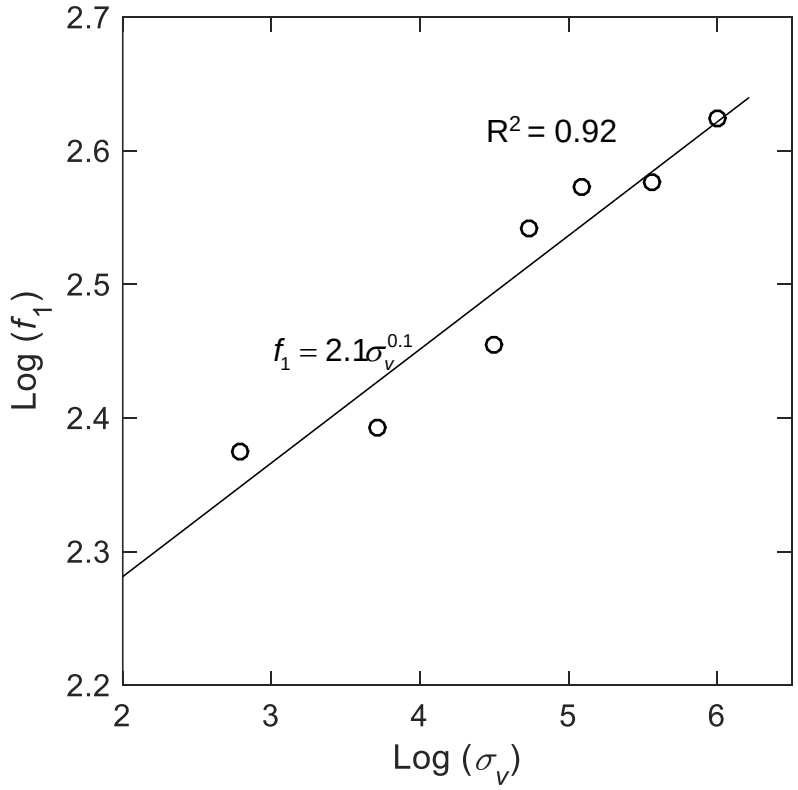

Fig. 5-21: Resonance frequency of the first mode of the transmitter inside the soil vs the vertical stress

The first mode damping ratio ξ_1 of the T_x at different vertical stresses are plotted in Fig. 5-22. The ξ_1 increases linearly up to about σ_v = 120 kPa and then stays more or less constant. The linear trend in damping ratio suggests that the damping ratio caused by friction between the fused quartz is prevalent in the T_x behavior over the damping ratio of the soil specimen. The first mode damping ratio of the T_x corresponding to the σ_v > 120 kPa is about 30% which is much higher than typical low strain damping ratios (<3 %) of soil samples (Cascante et al. 1997, Khan et al. 2008).

Several studies have attempted to estimate damping ratio using BE test without considerable success (Brocanelli and Rinaldi 1998); one of the possible reasons for these

unsuccessful attempts is the difficult to measure the damping ratio of the soil specimen when the damping ratio of the transmitter is much higher than that of the soil specimen

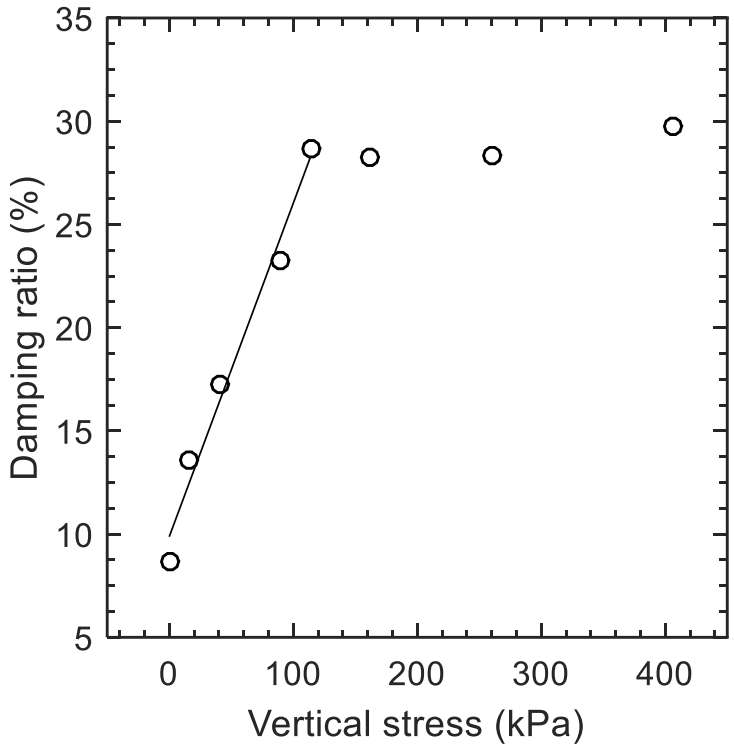

Fig. 5-22: Damping ratio of the transmitter inside the soil against the vertical stress

5.7.10 Mode shapes in soil

Fig. 5-23 shows the first three mode shapes of T_x inside the soil sample at $\sigma_v = 0$ and $\sigma_v \approx 41$ kPa. The peak ordinates values of the mode shapes are normalized with respect to the peak ordinate value of the first mode shape. The mode shapes under $\sigma_v = 0$ are very similar to the mode shapes in liquids (Fig. 5-18); however, the second and third mode shapes show the presence of higher modes, which indicates mode coupling in T_x behavior. Similarly, all three mode shapes under $\sigma_v = 41$ kPa indicate the presence of mode coupling. These mode shapes show that, as the confinement around the soil is increased, mode coupling in the T_x vibrations increases.

The peak values of the second and third modes under σ_v = 0 show that the contribution of the second and third mode shapes in the T_x response are 0.7% and 2%, respectively. This result indicates greater nonlinearity in the T_x behavior because of larger participation of the third mode. This nonlinearity increases for σ_v = 41 kPa because the contribution from the second and third modes increase to 24% and 16%, respectively. These results show that increase in σ_v in the soil around the T_x increases the participation of higher modes in the T_x response and the mode coupling.

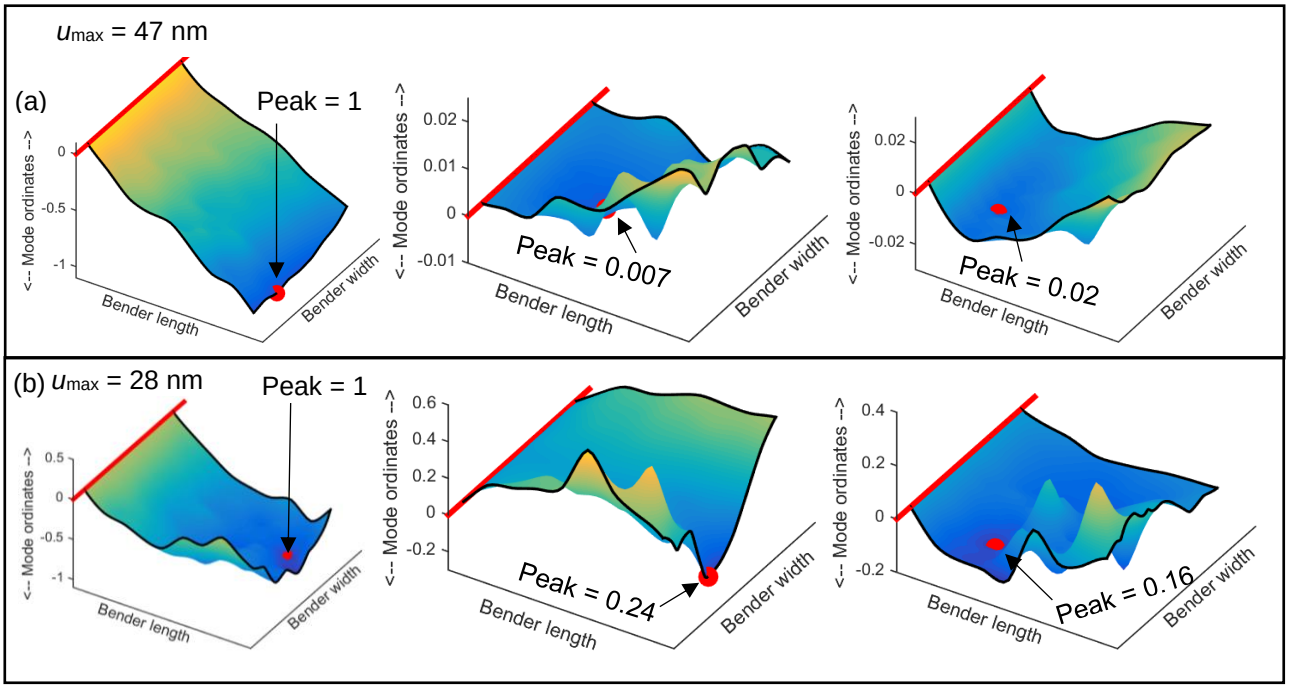

Fig. 5-23: Mode shapes in (a) soil without stress and (b) soil with stress

5.7.11 Comparison of experimental and numerical input signals

Fig. 5-24 shows a comparison between the input excitation signals of the experimental study and the numerical analysis. The first cycle of Eq. 5.6 is used as the input function for the numerical study and is compared with the sine pulse used as the input signal in the experimental study. These input signals are plotted using the following amplitudes and frequencies: $A = 3.6 \times 10^{-7}$ m, $f = 16.5$ kHz for Eq., and $A = 7.2 \times 10^{-9}$ m (selected to match the energy in Eq. 5.6) $f = 16.5$ kHz for sine pulse. The time signals are normalized to the maximum amplitude of 7.2×10^{-9} m of the sine pulse.

Fig. 5-24a shows that the maximum amplitude of Eq. 5.6 is about 2% less than that of the sine pulse while the minimum amplitude of Eq. 5.6 is about 83% less than the minimum amplitude of the sine function. The shapes of these time signals are very similar, which implies that the frequency contents of the signals are similar. Fig. 5-24b shows the frequency spectra of the two input signals along with the theoretical power spectrum of a single cycle sine pulse (Tallavo et al. 2009). The frequency spectrum of the experimental sine pulse and the theoretical power spectrum match very well even though the maximum magnitudes are very distinct. There is an order of magnitude difference in the maximum magnitudes of the theoretical power spectrum and the frequency spectrum of the sine pulse because one is a linear spectrum while the other one is a power spectrum.

The maximum magnitude of the frequency spectrum of Eq. 5.6 is about three times that of the experimental sine pulse. The maximum magnitude of the sine pulse occurs at the normalized frequency of 0.84, which is precisely the same normalized frequency of the theoretical power spectrum (Tallavo et al. 2009). But the maximum magnitude of Eq. 5.6 occurs at a normalized frequency of 0.7, which is 14 % less than that of the experimental sine pulse. Moreover, subsequent peaks in the frequency spectrum of Eq. 5.6 are not distinguishable unlike the frequency spectrum of the sine pulse. These differences occurred because of the non-symmetry of Eq. 5.6, i.e., the maximum amplitude is 70 % less than the absolute value of the minimum amplitude.

Although there are differences in the magnitudes of the frequency spectra of the input functions used for numerical and experimental studies, the numerical response of the transmitter with Eq. 5.6 as the input function matches very well with the experimental

transmitter response in air. Therefore, Eq. 5.6 with a central frequency of 16.5 kHz is found suitable for evaluating the numerical response of the transmitter in different media.

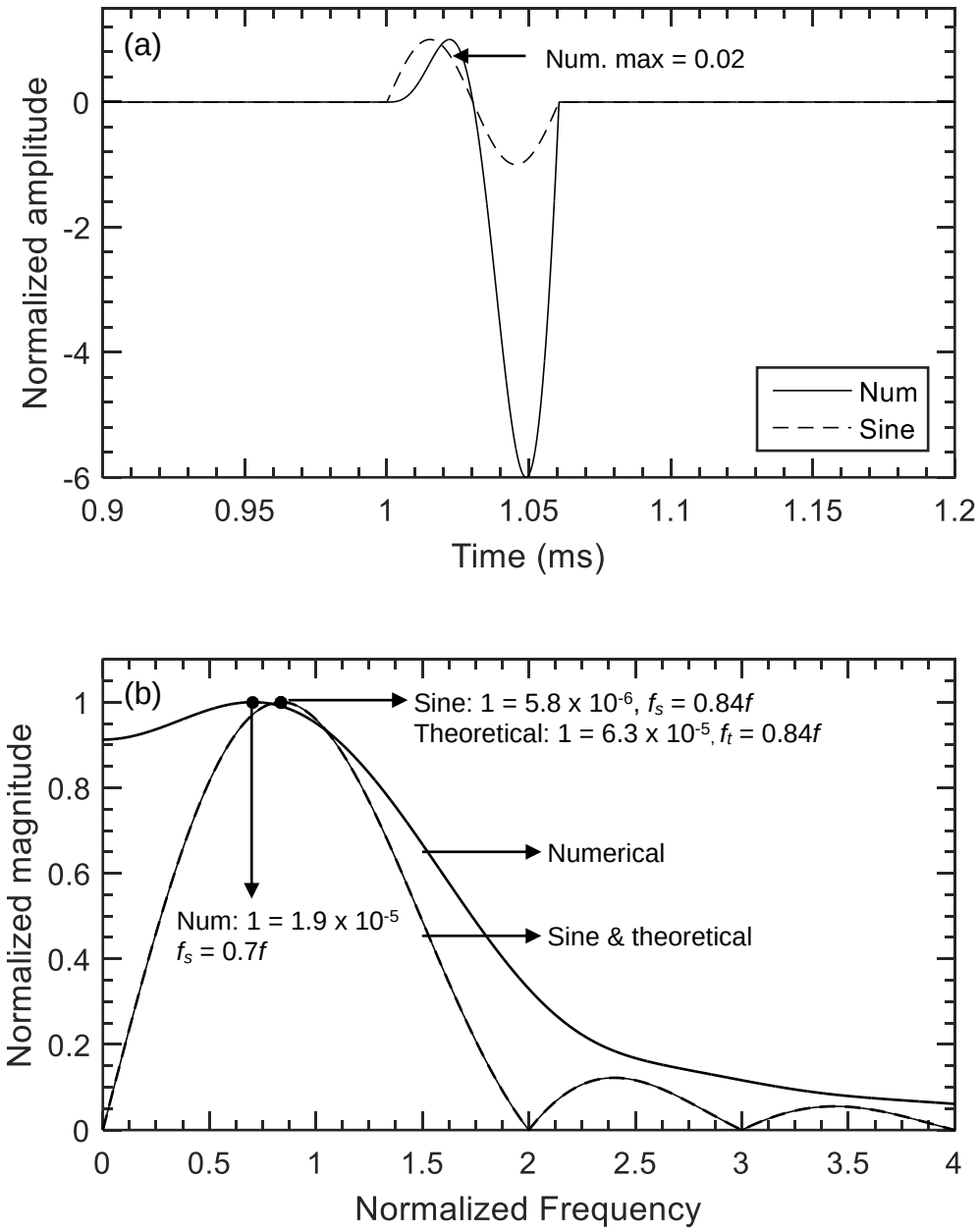

Fig. 5-24: Input function (Eq. 5.6) and sine pulse (a) time signals; (b) frequency spectra compared with the theoretical power spectrum of a sine pulse (after Tallavo et al. 2009).

5.7.12 Transmitter calibration

The transmitter is modelled as an elastic cantilever plate with an equivalent density as a typical bender element is a composite section consisting of piezo-ceramic sheets and epoxy-resin which is used as coating on the bender-element. Following the approach of Rio (2006), 70% of the BE volume is taken to be of epoxy and 30% of which to be composed of piezo-ceramic. For attaining the bender's resonant frequency (f_n) from laboratory data, the elastic modulus of the bender is computed using Eq. 5.10

$$f_n = \frac{k_{Ln}^2}{2\pi(\alpha L_b)^2}\sqrt{\frac{E_b I_b}{\rho_b A_b}} \qquad 5.10$$

where k_{Ln} is a characteristic number which depends on n (mode number) and the boundary conditions; L_b, I_b and ρ_b are the length, area moment of inertia ($I_b = bh^3/12$), and mass density of BE, respectively; b, h, and A_b ($A_b = bh$) are the width, thickness, and cross-sectional area of the BE, respectively; E_b is the Young's modulus of the piezoceramic element; α is the effective length factor with $\alpha = 1$ when the BE is perfectly fixed to the base and $\alpha > 1$ when there is flexibility in the connection between the BE and the base.

Next, the grid geometry and the damping ratio of the transmitter are adjusted to match the experimental transmitter response in air. The matched damping ratio of the transmitter in air is found to be 4.1%. The calibrated parameters and the geometry of the transmitter are presented in Table 5-1. Fig. 5-25 illustrates a snapshot of the BE response in air.

Table 5-1: Transmitter geometry and calibrated parameters

Geometry		Material Properties	
Bender height, h (m)	0.005	Elastic modulus, E_b (GPa)	51.6
Bender width, w (m)	0.013	Bulk modulus, K_b (GPa)	34.3
Bender thickness, t (m)	5.5×10^{-4}	Shear modulus, G_b (GPa)	20.6
Moment of inertia, I_b (m^4)	1.9×10^{-13}	Poisson ratio, v	0.25
Surface area, A_b (m^2)	7.7×10^{-6}	Epoxy density, ρ_{epoxy} ($kg.m^{-3}$)	1100
Bender volume, V_b (m^3)	3.9×10^{-8}	Piezo-ceramic density, ρ_{pi} ($kg.m^{-3}$)	7800
Epoxy volume, V_e (m^3) (= 70% of V_b)	2.7×10^{-8}	Equivalent density, ρ_{eq} ($kg.m^{-3}$)	3110
Piezo-ceramic volume V_p (m^3) (= 30% of V_b)	1.2×10^{-8}		

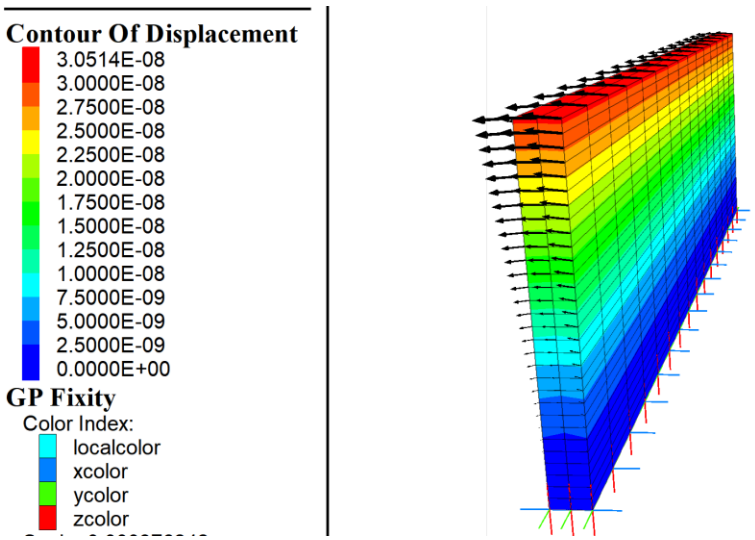

Fig. 5-25: Snapshot of the numerical transmitter response in air

5.7.13 Experimental versus numerical response in air

Fig. 5-26 shows the time signals and frequency spectra of the transmitter response in air, as obtained from the experimental study, along with the corresponding response obtained from the numerical simulation of the transmitter. The experimental and numerical response match very well, which implies that a robust calibration of the numerical model has been achieved. The difference in peak displacements of the time signals is about 6%, and the difference in the peak magnitudes of the frequency spectra is less than 0.01%. The reason for larger difference in the time signals is that the time signals usually have slight influence of higher modes while the frequency spectra are estimated after filtering the time signals to remove the higher frequencies. The resonance frequency of the first mode of the transmitter in both experimental and numerical responses are almost identical. These results indicate a thorough calibration exercise based on the actual transmitter response in air. Moreover, these results show that a single pulse of displacement excitation is generating the same response of the transmitter as that generated by the sine pulse input voltage in the experimental measurements. The displacement excitation is applied at the tip of the transmitter in the numerical simulation while, in the laboratory experiment, the input voltage is applied arbitrarily to the transmitter.

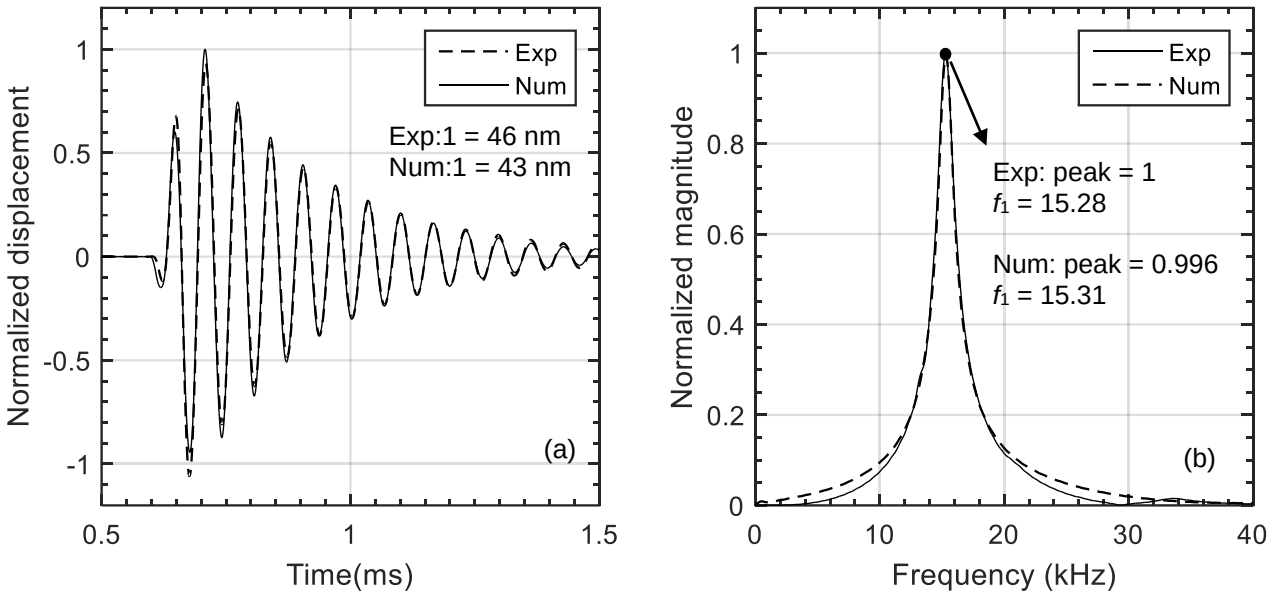

Fig. 5-26: Experimental and numerical transmitter responses in air (a) Time signals; (b) Frequency spectra

5.7.14 Experimental versus numerical responses in soil

A comparison of the input excitations used for the numerical transmitter response inside air and soil sample is presented in Fig. 5-27. The figure shows the time signals along with their frequency spectra. These input excitations are the first cycle of Eq. 5.6 with values of $A = 3.6 \times 10^{-7}$ m and $f = 16.5$ kHz used for air and $A = 2.6 \times 10^{-7}$ m and $f = 12$ kHz used for soil. The peak value of the input excitation time signal for soil response is 28% less than the that in air. The minimum value of the excitation used in air response is about 150% larger than that in soil. These differences suggest a displacement excitation with lesser energy than that in air is applied at the peak of the numerical model of the transmitter inside the soil. This difference in the peak amplitudes of the time signals is not observed in the peak magnitudes of the frequency spectra of the two excitations. The reason for this inconsistency is that the peak magnitudes of the frequency spectra do not correspond to the input central frequency (f_c) of the input excitations. In fact, the frequency spectra peak at frequencies = $0.7f_c$ (air = 16.5 kHz, soil = 12 kHz) as is observed in the input function analysis in section 5.7.11.

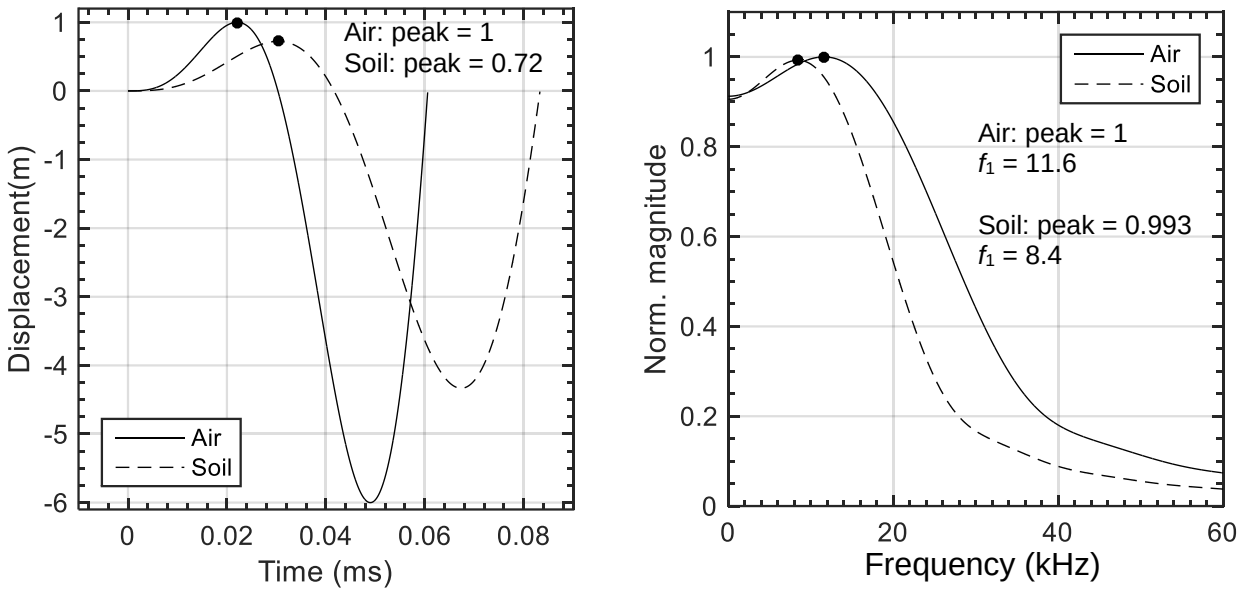

Fig. 5-27: Input excitations used for numerical transmitter responses in air and in soil

The calibrated parameters shown in are kept constant during the numerical simulation of the transmitter excitation in soil. The elastic properties of the soil sample are modified in FLAC until a reasonable match of the numerical and experimental responses is achieved. The soil is modelled as a cubic sample with the dimensions based on the internal dimensions of the square tube used to contain the transparent soil. The finalized soil properties and the soil dimensions are presented in Table 5-2.

Fig. 5-28 shows a comparison between the transmitter responses, as obtained from the experiment and the numerical analysis, inside the transparent soil without induced vertical stress. The soil sample density used for matching the experimental response with the numerical response is ρ_s = 1200 kg/m^3; this density is only 2.5% less than the density of the transparent soil (1230 kg/m^3) comprising of fused quartz and the mineral oil mixture (Ezzein and Bathurst 2011). The comparison of the experimental and numerical transmitter responses inside the soil shows a very good match. The time signals in Fig. 5-28 match very well after the first cycle (≈ 0.2 ms). The lack of agreement observed in the first cycles of the two time signals is because of the nonlinear behavior of the transmitter inside the unconfined soil; moreover, participation of higher modes of transmitter vibration is more inside the soil. The numerical model is developed based only

on the first mode of the transmitter vibration. The frequency spectra of the signals show that the energy in the first mode of the numerical response is only 8 % less than that in the experimental response; similarly, the resonance frequency of the numerical response is only 1 % more than that of the experimental response.

These results show that the numerical model developed in FLAC3D calibrated based on the experimental measurements in air is able to predict well the transmitter response in air with only 2.5 % difference in the density of the surrounding soil.

Table 5-2: Dimensions and elastic properties of soil sample used for matching the numerical transmitter response inside the soil

Geometry		Material Properties	
Soil sample height, h (m)	0.05	Bulk modulus, K_S (MPa)	0.38
Soil sample width, w (m)	0.032	Shear modulus, G_S (GPa)	0.23
Soil sample length, L (m)	0.032	Poisson ratio, v	0.25
		Sample density, ρ_S (kg.m^{-3})	1200

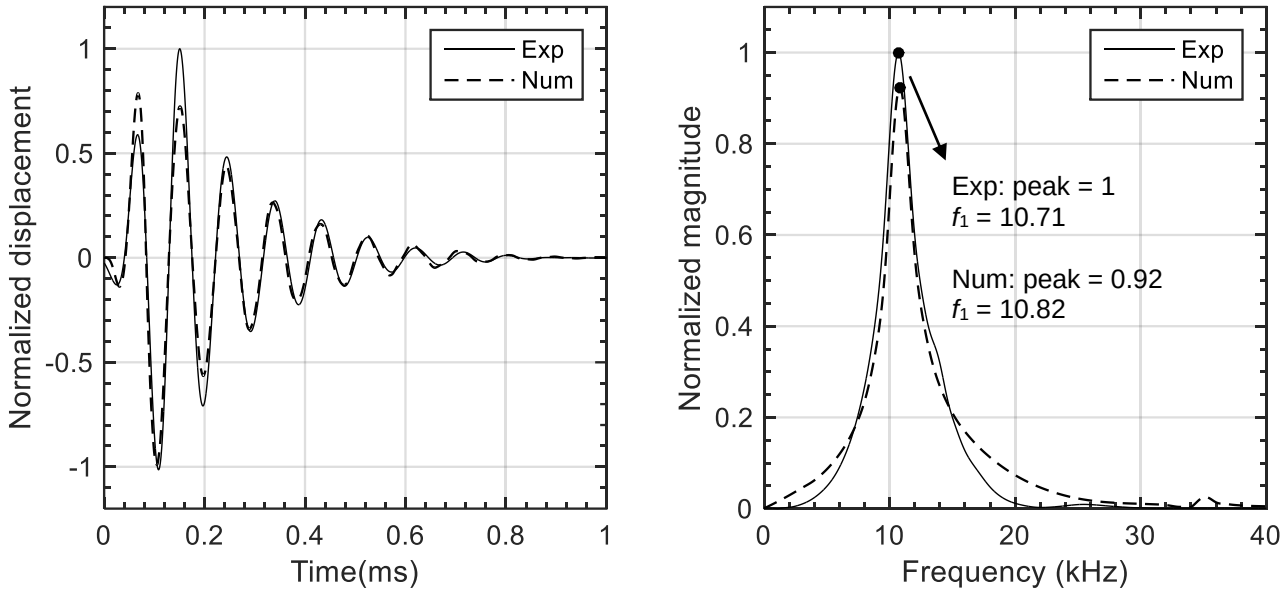

Fig. 5-28: Experimental and numerical transmitter responses inside the soil

5.7.15 Parametric study of numerical transmitter behavior

The soil sample parameters (*v*, *G*, *K*) in the numerical model have been customized () to match the resonance frequency and damping ratio of the experimental transmitter response in the transparent soil. A parametric study investigating the effects of changes in these soil parameters is performed. Effects of bulk modulus (*K*), shear modulus (*G*), and Poisson's ratio (*v*) on the resonance frequency and damping ratio of the transmitter are evaluated. The resonance frequency and damping ratio are estimated using the half-power bandwidth method performed on the frequency spectra of the numerical transmitter response.

Fig. 5-29 shows the variation of the resonance frequency against the bulk modulus with the initial bulk modulus labelled. The resonance frequency increases linearly with the bulk modulus of the soil sample; this increase is as expected because the bulk modulus is proportional to the vertical stress in the soil. However, the relationship between the numerical transmitter resonance frequency and the bulk modulus is linear unlike the power-law relationship between the resonance frequency and the vertical stress (Fig. 5-21). The slope of this increase in resonance frequency with bulk modulus is 0.13 kHz/MPa.

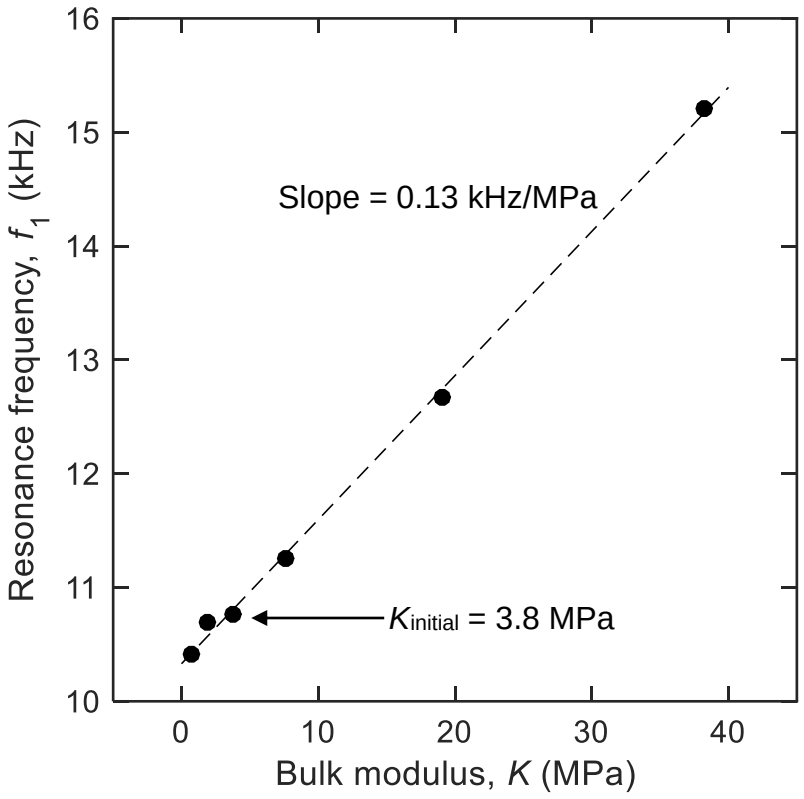

Fig. 5-29: Resonance frequency of the transmitter against the bulk modulus of the soil sample

Fig. 5-30 shows the variation of the damping ratio of the transmitter against bulk modulus. Except for the damping ratios at 0.7 MPa and 3.8 MPa ($K_{initial}$), the damping ratio increases linearly with the bulk modulus at a rate of 0.19 % / MPa. The damping ratio of the transmitter ranges between 10 to 20 % in the bulk modulus range between 2 to 40 MPa; this damping ratio is much higher than the damping ratio of the typical soil samples. Therefore, with these damping ratios of the transmitter, estimation of the damping ratio of the soil sample using BE test will be difficult; this result explains the unsuccessful attempts of estimating the damping ratio of a soil specimen using BE test (Cheng and Leong 2018).

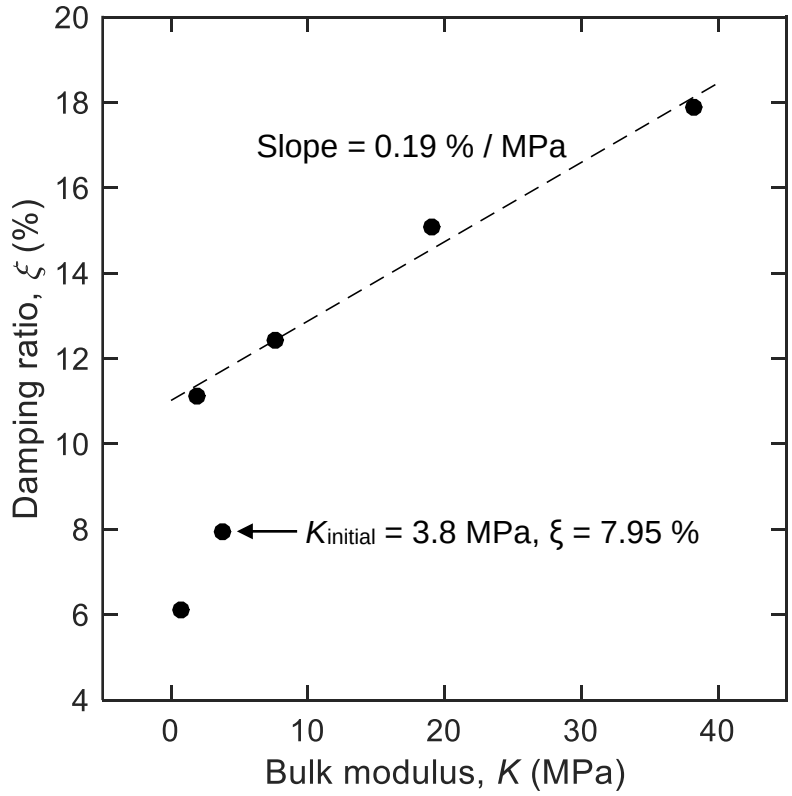

Fig. 5-30: Damping ratio of the transmitter against the bulk modulus of the soil sample

Fig. 5-31 shows the variation of the resonance frequency of the transmitter with the mass density of the soil sample. The effect of the mass density is similar to the bulk modulus i.e. the resonance frequency changes linearly; however, the resonance frequency decreases, rather than increases, with increase in the mass density of the soil samples. A very good linear relationship is observed between resonance frequency and mass density of the soil sample similar to the relationship between the resonance frequency and the mass density of the liquids (Fig. 5-13). The slope of the decrease in resonance frequency with the sample mass density is 1.8 kHz.mL / g.

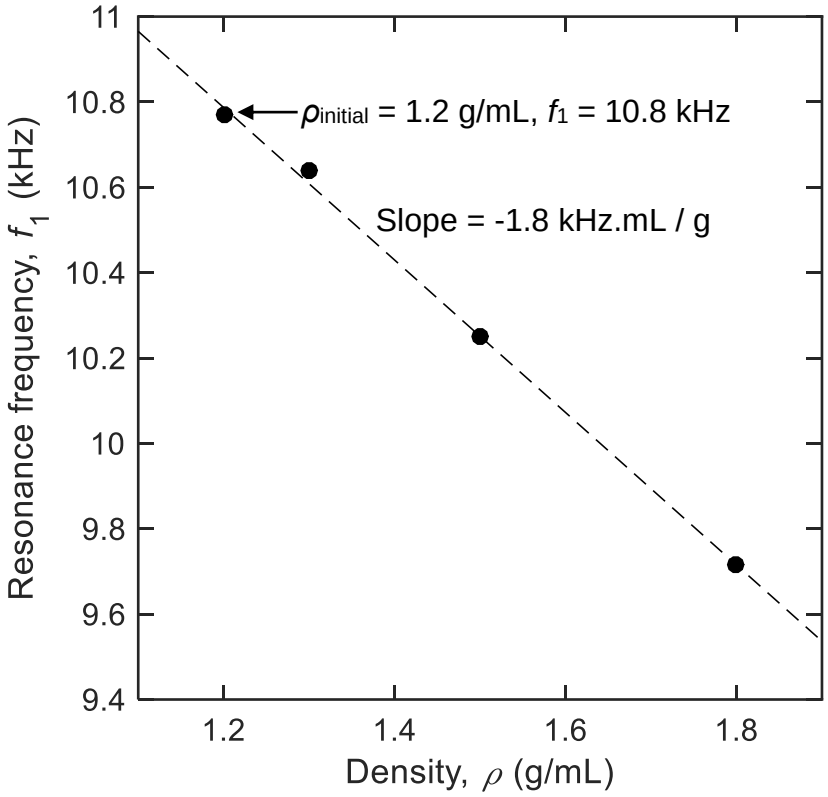

Fig. 5-31: Resonance frequency of the transmitter against the mass density of the sample

Fig. 5-32 shows the variation of the damping ratio of the transmitter against the mass density of the soil sample. The effect of the mass density on the damping ratio is similar to the effect of the bulk modulus i.e. except for the damping ratio at the initial mass density, the damping ratio increases linearly with the increase in mass density with a slope of 2.7 %mL/g. However, this linear relationship is different from the exponential relationship observed for the damping ratio of the experimental transmitter response against the mass density of the liquids.

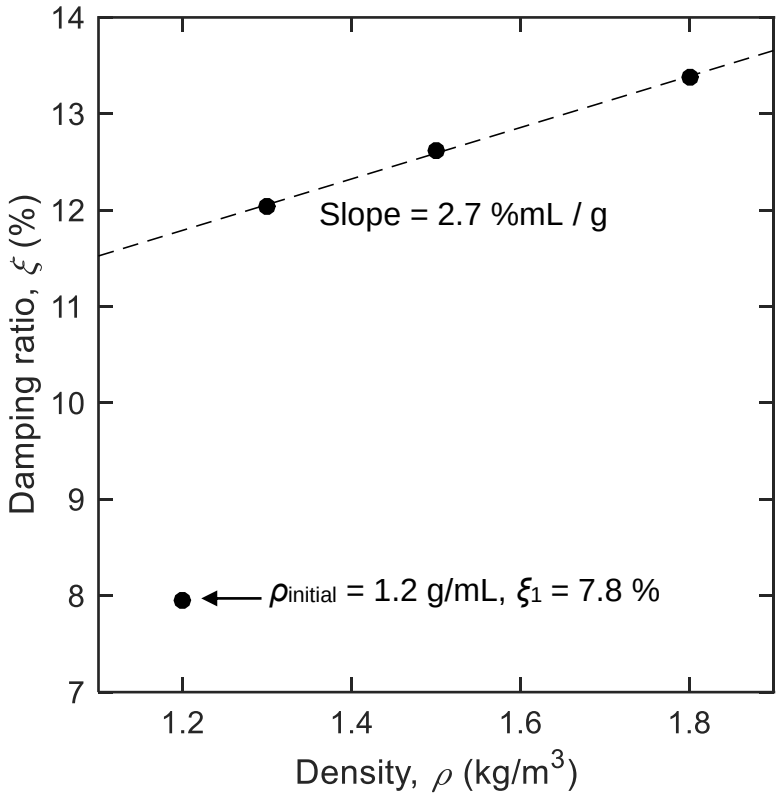

Fig. 5-32: Damping ratio of the transmitter with the mass density of the soil sample

The effects of the Poisson's ratio (with constant bulk modulus and changing shear modulus) on the resonance frequency and damping ratio of the transmitter are depicted in Fig. 5-33a and b. Similar to the above results, the resonance frequency decreases linearly with the Poisson's ratio at a rate of 0.13 kHz/unit; the initial resonance frequency measurement is an outlier of this linear trend. No trend is observed in the damping ratio against the Poisson's ratio of the soil sample.

When the bulk modulus and the shear modulus is kept constant, the resonance frequency increases linearly, rather than decrease, with increase in Poisson's ratio at a rate of 0.96 kHz/unit. Again, the damping ratio of the transmitter does not follow a specific trend with the Poisson's ratio.

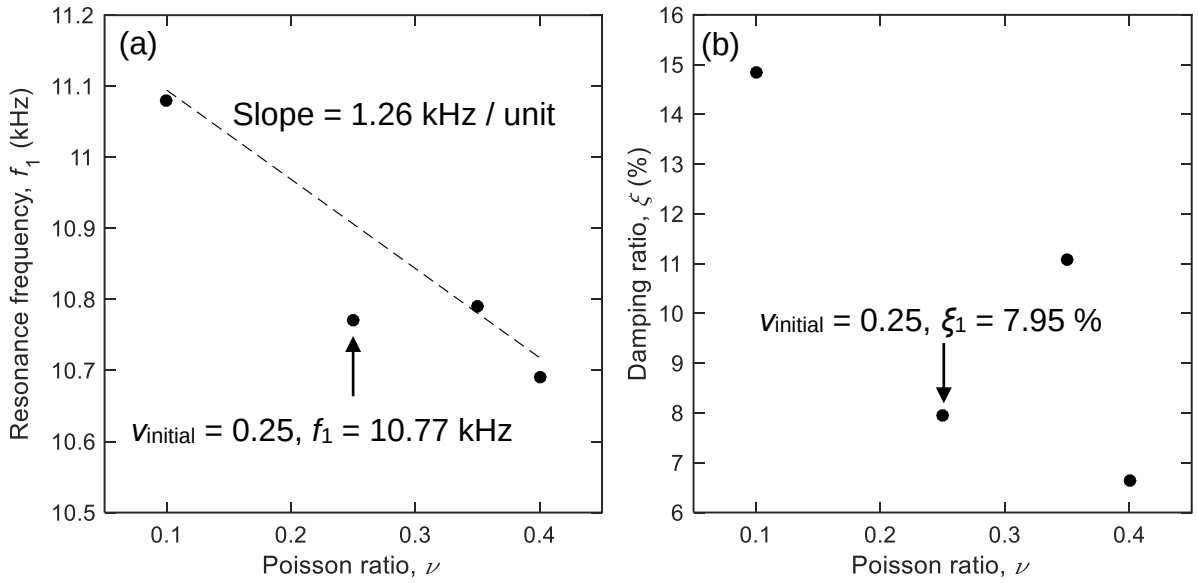

Fig. 5-33: (a) Resonance frequency and (b) damping ratio of the transmitter against the Poisson's ratio with a constant bulk modulus

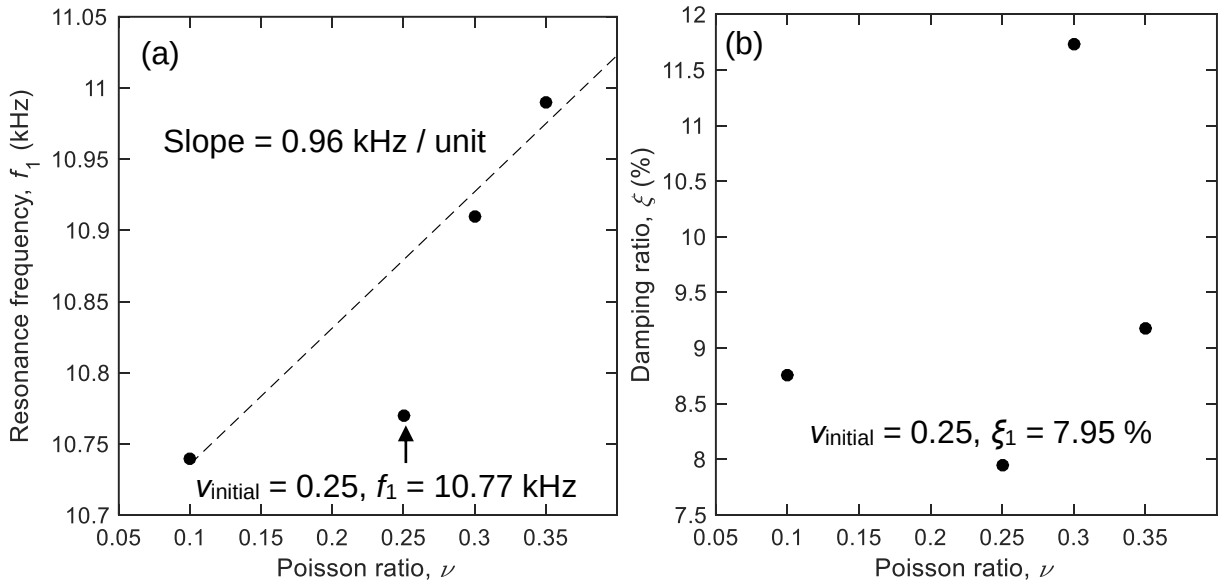

Fig. 5-34: (a) Resonance frequency and (b) damping ratio of the transmitter against the Poisson's ratio with a constant shear modulus

The above results suggest that the damping ratio of the transmitter, like the damping ratio of the soil sample, is not directly related to the elastic parameters of the soil sample. The resonance frequency of the transmitter follows regular trends with the different elastic parameters. This result suggests that the damping ratio estimation using the BE test is a complex problem which will be difficult to solve.

5.8 Conclusions

This chapter is part of a novel experimental program in which the actual vibrations of the BE inside the soil are measured using a state-of-the-art laser vibrometer and a recently developed transparent soil. In this study, results of an experimental modal analysis of the transmitter are analyzed. Resonance frequencies, damping ratios, and mode shapes of the transmitter are determined by calculating the frequency spectra of the transmitter response time signals and processing the laser-vibrometer measured time signals with a curve-fitting algorithm called the Second-order Blind Identification (SOBI) method. These properties of the transmitter are determined in air, in liquids of different mass densities, in transparent soil and in transparent soil with induced stress. The effects of input voltage on peak displacement of the transmitter are evaluated in air and in mineral oil mixture. The effects of mass density of liquids on the natural frequency and damping ratio of the transmitter are evaluated. The effects of induced vertical stress on the natural frequency and damping ratio of the transmitter are evaluated. Finally, the mode shapes of the transmitter in air, liquids and in soil are presented.

The numerical section of this study presents the results of a numerical study in which a FLAC3D model of the transmitter is developed based on measurements of actual vibrations of a transmitter (Atefi-Monfared, K. 2019). First, the transmitter model is robustly calibrated using the experimentally measured transmitter response in air. A displacement function applied at the tip of the transmitter is found to be suitable for inducing a transmitter response that matches very well with the experimental response of the transmitter. First cycle of the displacement function is applied as a velocity function in FLAC3D. The difference in the peak displacement of the experimental and numerical time signals is less than 5%.

The transparent soil sample dimensions used in the experimental section are used in the numerical model and the soil sample properties are modified until the numerical transmitter response inside the soil matches the experimental response. The modified soil density of the numerical model matches very well with the mass density of fused quartz surrounding the transmitter; however, the estimates of bulk and shear moduli of the numerical sample are very low compared to those of the fused quartz. The mismatch in the moduli is due to the non-homogeneity of the fused quartz soil sample which is not incorporated in the numerical model. Moreover, the non-linearity of the transmitter response inside the soil is also not yet incorporated. These changes will be executed in future when this numerical study will be completed.

The input excitation in a conventional BE testing is an electrical voltage the nature of application of which is unknown. However, it is known that the voltage is applied/distributed over the surface of the transmitter. In this numerical study, a displacement input function applied at the tip of the transmitter model is sufficient to replicate the experimental transmitter response

The results from this study show that a 50% increase in liquid density causes only a 5% decrease in the first resonance frequency but a 56% increase in the damping ratio. Similarly, a 35% increase in first resonance frequency is observed when the applied vertical stress in soil specimen is increased from 0 to 400 kPa; the corresponding increase in damping ratio is 30%. These results are key to understanding the BE-soil sample interaction because the frequency of vibration of the transmitter dictates the wave-length of the shear wave excited from the transmitter and affects the estimation of V_s. The wave-length of the shear waves must be, at maximum, equal to the length of the soil specimen; the recommended wave-length, to avoid near-field effects in the BE test, is less than one-fifth the length of the soil specimen. The damping ratio results of this study have highlighted the possible reasons for unsuccessful attempts on the estimation of damping ratio of soil specimens using the BE test.

Operational modal analysis (OMA) is performed on the transmitter response to estimate the modal parameters of the transmitter. The measured time signals of the actual transmitter vibrations are used with a mathematical solution for OMA called the second-

order-blind-identification (SOBI) method. Further, the effects of input voltage, mass density, Reynolds number, and applied vertical stress on the transmitter behavior are evaluated.

The study shows that the transmitter displacements in air and in oil are linearly related to the input voltage with a slope of 9.4 nm/V in air and 3.9 nm/V in oil. The experimental measurements of this study are in excellent agreement with a proposed theoretical equation available in the literature. First mode resonance frequencies of the transmitter in liquids match very well with a theoretical equation (available in the literature) with a maximum difference of 3.5%. Damping ratio of the first two modes increase exponentially when the mass density of liquids increases; this result is also in agreement with the findings in the literature. The first three mode shapes of the transmitter in air and in liquids are those of a typical cantilever plate; the presence of a liquid does not affect the mode shapes of the transmitter, which is in agreement with the related results available in the literature. The first resonance frequency and damping ratio have a power-law relationship with the Reynolds number of the fluid with exponents of 0.024 and 0.12, respectively. The β-exponent of the power-law relating the first mode resonance frequency and the applied vertical stress is 0.1 which is lower than the typical β values of sands. Lastly, the first three mode shapes of the transmitter in soils under vertical stress show that the participation of higher modes and mode coupling increase as the applied vertical stress is increased. The peak values of the second and third mode shapes are 0.7% and 2% of the first mode peak coordinate for the case of soil specimen without applied stress; these values increase to 24% and 16% under applied vertical stress of 41 kPa.

The parametric investigation using the numerical model of the BE-transmitter showed that there are significant effects of the elastic parameters on the resonance frequency of the transmitter. The resonance frequency varies linearly with all the elastic parameters. The resonance frequency increases with bulk modulus at a rate of 0.13 kHz/MPa and decreases with density at a rate of 1.8 kHz.mL/g. The resonance frequency increases at a rate of 1.3 kHz/unit with the Poisson’s ratio when the bulk modulus is kept constant while it decreases at a rate of 0.96 kHz/unit when the shear modulus is kept constant.

However, the damping ratio of the transmitter does not follow regular trends. This result suggests that estimating the damping ratio using the BE test is a complex problem which is the reason for the unsuccessful attempts to estimate the damping ratio using BE tests.

6 Novel evaluation of the transmitter-receiver bender-element system behavior

6.1 Introduction

Bender elements (BE) test is widely used in research and industrial laboratories for measuring the shear wave velocity of materials (V_S) such as soils, cemented soils and asphalt. BE test is simple to perform and is cheaper than other tests such as the resonant column and ultrasonic tests. Although BE test is simple, the interpretation of its results is not. The results interpretation is difficult because interaction between BE and soil when the BE are inserted inside the soil is not known. Many studies have attempted to present recommendations for correct interpretation of BE test results; however, there is no agreement on a single interpretation procedure.

This chapter presents the results of a novel experimental program in which BE and soil interaction is characterized using actual measurements of vibrations of the bender element transmitter and receiver inside the soil specimen. Laser vibrometer is used to measure the actual vibrations of the transmitter and receiver in air, liquids of different mass densities, and in a transparent soil specimen under different confinements. Different input excitations are used to understand the effects of input frequency content on the transmitter and receiver behavior in different media. Vibrations of the receiver measured using the laser vibrometer are compared to the output voltage of the receiver.

6.2 Experimental setup

Fig. 6-1 shows the schematic setup used in this chapter to measure the actual vibrations of the transmitter and receiver in different media. The setup is similar to what has been used in previous chapters except that now the receiver is added to the experimental setup. The transmitter and receiver used in this study are of a rectangular shape with surface dimensions of 14 mm x 5 mm x 0.5 mm (cross-section shown in Fig. 6-1).

A plexi-glass square tube with dimensions 38 mm x 38 mm x 75 mm inches (height) is used for measurements in liquids and soil; this tube is placed around the transmitter on the steel platen. The base of this tube is sealed with silicon sealant to prevent leakage. Upon filling the tube with liquid, the receiver casing is placed upside down on the top of

the square tube with the receiver submerged in the liquid to measure receiver vibrations in the liquid using the laser. A similar setup is used for receiver vibrations measurements in the transparent soil; however, the receiver casing is now placed directly on the transparent soil rather than on top of the square tube. To generate vertical stress in the soil, a hollow steel rod with a rectangular base of dimensions of 31.25 mm x 31.25 mm (internal dimensions of the square tube) is placed on the receiver casing; then, dead weights are stacked on the steel rod.

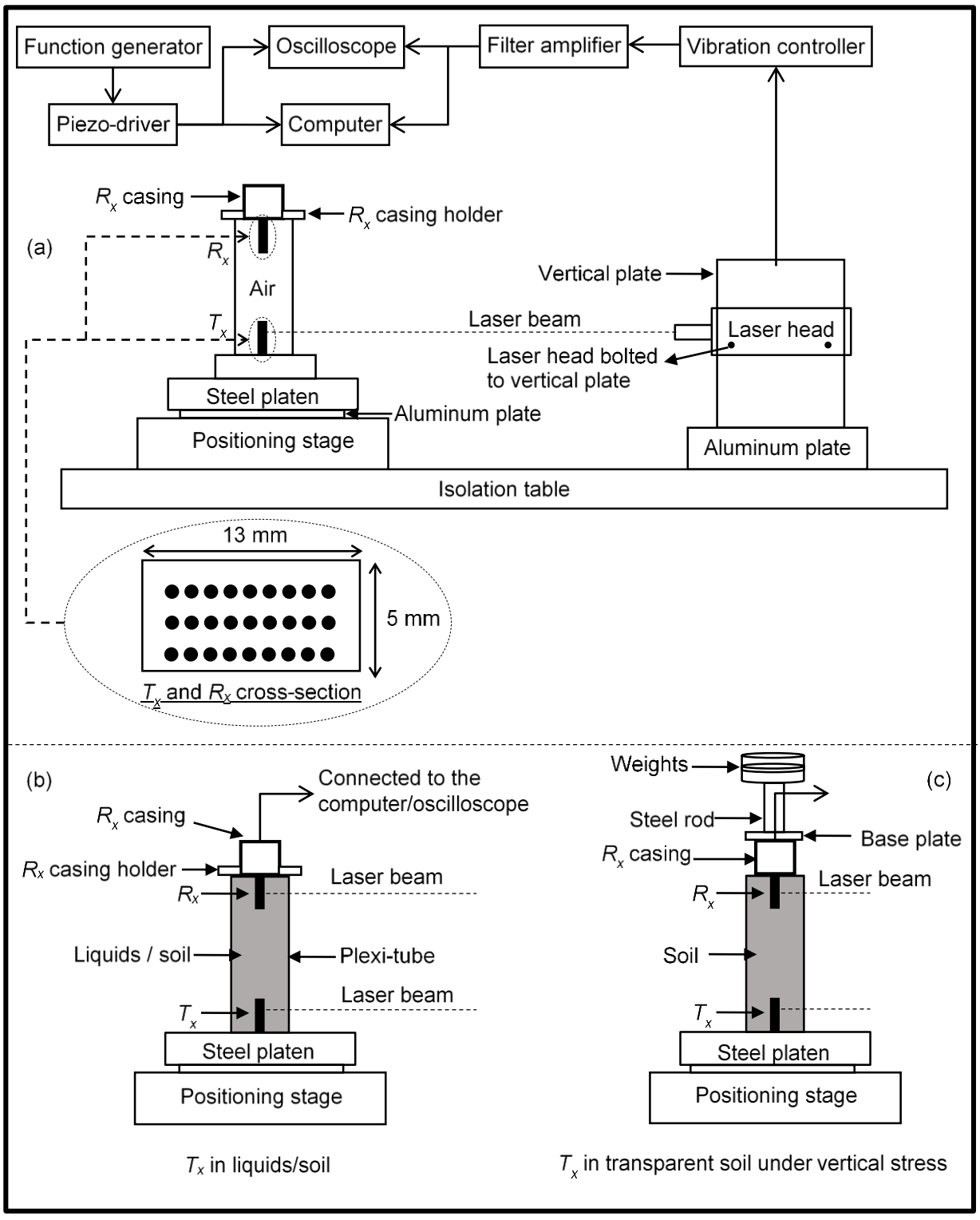

Fig. 6-1: Schematic of the setup used for (a) measurements in air, (b) measurements in liquids/soil, and (c) measurements in soil under stress

6.3 Experimental methodology

Unless noted otherwise, the vibrations of the transmitter and the receiver are measured at the center of the peak (free end) (shown on the transmitter cross-section in Fig. 6-1). A total of 500 iterations are run for each measurement, and an average of these 500 iterations is calculated to ensure minimization of noise presence in the signals.

6.3.1 Experiments in air

The transmitter and receiver vibrations are measured for different input excitations and at different locations on the surface. First, the transmitter response to a sine pulse of an arbitrary central frequency is measured. The frequency spectrum of this transmitter response is calculated to determine the resonance frequency of the first mode of the transmitter. This resonance frequency is used as the central frequency of a sine pulse which is used as the input pulse applied to the transmitter. The transmitter responses to this sine pulse are measured at multiple points; locations of these points are shown in Fig. 6-1. The receiver vibrations are measured with the laser beam pointed at the receiver. The transmitter is excited with the same input excitation as that used for measuring transmitter responses. Locations of receiver responses are also the same as those of the transmitter.

The transmitter and receiver responses are analyzed to determine time delays between the transmitter and receiver responses and to evaluate the effects of different input frequency content on the transmitter and receiver behavior. The output electrical voltage at the receiver end is also compared to the laser response of the receiver in air to estimate the transfer function of the electrical components between the receiver and the oscilloscope.

6.3.2 Measurements in liquids

The liquids of different mass densities (water, sucrose-30 %, and sucrose-60 %) are poured in the square tube to measure the transmitter and receiver responses in these liquids. After measurements in air, the square tube is placed on the steel platen and silicon sealant is applied at the base of the square tube; the sealant is left for three hours to cure. Then, the transmitter response in air with the square tube is measured and compared to

the response without the square tube to ensure that no errors are made during square tube placement. The diameter of the receiver casing is 25 mm i.e. slightly smaller than the width of the square tube; the casing holder of 38 inches width is used to ensure that the receiver casing does not fall into the tube. The liquid is gently poured until the tube is filled; then the receiver casing holder is bolted on top of the square tube with the receiver submerged in the liquid. Then, the transmitter and receiver responses to different input excitations to the transmitter are measured by moving the laser head vertically. The output electrical voltage from the receiver end is also measured using the oscilloscope and stored in the computer. Between the measurements in different liquids, the square tube is thoroughly washed to minimize the measurements errors due to mixture of liquids.

6.3.3 Measurements in soil

Upon completion of testing with the mineral oil mixture, a little portion of the mixture is removed from the tube because the liquid would overflow out of the square tube when the fused quartz are dropped in the tube. The fused quartz are gently air-pluviated into the square tube until the tube is filled with a transparent soil specimen; a short space is left at the top of the tube to avoid any leakage. The receiver casing holder is removed and only the receiver casing is placed upside down on the transparent soil specimen such that the receiver is submerged in the transparent soil specimen and the casing is resting freely on the soil. The transmitter and receiver responses with different input excitations are measured with the laser vibrometer, and the output electrical voltage on the receiver end is also saved.

The vertical stress in the soil is induced by placing dead weights on top of the receiver casing with the help of a hollow cylinder placed on top of the receiver casing. Vertical stresses are estimated using the Boussinesq's theory for vertical stress under a rectangularly loaded area. The effects of vertical stress on the transmitter and receiver responses are evaluated using the time signals and frequency spectra measured using the laser vibrometer.

6.4 Results and Analysis

6.4.1 Evaluating compressional wave interference

One of major problems associated with the bender elements test is the interference of compressional (*p*) wave with the shear (*s*) wave, especially with the soils with low effective stress (Lee and Santamarina 2005). The *p*-wave interference at the receiver end is coming either directly from the transmitter or the reflections from the wall. In partially saturated/saturated soils, the *p*-waves arrive much earlier than the *s*-wave which sometimes is helpful in distinguishing between *p* and *s* waves. However, there is no definitive guidance about how much percentage of saturation is sufficient for clear distinction between *p* and *s* waves; this makes this problem unresolved.

With the novel experimental setup of this study, the presence and interference of *p*-waves in the receiver response is evaluated. First, the measurements in air are studied.

Fig. 6-2 shows the transmitter and receiver responses in air to a sine pulse of 12 kHz input excitation. The novel experimental setup of this study allowed for the simultaneous measurement of the actual transmitter and receiver responses in air. These results are for vibrations measured at the tip of both the transmitter and receiver. The first mode resonance frequency of the transmitter used in this study is ≈ 12.5 kHz.

The peak displacement of the transmitter response is 56 nanometers and the peak displacement of the receiver response is ≈ 1.7 nm. This difference is expected because of significant attenuation of the waves as the wave travelled in air from the transmitter to the receiver.

Fig. 6-2 shows that there is a clear time delay between the transmitter and receiver responses. This time delay is estimated to be ≈ 0.21 ms; the tip to tip distance between the transmitter and receiver is ≈ 7 cm. Using this length and time, the wave velocity based on the first arrival is ≈ 333 m/s; this velocity is very close to the velocity of sound in air. These calculations confirm the presence of compressional wave interference in the bender elements even in air.

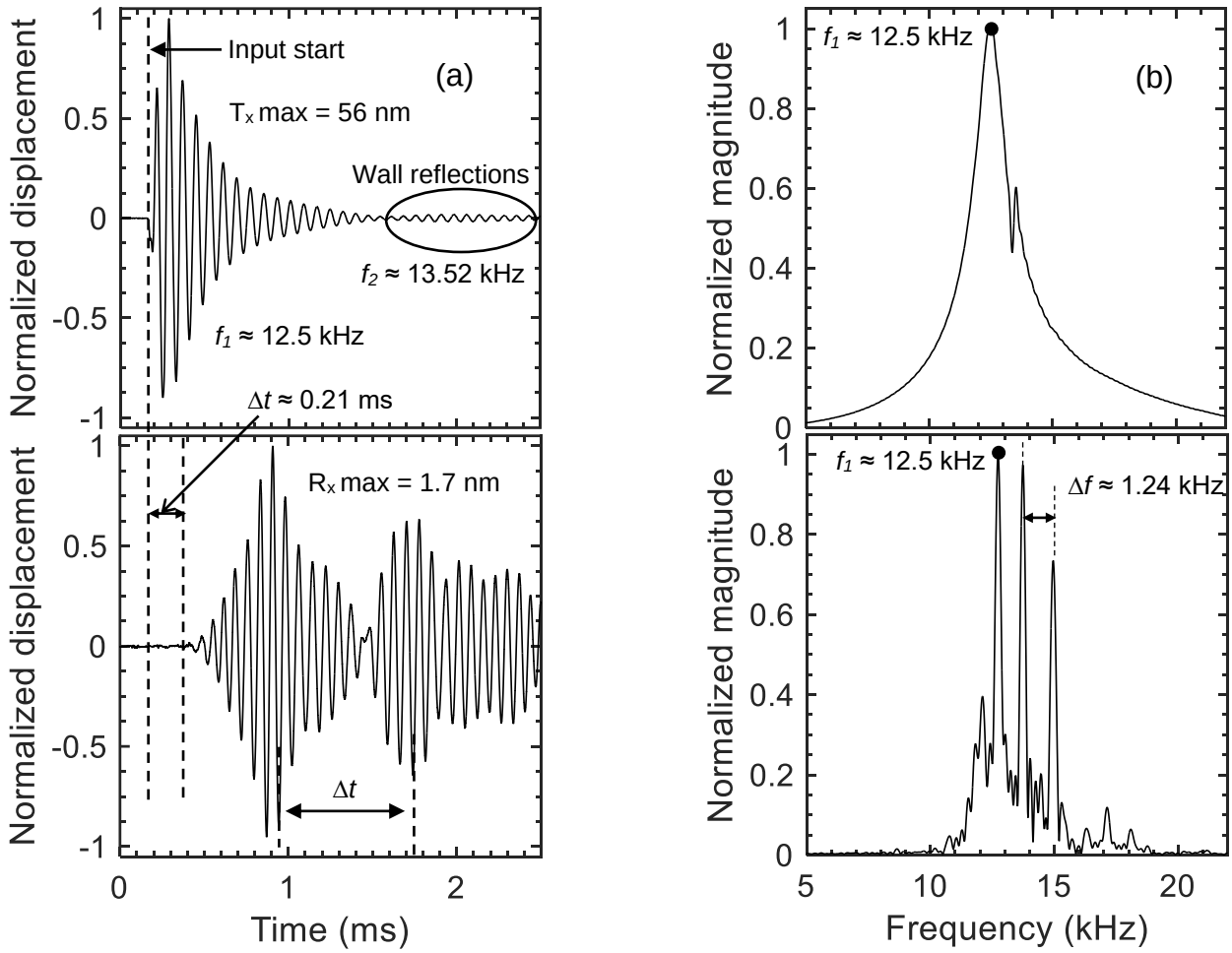

Fig. 6-2: Transmitter and Receiver responses in air to a sine pulse of 12.5 kHz (Δt = 0.87 ms) and the frequency spectra of the responses

Fig. 6-2a shows that the receiver is still vibrating with relatively larger amplitudes (at around 2 ms) even though the transmitter response has decayed to relatively low amplitudes; these vibrations are found to be the reflections of the *p*-waves from the plexi-glass. These reflections are also observed in the transmitter response (between 1.5 to 2.5 ms); however, the amplitude of these vibrations is very small compared to the actual transmitter response which leads to an apparent conclusion that the transmitter vibrations have completely diminished after about 1.5 ms. These reflections are further investigated using the frequency spectra of the transmitter and receiver responses which are shown in Fig. 6-2b

.

The first peak observed in the frequency spectra of both transmitter and receiver responses is at a frequency of ≈ 12.5 kHz (resonance frequency of the transmitter). The other two major peaks in the frequency spectrum of the receiver response are the reflections of this resonance frequency. One of these reflections is also observed in the transmitter response as seen in the small peak in the frequency spectrum).

The time intervals between peaks of the reflections seen in Fig. 6-2a is $\Delta t \approx 0.87$ ms; the corresponding frequency is $\Delta f \approx 1 / 0.87 = 1.24$ kHz. This frequency is very similar to the frequency interval observed frequency spectrum (labelled on Fig. 6-2b).

Further study is done to evaluate the presence of these reflections by measuring the displacements on the wall of the acrylic tube which is filled with water. Then, the response is compared to the receiver response (BE-R_x) in water at the peak of the receiver. These responses are obtained for a sine pulse of 12.5 kHz with an input voltage of 25 VPP. Fig. 6-3 shows the two-time signals with the response wall offset for clarity. The wall displacements are actually in the range of the response of the receiver tip; in fact, the peak displacement of the wall response is ≈ 3 nm compared to ≈ 2.3 nm of the receiver. Nevertheless, the wall is vibrating in air while the receiver is inside the water. Besides the amplitude, the frequency content of the two signals is also similar which shows that the square tube wall is also contributing in the interference in the receiver response caused by the reflections

These calculations show that there are reflections are also affecting the receiver response besides the actual compressional waves. The interference of these compressional waves and its reflections must be addressed in the conventional BE testing for a reliable BE test interpretation.

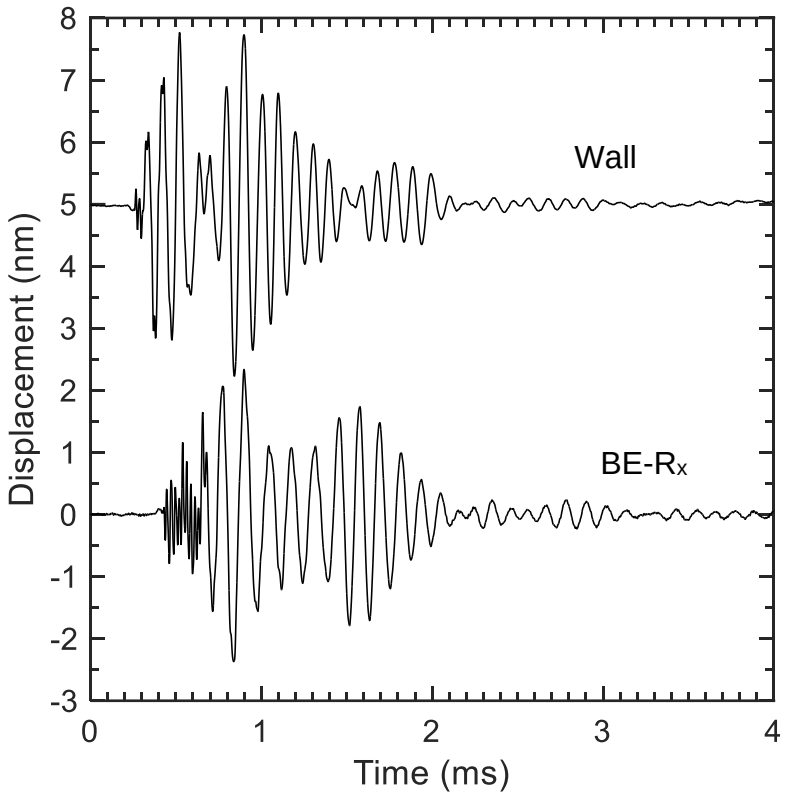

Fig. 6-3: Comparison of BE-receiver response in water at the tip with the vibrations of the acrylic tube wall

6.4.2 Comparison of laser response and output voltage

In conventional BE testing, the output electrical voltage is measured and stored at the receiver end; however, it is not possible to measure the actual receiver response because the receiver is inside the soil. Fig. 6-4a shows a comparison of the receiver response measured using the laser and the receiver output voltage in air; a shorter length of the time signal is shown for clarity. The results clearly show that the laser response is almost identical to the output voltage. Three outcomes can be observed from this figure:

(i) The peak amplitude of the laser response is one order of magnitude higher than that of the output voltage; this result is expected because the laser measures the actual receiver response and the output voltage is a result of the vibration of the receiver system.

(ii) There is a time delay of ≈ 0.008 ms between the laser response and the output voltage; the laser response is delayed because there are more electrical peripherals between the receiver and the oscilloscope on which response is measured and stored. The receiver output voltage is measured directly from the receiver system.

(iii) The fact that the laser response is very similar to the output electrical voltage is a proof of the validity of the laser measurements. The output electrical voltage is measured independently from the laser system. Therefore, this result helps in calibration of the laser vibrometer.

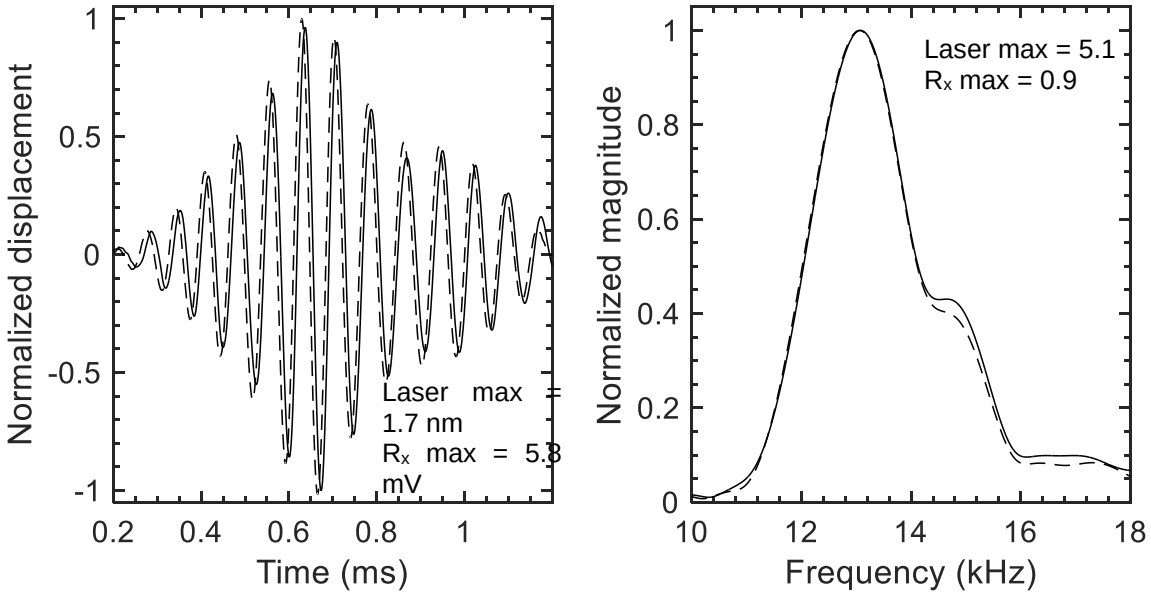

Fig. 6-4: (a) Receiver response from laser (solid line) and the output electrical voltage (dashed) and (b) Frequency spectra of the receiver response from the laser and the BE-receiver output voltage

The results from the time signals in Fig. 6-4a are further verified using the frequency spectra of the two signals shown in Fig. 6-4b; the time signals are normalized to each of its maximum before computing the frequency spectra; the energy in the frequency range of interest i.e. 10 to 20 kHz is very similar. Transfer function between the laser response and output voltage is computed and the transfer function dB magnitude is presented in

Fig. 6-5. The transfer function magnitude in frequency range of interest i.e. 10 to 18 kHz is well within the acceptable range of ±3 dB.

Another conclusion from the comparison in Fig. 6-4 is that the theoretical relationship between the bender displacement and the voltage applied/generated proposed by Leong et al. (2005) (Eq. 5.7), is not only valid for the peak-to-peak displacements, in fact the relationship can be used to correlate the whole of receiver output voltage to the receiver displacement. As observed in Fig. 6-4, the laser response of the receiver is related to the output voltage through a scaler value of ≈ 5.

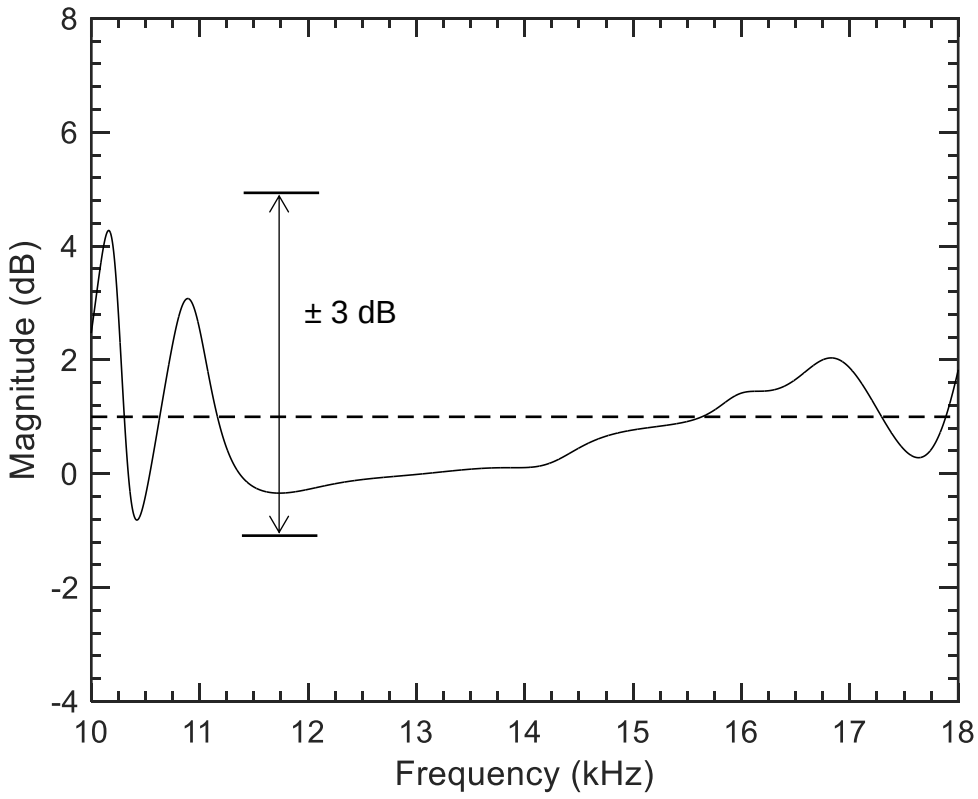

Fig. 6-5: Transfer function between the frequency spectra of laser response and the output voltage

The relationship between the laser response and the output voltage is further investigated by measuring the peak-to-peak (P-P) displacement from the receiver laser response and BE-output voltage at different input voltage amplitudes applied to the transmitter; these measurements show that the slope between the laser displacement and the BE-output

voltage is increasing with the input voltage amplitude at a rate of 130.6 nm/V i.e. the ratio of 5 between the laser displacement and the output electrical voltage is dependent on the input voltage amplitude.

6.4.3 Effects of input frequency on receiver response in liquids

The central frequency of the input pulse (f_c) affects the energy of high frequencies in the receiver (R_x) response; higher f_c results in more energy in high frequencies. Moreover, the compressional waves in liquid will travel faster than in air. This section presents a comparison of the transmitter (T_x) and receiver (R_x) responses in water (ρ_L = 1.0 g/mL) and sucrose of 60 % (ρ_L = 1.14 g/mL) concentration measured with sine pulse input excitations of different frequencies.

The T_x and R_x responses to f_c = 10, 20, and 50 kHz in water and sucrose-60% are shown in Figs. 6-6 and 6-7 respectively; the time window is restricted to 1.6 ms for clarity. The first arrival times are labelled for all signals using the solid dot; with the tip-to-tip distance between the benders ≈ 7 cm, the wave velocities in the two liquids are estimated to be ≈ 1483.1 m/s and ≈ 1647.1 m/s. These velocity estimates are similar to the sound velocity estimates in the three liquids (water = 1482 m/s, sucrose – 60 % = 1710 m/s) (Pryor and Roscoe 1954).

The effects of f_c on the receiver responses are clearly visible from the two figures. The amplitude of the high frequencies observed in between the time range of 0.4 to 0.8 ms increases as f_c increases. The receiver responses at frequencies 10 and 20 kHz are contaminated by the input signal because the wave arrival occurs before the input signal is completed. The response to f_c = 50 kHz in both liquids is not affected by the input signal contamination; the time of arrival in both liquids are also estimated using the responses to the 50 kHz sine pulse.

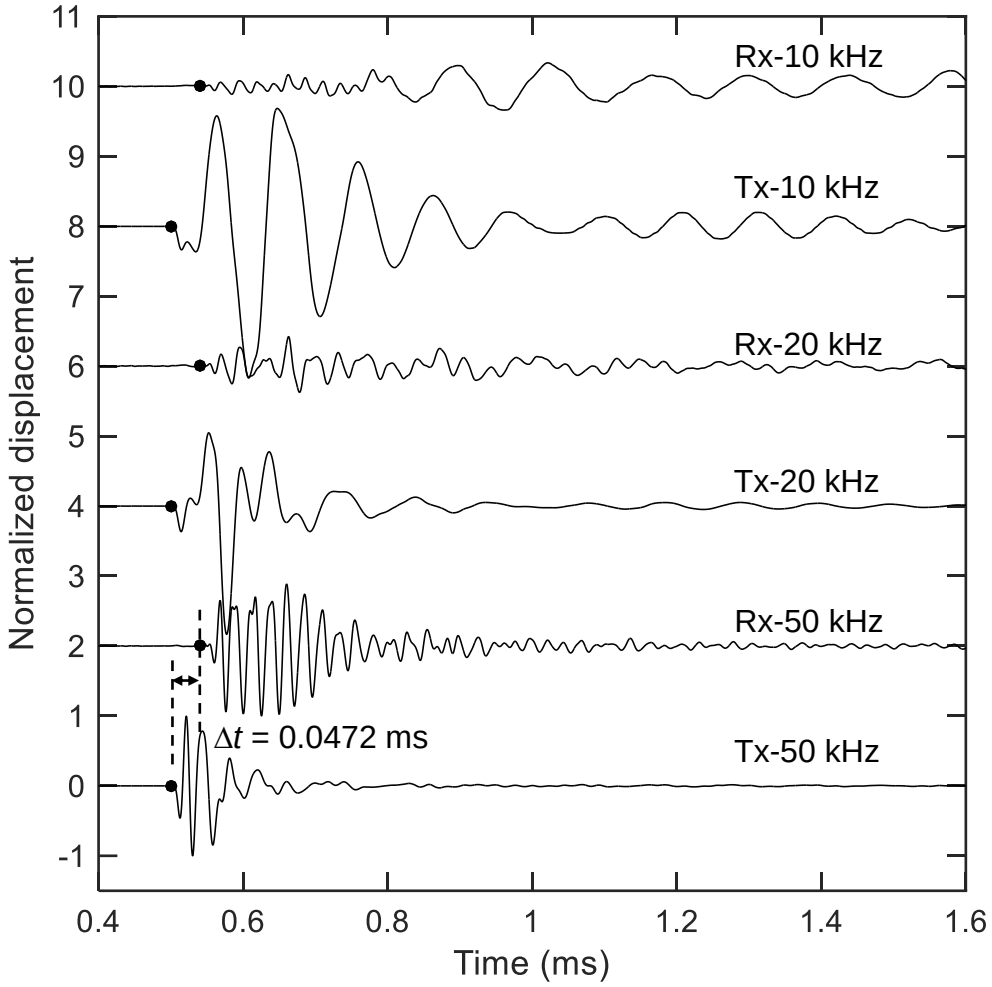

Fig. 6-6: T_x and R_x responses in water to input sine pulse of different frequencies

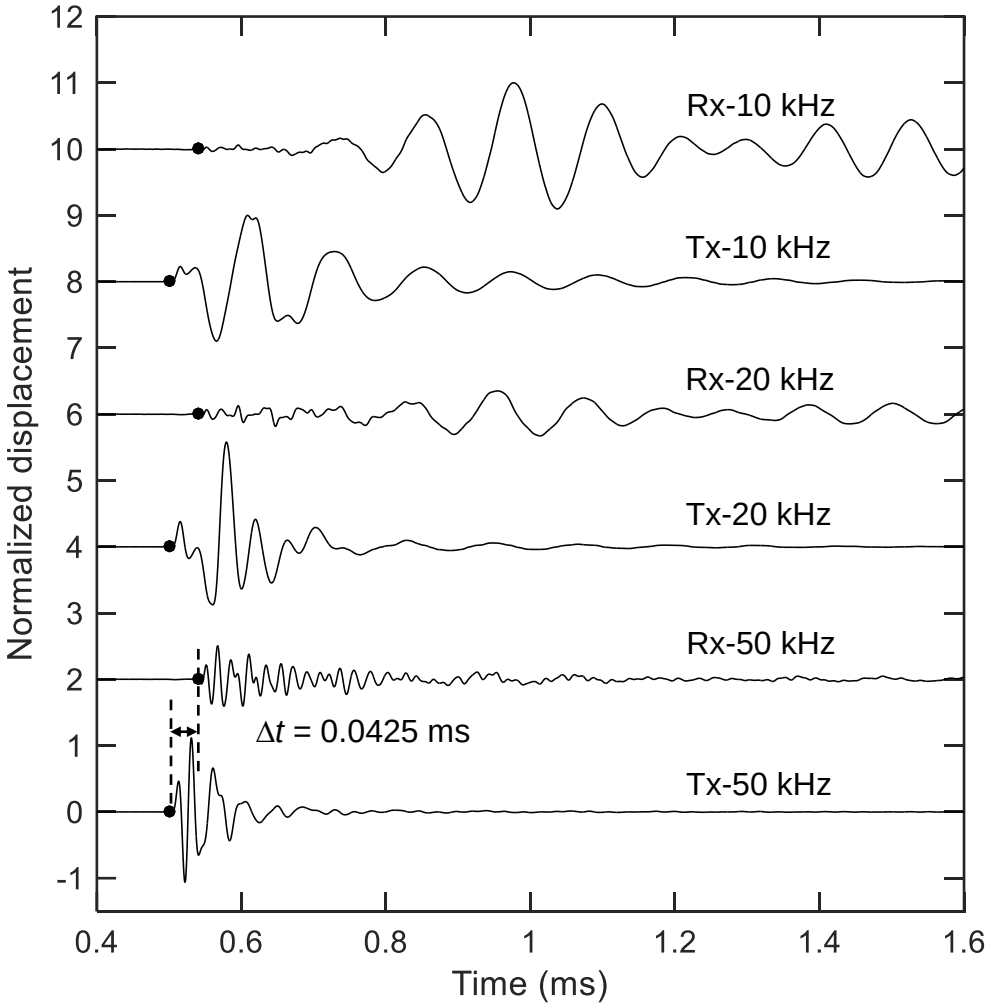

Fig. 6-7: T_x and R_x responses in sucrose-60% to input sine pulse of different frequencies

6.4.4 Effects of input voltage amplitude

The effects of input voltage amplitude on the peak-to-peak displacements of the transmitter (T_x) in air and in the mineral oil mixture have been studied in Chapter 5. In this chapter, this study is extended to liquids of different mass densities and in transparent soil to evaluate the effects of the density on the slope of the linear relationship between the peak-to-peak (P-P) displacement and the input voltage amplitude (V_{app}). Fig. 6-8 shows the variation of the P-P displacement with V_{app} in air, mineral oil mixture (oil), water, sucrose of 30 (S3) and 60 % (S6) concentration and in the transparent soil specimen (Soil

with σ_o = 0 kPa). The experimental data in all medium except in air is fitted with linear trendlines; the solid line corresponding to the data in air is the theoretical relationship (Eq. 5.7) between the bender displacement and the voltage applied/generated proposed by Leong et al. (2005). The theoretical relationship with a slope of 9.4 nm/V matches very well with the air data (9.6 nm/V). The variation of the slope of the experimental data with the density of the surrounding medium is observed as expected; with increase in density, the slope reduces. The rate of reduction in the slope with density is ≈ -6.8 (nm.mL / g.V).

The displacement at the tip of the bender (piezo electric transducer) is proportional to the induced strain which in turn is proportional to the electric field generated in the piezoelectric material when a voltage is applied to the transducer (Yuan 2016). This relationship between the peak displacement of the bender and the input voltage applied to the bender is observed not only in air, but also in liquids of different mass densities and soil without confinement (σ_o = 0 kPa).

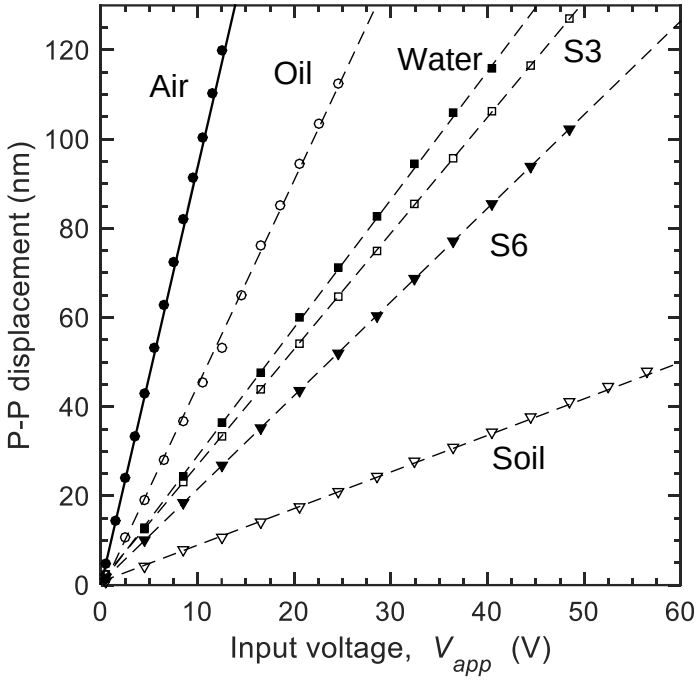

Fig. 6-8: Peak-to-peak displacement of the T_x against the input voltage amplitude in different media

6.4.5 Measurements in soil

First, a sine sweep is used to estimate the resonance frequency of the transmitter. A sine pulse input excitation with the central frequency equal to the resonance frequency of the transmitter is applied to the transmitter again; the transmitter and receiver responses to this sine pulse are measured at the tip of the transmitter and receiver inside the transparent soil.

Fig. 6-9a shows, for the first time in BE test literature, the transmitter and receiver responses to a sine pulse inside an unconfined soil. The estimated first arrival time is also indicated on the figure. Based on this arrival time and the tip-to-tip distance between the benders ($L_{t\text{-}t}$ = 0.07 m), the wave velocity estimated is ≈ 1505 m/s. The shear wave velocity (V_s) and compressional wave velocity (V_p) in fused quartz are much lower than this value (see resonant columns tests results below). On the other hand, the wave velocity in the mineral oil mixture is ≈ 1200 m/s. The wave velocity estimated from the first arrival in Fig. 6-9 is a result of a combination of the compressional wave velocities of the fused quartz and mineral oil mixture. Another possibility could be the attenuation of the wave velocities of fuzed quartz because of the zero confinement on the fused quartz transparent soil specimen. The energy in the oil wave velocity has masked the arrival of the fused quartz wave velocity. The wave velocities of the fused quartz are measured by performing conventional bender elements and resonant column tests on the dry fused quartz (section 6.4.6).

The frequency spectra of the transmitter and receiver signals are estimated by first normalizing both responses by their peak amplitude and then performing the FFT calculations. Fig. 6-9b shows the magnitude of the frequency spectra of the two signals. The magnitudes of each of the frequency spectra are normalized to their own maximum. The reflections from the receiver and the system affects the transmitter response as well; the figure shows that the modes of the transmitter in the frequency range less than 20 kHz are apparently coupled because of the high energy reflections in the system. The peaks in the receiver frequency spectrum in the range between 0 to 20 kHz also verify this observation. Nonetheless, the transmitter frequency spectrum shows three modes in the frequency range of 0 to 50 kHz. The higher modes with peaks at around 30 and 42

kHz in the transmitter frequency spectrum are in line with high energy observed in the receiver frequency spectrum.

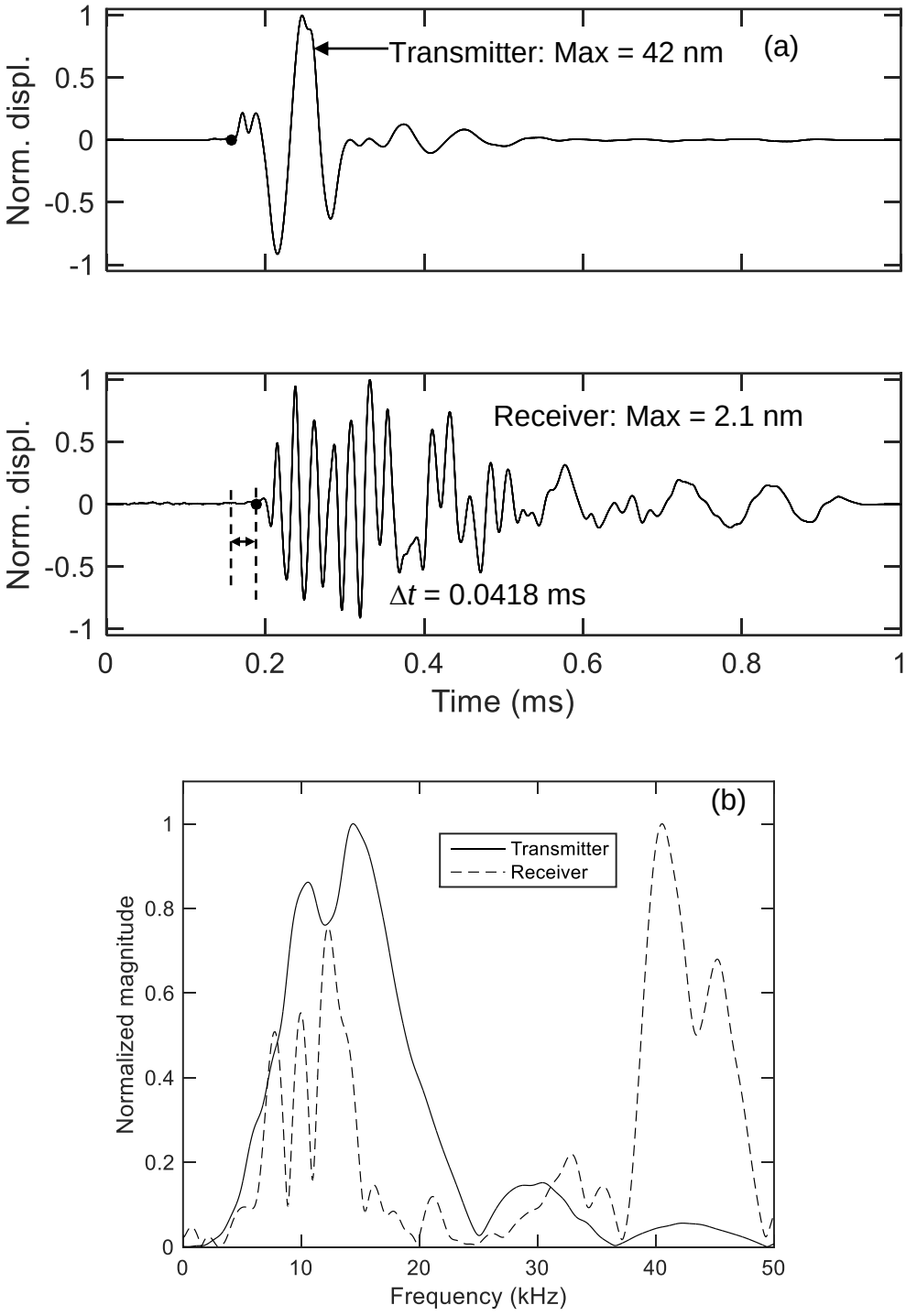

Fig. 6-9: (a) Transmitter and receiver responses to a sine pulse input excitation (σ_o = 0 kPa) and (b) their frequency spectra

Fig. 6-10 shows the T_x and R_x responses inside the transparent soil for a confining stress (σ_o) = 20 kPa. The time delay between the T_x and R_x responses at σ_o = 0 kPa is similar to that at σ_o = 20 kPa. This result shows that an increase in pressure of 20 kPa on the transparent soil specimen does not induce sufficient energy in fused quartz waves to appear in the time signals. The estimated velocity based on this time delay corresponds to the wave velocity of a liquid rather than the fused quartz. The frequency spectra of the T_x and R_x responses at the two different confinements (Figs. 6-11b and 6-12b) also are very similar as shown by the frequencies corresponding to the peaks of the frequency spectra. These results are limited to the confining stress of 20 kPa; further study will be required to evaluate the transmitter and receiver responses at higher confining stresses.

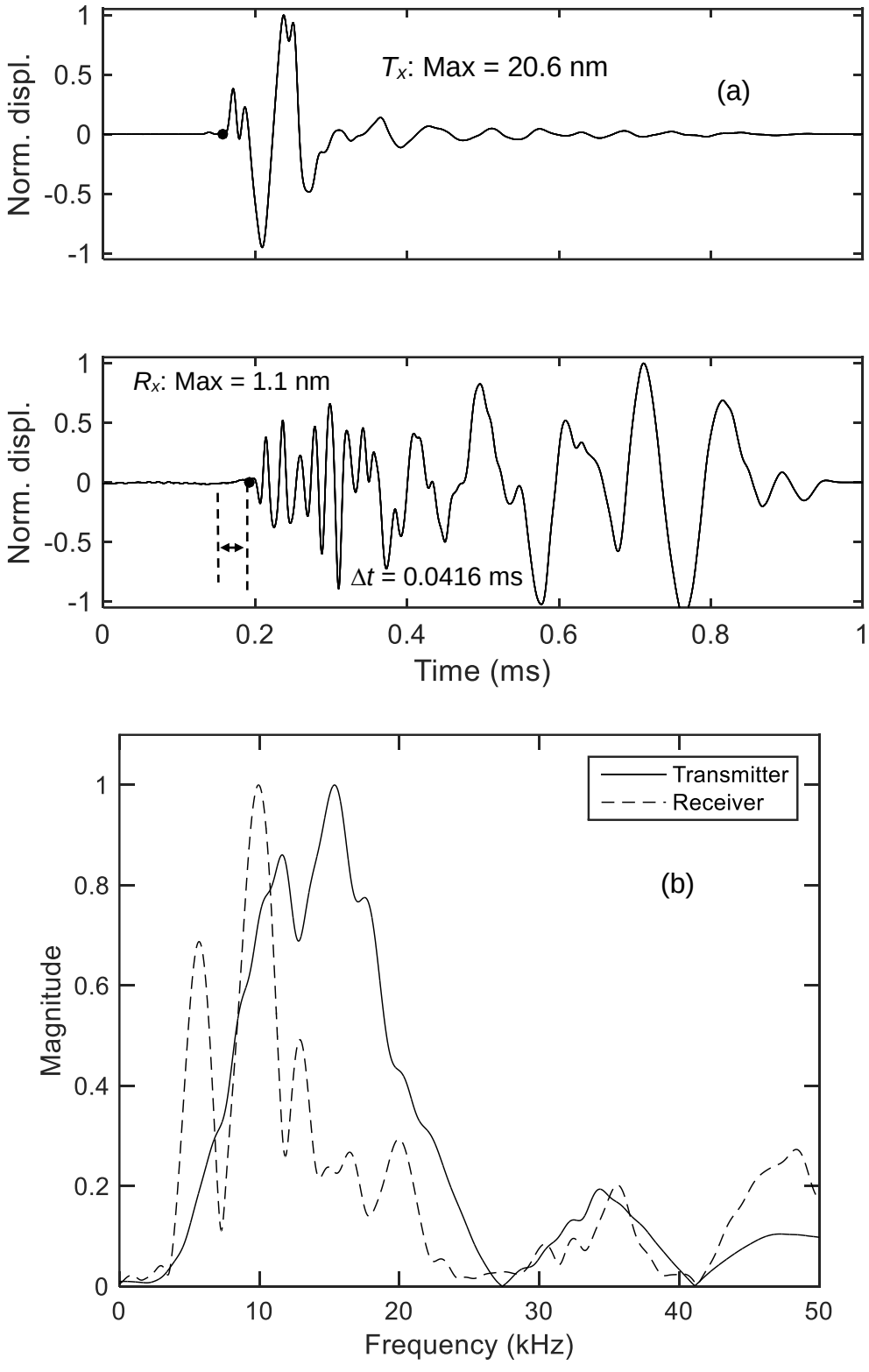

Fig. 6-10: (a) Transmitter and receiver responses to a sine pulse input excitation (σ_o = 20 kPa) and (b) their frequency spectra

6.4.6 Wave velocities of fused quartz

Shear wave (V_s) and compressional wave (V_p) velocities of fused quartz are measured using BE and RC tests under different confinements. Fig. 6-11 and Fig. 6-12 shows the time signals in response to two input frequencies (10 and 50 kHz) used to estimate the V_s and V_p using BE tests under seven different confinements; the arrival times of *p*-waves and *s*-waves from BE test and *s*-waves from RC tests are also marked on the figures. The *p*-wave arrivals are selected based on the first arrival method; and the *s*-wave arrivals for BE tests are selected as the first arrival of the event with more energy (larger amplitude). The back-calculated RC arrival times are different from the *s*-wave arrivals from BE for two possible reasons; (i) frequency effects on the shear wave velocity because the loading frequency range of benders is 1 to 15 kHz while the range in RC test is 20 to 200 Hz (Meng and Rix 2000) and (ii) the *s*-wave arrival selected might still be influenced by the *p*-wave arrival. The *p*-wave presence becomes more significant as the confinement in the soil increases as seen by the amplitude of the wave after the *p*-wave arrival marks.

Comparison of the two figures also shows that the *p*-wave arrival becomes more apparent when the input frequency is increased from 10 to 50 kHz. This result is corroborated by the conventional BE test results from dry sands obtained by Ferreira and da Fonseca (2019). These results show that a relatively reliable estimate of shear wave velocity (V_s) is possible by evaluating the compressional wave velocity (V_p) based on the first arrival using high input frequency (e.g. > 50 kHz) and Poisson ratio of the soil sample.

The wave velocities estimated based on these arrival times and RC-V_s at different confinements are plotted in Fig. 6-13 with the experimental data fitted with power-law. The power law parameters for different wave velocities are also shown. This figure corroborates the results shown in Figs. 6-11 & 6-12; there is a ≈ 15 % difference between the V_s from RC and BE tests. The increase in input frequency increases both V_s and V_p at all confinements showing the effects of loading frequency on the wave velocities.

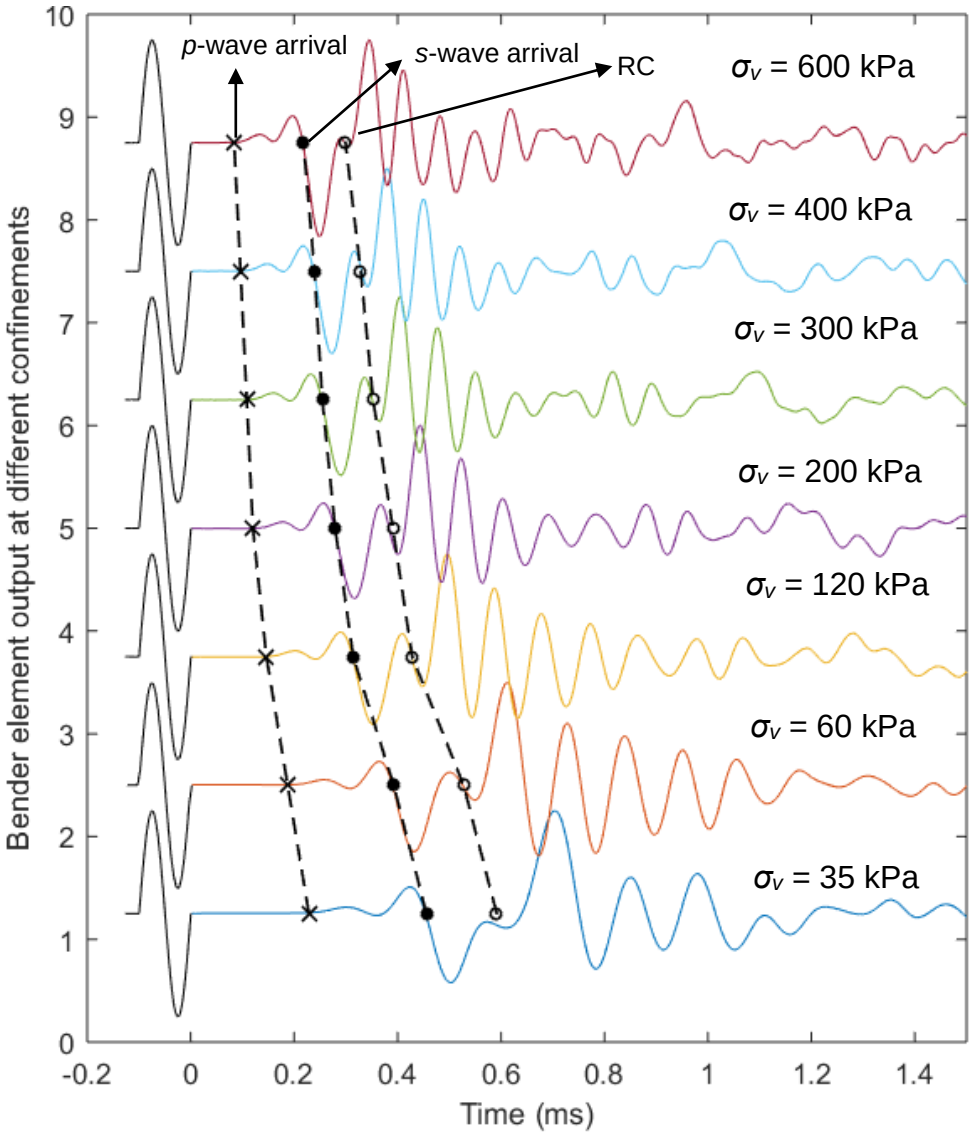

Fig. 6-11: Bender element output voltages inside the fused quartz at different confinements with *p* and *s* wave arrivals and RC time arrivals labelled (Input frequency = 10 kHz)

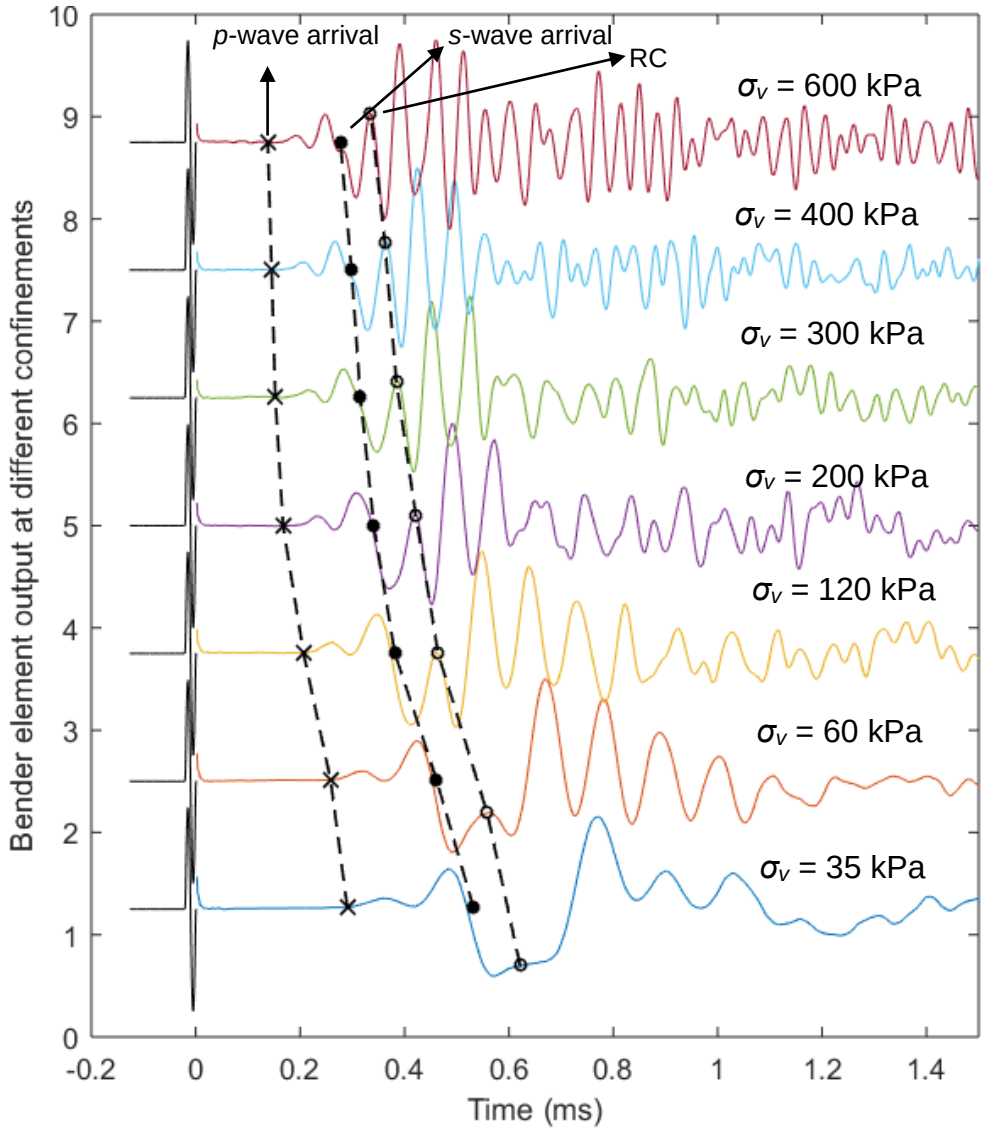

Fig. 6-12: Bender element output voltages inside the fused quartz at different confinements with p and s - wave arrivals and RC time arrivals labelled (Input frequency = 50 kHz)

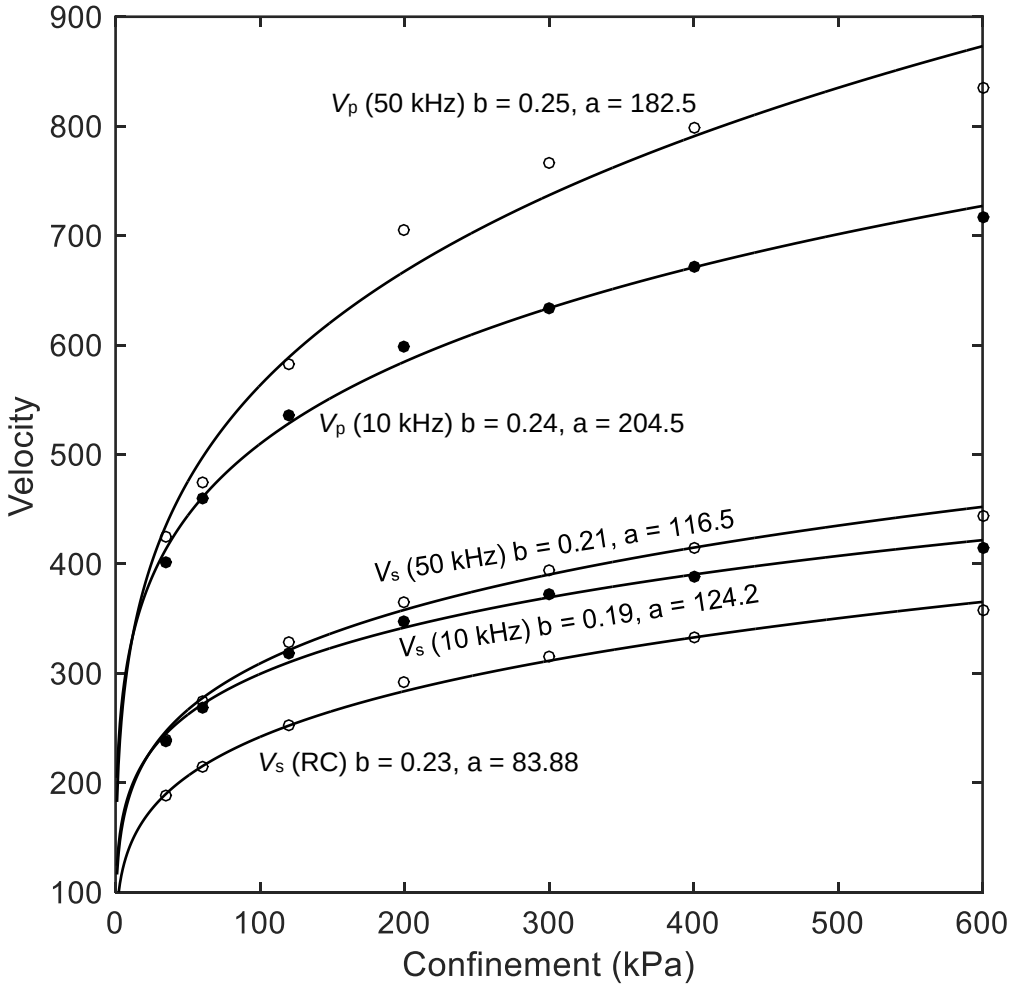

Fig. 6-13: Compressional wave velocity of the fused quartz at different confinements using BE (10 and 50 kHz input frequencies) and shear wave velocity using RC tests

6.5 Conclusions

In this chapter, results of actual BE-receiver response, measured for the first time in BE literature, are presented. BE transmitter and receiver vibrations are measured in air, liquids of different mass density, and in transparent soil using input excitation of different central frequencies and voltage amplitudes. The transmitter and receiver responses are measured at the peak of the benders except in the case of the effect of input voltage on the receiver response in which the response is measured at the center.

The results of this chapter have given several important insights on BE testing. From the measurements in air, it is concluded that there is a significant presence of compressional waves in BE testing. Since the target in conventional BE testing is to identify the shear waves arrival, presence of compressional waves will be treated as noise which must be distinguished from the shear waves. This problem is enhanced in short soil specimens and in saturated soils as has been predicted before (Lee and Santamarina 2005). This conclusion of compressional wave interference is corroborated from the results in water, sucrose-30 %, and sucrose-60 %. The compressional wave velocity estimated from the first arrival method in air and in liquids are similar to those in the literature.

Comparison of the receiver response measured from the laser at the receiver tip and the output electrical voltage in air from the receiver showed that the receiver response at the tip and the output voltage are very similar. Frequency spectra of the two signals showed that the frequency components in the two signals match very well. However, the amplitude of the laser measurement is higher than the output electrical voltage and there is a lag in the laser response because of the presence of more electrical peripherals between the laser beam and the data acquisition system. The laser response at the tip is ≈ 5.8 times higher than the output electrical voltage and there is a time delay of ≈ 0.005 ms. The effect of input voltage amplitude on the receiver response showed that this ratio between the laser response and the output electrical voltage has a standard deviation of ≈ 0.07. Moreover, the mean value of this ratio over an input voltage amplitude range of 0.1 to 200 V is 2.65 which is < 5.8 because the laser response is measured at the center for the study of effect of input voltage amplitude on the receiver displacement. The conclusion of a scalar relationship between the laser response and the output voltage is

further corroborated by the transfer function calculations. This scalar relationship also means that the theoretical relationship between bender displacement and voltage amplitude proposed by Leong et al. (2005) is valid for the whole of the displacement signal rather than just the peak-to-peak displacement of the bender.

The input excitation frequency also affects the frequency response of the receiver. The amplitude of high frequencies in the initial time range of the receiver response increases as the input excitation frequency is increased from 10 to 50 kHz. This exercise showed that the first arrival is easily detected by using a 50 kHz input excitation because the receiver response is not contaminated by the input signal especially if the wave velocity is more than 2000 m/s. Increase in mass density of the medium surrounding the benders also decreased the energy in the high frequencies compared to the energy in the resonance frequency of the transmitter.

The tests for effects of input voltage amplitude on the transmitter displacement in air, liquids, and in soil show that the slope of the linear relationship between the displacement and input voltage amplitude is linearly related and indirectly proportional to the mass density. The slope of the decrease in displacement with mass density is estimated to be ≈ 6.8 nm.mL / V.g based on six data points.

Finally, the measurements in soil showed that the wave velocity of fused quartz or the mineral oil mixture could not be estimated with the first arrival method because of the attenuation of compressional waves and low energy in the shear waves. Higher confinement and longer samples will be needed to be able to detect and distinguish the compressional and shear wave arrivals in the transparent soil specimen.

7 Small-strain dynamic characterization of Leda clay

7.1 Introduction

Marine silts and soft clays are known to significantly amplify seismic ground motions because of the large impedance contrast between these soils and the bedrock. For example, the amplification of seismic waves during the 1985 Mexico earthquake was found to be five times the ground motion at the bedrock (Celebi et al. 1987). These types of soils are abundantly found in many areas of the St-Lawrence River valley, Ottawa River valley, Saguenay-Lac-St-Jean, a part of the north-west of Quebec, eastern and northern Ontario, and some regions of the eastern provinces in Canada (Leroueil et al. 1983).

The Canadian bridge and building codes (e.g. CHBDC 2015, NBC 2015) have recently updated the seismic design requirements for Canada. The soil response during earthquakes (e.g. dynamic response) is an important part of seismic design. The dynamic response of soils during earthquakes is characterized by small-strain properties of soils such as the shear wave velocity (V_s), the shear modulus (G), and the damping ratio (ξ). Resonant column (RC) and bender element (BE) tests are the two main laboratory tests used to measure these properties. Many important structures in Canada such as bridges and dams are located on sites with ample presence of soft clays. The low-strain dynamic response of soft clays in Canada is not well understood because of the limited number of studies performed (Bouchard et al. 2017; LeBoeuf et al. 2016). The main reason for this shortage in studies is that undisturbed samples from these types of soils are very expensive to extract. The lack of understanding of the low-strain dynamic behavior of soft clays has led to over conservative seismic designs and safety evaluations of important structures (e.g. Leroueil et al. 1990).

The present study is part of an experimental program led by a team at Laval University to investigate the dynamic response of Leda clays found in Eastern Canada (LeBoeuf et al. 2017). Advanced in-situ extraction was performed to obtain the undisturbed Leda clay samples for laboratory tests. The objective of this study is to advance the understanding of the small-strain behavior of the Leda clays found in Eastern Canada. Resonant column and bender elements tests are performed on four Leda clay samples collected from two sites (site-1 and site-2) located near the St. Lawrence river valley in Quebec, Canada. Three samples (s1, s2, and s3) are from site-1 and one sample

(s4) is from site-2. Limited number of samples are used because of the expense (≈ $20,000 per borehole) involved in the extraction of these unique Leda clay samples. The effects of shear strain, confinement and frequency on shear modulus and damping ratio of these soil samples are evaluated. The effect of shear strain on shear modulus and damping ratio is evaluated for a strain range of 10^{-4} - 10^{-2} %, while the effect of confinement on shear wave velocity is evaluated for a stress range of 50-400 kPa. The effect of frequency is evaluated using a recently proposed methodology called the 'carrier frequency' (CF) method, which is used with the RC setup (Khan et al. 2008). BE tests are also performed and the results are compared with the RC test results to evaluate the effect of frequency on shear modulus because the loading frequency ranges in BE and RC tests are significantly different. The CF and the equal strain (ES) methods are used to compare the results of effects of shear strain to the results obtained using conventional RC methodology. The results show that the stiffest sample amongst the four (s4) degrades the most with increase in shear strain; although, the modulus reduction rate of s4 decreases with increase in confinement. Only 5% difference is observed between the shear velocity estimates from RC and BE tests. The damping ratio estimates from the CF method are the lowest at mid to high strains because of the low participation of the random noise in the transfer function. Further, the shear modulus and damping ratio of the Leda clay samples appear to be not affected by the loading frequency.

7.2 Literature review on Leda clays

Leda clay (also called Champlain Sea clay) is a type of sensitive clay found in abundance along the St. Lawrence river and the Ottawa river valleys in Eastern Canada (Penner 1965). Leda clays are comprised of plagioclase, quartz, microcline, hornblende, dolomite and calcite (Locat et al. 1984). They are strongly bonded and their sensitivity increases with depth (Crawford 1963).

Several natural disasters (such as landslides) in Eastern Canada have resulted because of the presence of Leda clay in soil deposits (Eden and Mitchell 1969). These events have diverted the attention of many researchers towards studying the behavior of Leda clays in different conditions. Eden and Mitchell (1969) studied the drained shear strength of Leda clays to understand the mechanics of landslides in Leda clay. Drained and

undrained triaxial tests and simple shear tests have been conducted on Leda clay soil specimens to understand its shear strength characteristics (Lee 1979; Lefebvre and Leboeuf 1987). Cyclic shear strength characteristics of Leda clay have also been the focus of a few studies in which cyclic simple shear tests (Lefebvre and Pfendler 1996) and cyclic triaxial tests (Javed 2011) were conducted with Leda clay soil samples.

Although considerable research has been performed on understanding the static and cyclic shear strength characteristics (at high strains) of Leda clay, no study to date has been performed to investigate the low-strain behavior of Leda clays. Low strain behavior of other soft clays such as Detroit clay, Ford clay, Eaton clay, and San Francisco Bay Mud has been investigated (Anderson and Woods 1975; Lodde and Stokoe 1981; Kokusho et al. 1982). Analysis on a collection of experimental data on these soft clays by Dobry and Vucetic (1987) has shown that modulus reduction and damping ratio variation with shear strain of soft clays mainly depends on the plasticity index and void ratio of soft clays. Soft clays behave more linearly compared to the less-plastic clays and sands. This linear behavior of soft clays played a significant role in the large amplification of ground motions in the Mexico City earthquake. Linear behavior of Leda clays has the potential to cause large site amplification and huge destruction. Despite this concern with Leda clays, there are no studies which have investigated the low-strain behavior of Leda clays. The objective of this study is to investigate the low-strain behavior of Leda clays by performing resonant column and bender element tests on Leda clay soil samples extracted from two sites near St. Lawrence river and Ottawa valley.

7.3 Site description

The soil samples tested in this study are from two sites near the St. Lawrence River valley in Quebec. The sample named TM4a is from a 2013 site investigation performed at a site near the intersection of the St. Lawrence and Outardes river in Quebec (Duguay-Blanchette 2016b). The right side of the site is mostly bedrock, the center is dominated by clay and sand deposits, and the left side is mostly peat bog.

Following is a brief description of the geology of this site (Duguay-Blanchette 2016b): The littoral region of the North Shore of the St. Lawrence River is located in the Grenville Geological Province. The bedrock of this region is made of metamorphic rocks. Loose

silt, clay, and sand deposits of varying thicknesses formed in the Goldthwait sea after melting of glacier. A total of six samples of 200 diameter and 390 mm height were extracted from layers between 8 m to 21 m; the sample used in this study is from a sample between the depth of 14.73 and 15.13 meters.

The samples named s1, s2, and s3 are from the site investigation performed at a site located on the east of the Beauharnois canal just before the St. Lawrence river crossing (SM LABO INC. 2014). Mostly, herbaceous vegetation and agricultural crops cover the land. The bedrock is formed of quartzite sandstone belonging to the cairnside formation. A total of 21 samples, each of 200 mm diameter (using Laval University sampler) and 580 mm height, were extracted from a 14.8 m thick layer of silty clay of very soft to stiff consistency with sand traces and gray in color. The samples tested in this study are from 3 of those 21 samples.

7.4 Experimental setup

Fig. 7-1 presents the schematic of the test setup with resonant column and bender elements equipment. A modified Stokoe-type resonant column is used with a fixed-free configuration. The built-in source in the spectrum analyzer (HP-35670A) is used to apply a sinusoidal sweep input voltage which is amplified by a power amplifier (Bogen GS-250) because the output voltage amplitude of the built-in source is limited. The amplified input voltage is used to induce alternating current in the coils which are mounted on the driving plate. This alternating current causes the magnets to vibrate which in turn cause torsional excitations on the soil sample. The response of the specimen to these torsional excitations is characterized in terms of the acceleration of the accelerometers (PCB 353A78 and PCB 353B65) mounted on the driving plate. The current in the coils and the acceleration are amplified and filtered (200 Hz low pass) using a filter amplifier (Krohn-Hite 3384) before being sent to the spectrum analyzer for transfer function calculations; the spectrum analyzer calculates the transfer function in real time. Resonance frequency and damping ratio of the soil specimen are estimated from the transfer function.

The RC driving system with the soil specimen is placed in a confinement chamber. A pneumatic pressure panel (Brainard and Kilman), which has a maximum confinement

capacity of 700 kPa, is used to exert the confinement on the soil sample. Axial strain of the specimen is monitored using a Linear-Voltage-Displacement-Transducer (LVDT) (Trans-Tek, 0242-0000 D-6) which is mounted on the driving plate.

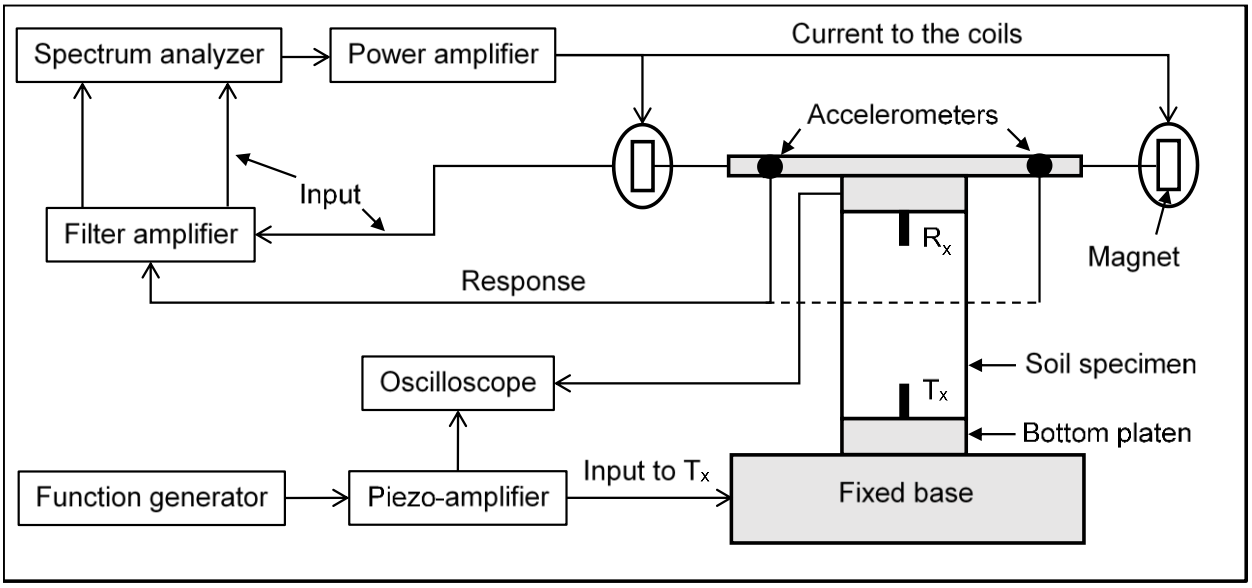

Fig. 7-1: Schematic of resonant column and bender element tests

7.5 Sample preparation

The soil samples received at the University of Waterloo geotechnical laboratory were large in size. Sample s4 was received in a cake form covered with wax, and was 200 mm in diameter and 135 mm in height. Samples s1-s3 were received in three specially manufactured boxes that contained the waxed soil samples with dimensions of 200 mm diameter and 355 mm height. These samples were stored in a refrigerator to maintain the moisture content. The sample dimensions required for RC test are 70 mm diameter and 140 mm height. The procedure for specimen preparation for RC test is described next.

The wax covering for a portion of the soil sample is first peeled off and a chunk of soil larger in volume than the required sample dimensions is cut. The remaining sample is re-covered with wax and stored back in the refrigerator to avoid sample disturbance. A wire saw is used to cut-off some part of the chunk of clay before placing it on a sample pedestal; then, the sample is trimmed to a diameter of 70 mm. Fig. 7-2a shows one of the

trimmed soil sample on the sample pedestal. The top cap of the pedestal is gently pulled up to release the sample before using a split mould (approximate dimensions: 70 mm diameter and 140 mm height) to hold and release the sample from the pedestal. A wire saw is used to cut the clay sample to a height close to 140 mm before using a scraper to trim the sample to 140 mm height. With the known mass of the split mould, the split mould with the clay sample is weighed and the mass of the clay sample is calculated. About 200 g of sample from the wasted clay chunk is used for water content measurement using the oven-dried method. Indentations are created on one side of the clay sample to facilitate the insertion of bender elements and the blades for improved coupling (Ali et al. 2016). Finally, the sample is placed on the bottom platen of the resonant column setup (Fig. 7-2b). Vacuum grease is applied on the top and bottom platens. Then, the soil sample is covered with a latex membrane with the help of vacuum and a cylindrical pipe. The membrane is gently pulled to remove any air bubbles between the sample and the membrane. Finally, gaskets are placed on the top and bottom platens on top of the membranes to ensure minimum air flow.

Fig. 7-2:(a) Trimmed soil sample on a pedestal; (b) Sample on the resonant column base platen.

7.6 Experimental methodology

7.6.1 Calibration of the power amplifier

The power amplifier is used to amplify the input voltage used for inducing current in the coils of the RC driving system. The power amplifier also has a frequency range in which its response is non-linear; it is important to ensure that the amplifier has a linear response in the frequency range that will be encountered in the RC tests. This process of ensuring linear response in the working frequency range is called the calibration of the power amplifier. This calibration is performed by evaluating the transfer function of the power amplifier at different amplification levels using the spectrum analyzer. Fig. 7-3 shows the schematic used for calculating the transfer functions. The ‘source’ feature of spectrum analyzer is used for sending an input voltage to the power amplifier; this input voltage is simultaneously sent to channel 1 of the analyzer as the input for the transfer function of the power amplifier. This input voltage is amplified by the power amplifier; then, the voltage across a 10 Ohm resistor for different frequency ranges is measured and sent to

channel 2 of the spectrum analyzer as the output for the transfer function. A 10 Ohm resistor is used because the impedance of the outlet of the power amplifier is different from the impedance of the spectrum analyzer.

The input voltage from the source to the power amplifier is fixed at 25 mV; the frequency ranges for which the transfer functions are evaluated are 0-200 Hz and 0-50 Hz. The range of 0 to 200 Hz is more than sufficient because the maximum resonance frequency of any soil would not be more than 200 Hz (Rix and Meng 2005); frequency range of 0 – 50 Hz is selected to focus the transfer function in a range which is more commonly utilized in this study. The amplification level of the power amplifier is varied from 2 to 25.

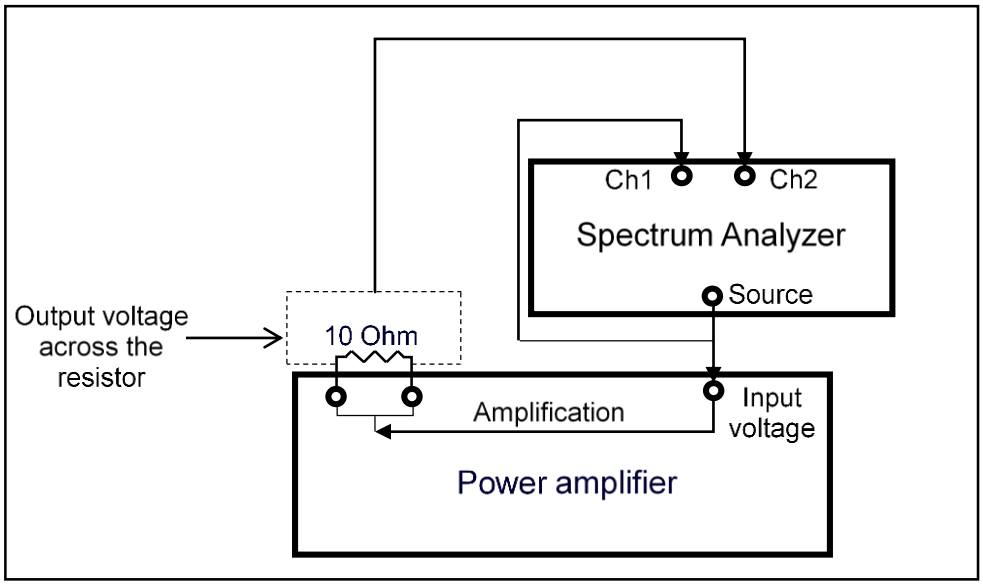

Fig. 7-3: Schematic of the setup to calculate the transfer function of the power amplifier

Selected transfer functions for different amplification levels are shown in Fig. 7-4 (frequency range = 0 - 200 Hz) and Fig. 7-5 (frequency range = 0 - 50 Hz). The maximum amplification level that will be used in the RC testing is 20. The transfer functions at all the amplification levels are flat i.e. the power amplifier behaves linearly except at frequencies lower than 13 Hz. However, the lowest resonance frequency of any soil sample in a RC test is 20 Hz (Rix and Meng 2005); therefore, this power amplifier is suitable to be used for frequency range between 20 – 200 Hz and for amplification levels from 2 to 25.

The maximum magnitudes of these transfer functions are plotted against the amplification levels of the power amplifier in Fig. 7-6. Note that the no. of transfer functions in Fig. 7-4 and in Fig. 7-5 are less than the experimental points shown in Fig. 7-6; this difference is because selected transfer functions are plotted for clarity. The magnitude vs amplification clearly has a trend i.e. the magnitude increases exponentially with the amplification level. This information is important in the RC test to ensure that the power amplifier is performing the amplification as is expected.

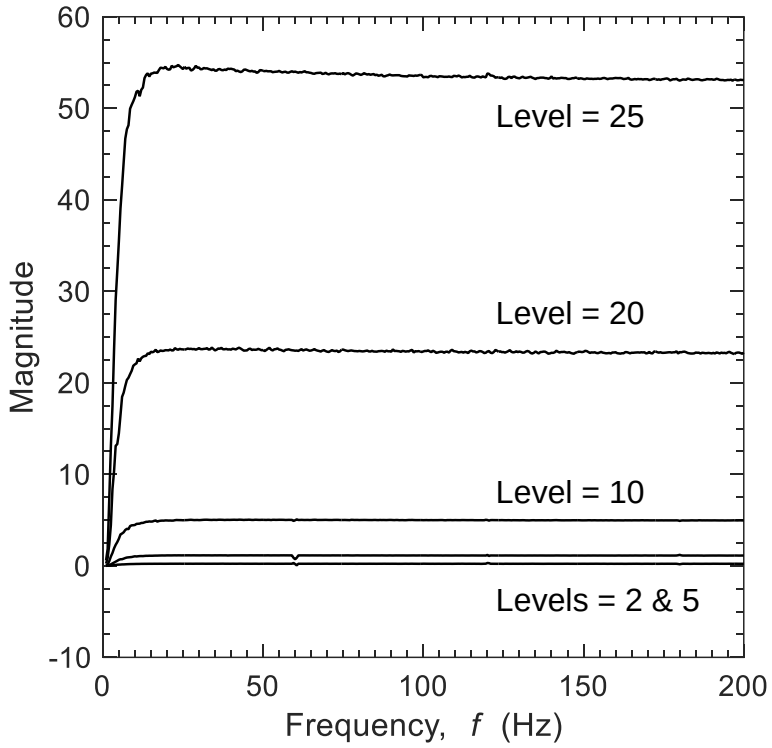

Fig. 7-4: Transfer functions of the power amplifier at different amplification levels (0 -200 Hz)

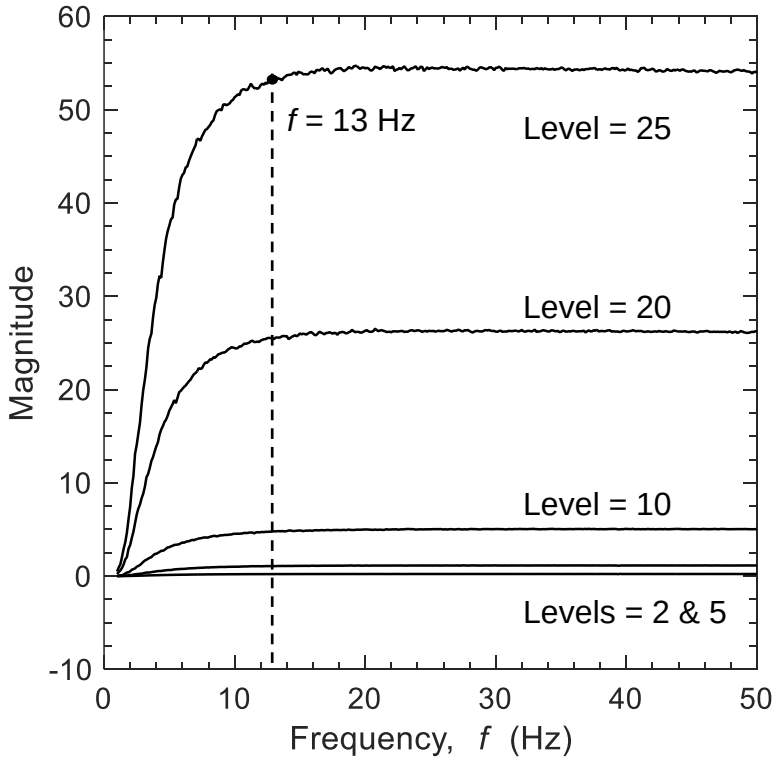

Fig. 7-5: Transfer functions of the power amplifier at different amplification levels (0 - 50 Hz)

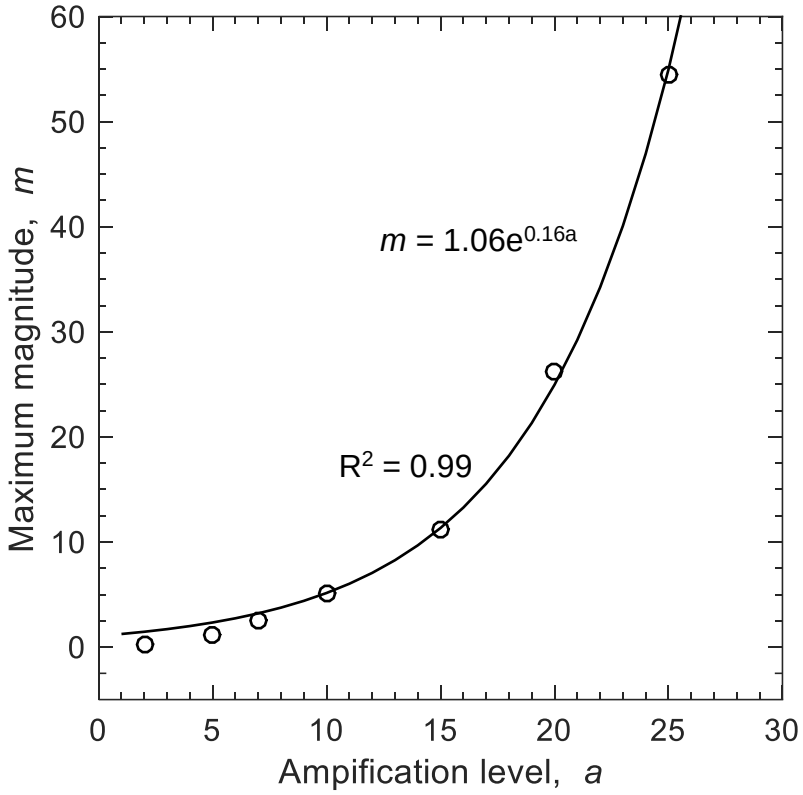

Fig. 7-6: Maximum magnitudes of the transfer functions of the power amplifier against the amplification levels

7.6.2 Calibration of the filter amplifier

Filter amplifier is used for filtering the extraneous frequency components from input and output voltages while performing the sine-sweep in the RC test. The cut-off frequency of the filter amplifier is set at 200 Hz because most soils have resonance frequencies less than 200 Hz (Rix and Meng 2005). The dB-amplification is set at 20 dB for strains in the range of 10^{-2} to 10^{-3} % and 10 dB for strains close to 10^{-2} %.

The filter amplifier is a system with transfer function like any other electrical component. To ensure accuracy of the resonant column results, the filter amplifier should be a linear-time invariant system. Linearity of the filter amplifier is investigated here using the transfer function which is calculated by the spectrum analyzer. First, the transfer function is estimated with a cut-off frequency of 20 kHz with no amplification and compared to the analytical transfer function of a low-pass filter (Eq. 6.1). Then, the transfer function of the

four channels of the filter amplifier is estimated with 20 dB amplification and a cut-off frequency of 200 Hz.

$$\left|H(\omega)\right|^2 = \frac{G_0^2}{1+\left(\frac{f}{f_c}\right)^{2n}} \qquad 6.1$$

Where G_0 is the DC gain, f_c is the cut-off frequency, f is the frequency, and n is the order of the filter.

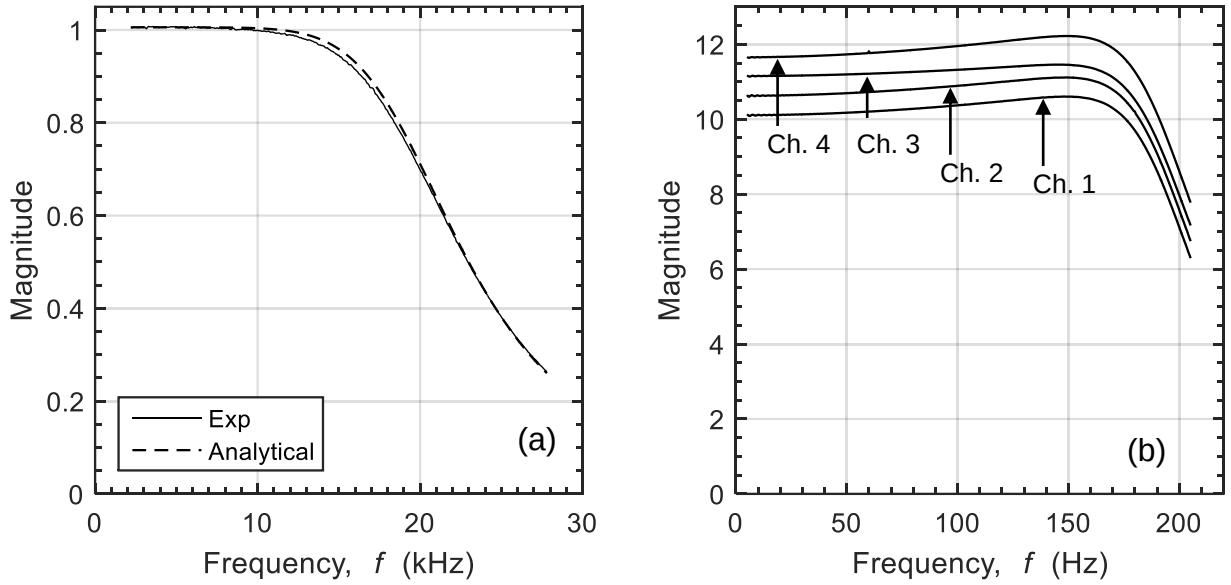

Fig. 7-7: (a) Experimental and analytical transfer functions of the filter amplifier; (b) Experimental transfer functions (offset for clarity) of the four channels of the filter amplifier with resonant column conditions

Fig. 7-7a shows the analytical and experimental transfer functions; the analytical transfer function is calculated with f_c = 20 kHz, n = 4, and G_0 = 1 (no amplification). The experimental transfer function matches very well with the analytical transfer function with an estimated attenuation slope of ≈ 20 dB / octave for both. This result means that this filter amplifier is suitable for use with the resonant column test. Fig. 7-7b shows the transfer function estimated with the settings used for a typical resonant column setup: f_c

= 200 Hz and amplification of 20 dB. There are four channels in the filter amplifier which can be used for filtering and amplifying electrical signals; transfer functions of all four channels (with 0.5 magnitude offset added for clarity) are shown. The dB magnitude at the cut-off frequency (200 Hz) is -3.06 which is approximately the well-known theoretical dB magnitude of a Butterworth low-pass filter.

7.6.3 Calibration of the accelerometer conditioning unit

The accelerometers' signal used for measuring the response of the soil specimen in a resonant column setup (PCB 353A78 and PCB 353B65) is usually affected by noise because of the low amplitudes of the signals. The accelerometers' responses are conditioned by a PCB conditioning unit which is specifically designed for accelerometers of the type used in this study. This conditioning unit has to be calibrated to ensure its usability with the resonant column setup. The spectrum analyzer is used to estimate the transfer function of the two channels used for the two accelerometers. Fig. 7-8 shows the transfer functions of the two channels (one transfer function offset for clarity). Magnitudes of both transfer functions are constant (≈1) at all frequencies between 0 – 200 Hz which means the output signal is equal the input signal coming from the accelerometers. This result shows that this conditioning unit is suitable for use.

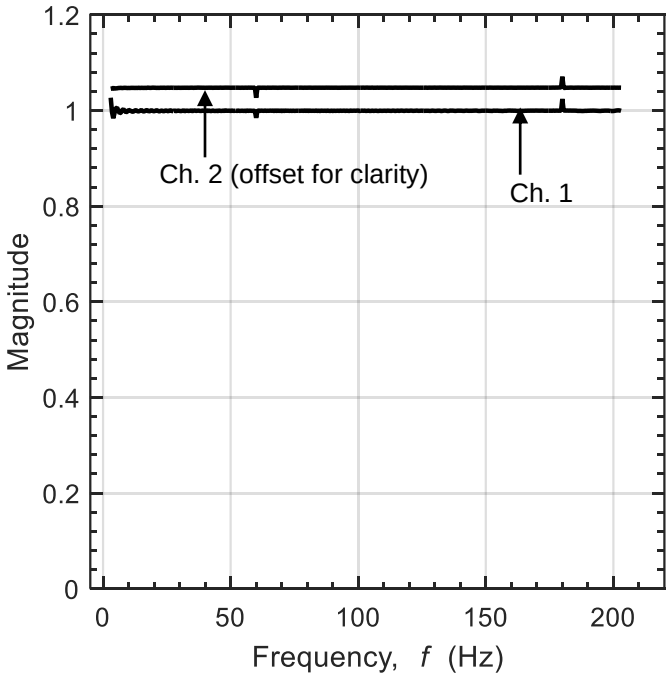

Fig. 7-8: Transfer function of two channels of the accelerometer conditioning unit

7.6.4 Calibration of RC system

The shear modulus (G) of the soil sample is estimated using Eq. 2.2 where the shear wave velocity of the soils (V_s) is estimated using Eq. 3.2. Eq 3.2 requires the estimate of the moment of inertia of the sample (I) and the moment of inertia of the driving plate and resonant column top cap (I_o). I is simple to estimate based on the geometry of the soil sample (cylinder); however, the driving system in the RC setup has a complex geometry which makes it difficult to estimate the I_o; therefore, I_o is typically estimated experimentally. An aluminum probe with a known resonant frequency (f_o) is used for this purpose along with a measured mass assuming a single-degree-of-freedom system with total mass equal to the mass of the driving system plus the additional measured mass. The aluminum probe is made from a pipe section which is attached to the rectangular bars at the bottom and at the top. The results I_o for the driving plate of RC system used in this study is 67.4 g-cm-s^2. Details of the calculation of this I_o is give in the appendix A. Details of the probes used to verify the calibration of the driving system are given in Table 7-1

Table 7-1: Properties of the calibration aluminum specimens

Probe	Outside diameter (mm)	Length (mm)	Resonance frequency (Hz)	Damping ratio (x 10^{-3})
AL 1	19	227	50.75	1.13
AL 2	25	225	98	2.5
AL-3	10	225	11	10.7
AL-4	6.5	223	8.3	11
AL-5	19	225	81	3

7.6.5 Linear voltage displacement transducer (LVDT) calibration

The consolidation of the soil sample is monitored by the change in height of the soil sample. When the soil sample is not in the pressure chamber, the height of the sample is measured using a Vernier caliber; however, the access to the soil sample is difficult when the soil sample is inside the chamber. Hence, a linear voltage displacement transducer (LVDT) is used for measuring the change in height inside the chamber.

The LVDT is mounted on a vertical caliber in a position similar to that in a RC test (Fig. 7-9). The LVDT rod is let loose on the vertical caliber and an initial voltage reading is noted. Then, the measurement of the vertical caliber is changed by a particular displacement increment and the corresponding voltage change is noted. This step is repeated for multiple displacement increments and the displacement is plotted against the voltage; the voltage range in which the slope of the plot is linear is recorded and the slope of that linear range is estimated by curve-fitting the experimental data. This slope is then used to estimate the actual height of the sample during the consolidation stage (section 7.6.6) or during the testing stage (section 7.6.7.2). Moreover, the LVDT measurements in an actual RC test are ensured to stay within the linear voltage range. The calibration of the LVDT used in this study is presented in the Fig. 7-10 below

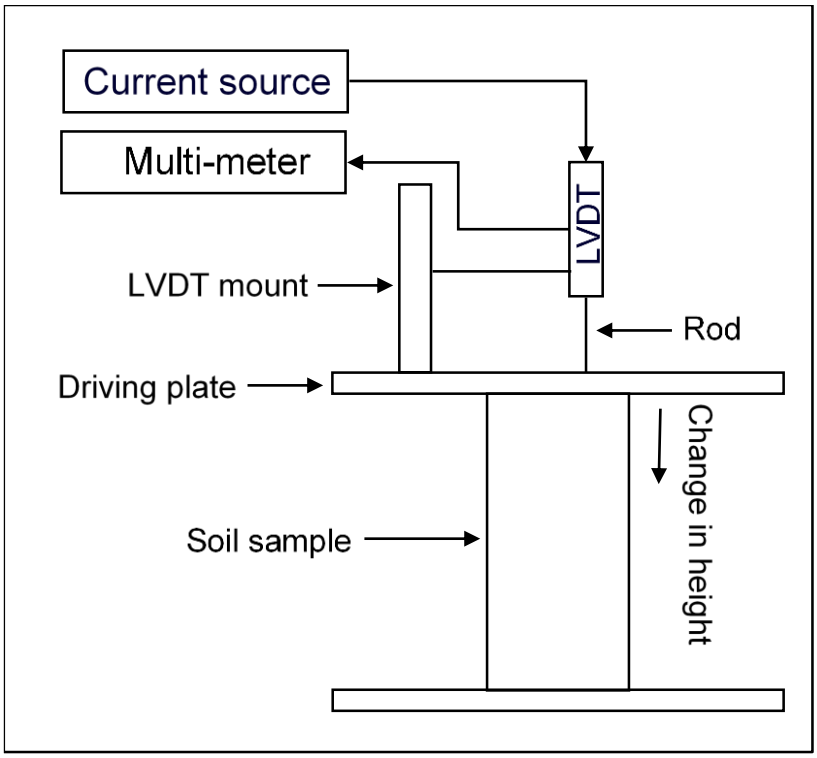

Fig. 7-9: Schematic of the setup for LVDT measurements

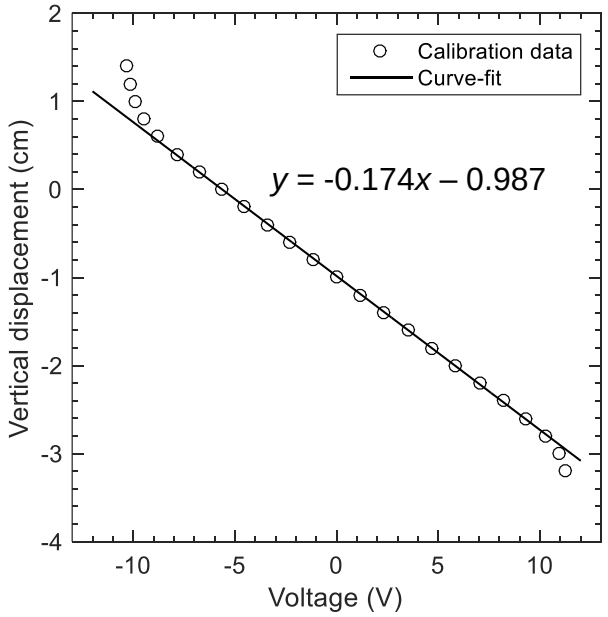

Fig. 7-10: LVDT calibration to estimate the LVDT constant required for estimating the height of the sample

Fig. 7-10 shows that the estimated slope of the LVDT used in this study is 0.174 cm/V and the linear range of the LVDT is ≈ -9 V to +9 V (total = 18 V). This result means that the change in height by 1.74 mm will be indicated by a change in voltage by 1 V in the linear range; therefore, the total allowable change in height is 1.74 mm/V x 18 V ≈ 31 mm which is more than sufficient for a RC test.

7.6.6 Consolidation

The stress increase in saturated clay soils causes a sudden increase in the pore water pressure in the soil. Due to the low permeability of the clay soils, the decrease in pore-water pressure (and thus, the settlement) may take a long time to stabilize although the elastic settlement in soils will occur immediately. The volume change associated with the pore-pressure decrease over time in a soil sample must be completely (or mostly) finished before the RC test can be performed because the geometry of the soil sample is important in the estimation of the dynamic properties of soils. This condition means that the primary consolidation should be completed before performing the measurements; therefore, at every applied confinement, the soil sample is consolidated until the beginning of the secondary compression stage as shown in Fig. 7-11. The deformation (axial) of the sample inside the pressure chamber during the confinement is measured using an LVDT.

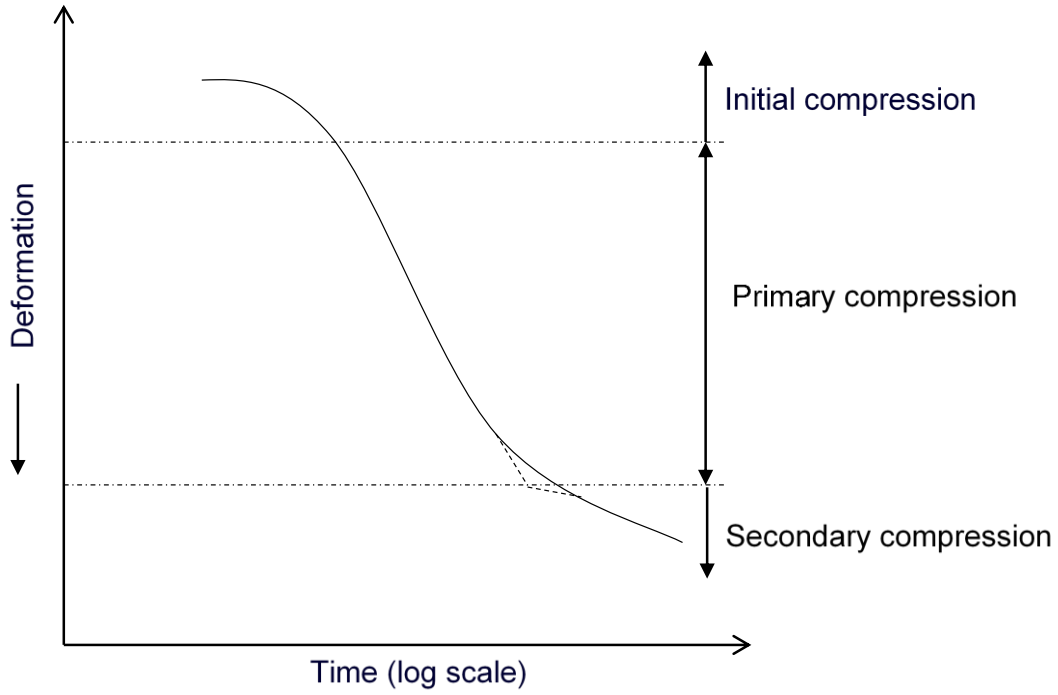

Fig. 7-11: Deformation-time plot for a given confinement

An example of the consolidation plot of one of the soil samples used in this study is presented in Fig. 7-12 with the consolidation stages labelled. The confinement on the soil sample reduces the sample height; which reduces the gap between the magnets and the base of the coils. Therefore, the confinement has to be removed; and the pressure chamber has to be opened to realign the magnets of the driving plate to bring the magnets in the center of the coils. Upon closing the pressure chamber, the soil sample is subjected back to the same confinement. This process is termed as ‘reconsolidation’ in Fig. 7-12. Note that the slope of the ‘reconsolidation’ phase is very similar to that of the secondary compression stage of the ‘consolidation’ phase; hence, the RC tests are performed on this sample without waiting for the time that is spent for the consolidation stage.

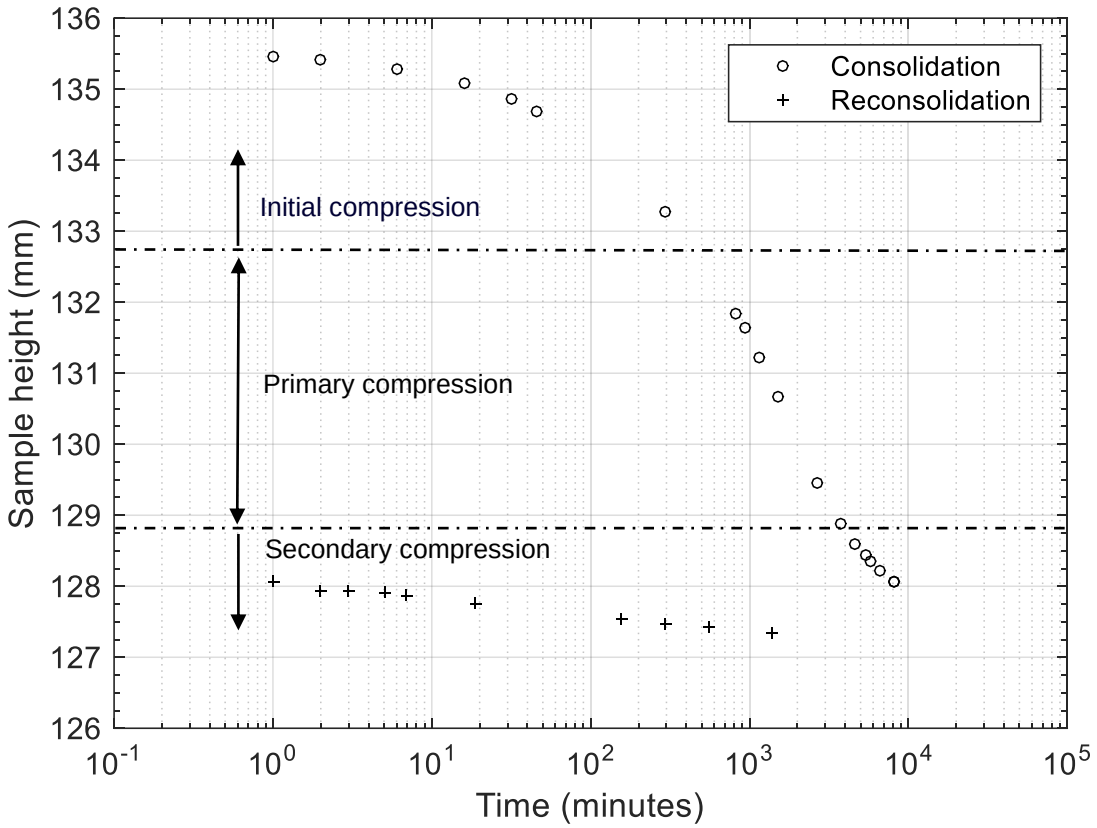

Fig. 7-12: Example of the consolidation plot of a soil sample used in this study with the consolidation stages labelled.

7.6.7 Sample calculations

7.6.7.1 Transfer function curve-fit

The spectrum analyzer performs sinusoidal sweep using burst chirp excitation (Fig. 5-7) and calculates the transfer function in real time at each induced shear strain level. From the transfer function, the resonance frequency (f_o) of the soil sample and the damping ratio are recorded from the analyzer. The analyzer performs this calculation by curve fitting the one-dimensional transfer function between the acceleration and the current across the coils of the RC driving plate; this transfer function is presented as Eq. 6.2 below (Cascante et al. 2005)

$$H(\beta) = \frac{B1}{M}\frac{-R_a R_m \beta^2}{1-\beta^2 + i2\xi\beta} \qquad 6.2$$

Where $B1/M$ is the magnetic force factor of the coils, R_a is the distance between the accelerometer and the center of the specimen, R_m is the distance between the center of the magnet and the center of the specimen, ξ is the damping ratio, and β is the ratio between the radial frequency (ω) and the radial resonance frequency (ω_o) of the specimen.

This curve fitting can be done manually using Mathcad™ or MATLAB™ to confirm the results from the spectrum analyzer. A typical set of calculations for this curve-fit using Mathcad is presented below in Appendix B.

7.6.7.2 Shear modulus and damping ratio from conventional RC test

The estimated damping ratio (ξ) at a particular shear strain is estimated directly from the transfer function curve-fit equation (Eq. 6.2). In the example in Appendix B, ξ would be 0.7 %.

The induced shear strain (γ) for each pair of shear modulus (G) and damping ratio is estimated using the Eq. 6.3 below (Drnevich et al. 1978)

$$\gamma = \frac{V_{rms}\, d\, g\, 0.707 V_{out}}{\pi^2\, 16\, R_a\, Sens\, H\, f_o^2\, 10^{\frac{a}{20}}} \qquad 6.3$$

Where V_{rms} is the root-mean-square voltage which depends on the input voltage (1 for burst chirp), d is the diameter of the specimen, g is the gravitational acceleration, V_{out} is the maximum output voltage from the accelerometer, R_a is the distance between the accelerometer and the center of the specimen, $Sens$ is the sensitivity of the accelerometer (493.05 mV/g for the accelerometer used in this study), H is the height of the specimen, f_o is the resonance frequency from the transfer function, $10^{a/20}$ is the gain, and a is the db output

Sample γ calculations for a sample of d = 7 cm, H = 14 cm, and f_o = 52.6 Hz are shown in Appendix B. The estimate value of γ is 7.5 x 10^{-4} %.

The shear wave velocity (V_s) of the soil specimen is estimated using the Eq. 6.4 (refer section 2.1.2)

$$\frac{I}{I_o} = \frac{\omega_o H}{V_S} \tan \frac{\omega_o H}{V_S} \qquad 6.4$$

Where I is the mass moment of inertia of the sample and I_o is the mass moment of inertia of the driving plate

Estimate of V_s is obtained by rearranging the Eq. 6.4 and finding the root (β) of the rearranged equation (Eq. 6.5)

$$f(\beta) = \beta \tan \beta - \frac{I}{I_o} \qquad 6.5$$

Where $\beta = \frac{2\pi f_o H}{V_s}$

Sample calculations for finding the root (named 'a') and estimating the V_s using Mathcad are presented in Appendix B. The equation of β is used to back calculated the V_s; note that 100 is the conversion factor between cm and m to convert the V_s in m/s

V_s and G are related through the Eq. 6.6

$$G_{\max} = \rho V_s^2 \tag{6.6}$$

Where ρ is the mass density of the soil sample which calculated based on the measured lab weight and height of the specimen and G_{max} is the shear modulus at low strains. Mass, diameter and height of the specimen are recorded before the soil sample is subject to testing; using these properties, the density of the soil sample is estimated which is then used along with Eq. 6.6 to estimate the G_{max}. Sample calculation of the G_{max} is shown in Appendix B.

Sample calculations for the change in height after performing a test using the LVDT constant (section 7.6.5) are presented in Appendix B. Note that the voltage measurements in these calculations are exaggerated for demonstration purpose.

7.6.8 Testing procedure

The driving plate is attached and levelled to the top platen. The pressure chamber is placed around the RC system and the sockets between the driving system and the pressure chamber wall are connected. A preliminary RC test is run with the open pressure chamber to ensure that the wires are connected correctly. The pressure chamber lid is placed and the pressure panel is turned on to generate confining stress in the chamber. All soil samples are consolidated until the secondary compression stage. The effective confinement stresses (σ'_o) at which the tests are conducted are 50, 100, 200, and 400 kPa. These stresses are selected such that each of the soil sample tested subjected to a confinement above its pre-consolidation stress (σ_c). The effects of shear strain, confinement, and frequency on shear modulus and damping ratio are evaluated. The effects of frequency are evaluated using the carrier frequency method, while the effects of shear strain and confinement are evaluated using the resonant column, carrier frequency and equal strain methods. These methods are described below

7.6.8.1 Conventional resonant column technique

First, a burst chirp (fixed amplitude) of a frequency span of 200 Hz is applied to determine the range in which the resonance frequency lies; then, the frequency span is reduced to 50 Hz with the resonance frequency as the central frequency of the burst chirp. A total of 10 sine sweeps are performed and the average of the 10 transfer functions is calculated. Resonance frequency and damping ratio are estimated from the transfer function using the curve-fitting procedure. Peak output voltage (V_{out}) from the soil response to sine sweep is noted and used with Eq. 6.7 (Cascante and Santamarina 1997) to estimate the induced shear strain (γ) in the sample

$$\gamma = \frac{0.707\, V_{rms}\, d\, g\, V_{out}}{16\, \pi^2\, r_a\, S\, H\, f_o^2\, 10^{\frac{A}{20}}} \qquad 6.7$$

Where V_{rms} is the root mean square voltage factor (1 for burst chirp), d is the diameter of the sample, g is the gravitational acceleration, r_a is the distance between the center of the specimen and the accelerometers, S is the sensitivity factor of the accelerometer, H is the height of the sample, f_o is the resonance frequency, and A is the amplification factor to estimate the gain.

A total of 9 different shear strain levels (10 minutes apart) are induced by increasing the input voltage (loading process), and 5 shear strain levels in the unloading process. Shear modulus and damping ratio are estimated and plotted against the induced shear strains.

7.6.8.2 Carrier frequency (CF) technique

CF method is proposed by Khan et al. (2011) to evaluate the loading frequency effects on shear modulus and damping ratio. In this method, the loading frequency on the soil specimen is independently controlled at a fixed strain level. To execute this method, the conventional RC technique must be implemented first. The setup for CF method is the same as that of the conventional RC method.

Frequency effects

The procedure to evaluate the frequency effects is described here. A sine sweep using the conventional RC technique is performed first; then, the induced shear strain resulting from this sine sweep is estimated. This strain is used, along with Eq. 6.7 to create a set of pairs of frequencies (frequency range = 200 Hz) and voltage outputs. For a single measurement, the oscilloscope cursors are fixed to a voltage (from the set of pairs determined using Eq. 6.7) and the corresponding frequency is set as the frequency of a continuous sine signal in a function generator. The continuous sine signal is applied first; and the amplitude of the continuous sine is increased/decreased until the output voltage from the soil reaches the voltage set on the oscilloscope. Then, random noise signal with an amplitude of 5 % of the amplitude of the continuous sine is added to the input signal using the built-in source of the spectrum analyzer. Once the added input and soil response signals are stable, the spectrum analyzer is run to calculate the transfer function. The resonance frequency and damping ratio from this transfer function corresponds to one loading frequency (frequency of the continuous sine signal). This test is repeated for different frequencies and the shear modulus and damping ratio are plotted against loading frequencies.

Effects of shear strain

The CF methodology can also be used to estimate shear modulus and damping ratio at different shear strains. Instead of using the pairs of frequencies and voltages from Eq. 6.7 , the pair of resonance frequencies and peak output voltages resulting from a full run of the conventional RC technique are used. The process described above for effects of frequency is repeated with this set of pairs and the corresponding shear modulus and damping ratio are plotted against the induced shear strains.

7.6.8.3 Equal strain (ES) technique

The ES method is the method originally used for processing the RC data before the now conventional RC technique was proposed (Hardin 1978). In conventional RC method, the excitation voltage of the burst chirp is constant but the induced strain is not the same for all loading frequencies of the burst chirp.

The conventional resonant column test is performed and the resulting pair of resonance frequency and peak output voltage is used with Eq. 6.7 to generate a set of pairs of frequency and peak output voltage for fixed strain. In a typical test, a continuous sine signal of a particular frequency from the set generated above is applied and the input voltage of this continuous sine is increased/decreased to match the peak output voltage of the soil response. Then, the transfer function is calculated and the magnitude of the transfer function at the frequency of the continuous sine is noted. This procedure is repeated for a variety of frequencies to collect sufficient data using which a transfer function is plotted. The resonance frequency and damping ratio estimated from this transfer function corresponds to strain through which the set of frequencies and peak output voltages were generated above. This process above is repeated for different strains to accumulate a data of shear modulus and damping ratio for different induced shear strains. This process is most accurate amongst the three techniques; however, this method is also the most time consuming.

7.7 Results and discussion

Table 7-2 shows the properties of the soil samples tested in this study. The water content (*w*) was estimated using the oven-dried method but the other properties of the samples are extracted from the site investigation reports of the Beuharnois canal and Outardes river sites (Duguay-Blanchette 2016)**.** There is a significant difference in the water content between the samples obtained from the two sites; the water content of the sample obtained from the Beauharnois canal site is 150% more than those of the samples obtained from the Outardes river site. The void ratio of s4 is also much lower than the void ratios of the samples s1-s3 obtained from the Beauharnois canal site. Although the unit weights of the three samples from Beuharnois are similar, the pre-consolidation

pressure of s3 is more than double that of s1 and s2. The in-situ shear wave velocity information is useful for a rough idea about the frequency effects on the shear wave velocity of soils. The shear wave velocity in the field is estimated from the seismic cone penetration test in which the loading frequencies are less than 10 Hz, which is much lower than the loading frequencies of the resonant column and bender element tests.

Table 7-2: Properties of the soils tested in this study (Duguay-Blanchette 2016a; SM LABO INC. 2014)

Site	Sample	Description	z (m)	z_w (m)	γ_b (kN/m^3)	w (%)	σ_c (kPa)	e	$V_{s\text{-}in}$ (m/s)
Beauharnois	s1	Greenish gray clay with firm consistency	2.4	0.0	15.8	76.7	100	1.94	70
	s2		6.8		15.4	77.3	100	2.11	100
	s3	Brownish-pinkish gray clay with fragments	10.9		17.8	76	225	1.67	150
Outardes	s4	Silty clay with sand traces	14.9	0.0	18.5	27.1	395	0.74	NA

d_p: depth, γ: unit weight, w: water content, σ_p': pre-consolidation pressure, $V_{s\text{-}in}$: in-situvelocity using SCPT, e: void ratio, z_w: water table

7.7.1 Effects of shear strain

Fig. 7-13 shows the normalized shear modulus G/G_{max} (G_{max} is the maximum shear modulus) of the four samples as a function of the induced shear strain at four different confinements. The figure compares the reduction of the shear modulus of these different samples that have different values of the ratio k between the effective confinement stress (σ'_c) and pre-consolidation stress (σ'_p) shown in the figure. The figure also shows the range of modulus reduction curves from the laboratory tests of Dobry and Vucetic (1987). Note that the confining stresses of 50 kPa and 100 kPa are lower than or equal to the pre-consolidation stresses of the four samples, while the confining stress of 200 kPa is above the pre-consolidation stresses of s1 and s2, and below those of s3 and s4. The confining stress of 400 kPa is above the pre-consolidation stress of all the four samples. The three samples from the Beauharnois site (s1-s3) show a similar trend of modulus reduction at all the confinements while s4 degrades faster than the samples from Beauharnais site. This difference is expected because of the low void ratio of s4 (Dobry and Vucetic 1987). Moreover, Beauharnois site clays are more structured and sensitive as compared to the Outardes site clays. However, this difference in modulus reduction rate decreases with increase in the confining stress.

The induced shear strain in all the samples reduces as the confining stress on the sample is increased. The maximum induced strain among all the samples is in s1 — 1.1% for σ'_o = 50 kPa and 0.1% for σ'_o = 400 kPa. This difference is expected because increase in confining stress reduces the modulus reduction at a particular strain (Santamarina et al. 2001). Amongst the three samples of Beaharnois site, the induced shear strain is the maximum for s1 considering all samples because s1 was extracted from the shallowest depth with the least in-situ stresses. At σ'_o = 400 kPa, the shear modulus of both s1 and s4 at all strains are similar; the difference is in the modulus reduction rate which is faster of s4.

All the four samples show that the modulus reduction curves mostly lie within the range of the laboratory results of Dobry and Vucetic (1987). The sample s4 is on the lower end of the Dobry and Vucetic range of curves while s1-s3 are on the higher end of the range. This means that the samples s1-s3 will have more site amplification than s4 because s1-s3 maintain linearity for larger strain values than s4 (Dobry and Vucetic

1987). The reason sample s4 exhibits nonlinearity at smaller strain values is because of the low void ratio. The linearity of soft clays increases with increase in void ratio (Dobry and Vucetic 1987). At 50 kPa, the modulus reduction behavior of samples s1-s3 are closer to those of the Leda clay samples tested by Anderson and Richart (1976).

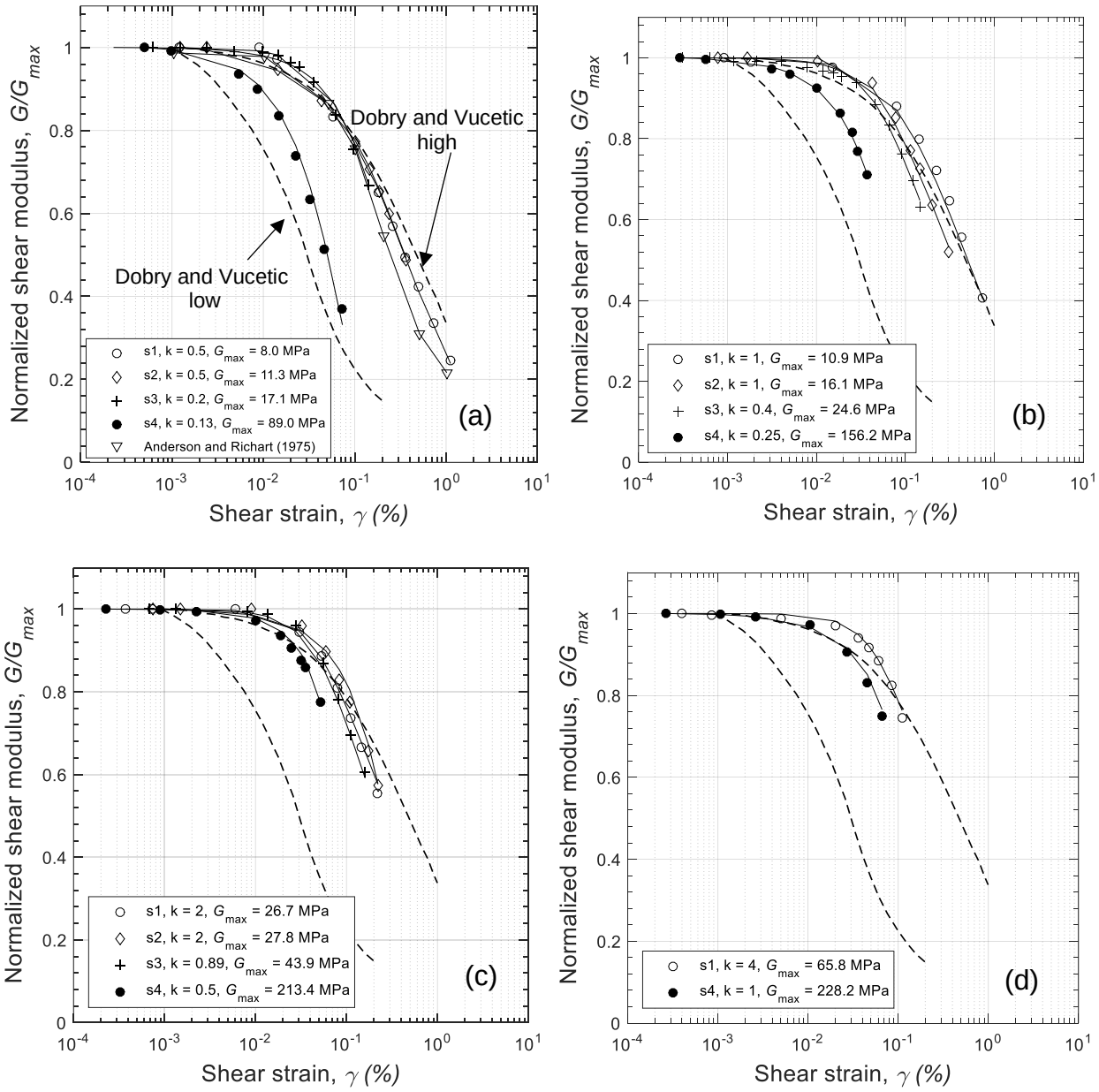

Fig. 7-13: Normalized shear modulus versus shear strain for different samples at confining stresses of (a) 50 kPa, (b) 100 kPa, (c) 200 kPa and (d) 400 kPa (k = σ'_o/σ_c)

Fig. 7-14 shows the shear modulus, normalized shear modulus and damping ratio versus induced shear strain of the sample s1 at four different confining stresses σ'_o. The shear modulus ranges from a very low value of 2 MPa at σ'_o = 50 kPa to 66 MPa at σ'_o = 400 kPa. This result shows that at σ'_o = 50 kPa, the sample s1 is in a rather dangerous state because of its extremely low stiffness. The normalized shear modulus plot shows that the slope of the modulus reduction curves corresponding to σ'_o = 50, 200, and 400 kPa are closer to each other than the slope of the modulus reduction curve corresponding to σ'_o = 100 kPa

The maximum induced shear strain of s1 reduces with increase in confinement, as is expected, because the increased confinement makes it difficult for the soil particles to displace. The shear modulus and damping ratio plots show that the lowest value of the induced strain decreases from 0.001% to 0.0003% as the confinement is increased from 50 to 400 kPa. While the highest value of the induced strain decreases from 1.87 to 0.11 %.

The damping ratio of s1 ranges from 1.6 to 8% over the confinement range of 50 to 400 kPa. The damping ratio of s1 at low strains (10^{-3}-10^{-2}%) for all confinements is about 2%. The damping ratio increases with increase in strain, but the difference in the damping ratios at different confinements is about 2% for strains greater than 10^{-1}%.

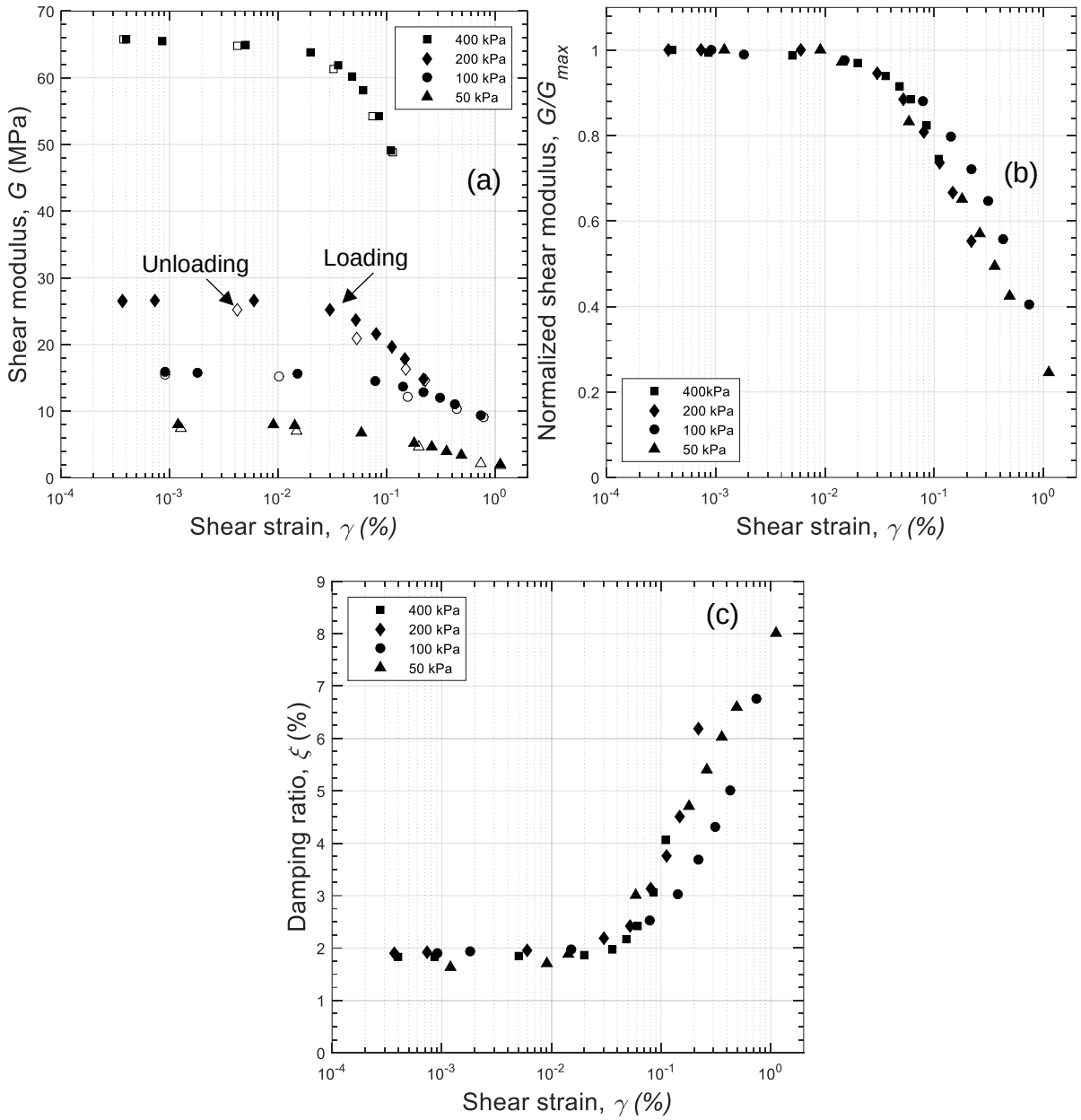

Fig. 7-14: (a) Shear modulus (MPa), (b) Normalized shear modulus and (c) Damping ratio (%) against the induced shear strain of s1 at different confinements

Fig. 7-14 also shows the shear modulus versus shear strain for the unloading stage at different confining stresses. The unloading shear modulus at all strains and all confinements is less than that of the loading stage because of the modulus reduction

effects experienced by the sample in the unloading stage. The difference between the loading and unloading shear modulus decreases as the confining stress increases.

A similar behavior is observed for the samples s2 and s3. However, because these samples were extracted from greater depths, the shear modulus and damping ratio ranges of these samples are different than those of s1. The shear modulus and damping ratio ranges of s2 are 5.3-28 MPa and 0.7- 6.8%, respectively (for σ'_o = 50-200 kPa), over the shear strain range of 0.00075-0.38%. The shear modulus and damping ratio ranges of s3 is 11-44 MPa and 0.73-3.7%, respectively (for σ'_o = 50-200 kPa), over the shear strain range of 0.0003-0.16%.

Fig. 7-15 shows the shear modulus, normalized shear modulus and damping ratio of sample s4 as functions of the shear strain for applied confining stresses of 50, 100, 200, and 400 kPa. The shear modulus and damping ratio ranges of s4 are 32-228 MPa and 1.04-17%, respectively (for σ'_o = 50-400 kPa), over the shear strain range of 0.0002-0.07%. The lower end of the strains induced in the sample reduces as the confining stress is increased. The slopes of the modulus reduction and damping ratio curves decrease with increase in confinements at higher induced shear strains. The shear modulus at a strain of 0.07% increased by 35% while the damping ratio decreased by 14% as the confining stress increased from 50 to 400 kPa.

The unloading results of shear modulus show that the shear modulus degrades more as the confinement increases. The maximum difference between the loading and unloading shear moduli is about 2% at σ'_o = 50 kPa and it increases to about 4 % at σ'_o = 400 kPa.

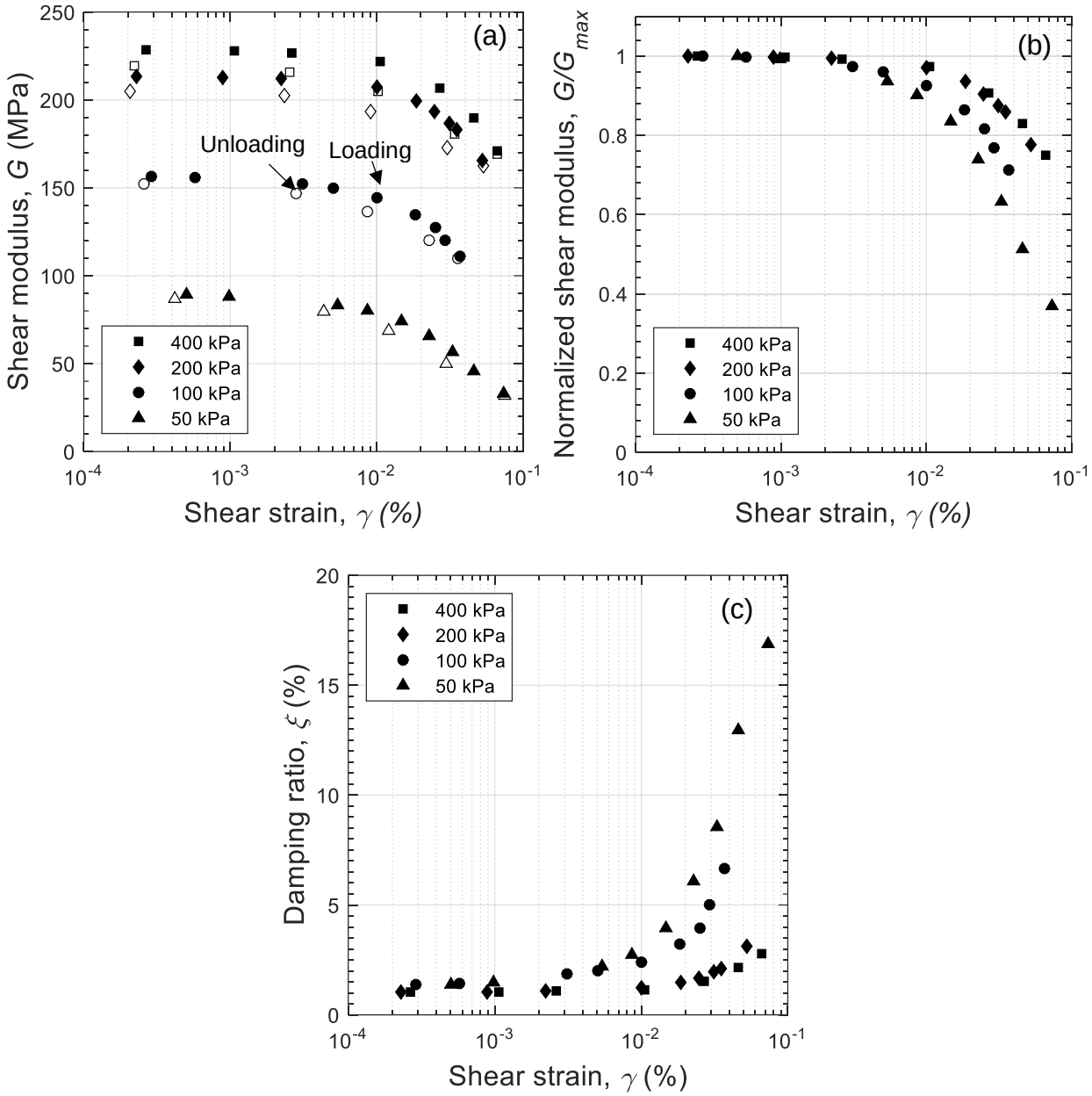

Fig. 7-15: (a) Shear modulus, (c) Damping ratio, and (c) Norm. shear modulus against the induce shear strain of TM4a at different confinements

7.7.2 Effects of confinement

The shear wave velocity of soils (V_s) and isotropic effective confining stress (σ'_o) in soil are related through a power-law expressed as (Santamarina et al. 2001)

$$V_S = \alpha(\sigma'_o)^{\beta} \qquad 6.8$$

where α and β are power law parameters. The parameter α is related to the packing of soil particles while β is related to the contact behavior between the soil particles. For dense sands, over-consolidated clays, and soft rocks, the parameter α is relatively high and the exponent β is relatively low. For loose sands, normally consolidated clays, and high plasticity clays, the parameter α is relatively low and the exponent β is relatively high.

The samples s2 and s3 are tested at confining stresses of 50, 100, and 200 kPa; and the samples s1 and s4 are tested at an additional confining stress of 400 kPa. The shear wave velocities in these samples are estimated using the resonant column (RC) test and the bender element (BE) test. Fig. 7-16 shows the effects of confinement on the shear wave velocity of these soil samples estimated from RC tests. The experimental data is fitted with the power law equation given by Eq. [6.8] with values of the power-law parameters indicated for each soil sample in the figure. Fig. 7-17 shows the V_s estimated using both RC and BE tests; the solid experimental data points represent the estimated values from the RC test and the hollow data points represent the results from the BE test. The maximum difference between the RC and BE test results is ≈ 15% which occurs for the shear wave velocity of the sample s3 at a confining stress of 200 kPa. These results show that, although the excitation frequency of the BE test is in kHz and the excitation frequency of the RC test ranges between 20 to 220 Hz, the difference in excitation frequency does not significantly affect the shear wave velocity of the soft clay samples. The small difference between the RC and BE techniques can be attributed to the subjective selection of the shear wave because of the *p*-wave interference (see section 6.4.6). The time signals used to estimate the BE V_s are presented in Fig. 7-18

Santamarina et al. (2001) estimated the β value for soft clays to be 0.32; the experimental values of β for s2 and s3 are relatively closer to the values obtained by Santamarina et al. (2001). Note that the coefficient of determination (R^2) for all the power-law curve-fits are greater than 0.95.

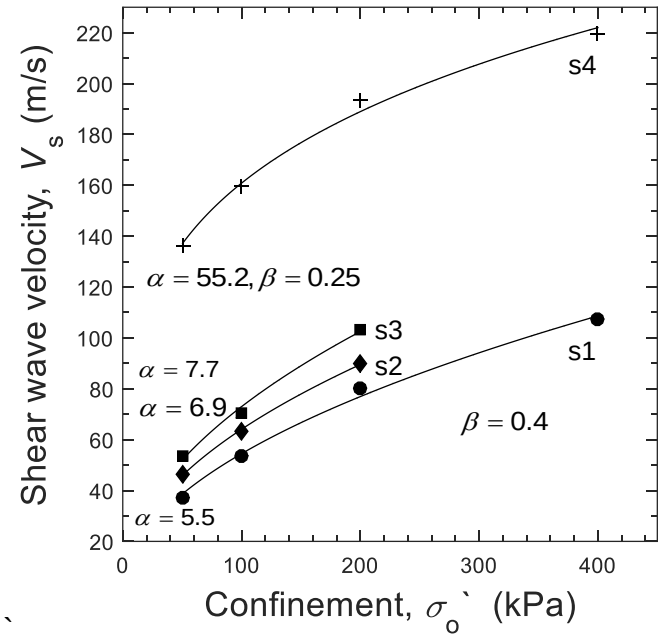

Fig. 7-16: Shear wave velocity versus isotropic effective confining stress of the four Leda clay samples as obtained from resonant column (RC) tests with curve fit of Eq. 6.8 (Note: β = 0.4 for s1, s2, and s3)

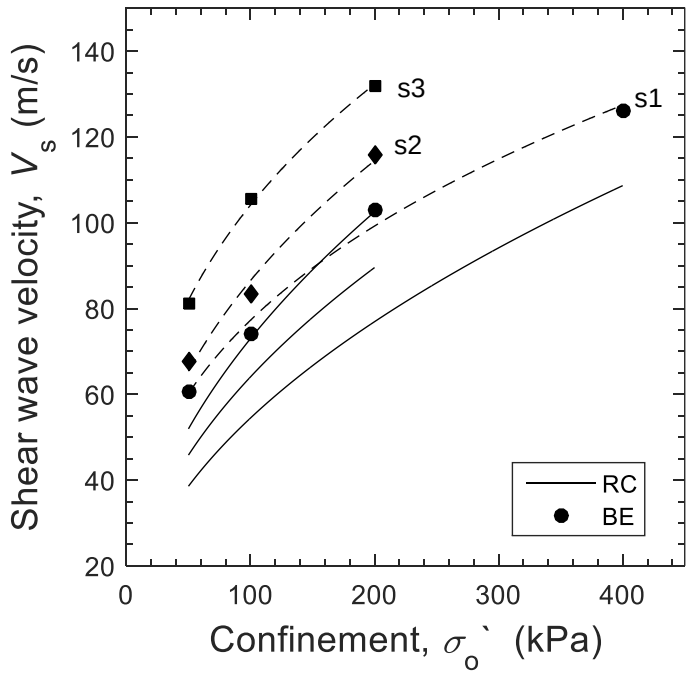

Fig. 7-17: Shear wave velocity versus isotropic effective confining stress of the four Leda clay samples as obtained from resonant column (RC) and bender element (BE) tests

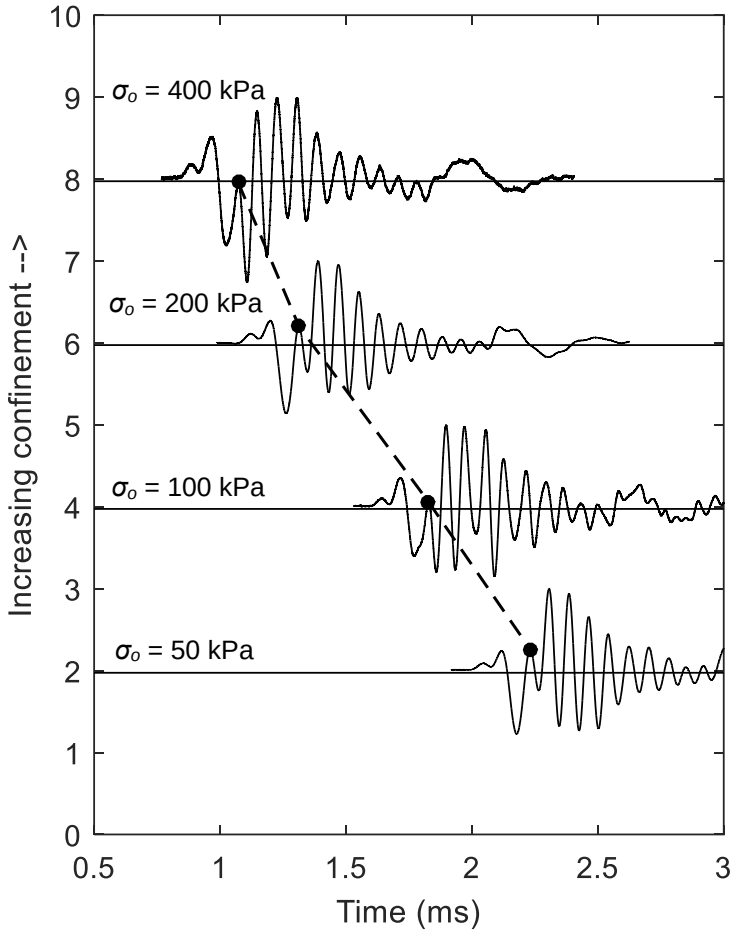

Fig. 7-18: BE time signals for the sample 's1' used to estimate the V_s at different confinements (Note: excitation frequency = 10 kHz)

The shear wave velocity of soils (V_s) is related to the maximum shear modulus (G_{max}) through Eq. 2.20; G_{max} is used in site response analysis which is part of the seismic design process. Therefore, it is interesting to study the relationship between G_{max} and preconsolidation stress (σ_c) of Leda clays. Fig. 7-19 shows the measured G_{max} of the four Leda clay samples as a function of σ_c for different effective confining stresses (σ'_o). The plot corresponding to σ'_o = 400 kPa is not shown because the measurements for two of the four samples are not available. The experimental data is curve-fitted with the exponential equation and a very good match is observed for the plots corresponding to the three confining stresses (R^2 = 0.97).

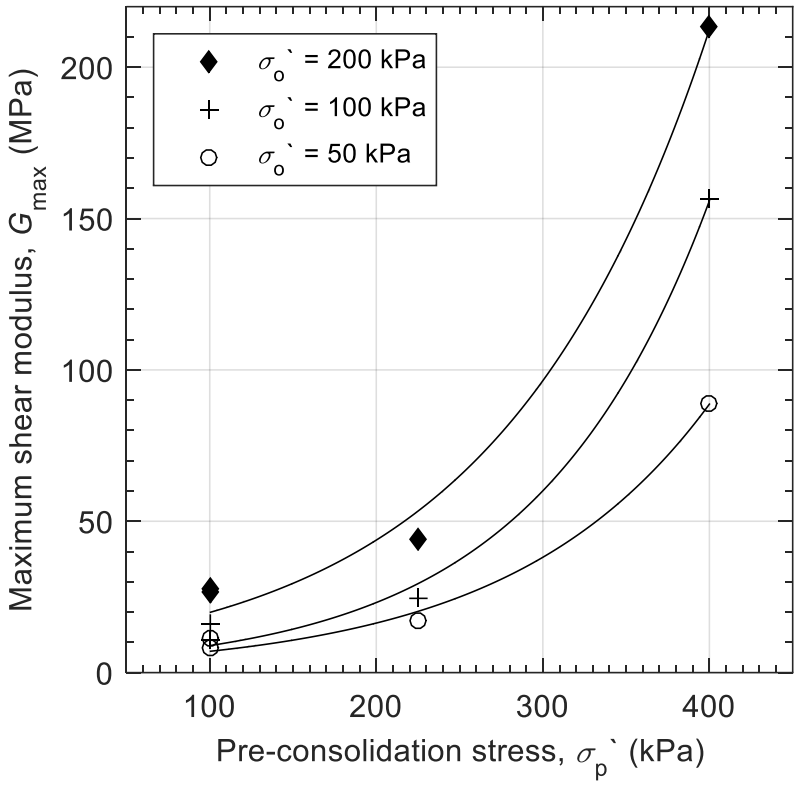

Fig. 7-19: Maximum shear modulus versus pre-consolidation stress for different effective confinement stresses

7.7.3 Effects of shear strain using multiple techniques

The carrier-frequency (CF) and equal strain (ES) methods are used to estimate the shear modulus and damping ratio at different shear strains for the samples tested in this study. Fig. 7-20 shows the variation of shear modulus and damping ratio of s3 at σ'_o = 200 kPa, with the induced shear strain estimated using the three resonant column measurement techniques. The shear modulus and damping ratio of s3 for σ'_o = 200 kPa range from 44 MPa to 20 MPa and from 1% to 5.5%, respectively, over the shear strain range of 0.0007% to 0.16%. For shear strains below 0.013%, the shear modulus and damping ratio from the three measurement techniques are very similar. The difference between the results of the three techniques are observed at mid to high strains; the RC (conventional resonant column) technique shows the largest reduction in shear modulus and largest increase in damping ratio while the CF method shows the least reduction in shear modulus and least increase in damping ratio. The shear modulus and damping ratio

estimated using the ES method are in the range between the corresponding results obtained from the RC and CF methods. These results are similar to those presented by Khan et al. 2008 for dry sands where it was shown that the results obtained from ES are in between the results obtained from RC and CF methods.

The equal strain method would be the most accurate amongst the three methods because the induced shear strain of the sample is better controlled when estimating the transfer function of the sample. The damping ratio of the CF method is lowest because of the low amplitude of the random noise added to the continuous sine input used to estimate the transfer function. The random noise input voltage is deliberately kept low to minimize the effects of the random noise when evaluating the frequency effects on the shear modulus and damping ratio. The low damping ratio also correlates well with the least reduction of the shear modulus at strains higher than 0.013%. However, the percentage reduction in shear modulus over the shear strain of 0.01% to 0.4% (mid to high) is ≈ 42% while the percentage increase in damping ratio over the same shear strain range is 130%.

The changes in both the shear modulus and damping ratio over the analyzed shear strain range correlate well for the three techniques; the shear modulus and damping ratio using the ES method fall in the mid range between the corresponding results of RC and CF methods. This result along with the results of Khan et al. (2008) show that the ES technique is the most suitable technique for evaluating the effects of shear strain on the dynamic properties of soils using the resonant column equipment.

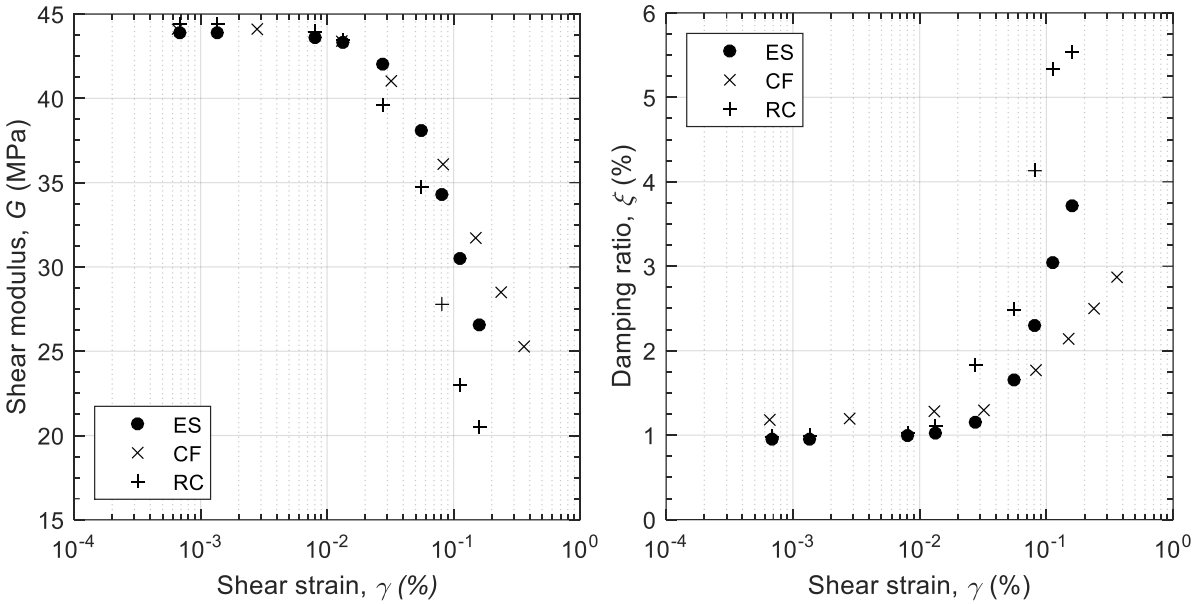

Fig. 7-20: Shear modulus and damping ratio for different shear strains of sample s3 at a confining stress of 200 kPa using different resonant column techniques

7.7.4 Effects of random noise in CF method

Random noise excitation is added to the continuous sine signal in the carrier frequency (CF) method to calculate the transfer function of the soil sample. The amplitude of the random noise signal is very low compared with that of the sine signal because of which the damping ratio of the soil sample estimated using the CF method is the lowest amongst the three techniques, as shown in the previous section. On certain occasions, the random noise signal amplitude has to be increased for noise-free calculations of the transfer functions. However, the aim of the CF method is that the dynamic properties of soil are calculated in response to a single frequency. Therefore, the effect of the energy of the random noise signal have to be minimized for appropriate use of the CF method. In this section, the effect of random noise signal amplitude on the shear modulus and damping ratio of a soil sample (s3, specifically) is evaluated. Fig. 7-21 shows the variation of the shear modulus and damping ratio of s3 with percentage of random noise (RN) in the input signal comprising of a continuous sine and random noise signals. The percentage of the random noise is calculated based on the principle explained next: if a

1 V peak-to-peak continuous sine signal is used, 10% random noise signal means that the peak-to-peak amplitude of the random noise signal is 0.1 V.

Both the plots of Fig. 7-21 show that, at low shear strain ($\gamma = 10^{-4}$ %), the shear modulus and damping ratio of the soil are roughly constant over the percentage range of random noise from 10% to 90%. However, at high shear strain ($\gamma = 10^{-2}$ %), the random noise percentage seems to have a slight effect on the shear modulus and damping ratio. The curve fitted experimental data shows that the shear modulus reduces roughly linearly with a small slope of 0.36 kPa/% of random noise while the damping ratio increases roughly linearly with a slope of 0.0032%/% of random noise. However, the percent change in damping ratio over the total percentage range of random noise is much higher than the percent change in shear modulus. The shear modulus decreases by 0.03% over the 10-90% range of random noise, while the damping ratio increases by 16% over the same range. Thus, the damping ratio is affected more by the increase in random noise energy in the input signal because the transfer function of the soil sample becomes wider around the resonance.

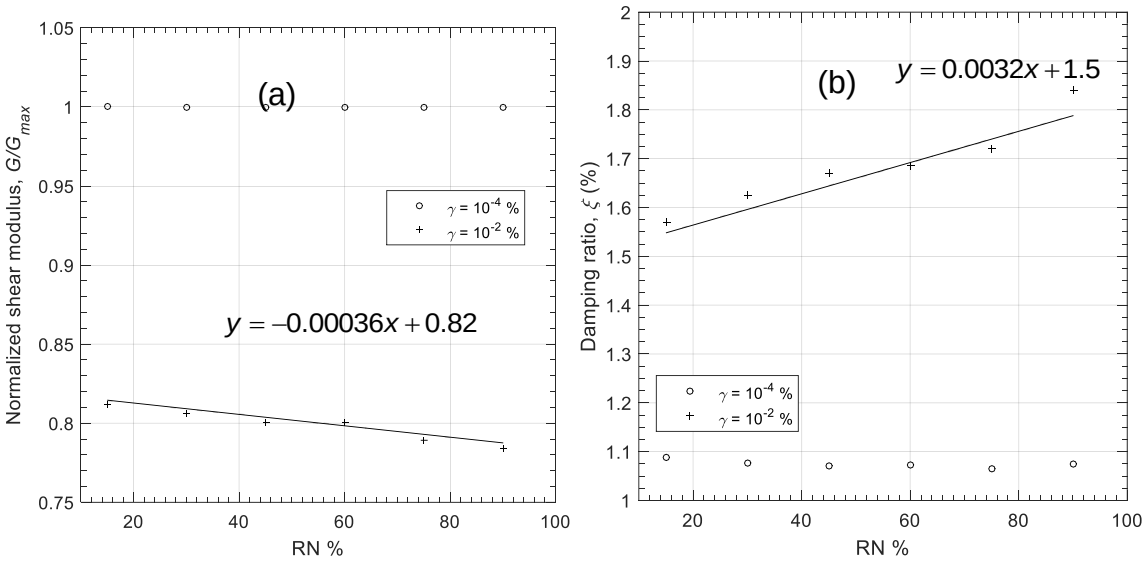

Fig. 7-21: (a) Normalized shear modulus and (b) damping ratio of s3 versus percentage of random noise (RN) in input signal comprising of a continuous sine and random noise signals

7.7.5 Effects of loading frequency

The effect of frequency on shear modulus and damping ratio is evaluated in this study using the carrier frequency (CF) method. The resonance frequency and peak output voltage representing a fixed strain from the conventional RC technique is used to develop a set of frequencies and output voltages. This set of frequencies is then used as central frequency of a continuous sine along with the random noise to calculate the transfer function, from which the shear modulus and damping ratio are estimated. The results of the carrier frequency method applied to sample s3 at a confining stress of 100 kPa are presented in Fig. 7-22. The figure shows the variation of shear modulus and damping ratio with frequency at three shear strain levels. The frequency ranges for these strain levels are: 20 to 90 Hz at low strain ($\gamma = 10^{-3}$ %), 20 to 70 Hz at mid strain ($\gamma = 0.005$ %), and 10 to 38 Hz at high strain ($\gamma = 0.05$ %). Different frequency ranges are used because of the limitations of the RC equipment; achieving higher frequency levels requires very high input voltages (≈ 50 V) which is not possible with the RC setup because the RC setup starts to vibrate and the magnet-coils respond non-linearly to the current. Moreover, the power amplifier gives inconsistent power at frequencies less than 20 Hz for low and mid strains.

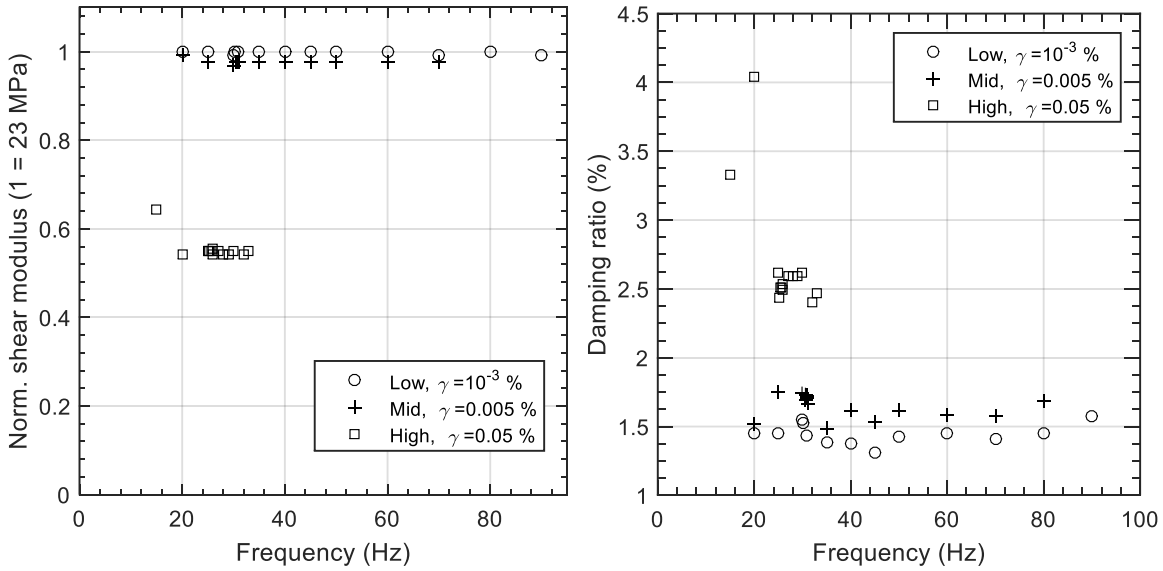

Fig. 7-22: (a) Normalized shear modulus and (b) damping ratio of soil sample s3 at different frequencies

The shear modulus at low and mid strains are approximately constant in the respective frequency ranges tested; the shear modulus at high strain is also constant except at 15 Hz. However, there are small variations observed in the damping ratio of the soil even at low and mid strains. At high strain, the damping ratio varies more significantly than at low and mid strains. There are no clear trends in damping ratio observed at any of the three strain levels. The mild variations in the shear modulus and damping ratio appear to be the result of the effect of the number of load cycles on the soil sample or modulus reduction over time which is observed in the results of the unloading stage in the study of the effect of shear strain.

Similar results are observed for confining stresses of 50 kPa and 200 kPa and with the soil samples s1 and s2. These results suggest that the loading frequency of range 10-100 Hz does not have a significant effect on the shear modulus and damping ratio of the soil. This is a tentative conclusion reached with the carrier frequency method applied to the Leda clay samples. A thorough study with different types of soil samples such as dry and saturated sands and stiff clays has to be performed to evaluate the accuracy and reliability of the carrier frequency method.

7.7.6 Effects of loading cycles

A continuous sine signal along with the random noise excitation with an amplitude of 5% of the continuous sine signal is used to evaluate the effect of number of loading cycles on the shear modulus and damping ratio of Leda clay. The soil sample s3 is tested for this purpose at a confining stress of 200 kPa. Fig. 7-23 shows the variation of shear modulus and damping ratio with the number of cycles of the continuous sine signal. The shear modulus is constant at all strain levels with the number of cycles up to 60,000. The damping ratio is also constant with the number of cycles at low strain level; however, the damping ratio varies slightly at mid strain level and fluctuates significantly in an irregular manner at high strain level. There is no clear trend in the variation of the damping ratio

with the number of cycles; these variations can be attributed to the modulus reduction, which is observed in the results related to the effect of frequency as well.

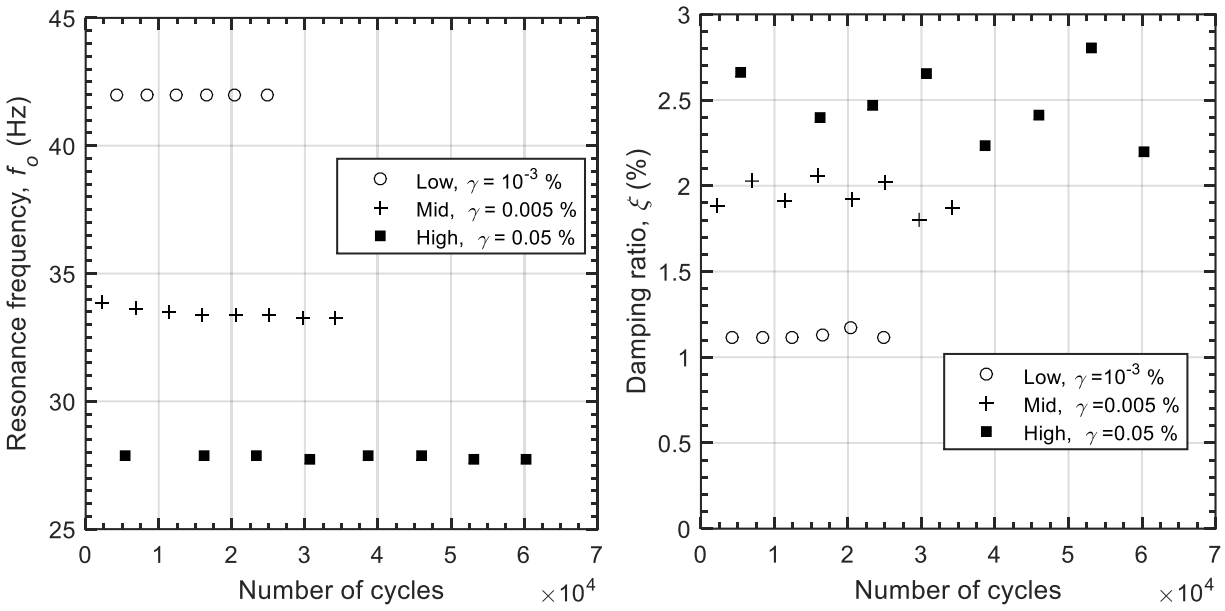

Fig. 7-23: (a) Resonance frequency and (b) damping ratio of sample s3 as functions of the number of cycles of a continuous sine signal

7.8 Conclusions

Marine silts and Leda clay are known to amplify ground motions to dangerous levels even if the earthquakes are of low intensity. Previous case studies related to these types of soil, as observed in Mexico City (Celebi et al. 1987) for example, have shown that the ground motion intensity can be amplified by up to five times. Despite this vulnerability of the marine silts and Leda clay, the dynamic response of these types of soils, is not understood well. The objective of the present study was to advance the understanding of the small-strain dynamic behavior of Leda clay. Small-strain dynamic behavior of soils is characterized by the shear modulus, damping ratio, and shear wave velocity of soils

The sample s4 from Outardes river site has a much higher preconsolidation pressure than all the three samples s1-s3 from Beauharnois canal site.. The initial void ratio of s4 is much lower, i.e., 0.74 compared with the void ratios of 1.6-2.11 of the samples s1-s3. These properties suggest that the sample s4 is much stiffer than the samples from the Beauharnois canal site.

The results from the effect of shear strain show that, at a confining stress of 50 kPa, the rate of modulus reduction of s4 is the maximum among the four samples. Similar observations were made for all the cases with different confining stresses; however, this difference in the modulus reduction rate decreases as the confinement increases. The modulus reduction curves at middle to high strains for the three samples s1-s3 obtained from Beauharnois site are very similar.

As expected, the stiffness range of s2 is lowest amongst the samples s1-s3, i.e., 2-9 MPa for a confining stress of 50 kPa, 9-15 MPa for a confining stress of 100 kPa, and 15-28 MPa for a confining stress of 200 kPa. The damping ratio of s1 ranges from 1.6 to 8% over the confining stress range of 50 to 400 kPa; this damping ratio is highest amongst the samples from the Beauharnois canal site.

The study of effects of confinements shows that the β exponents of the velocity-stress power-law relationship of the different samples are s1 = 0.4, s2 = 0.36, s3 = 0.3, and s4 = 0.25; these results agree to the hypothesis that normally consolidated and loose soils have a higher β exponent while over-consolidated and dense soils have lower β exponent (Santamarina et al. 2001).

The study of effects of shear strain using multiple techniques shows that the ES method results fall in the mid-range between the results of RC and CF methods. This result is expected because the shear modulus and damping ratio estimated with the ES method correspond to the actual induced strain of the soil sample because the strain remains constant for all frequencies. Damping ratio from the CF method is the lowest amongst the three methods at mid to high shear strains because of low amplitude random noise used for calculating the transfer function.

The loading frequency in the range of 10 to 100 Hz does not significantly affect the shear modulus and damping ratio of the Leda clay for the shear strain range of 10^{-3}-0.05%. For strains around 0.05%, there are irregular variations in shear modulus and damping ratios; these variations can be attributed to the modulus reduction of the soil sample rather than the effects of loading frequency. These reduction effects are also observed in the study on the effect of loading cycles on shear modulus and damping ratio.

8 Conclusions and future research

8.1 Conclusions

A reliable seismic design is important to minimize the large-scale losses caused by earthquakes. Evaluation of the low-strain dynamic behavior of soils using properties such as shear modulus (wave velocity) and damping ratio is a requirement in modern seismic design. These low-strain dynamic properties are mainly measured using laboratory procedures such as bender element (BE) and resonant column (RC) tests. BE test is a widely used and simple-to-operate laboratory test for measuring V_s. RC test is an ASTM standard test widely used for measuring shear modulus and damping ratio of the soil at strains between 10^{-6} and 10^{-4}.

BE and RC have limitations which reduce the accuracy of the test results which in turn reduce the reliability of the seismic design. In addition, the loading frequency range of seismic loads (0.1-10 Hz) (Shibuya et al. 1995) is different from that of BEs (e.g. 1-15 kHz) and RC device (e.g. 20-200 Hz) (Lee and Santamarina 2005; Meng and Rix 2003). There is no established guidance on the effects of loading frequency on the dynamic properties of soils.

The main objectives of this study were to better understand the BE-soil sample interaction which will provide the basis for developing a reliable standard for BE testing; and to verify the BE test results using the standard RC device. A major limitation in BE testing is that there is no standard procedure mainly because the BE-soil sample interaction is not well understood. In RC testing, the dynamic properties cannot be evaluated simultaneously as function of frequency and strain. In a typical narrow-band excitation (e.g. sine sweep, random noise), the induced shear strains are different at each frequency component. In addressing these and other limitations, several important insights and advancements in BE-soil sample interaction are achieved as are listed below:

- The measurements of the actual transmitter vibrations show that the transmitter response inside the soil specimen is significantly different from the input voltage. This result raises questions on the reliability of the BE test analysis using frequency domain methods because these methods assume that the transmitter response has the same shape as the input excitation.
- The evaluation of the effects of input excitation on the transmitter response in air shows that the maximum displacement of the transmitter response to a square input pulse is 50 % more than that of the responses to step and sine pulses. The square and step input pulses cause greater participation of the higher modes in the transmitter response than the sine input pulse. The simulations of the actual transmitter response to sine and square input pulses also corroborate the conclusion that the square pulse excites higher modes more than the sine pulse.
- Transmitter responses measure in liquids show that a 50 % increase in density causes a decrease in first mode resonance frequency (f_1) by about 12 % and an increase in first mode damping ratio (ξ_1) by about 95 % for the range medium density considered in this study (0.8 – 1.3 g/mL). The first mode resonance frequencies of the transmitter in liquids match very well with the corresponding frequencies obtained from a theoretical equation with a maximum difference of 3.5%. The damping ratio of the first two modes increase exponentially with increase in the mass density of liquids; this result is also in agreement with the findings in the literature. The first resonance frequency and damping ratio of the transmitter inserted into liquids have a power-law relationship with the Reynolds number of the liquids.
- Three modes of vibrations of the transmitter in air are identified from the transfer function of the transmitter calculated using a sine-sweep; their natural frequencies are 9.8 kHz, 27.5 kHz, and 47.2 kHz, and the corresponding damping ratios are 2.9 %, 4.1 %, and 5.9 %. Transfer function of the transmitter inside the soil showed that the transmitter modal properties changed significantly as expected. BE measurements in soil and oil show that the time delay between input excitation and T_x response is not constant but it decreases with the increase in frequency. This result also explains why frequency-based methods tend to work better at higher frequencies.

- Mode shapes of the transmitter show that the BE vibrates as a cantilever plate inside a soil specimen; however, the first mode of the transmitter in air and inside the liquids is a cantilever beam mode. This result is the reason for inapplicability of the theoretical resonance frequency equation to predict the resonance frequencies of the second mode of vibration (and beyond) of a transmitter. This result significantly affects the reliability of BE test results because the assumption of the BE behaving as a cantilever beam is very critical in the interpretation of BE test results. The first three mode shapes of the transmitter in air and in liquids are close to those of a cantilever plate; the presence of a liquid does not affect the mode shapes of the transmitter, which is in agreement with the related results available in the literature. The first three mode shapes of the transmitter in soils under different vertical stresses show that the participation of higher modes and mode coupling increase as the applied vertical stress increases. The peak values of the second and third mode shapes are 0.7% and 2% of the first mode peak coordinate for the case of soil specimen without applied stress; these values increase to 24% and 16%, respectively, under the applied vertical stress of 41 kPa.
- Measurements of the transmitter response inside the soil show that a 35 % increase in first resonance frequency is observed when the applied vertical stress in soil specimen is increased from 0 to 406 kPa; the corresponding increase in damping ratio is 30%. These results are key in understanding the BE-soil sample interaction because the frequency of vibration of the transmitter governs the wave length of the shear wave generated from the transmitter and affects the estimation of V_s. The wave length of the shear waves must be, at the maximum, equal to the length of the soil specimen for a good signal-to-noise ratio; the recommended wave-length for the optimum signal-to-noise ratio is less than one-fifth the length of the soil specimen, and this required to avoid near-field effects in the BE test. The damping ratio results of this study have highlighted the possible reasons for unsuccessful attempts on the estimation of damping ratio of soil specimens using the BE test.

- There is a significant compressional (*p*) wave interference in the bender vibrations which must be carefully evaluated for the correct interpretation of the results. Reflections from the transmitter anchor, the acrylic tube wall and other parts of the system also affect the transmitter and receiver responses.
- The *p*-wave interference increases with increase in confinement and input frequency. This interference masks the shear wave arrivals which can cause a 25 % error in shear wave velocity estimations. The results from the RC and BE tests on fused quartz confirm the conclusion that high input frequencies enhance the generation of *p*-waves
- The *p*-wave arrival can be better identified by using an excitation with input frequency greater than 50 kHz. Reliable estimate of shear wave velocities can be obtained by first evaluating the compressional wave velocity and using typical Poisson ratios of the soil samples.
- The receiver response measured from the laser is very similar to the BE-output electrical voltage. Time signals and the frequency spectra of the two signals showed that similar frequency components are present in both the signals, and the amplitude of the output electrical voltage is ≈ 5 times smaller than amplitude of the receiver response measured using laser at the peak of the receiver. These results show that the relationship of Leong et al. (2005) is not only valid for the maximum displacement, but for the whole-time signal.
- The maximum bender displacement is linearly related to the input voltage amplitude in air, liquids of different mass density and in the transparent soil sample because the maximum displacement in a piezo-electric transducer is proportional to the applied voltage. The slope of this linear relationship decreases as the mass density of the material surrounding the bender increases. This experimental result also verifies a theoretical relationship between the bender displacement and the voltage amplitude proposed by Leong et al. (2005). This theoretical relationship linearly relates the bender displacement with the voltage amplitude; the bender dimensions and a piezo-electric constant act as constants.
- Comparison of results from BE and RC tests at different confinements showed that there is a 15 % difference between the shear wave velocities from BE and RC tests; this difference might be due to the masking of shear wave arrivals by the

compressional wave arrivals. BE tests on Leda clays showed that using high input frequencies enhance the generation of *p*-waves; hence, easier to identify *p*-wave interference

- The stiffest Leda clay sample showed the highest degradation with increasing shear strain; this result is in agreement with sensitive clay behaviour documented in the literature
- The study of effects of confinements on the four Leda clay samples agree to the hypothesis that normally consolidated and loose soils have a higher β exponent while over-consolidated and dense soils have lower β exponent.
- The study of effects of shear strain using multiple techniques shows that the ES method results fall in the mid-range between the results of RC and CF methods. This result is expected because the shear modulus and damping ratio estimated with the ES method correspond to the actual induced strain of the soil sample because the strain remains constant for all frequencies. Damping ratio from the CF method is the lowest amongst the three methods at mid to high shear strains because of low amplitude random noise used for calculating the transfer function.
- While RC tests at frequencies below 100 Hz showed no effect of loading frequency on shear modulus and damping ratio, BE tests at frequencies centred at 12kHz showed a 15% change in wave velocity; which could be attributed to the loading frequency or to the complex interaction of between p-waves and s-wave in BE testing. Loading frequency in BE tests does have a significant effect in the results, up to 40% error in the estimation of s-wave velocity, as the interaction between p-waves and s-waves increases with frequency

8.2 Future research

The novel experimental setup used in this study will be important in the process of bender element (BE) test standardization. Few areas where further research is required are listed below:

- The induced vertical stress estimated in this study is based on the Boussienesq theory. This theory might not be accurate to estimate the actual vertical stress inside the soil. Moreover, the effects of isotropic confinement, and not the vertical stress, on the actual bender behavior will be critical in characterizing the BE-soil sample interaction. A mechanism in which the actual confinement pressure inside the soil can be estimated/measured will be important to develop a more comprehensive understanding of the effect of confinement pressure. Pressure or strain transducers can be fitted close to the benders inside the transparent soil for this purpose.
- The numerical bender responses in liquids of different mass densities and soil with different confinements have to be studied to determine if the numerical model that is developed in this study is able to predict the transmitter response in these different media.
- The transmitter and receiver responses in soil with different confinements needs further research. The target from this research would be to estimate the shear wave velocity of fused quartz using the actual transmitter and receiver responses inside the transparent soil.
- Perform a numerical study with both transmitter and receiver inside different media.
- Conduct tests on leda clay samples present at the University of Waterloo to establish statistical reliability of the low-strain dynamic properties of leda clays and develop a firm understanding of the low-strain dynamic behavior of soft clays found in Quebec, Canada.
- A thorough study of the carrier frequency and equal strain methods with different soil samples to establish the reliability of these methods to evaluate loading frequency and shear strain effects on the low-strain dynamic properties of soils.

References

1. Alvarado, G., & Coop, M. R. (2012). "On the performance of bender elements in triaxial tests." *Géotechnique,* 62(1), 1.

2. Arroyo, M., Wood, D. M., Greening, P. D., Medina, L., & Rio, J. (2006). "Effects of sample size on bender-based axial G0 measurements." *Géotechnique,* 56(1), 39-52.

3. Arroyo, M., Medina, L., & Muir Wood, D. (2002). "Numerical modelling of scale effects in bender-based pulse tests." *NUMOG VIII, Pande, GN & Pietruszczak, S.(Eds),* , 589-594.

4. Arroyo, M., Wood, D. M., & Greening, P. (2003). "Source near-field effects and pulse tests in soil samples." *Géotechnique,* 53(3), 337-345.

5. Arulnathan, R., Boulanger, R. W., & Riemer, M. F. (1998). "Analysis of bender element tests." *ASTM Geotechnical Testing Journal,* 21(2), 120-131.

6. Atkinson, C., & de Lara, M. M. (2007). "The frequency response of a rectangular cantilever plate vibrating in a viscous fluid." *Journal of Sound and Vibration,* 300(1-2), 352-367.

7. Avitabile, P. (2001). "Experimental modal analysis." *Sound and Vibration,* 35(1), 20-31.

8. Bouchard, S., Ali, H., LeBoeuf, D., Leroueil, S., & Cascante, G. (2017). Dynamic properties of a sensitive clay deposit. *Landslides in Sensitive Clays* (pp. 167-176) Springer.

9. Brignoli, E., Gotti, M., & Stokoe, K. H. (1996). "Measurement of shear waves in laboratory specimens by means of piezoelectric transducers." *ASTM Geotechnical Testing Journal,* 19(4), 384-397.

10. Brocanelli, D., & Rinaldi, V. (1998). "Measurement of low-strain material damping and wave velocity with bender elements in the frequency domain." *Canadian Geotechnical Journal,* 35(6), 1032-1040.

11. Camacho-Tauta, J., Ali, H., Cascante, G., & Viana da Fonseca, A. (2016). "Experimental and Numerical Observations of the Frequency-Domain Method in Bender-Element Testing." *Journal of Geotechnical and Geoenvironmental Engineering,* , 04016096.

12. Camacho-Tauta, J., Cascante, G., da Fonseca, A. V., & Santos, J. (2015). "Time and frequency domain evaluation of bender element systems." *Géotechnique,* 65(7), 548-562.

13. Cardoso, J. (1998). "Blind signal separation: statistical principles." *Proceedings of the IEEE,* 86(10), 2009-2025.

14. Cascante, G., & Santamarina, C. (1997). "Low strain measurements using random noise excitation." *Geotechnical Testing Journal,* 20, 29-39.

15. Cascante, G., Vanderkooy, J., & Chung, W. (2005). "A new mathematical model for resonant-column measurements including eddy-current effects." *Canadian Geotechnical Journal,* 42(1), 121-135.

16. Celebi, M., Prince, J., Dietel, C., Onate, M., & Chavez, G. (1987). "The culprit in Mexico City—Amplification of motions." *Earthquake Spectra,* 3(2), 315-328.

17. Cheng, Z., & Leong, E. (2018). "Determination of damping ratios for soils using bender element tests." *Soil Dynamics and Earthquake Engineering,* 111, 8-13.

18. Chon, J. W., Mulvaney, P., & Sader, J. E. (2000). "Experimental validation of theoretical models for the frequency response of atomic force microscope cantilever beams immersed in fluids." *Journal of Applied Physics,* 87(8), 3978-3988.

19. Chu, W. (1963). "Vibration of fully submerged cantilever plates in water." *South-West Research Institute, Technical Report,* (2)

20. Clough, R. W., & Penzien, J. (2003). "Dynamics of Structures. Berkeley, CA, USA: Computers & Structures."

21. Drnevich, V. P. (1967). *Effect of Strain History on the Dynamic Properties of Sand* (Ph.D. Dissertation, University of Michigan 151 p.).

22. Drnevich, V. P., Hardin, B. O., & Shippy, D. J. (1978). "Modulus and damping of soils by the resonant column method." *Dynamic Geotechnical Testing,* 654, 91-125.

23. Duguay-Blanchette, J. (2016a). *Étude Du Comportement Statique Et Cyclique De Deux Argiles Sensibles De L'Est Du Canada,*

24. Duguay-Blanchette, J. (2016b). "Étude du comportement statique et cyclique de deux argiles sensibles de l'Est du Canada."

25. Dyvik, R., & Madshus, C. (1985). Lab Measurements of G_{max} Using Bender Elements. *Advances in the Art of Testing Soils Under Cyclic Conditions,* 186-196.

26. Ezzein, F. M., & Bathurst, R. J. (2011). "A transparent sand for geotechnical laboratory modeling." *ASTM Geotechnical Testing Journal,* 34(6), 590-601.

27. Faria, C. T., & Inman, D. J. (2014). "Modeling energy transport in a cantilevered Euler–Bernoulli beam actively vibrating in Newtonian fluid." *Mechanical Systems and Signal Processing,* 45(2), 317-329.

28. Gohl, W., & Finn, W. (1991). Use of piezoceramic bender elements in soil dynamics testing. *Recent Advances in Instrumentation, Data Acquisition and Testing in Soil Dynamics,* 118-133.

29. Greening, P. D., & Nash, D. F. (2004). "Frequency Domain Determination of G~ 0 Using Bender Elements." *Geotechnical Testing Journal,* 27(3), 288-294.

30. Guzman, I. L., & Iskander, M. (2013). "Geotechnical properties of sucrose-saturated fused quartz for use in physical modeling."

31. Hardin, B. O. (1978). The nature of stress-strain behavior for soils. *From Volume I of Earthquake Engineering and Soil Dynamics--Proceedings of the ASCE Geotechnical Engineering Division Specialty Conference, June 19-21, 1978, Pasadena, California. Sponsored by Geotechnical Engineering Division of ASCE in Cooperation with:* (Proceeding)

32. Hardin, B. O., & Music, J. (1965). "Apparatus for vibration of soil specimens during the triaxial test." *Astm, Stp,* 392, 55-74.

33. Hardin, B. O., & Richart Jr, F. E. (1963). "Elastic wave velocities in granular soils." *Journal of Soil Mechanics & Foundations Div,* 89(Proc. Paper 3407)

34. Haykin, S., & Van Veen, B. (2007). *Signals and systems* John Wiley & Sons.

35. Isenhower, W. M. (1979). *Torsional simple shear/resonant column properties of San Francisco Bay mud* (PhD).

36. Iskander, M. (2010). *Modelling with transparent soils: Visualizing soil structure interaction and multi phase flow, non-intrusively* Springer Science & Business Media.

37. Jovicic, V., Coop, M., & Simic, M. (1996). "Objective criteria for determining Gmax from bender element tests." *Geotechnique,* 46(2), 357-362.

38. Kerschen, G., Poncelet, F., & Golinval, J. (2007). "Physical interpretation of independent component analysis in structural dynamics." *Mechanical Systems and Signal Processing,* 21(4), 1561-1575.

39. Khan, Z. H. (2007). *Dynamic characterization of soils: Effect of frequency and loading amplitude* (PhD. Uinversity of Western Ontario).

40. Khan, Z. H., Cascante, G., & El-Naggar, M. (2008). "Evaluation of the first mode of vibration and base fixidity in resonant-column testing." *ASTM Geotechnical Testing Journal,* 31(1), 65-75.

41. Khan, Z. H., El Naggar, M. H., & Cascante, G. (2011). "Frequency dependent dynamic properties from resonant column and cyclic triaxial tests." *Journal of the Franklin Institute,* 348(7), 1363-1376.

42. Lai, C. G., & Rix, G. J. (1998). *Simultaneous inversion of Rayleigh phase velocity and attenuation for near-surface site characterization* School of Civil and Environmental Engineering, Georgia Institute of Technology.

43. Lai, C. G., Pallara, O., Lo Presti, D. C., & Turco, E. (2001). "Low-strain stiffness and material damping ratio coupling in soils." *Advanced Laboratory Stress–strain Testing of Geomaterials, Balkema, Lisse,* , 265-274.

44. LeBoeuf, D., Duguay-Blanchette, J., Lemelin, J., Péloquin, E., & Burckhardt, G. (2016). Cyclic softening and failure in sensitive clays and silts. *1st International Conference on Natural Hazards and Infrastructure. Chania, Greece,*

45. LeBoeuf, D., Sivathayalan, S., Irfan, M., Cascante, G., & Ali, H. (2017). *Dynamic characterization of soft clays of Eastern Canada; NSERC CRD project.* Unpublished manuscript.

46. Lee, J., & Santamarina, J. C. (2005). "Bender elements: performance and signal interpretation." *Journal of Geotechnical and Geoenvironmental Engineering,* 131(9), 1063-1070.

47. Leissa, A. W. (1969). *Vibration of Plates,*

48. Leong, E. C., Yeo, S. H., & Rahardjo, H. (2005). "Measuring shear wave velocity using bender elements." *Geotechnical Testing Journal,* 28(5), 488.

49. Leroueil, S., Tavenas, F., & Bihan, J. L. (1983). "Propriétés caractéristiques des argiles de l'est du Canada." *Canadian Geotechnical Journal,* 20(4), 681-705.

50. Ljung, L. (1987). "System identification: theoryfor the user." *Englewood Cliffs (Cit.on P.3),*

51. Lo Presti, D., Pallara, O., & Cavallaro, A. (1997). Damping ratio of soils from laboratory and in-situ tests. *Proceedings, 14th International Conference on Soil Mechanics and Foundation Engineering,* 6-12.

52. Meng, J., & Rix, G. (2003). "Reduction of equipment-generated damping in resonant column measurements." *Géotechnique,* 53(5), 503-512.

53. Pallara, O. V., Mattone, M. C., & Lo Presti, D. C. (2008). "Bender elements: bad source-good receiver." *Deformational Characteristics of Geomaterials,* , 697-702.

54. Pennington, D. S., Nash, D. F., & Lings, M. L. (2001). "Horizontally mounted bender elements for measuring anisotropic shear moduli in triaxial clay specimens." *ASTM Geotechnical Testing Journal,* 24(2), 133-144.

55. Polytec. (2013). User's manual of OFV-2570 vibration controller. Retrieved from http://www.polytec.com

56. Popescu, T. D. (2010). "Analysis of traffic-induced vibrations by blind source separation with application in building monitoring." *Mathematics and Computers in Simulation,* 80(12), 2374-2385.

57. Popescu, T. D. (2011). "A new approach for dam monitoring and surveillance using blind source separation." *Int J Innov Comput Inf Control (IJICIC),* 7(6), 3811-3824.

58. Poulos, H. G., & Davis, E. H. (1974). *Elastic solutions for soil and rock mechanics* John Wiley.

59. Pryor, A., & Roscoe, R. (1954). "The velocity and absorption of sound in aqueous sugar solutions." *Proceedings of the Physical Society.Section B,* 67(1), 70.

60. Rainieri, C., Fabbrocino, G., & de Magistris, F. S. (2012). "An integrated seismic monitoring system for a full-scale embedded retaining wall." *Geotechnical Testing Journal,* 36(1), 40-53.

61. Richart, F. E., Hall, J. R., & Woods, R. D. (1970). "Vibrations of soils and foundations."

62. Rio, J. F. M. E. (2006). *Advances in laboratory geophysics using bender elements* (Ph.D.). Available from ProQuest Dissertations & Theses: UK & Ireland. (301675421).

63. Rix, G. J., & Meng, J. (2005). "A non-resonance method for measuring dynamic soil properties." *Geotechnical Testing Journal,* 28(1), 1-8.

64. Sachse, W., & Pao, Y. (1978). "On the determination of phase and group velocities of dispersive waves in solids." *Journal of Applied Physics,* 49(8), 4320-4327.

65. Sader, J. E. (1998). "Frequency response of cantilever beams immersed in viscous fluids with applications to the atomic force microscope." *Journal of Applied Physics,* 84(1), 64-76.

66. Sadhu, A., & Narasimhan, S. (2014). "A decentralized blind source separation algorithm for ambient modal identification in the presence of narrowband disturbances." *Structural Control and Health Monitoring,* 21(3), 282-302.

67. Sadhu, A., Narasimhan, S., & Antoni, J. (2017). "A review of output-only structural mode identification literature employing blind source separation methods." *Mechanical Systems and Signal Processing,* 94, 415-431.

68. Santamarina, J. C., & Fratta, D. (2005). *Discrete signals and inverse problems: an introduction for engineers and scientists* John Wiley & Sons.

69. Santamarina, J. C., Klein, A., & Fam, M. A. (2001). "Soils and waves: Particulate materials behavior, characterization and process monitoring." *Journal of Soils and Sediments,* 1(2), 130-130.

70. Schultheiss, P. J. (1981). "Simultaneous measurement of P & S wave velocities during conventional laboratory soil testing procedures." *Marine Georesources & Geotechnology,* 4(4), 343-367.

71. Seppänen, J., Turunen, J., Koivisto, M., & Haarla, L. (2015). "Measurement based analysis of electromechanical modes with Second Order Blind Identification." *Electric Power Systems Research,* 121, 67-76.

72. Shibuya, S., Mitachi, T., Fukuda, F., & Degoshi, T. (1995). "Strain rate effects on shear modulus and damping of normally consolidated clay." *ASTM Geotechnical Testing Journal,* 18(3), 365-375.

73. Shirley, D. J. (1978). "An improved shear wave transducer." *The Journal of the Acoustical Society of America,* 63(5), 1643-1645.

74. Shirley, D. J., & Hampton, L. D. (1978). "Shear-wave measurements in laboratory sediments." *The Journal of the Acoustical Society of America,* 63(2), 607-613.

75. SM LABO INC. (2014). *Programme d'investigations geotechniques.* (). Quebec:

76. Tallavo, F., Cascante, G., & Pandey, M. D. (2009). "New methodology for source characterization in pulse velocity testing." *ASTM Geotechnical Testing Journal,* 32(6), 537-552.

77. Vazquez, J., Rivera, M., Hernando, J., & Sanchez-Rojas, J. (2009). "Dynamic response of low aspect ratio piezoelectric microcantilevers actuated in different liquid environments." *Journal of Micromechanics and Microengineering,* 19(1), 015020.

78. Viana Da Fonseca, A., Ferreira, C., & Fahey, M. (2009). "A framework interpreting bender element tests, combining time-domain and frequency-domain methods." *Geotechnical Testing Journal,* 32(2), 91-107.

79. Viggiani, G., & Atkinson, J. (1995). Interpretation of bender element tests. *International Journal of Rock Mechanics and Mining Sciences and Geomechanics Abstracts, , 32*(8)

80. Vucetic, M. (1994). "Cyclic threshold shear strains in soils." *Journal of Geotechnical Engineering,* 120(12), 2208-2228.

81. Wang, Y., Lo, K., Yan, W., & Dong, X. (2007). "Measurement biases in the bender element test." *Journal of Geotechnical and Geoenvironmental Engineering,* 133(5), 564-574.

82. Weast, R., Astle, M., & Beyer, W. (1981). *Handbook of Chemistry and Physics* (62nd ed., pp. E-103). Boca Raton, FL: CRC Press.

83. Winkler, K., & Nur, A. (1979). "Friction and seismic attenuation in rocks." *Nature,* 277, 528-531.

84. Yuan, F. (2016). *Structural health monitoring (SHM) in aerospace structures* Woodhead Publishing.

Appendices

Appendix A: Calculation of the moment of inertia of the RC driving plate

Method 1

MOMENTS OF INERTIA FOR RESONANT COLUMN DRIVING PLATEN & TOP CAP

Units involved: grams, centimeters, seconds, radians.

Inertia of the top-bar : $a := 7.12$ $b := 3$ $t := 1.27$

$\rho := 0.00274$ Aluminum density

$$I_{tb} := \left[\frac{1}{12}\cdot\rho\cdot a\cdot b\cdot t\cdot\left(a^2 + b^2\right)\right] \qquad I_{tb} = 0.37 \quad [gr\text{-}cm\text{-}s^2]$$

Inertia of added mass : $a := 8.038$ $b := 5.08$ $t := 1.96$

$m_m := 614$ Mass of calibration mass

$g := 981$

$r_{sh} := 0.182$ Radius of the screw hole

$$V_m := a\cdot b\cdot t - 2\cdot t\cdot\pi\cdot r_{sh}^{\ 2} = 79.625$$ Volume of calibrated mass

$$\rho_m := \frac{m_m}{V_m\cdot g} = 7.861\times 10^{-3}$$

$$I_m := \left[\frac{1}{12}\cdot\rho_m\cdot a\cdot b\cdot t\cdot\left(a^2 + b^2\right) - 2t\cdot\pi\cdot r_{sh}^{\ 2}\cdot 2\right] \qquad I_m = 3.924 \quad [gr\text{-}cm\text{-}s^2]$$

DRIVEN PLATE INERTIA (I)

The inertia of driven plate includes two accelerometers and their connections

I_{tb}= mass polar moment of inertia of top bar of calibration specimen. I_m= mass polar moment of inertia of added mass and screws. I_{tc}= mass polar moment of inertia of the top cap.

Calculation for the aluminum rod ϕ=0.636 $\rho := 0.00274$

$\omega_1 := 50.75 \cdot 2 \cdot \pi$ $\omega_2 := 49.25 \cdot 2 \cdot \pi$

Resonant frequencies without mass (without top cap) and with mass (without top cap) for the aluminum specimen (No.1)

Mass polar moment of inertia for the Driven Plate:

$$I_a := \frac{(I_{tb} + I_m) \cdot \omega_2^{\,2} - I_{tb} \cdot \omega_1^{\,2}}{\left(\omega_1^{\,2} - \omega_2^{\,2}\right)} \qquad I_a = 63.0861 \quad [\text{gr-cm-s}^2]$$

Mass polar moment of inertia of the top cap using resonance frequencies

$\omega_2 := 49.25 \cdot 2 \cdot \pi$ $\omega_3 := 47.69 \cdot 2 \cdot \pi$

Resonant frequencies with mass (without top cap) and with mass (with top cap) for the aluminum specimen (No.1)

$I_{mtb} := I_m + I_{tb} = 4.294$

Mass polar moment of inertia of the top cap

$$I_{tc} := \frac{I_a \cdot \left(\omega_2^{\,2} - \omega_3^{\,2}\right) - I_{mtb} \cdot \left(\omega_3^{\,2} - \omega_2^{\,2}\right)}{\omega_3^{\,2}} = 4.48 \quad [\text{gr-cm-s}^2]$$

Mass polar moment of inertia of the driving plate + top cap

$I_o := I_{tc} + I_a = 67.566$ [gr-cm-s^2]

EVALUATION OF ROOT "a" TO COMPUTE WAVE VELOCITY

I_d = mass polar moment of inertia of the driven plate

Inertia of driving plate + top platten : $I_d := I_o$ [gr-cm-s^2] $g := 981$ [cm/s^2]

Iterative equation for shear wave velocity: $f(\beta, I_{sp}, I_d) := \beta \cdot \tan(\beta) - \frac{I_{sp}}{I_d}$ (1)

Root "a" for Fused quartz:

$W_t := 629.4$ $\phi := 6.681$ $H := 14.266$ $I_{sp} := \frac{1}{2} \cdot \left(\frac{W_t}{g}\right) \cdot \left(\frac{\phi}{2}\right)^2$

$I_d = 67.566$

Initial values to start iteration: $\beta := 0.40$ $I_{sp} = 3.58$

First root of equation (1): $a := root(f(\beta, I_{sp}, I_d), \beta)$ $a = 0.22816$

Total Inertia of sand sample: $I_t := I_d + I_{sp}$ $I_t \cdot 9.81 \cdot 10^{-5} = 6.979 \times 10^{-3}$

$I_{sa} := \frac{1}{2} \cdot (W_t) \cdot \left(\frac{\phi}{2}\right)^2$ $I_{sa} = 3.512 \times 10^3$

$I_{dn} := 981 \cdot I_d$ $I_{dn} = 6.628 \times 10^4$ $a := root(f(\beta, I_{sa}, I_{dn}), \beta)$

$a = 0.22816$

Method 2

MOMENTS OF INERTIA FOR RESONANT COLUMN DRIVING PLATE AND TOP CAP

Units involved: grams, centimeters, seconds, radians.

Inertia of the top-bar : $a := 7.12$ $b := 3$ $t := 1.27$

$\rho := 0.00274$ Aluminum density [gr/cm^3]

$$I_{tb} := \left[\frac{1}{12}\cdot\rho\cdot a\cdot b\cdot t\cdot\left(a^2 + b^2\right)\right] \qquad I_{tb} = 0.37 \quad [\text{gr-cm-s}^2]$$

Inertia of added mass : $a := 8.038$ $b := 5.08$ $t := 1.96$

$m_m := 614$ Mass of calibration mass [gr]

$g := 981$

$r_{sh} := 0.182$ Radius of the screw hole [cm]

$$V_m := a\cdot b\cdot t - 2\cdot t\cdot\pi\cdot r_{sh}^{\,2} = 79.625$$ Volume of calibrated mass [cm^3]

$$\rho_m := \frac{m_m}{V_m\cdot g} = 7.861\times 10^{-3}$$

$$I_m := \left[\frac{1}{12}\cdot\rho_m\cdot a\cdot b\cdot t\cdot\left(a^2 + b^2\right) - 2t\cdot\pi\cdot r_{sh}^{\,2}\cdot 2\right] \qquad I_m = 3.924 \quad [\text{gr-cm-s}^2]$$

DRIVEN PLATE INERTIA (I)

The inertia of driven plate includes two accelerometers and their connections

I_b= mass polar moment of inertia of top bar of calibration specimen. I_m= mass polar moment of inertia of added mass and screws. I_{tb}= mass polar moment of inertia of the top cap.

$\omega_1 := 50.75 \cdot 2 \cdot \pi$ $\omega_2 := 49.25 \cdot 2 \cdot \pi$ Resonant frequencies without mass (with top cap) and with mass (with top cap) for the aluminum specimen (No.1)

Mass polar moment of inertia for the Driven Plate:

$$I_a := \frac{(I_{tb} + I_m) \cdot \omega_2^2 - I_{tb} \cdot \omega_1^2}{\left(\omega_1^2 - \omega_2^2\right)} \qquad I_a = 63.0861 \quad [\text{gr-cm-s}^2]$$

Mass polar moment of inertia of the top cap using resonance frequencies

$\omega_{1w} := 49.313 \cdot 2 \cdot \pi$ $\omega_{2w} := 47.945 \cdot 2 \cdot \pi$ Resonant frequencies with top cap (without mass) and with top cap (with mass) for the aluminum specimen (No.1)

Mass polar moment of inertia of the driving plate + top cap

$$I_{atc} := \frac{(I_{tb} + I_m) \cdot \omega_2^2 - I_{tb} \cdot \omega_1^2}{\left(\omega_1^2 - \omega_2^2\right)} = 67.43 \quad [\text{gr-cm-s}^2]$$

Mass polar moment of inertia of the top cap (for checking only)

$I_{tc} := I_{atc} - I_a = 4.344$ [gr-cm-s^2]

EVALUATION OF ROOT "a" TO COMPUTE WAVE VELOCITY

I_d = mass polar moment of inertia of the driven plate

Inertia of driving plate + top cap : $I_d := I_{atc}$ [gr-cm-s^2] $g := 981$ [cm/s^2]

Iterative equation for shear wave velocity: $f(\beta, I_{sp}, I_d) := \beta \cdot \tan(\beta) - \frac{I_{sp}}{I_d}$ (1)

Root "a" for Fused quartz:

$W_t := 629.4$ $\phi := 6.681$ $H := 14.266$ $I_{sp} := \frac{1}{2} \cdot \left(\frac{W_t}{g}\right) \cdot \left(\frac{\phi}{2}\right)^2$ $I_d = 67.43$

Initial values to start iteration: $\beta := 0.40 \qquad I_{sp} = 3.58$

First root of equation (1): $a := \text{root}(f(\beta, I_{sp}, I_d), \beta) \qquad a = 0.22839$

Total Inertia of sand sample: $I_t := I_d + I_{sp} \qquad I_t \cdot 9.81 \cdot 10^{-5} = 6.966 \times 10^{-3}$

$$I_{sa} := \frac{1}{2} \cdot (W_t) \cdot \left(\frac{\phi}{2}\right)^2 \qquad I_{sa} = 3.512 \times 10^{3}$$

$I_{dn} := 981 \cdot I_d \qquad I_{dn} = 6.615 \times 10^{4} \qquad a := \text{root}(f(\beta, I_{sa}, I_{dn}), \beta)$

$a = 0.22839$

Appendix B: Sample calculations

TYPICAL CURVE FITTING PROCEDURE WITH EQUATION [7.4]

Data file cantaining frequencies in first column and amplitudes of transfer function in second column(Low strain function)

$TF := READPRN("curvefit.txt")$ Damping ratio(from spectrum analyzer) $\xi := 0.00699$

Resonant frequency $f_o := 52.6$ [Hz] $\omega_o := 2\cdot\pi\cdot f_o$ Number of points $N := rows(TF)$ $i := 1..N$

Accelerometer's position from center $Ra := 0.0688$ [m] Distance of magnets from center $Rm := 0.11709$ [m]

Ratios of frequencies to resonant frequencies $\beta 1_i := \frac{TF_{i,1}}{f_o}$ $TFmeasured_i := TF_{i,2}$

$$H(Bl,M,\xi,\beta) := \left| \frac{Bl}{M} \cdot \frac{-Ra\cdot Rm\cdot\beta^2}{\left(1-\beta^2\right)+(2\cdot\xi\cdot\beta)\cdot i} \right|$$

Points to curve fit around resonance

$$n := \left| \begin{array}{l} \text{for } i \in 1..N \\ \quad k_1 \leftarrow i \text{ if } \beta 1_i \le 0.20 \\ \quad k_2 \leftarrow i \text{ if } \beta 1_i \le 1.80 \\ k \end{array} \right.$$

$Np := n_2 - n_1$

$Np = 336$

$M := 1.83 \times 10^{-3}$ $Bl := .09$

To curve fit the measured transfer function the summation of differences at all points should be "0"

$$SEE(Bl,M,c,TrF,\beta,n1,n2) := \sum_{k=n1}^{n2} \left(|TrF_k| - H(Bl,M,c,\beta_k) \right)^2$$

Given

$SEE(Bl,M,\xi,TFmeasured,\beta 1,n_1,n_2) = 0$

$\begin{pmatrix} Bl \\ M \\ \xi \end{pmatrix} := Minerr(Bl,M,\xi)$ $Bl > .00001$ $\xi > 0.0020$

$Bl = 0.0545$ $M = 3.0036 \times 10^{-3}$ $\xi = 0.007262$ $SEE(Bl,M,\xi,TFmeasured,\beta 1,n_1,n_2) = 2.4087$

$Bl := 0.055$ $c := .007262$ $TFfitted_i := H(Bl,M,c,\beta 1_i)$ $SEE(Bl,M,c,TFmeasured,\beta 1,n_1,n_2) = 2.4559$

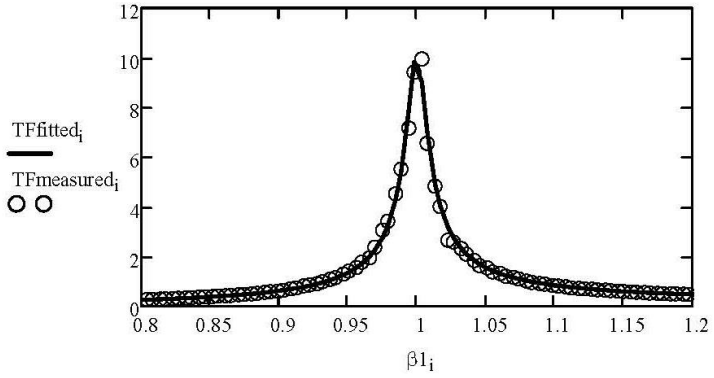

Calculations of induced shear strain

Sensitivity	$Sens := 493.05$	mV/g	$i := 1..200$
Amplification	$Ampl := 20$	dB	
Acceleration due to gravity	$g := 981$	cm /s2	
Voltage factor RMS	$Vrms := 1$		1.13 for random noise 1 for burst chirp
Accelerometer dist from center	$Ra := 6.8$	cm	
Voltage out	$Vout := 317$	mV	
Height of specimen	$Ht := 14$	cm	
Diameter of specimen	$D := 7$	cm	
Resonant frequency	$F_o := 52.6$	Hz	

Shear strain

$$\gamma := \frac{Vrms \cdot D \cdot g \cdot 0.707 \cdot Vout}{\pi^2 \cdot 16 \cdot Ra \cdot Sens \cdot Ht \cdot F_o^2 \cdot 10^{\left(\frac{Ampl}{20}\right)}} \qquad \gamma = 7.50458 \times 10^{-6}$$

EVALUATION OF ROOT "a" TO COMPUTE WAVE VELOCITY

Iterative equation for shear wave velocity:

$$f(\beta, I, I_o) := \beta \cdot \tan(\beta) - \frac{I}{I_o} \qquad (1)$$

Root "a" for a sample

$W_t := 935.67$ $\quad \phi := 7$ $\quad H := 14$ $\quad I_{sp} := \frac{1}{2} \cdot \left(\frac{W_t}{g}\right) \cdot \left(\frac{\phi}{2}\right)^2$

Initial values to start iteration: $\beta := 0.40$

First root of equation (1): $a := root\left(f\left(\beta, I_{sp}, I_d\right), \beta\right)$ $\quad a = 0.2688$

Resonance frequency $f_o := 52.6$

Computing the shear wave velocity

$$V_s := \frac{2 \cdot \pi \cdot H \cdot f_o}{a \cdot 100} = 172.1353 \quad [m/s]$$

Estimation of the shear modulus of the soil sample

$W_t := 935.67 \cdot gm$ $\phi := 7 \cdot cm$ $H := 14 \cdot cm$

Mass of the soil specimen: $W_t = 0.9357\,kg$

Diamater of the soil specimen: $\phi = 0.07\,m$

Height of the soil specimen: $H = 0.14\,m$

Volume of the soil specimen: $V := \frac{\pi \cdot \phi^2 \cdot H}{4} = 5.3878 \times 10^{-4}\,m^3$

Bulk density of the soil specimen: $\rho := \frac{W_t}{V} = 1.7366 \times 10^{3}\,kg \cdot m^{-3}$

$G_{max} := \rho \cdot V_s^{\,2} = 51.4575\,MPa$

Calculation of change in height using LVDT constant

LVDT constant from calibration: $L := 0.1739 \frac{cm}{V}$

Measured initial height: $H_1 := 14cm$

Measured initial voltage: $V_1 := 2.8V$

Measured final voltage: $V_2 := 2V$

Calculated final height: $H_2 := H_1 - (|V_1 - V_2|) \cdot L = 13.8609\,cm$

$\Delta H := H_1 - H_2 = 0.1391\,cm$

Therefore the height reduced by about 0.14 cm

Appendix B: Computation of Fast Fourier Transform (FFT)

A time signal is defined as the variation of any variable with time, for example, the displacement with time. A signal can also represent a variation with space; however, signals with variation in space are out of the scope of this study.

Signal processing techniques are used to extract important information from time signals. Several techniques have been developed over the years. For this study, the technique to extract frequency domain information is most relevant. This technique is called 'Fourier Transform' named after the mathematician Joseph Fourier (1768-1830).

Fourier transform (FT)

FT is a process of decomposing a time signal into weighted sums of sines and cosines of increasing frequencies. The objective is to match sines and cosines of different frequencies and determine the level of presence of those frequencies. Different types of FT can be used in theory depending on if the time signal is discrete or continuous and periodic or non-periodic (Haykin and Van Veen 2007). However, the FT used in digital computers is the Discrete Fourier Transform (DFT). DFT is performed on signals which are discrete and (assumed) periodic.

DFT of a discrete signal *x[n]* is given by the equation

$$X[i] = \sum_{n=0}^{N-1} x[n].e^{-j(i\frac{2\pi}{N}n)} \qquad 7.1$$

where *n* = sample no. of the signal, *N* = total no. of samples of *x[n]* and *i* is the sample no. representing the frequency. Eq. 7.1 shows that both the time signal (*x*) and frequency function (*X*) are discrete. If both time and frequency are continuous functions, then the equivalent of Eq. 7.1 would be

$$X(\omega) = \int_{-\infty}^{\infty} x(t).e^{-j\omega t}dt \qquad 7.2$$

Eq. 7.2 shows that the summation becomes integral in continuous domain; this represents another type of FT.

The exponential in Eq. 7.2 is related to the complex sinusoids through the Euler's identity

$$e^{\pm jx} = \cos x \pm j \sin x \qquad 7.3$$

DFT computes the inner product of signal *x[n]* and the complex sinusoids to determine the level of presence of these complex sinusoids in the signal *x[n]*. The resulting values of *X[i]* are complex numbers as a function of frequencies ranging from *i = 0* to *i = (N-1) (2π / N)*. The magnitude of the complex number at a particular frequency *i (2π / N)* indicates the level of presence of the sinusoid of that frequency; phase angle of that complex number represents the phase of the sinusoid. An example using the programming language MATLAB™ is presented below to explain this concept. The 'fft' command of MATLAB™ computes the magnitude and phase information of any given time signal. Note that MATLAB™ uses the Fast Fourier Transform (FFT) algorithm to compute the DFT of the signal.

Fast Fourier Transform (FFT): executing the DFT formula on a time signal can be extremely slow. Several algorithms have been developed to increase the computing speed to calculate the frequency spectrum of a signal; these are called the Fast Fourier Transform (FFT) algorithms. The most commonly used FFT algorithm is the Cooley–Tukey algorithm where Cooley and Tukey showed that the summation in Eq. 7.1 can be split in two terms; one for the odd numbered values (n = 2m) and one for the even numbered values (n = 2m+1) as shown in Eq. 7.4 below

$$X[i] = \sum_{n=0}^{N-1} x[n].e^{-j(i\frac{2\pi}{N}n)}$$

$$X[i] = \sum_{m=0}^{N/2-1} x[2m].e^{-j(i\frac{2\pi}{N}2m)} + \sum_{m=0}^{N/2-1} x[2m+1].e^{-j(i\frac{2\pi}{N}2m+1)} \qquad 7.4$$

$$X[i] = \sum_{m=0}^{N/2-1} x[2m].e^{-j(i\frac{2\pi m}{N/2})} + e^{-j(i\frac{2\pi}{N})}.\sum_{m=0}^{N/2-1} x[2m+1].e^{-j(i\frac{2\pi m}{N/2})}$$

Eq. 7.4 shows that the summation in Eq. 7.1 is simply split into smaller DFTs. Since the range of i is $0 \leq i < N$ and of m is $0 \leq m < N/2$, the symmetric properties of the summation allow the computations to be reduced by half for each sub-summation in Eq. 7.4. Therefore, the computations reduced from the order of N^2 to the order of M^2 where M =

N/2. This process can continue as long as the sub-DFT has an even valued *M*; this process continues until the computation reduced to the asymptotic limit of the order of *N log N*.

For a signal which does not have the required samples for the Cooley-Tukey algorithm to be executed, MATLAB™ adds the samples of zeros to prolong the signal to a length of a power of 2 (zero-padding, see below).

Consider a time signal *x[n]* given as

$$x[n] = 3\cos(2\pi f_1 n\Delta t + 0.2) + \cos(2\pi f_2 n\Delta t - 0.3) + 2\cos(2\pi f_3 n\Delta t - 2.4) \qquad 7.5$$

where f_1, f_2, and f_3 are 20 Hz, 30 Hz, and 40 Hz respectively and Δt is the time step.

Note that the above signal is composed of three sinusoids with the three frequencies f_1, f_2 and f_3, each with a magnitude and a phase. The amplitudes of these sinusoids are a_1 = 3, a_2 = 1, and a_3 = 2 respectively while the phase angles are φ_1 = 0.2, φ_2 = -0.3 and φ_3 = -2.4 respectively. The DFT computed for the above signal should show the information about the magnitudes and phase angles of the sinusoids in the time signal *x[n]*. Fig. 8-1 shows the time signal *x*[*n*] plotted against the sample numbers; sampling frequency (f_s) is taken to be 1000 Hz and the total time for which the time signal is plotted is 1.5 seconds. f_s is required for evaluating the FFT; and, to avoid aliasing, half of the f_s or the Nyquist frequency (f_{nyq}) (500 Hz in this case) has to be higher than the largest expected frequency in the time signal (40 Hz in our example);

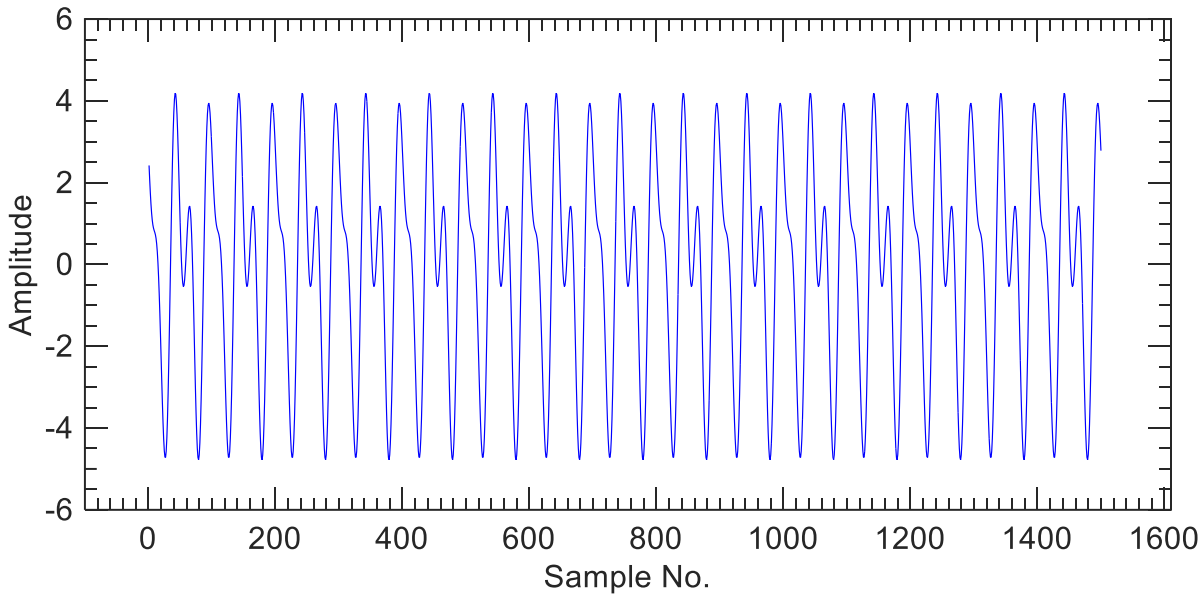

Fig. 8-1: Amplitude of the time signal x[n] against the sample number

Fig. 8-2 shows the FFT magnitude against the frequency bins (frequency samples) of the signal $x[n]$ computed using MATLAB™ fft function. Note that the 'fft' function will result in a complex number; and each complex number has a magnitude and a phase angle. The magnitude of those complex numbers is what is plotted in Fig. 8-2. Moreover, the length of the FFT magnitude is the same as the length of the time signal $x[n]$.

The original signal $x[n]$ is made up of three frequencies; therefore, three peaks are observed on the left and right side of the magnitude spectrum. The three peaks on the right are a mirror side of the left peaks because of the symmetric property of the summation of the DFT discussed above (Eq. 7.4) . Subsequently, only half of the magnitude spectrum is required for further analyses which means that the spectrum up to half the f_s (500 Hz) is needed to be analyzed.

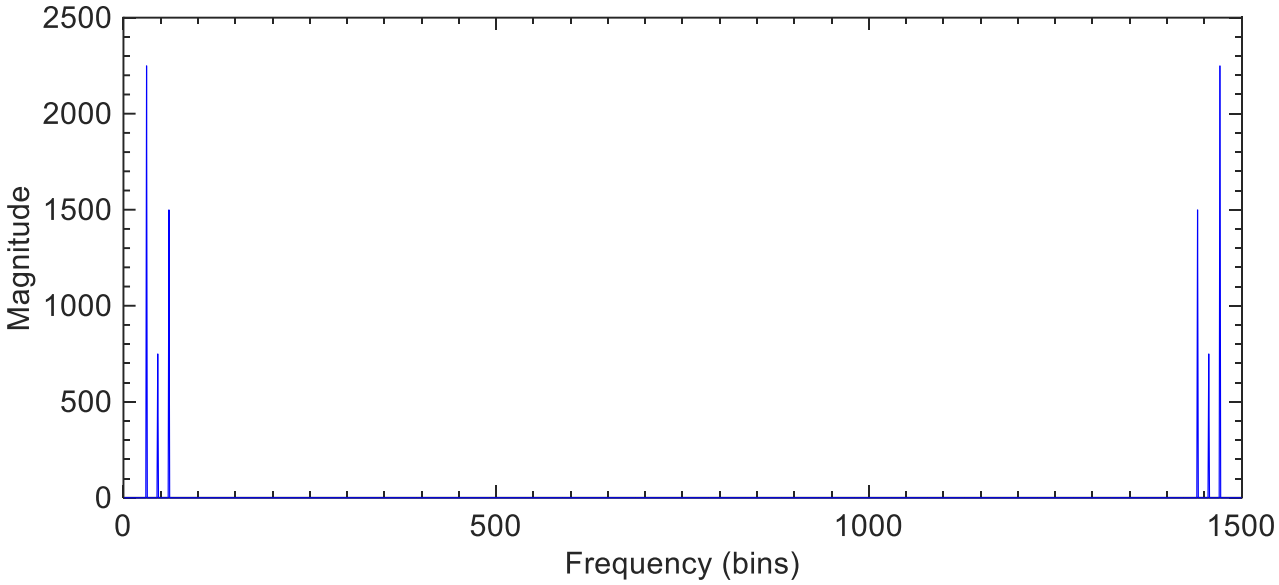

Fig. 8-2: Fast Fourier Transform (FFT) magnitude against the frequency bins (samples)

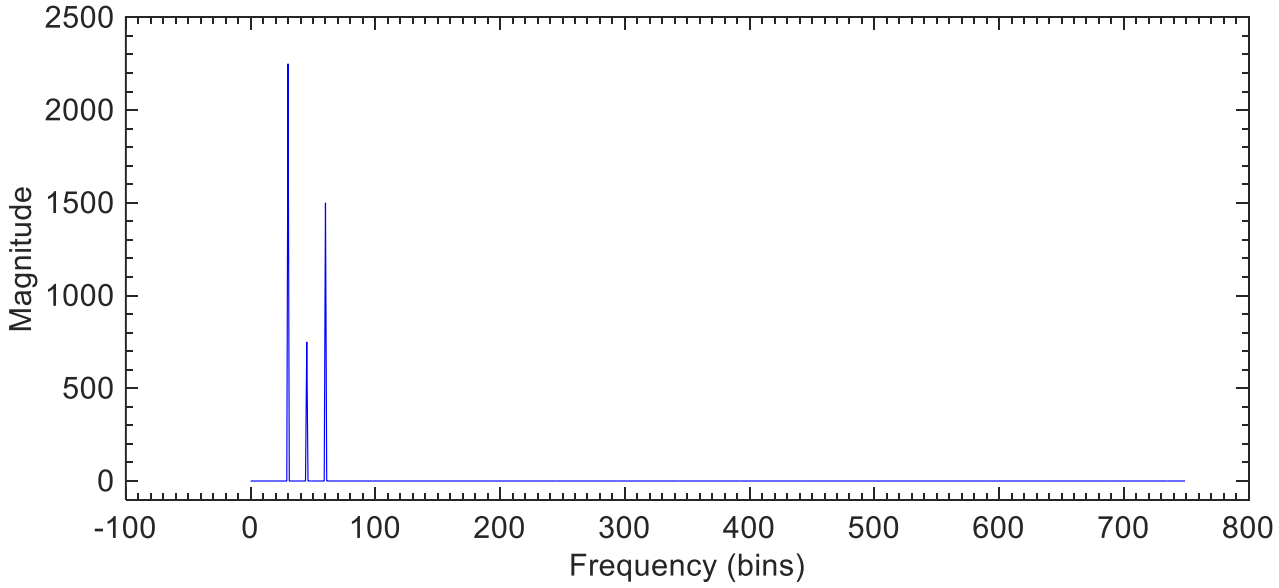

Fig. 8-3: Half of the FFT magnitude spectrum against the frequency bins

The first half of the FFT magnitude spectrum is shown in Fig. 8-3. Note that the last frequency bin (750) in the FFT magnitude spectrum in represents the f_{nyq} (500 Hz); hence, frequency bin = 100 will correspond to 500 Hz / 750 bin * 100 bin ≈ 67 Hz. All the three

peaks shown in Fig. 8-3 are below 67 Hz which makes sense because all three sinusoids in Eq. 7.5 are less than 67 Hz. Note also that all other frequency bins correspond to zero magnitude because there are no other frequencies present in the time signal that is analyzed.

Fig. 8-4 shows the magnitude spectrum up to frequency bin = 100 with labels on the peaks of the spectrum. Note that the magnitude of the lowest frequency (f_1) is 2250 which is twice the magnitude of f_3 and thrice the magnitude of f_2; this observation corroborates the amplitudes of the sinusoids of $x[n]$ in Eq. 7.5 i.e. $a_1 = 3a_2$ and $a_3 = 2a_2$. This observation also infers a rule for computations with fft; the amplitude of the sinusoid of the time signal is extracted from the FFT magnitude spectrum by dividing the magnitude of the peak by the half of the total no. of frequency bins. In this example, total frequency bins = N = 1500; a_1 = 2250 / 750 = 3, a_2 = 750/750 = 1, and a_3 = 1500 / 750 = 2.

Fig. 8-4 is plotted again in Fig. 8-5 with the actual frequency vector along the x axis; which shows that the frequency bin (k) and the frequency at every bin ($f(k)$) are related through the equation

$$f(k) = \frac{kf_s}{N} \tag{7.6}$$

Where N is the total no. of frequency bins. Note that the labels on the peaks in Fig. 8-5 show the frequencies f_1, f_2, and f_3 which are the same as that used for the time signal $x[n]$

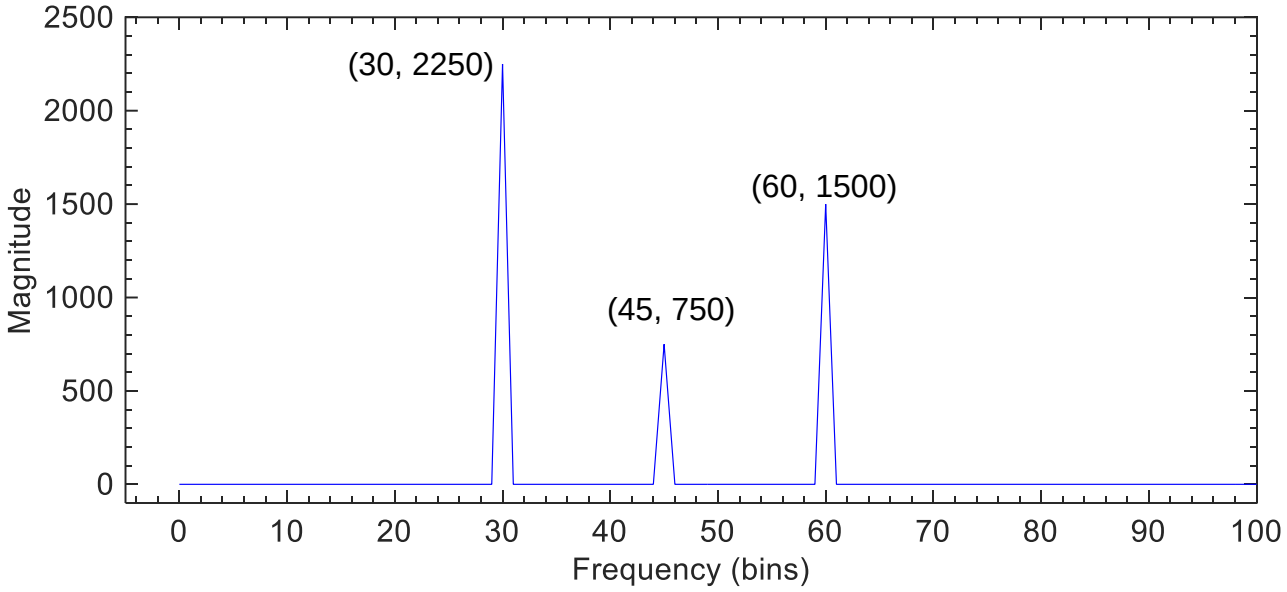

Fig. 8-4: FFT magnitude spectrum for frequency bin from 0 to 100 bins (≈ 67 Hz)

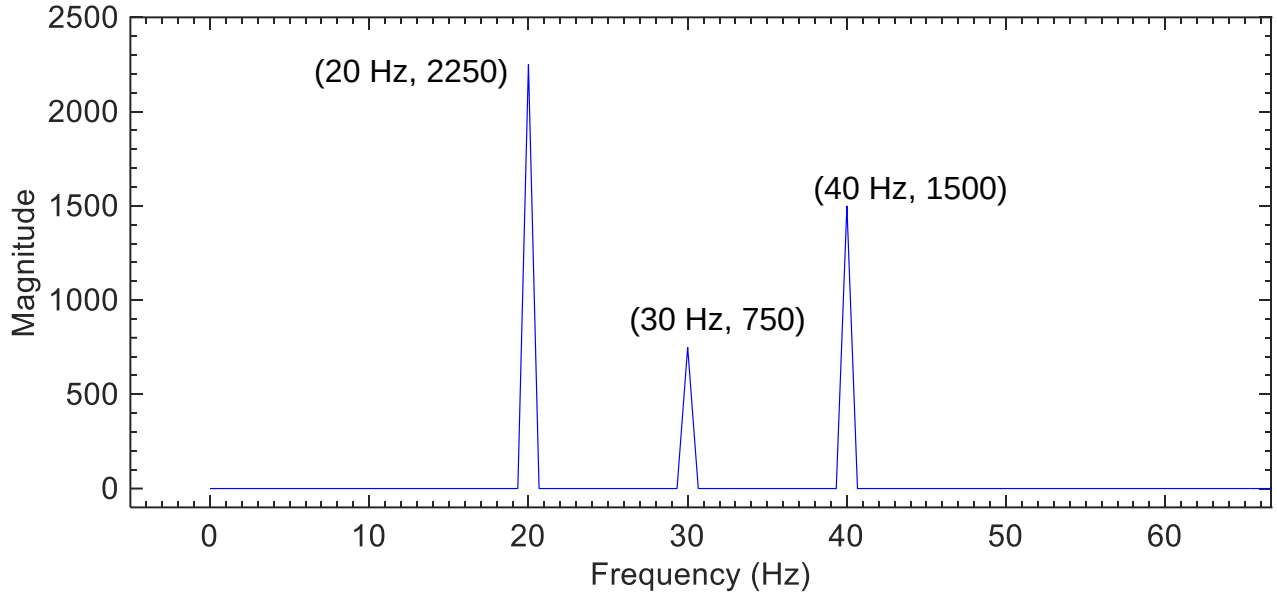

Fig. 8-5: FFT magnitude spectrum with the frequency vector from 0 to ≈ 67 Hz

The MATLAB™ function ‘fft’ also gives the phase angles of the sinusoids. The bins at which the magnitude spectrum shows the peaks are used to retrieve the phase angles

at those frequency bins. The corresponding phase angles are $\varphi_1 = 0.2$, $\varphi_2 = -0.3$ and $\varphi_3 = -2.4$ which are exactly values of phase angles in in Eq. 7.5

In conclusion, the DFT of any signal can be calculated using the 'fft' function of MATLAB™ because all time signals are composed of sinusoids. This function has been extensively used in this study to understand frequency response of the bender elements in different media.

In the time signal *x[n]*, the total no. of samples (*N*) were selected at a particular time interval (Δt). This time interval has to be selected carefully to prevent loss of important information from the signals. This selection of time interval requires understanding of the concept of 'Digitization'.

Digitization

Proper digitization of a time signal is important for calculating the Fourier transform of a time signal (Santamarina and Fratta 2005)**.** For signals to be processed, the signals have to be digitized; this digitization is done by sampling values of the time signals at discrete time interval (Δt). To avoid losing important information from the signal, a criterion called 'Nyquist criterion' has to be fulfilled. 'Nyquist criterion' requires that the sampling frequency of the signal (f_s) should be greater than the Nyquist frequency (f_{nyq}). The equation relating f_{nyq} and f_{samp} is

$$f_s = \frac{1}{\Delta t} > f_{ny} = \frac{2}{T} \qquad 7.7$$

where *T* is the smallest period of the signal being analyzed. The consequence of not satisfying the 'Nyquist criterion' will cause 'aliasing' of the signal. Fig. 8-6 shows an example to illustrate 'aliasing' in a signal of frequency of 10 Hz. The 10 Hz signal is sampled at Δt which doesn't satisfy the Nyquist criterion; as a result, the frequency of the same 10 Hz signal becomes 2 Hz (apparently). In practice, a minimum of 10 samples per cycle are recommended (Santamarina and Fratta 2005).

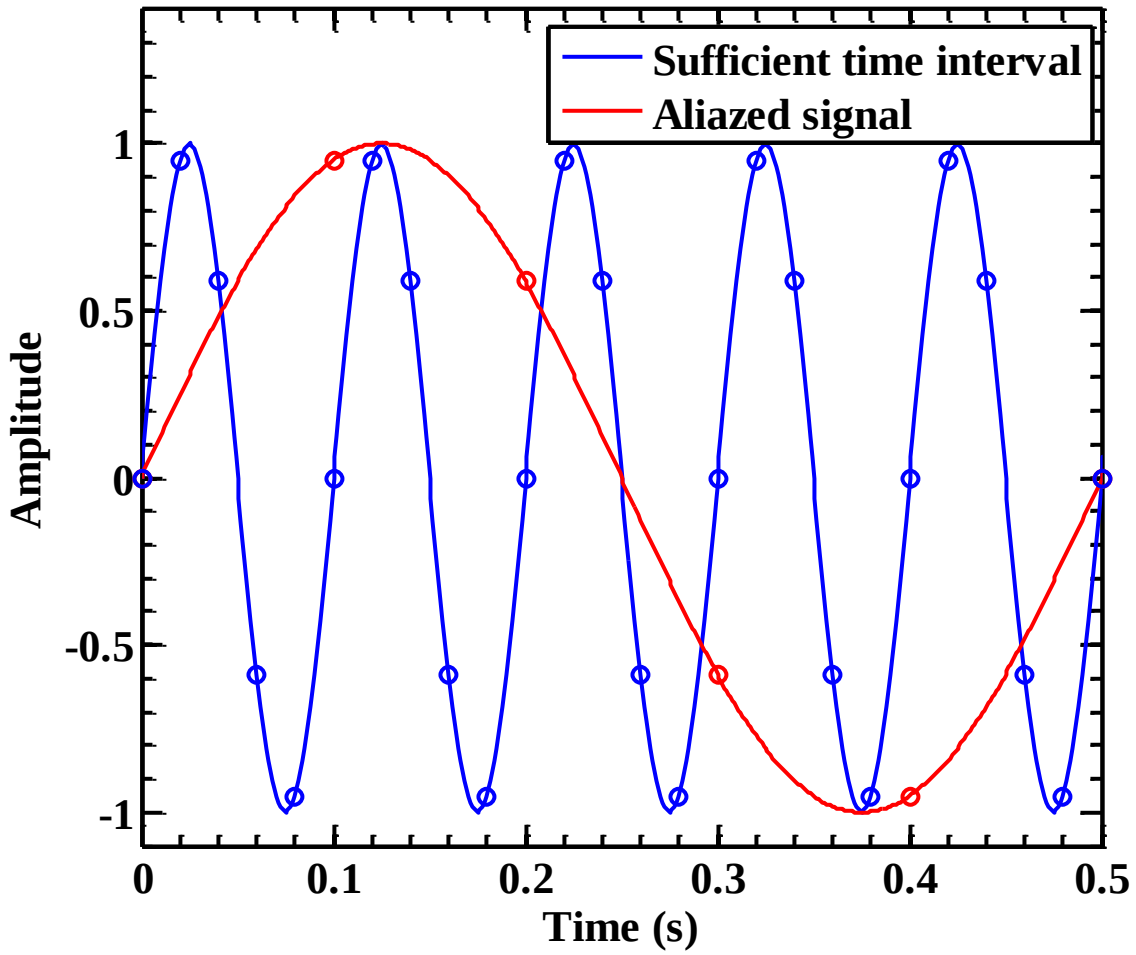

Fig. 8-6: Illustration of aliasing

Zero-padding

Zero-padding is a signal processing technique to improve the DFT process. It is a simple process of adding zeros to the time signal to improve the resolution of the frequency spectrum. Adding the zeros to signal increases the value of *N* (Eq. 7.4) which in turn increases the frequency increment of the frequency vector; this process is performed to avoid aliasing in the FFT spectrum. This process is explained by considering a simple example below

Consider a time signal with a single sinusoid given as

$$x[n] = 0.5\cos(2\pi f_1 n\Delta t + 0.2) \qquad 7.8$$

Where f_1 = 2 Hz i.e. 2 cycles in one second of the time signal. This time signal and its FFT magnitude spectrum is presented in Fig. 8-7. The peak magnitude in the FFT magnitude spectrum corresponds to 2 Hz as is expected. The amplitude of the sinusoid is estimated from peak magnitude as 250 / 500 = 0.5 where 250 is the peak magnitude and 500 is half of the sampling frequency. Note that the time signal has 2 cycles in the duration.

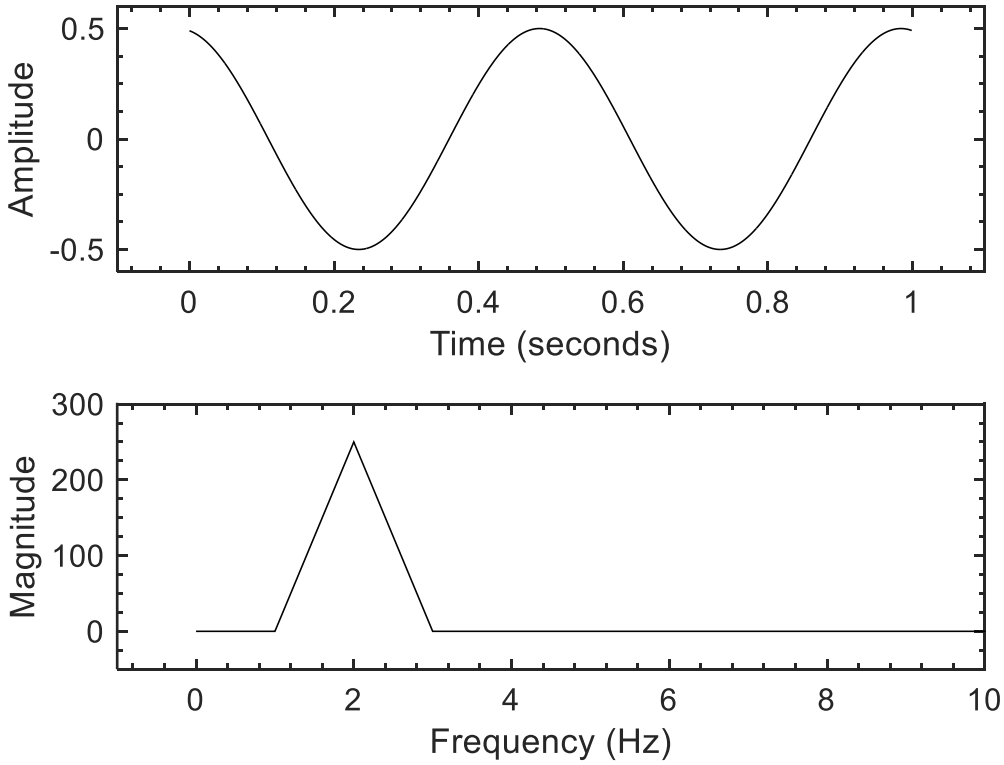

Fig. 8-7: Time signal $x[n]$ (Eq. 7.8) with f_1 = 2 Hz and its FFT magnitude spectrum

Now, the frequency (f_1) of the time signal $x[n]$ is increased to 2.5 Hz. The new time signal and its FFT magnitude spectrum are presented in Fig. 8-8. Note the changes in the FFT magnitude spectrum; the peak has reduced from 250 to ≈ 180, the frequency at the peak magnitude does not exactly equal to 2.5 Hz, and the magnitudes at other frequencies have increased. These changes happened because the no. of cycles of the time signal became a non-integer value (2.5 from 2). There is no sinusoid in DFT summation (Eq. 7.4) which matches perfectly to this new time signal; this, in fact, is the case for typical time

signals obtained from experiments. To minimize this effect of non-integer no. of cycles in the time signal, zero-padding is applied.

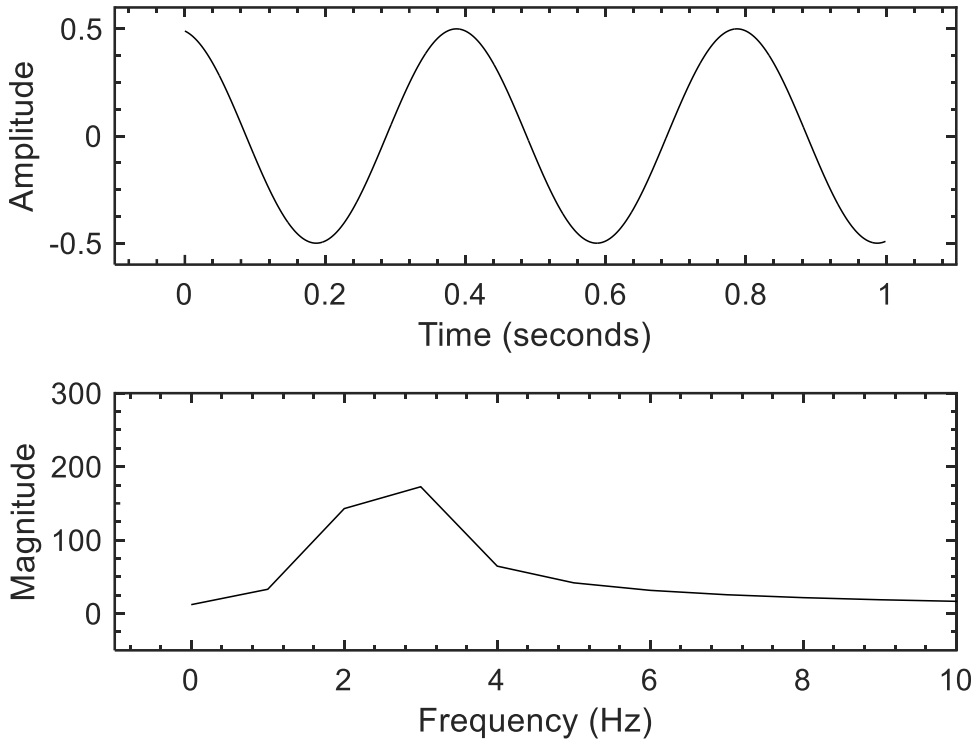

Fig. 8-8: Time signal x[n] (Eq. 2.31) with f1 = 2.5 Hz and its FFT magnitude spectrum

Fig. 8-9 shows the time signal with added zeros such that the total duration has to increase to 10 seconds. Note the changes in the FFT magnitude spectrum; the peak magnitude is back to 250 (corresponding to amplitude 0.5 as in the original signal in Fig. 8-7) and the frequency at the peak magnitude (main lobe) is back to 2.5 Hz. However, there is still ‘leakage’ in the energy of the spectrum i.e. the magnitude at other frequencies (side lobes) is still high compared to zero in the original signal; this problem is minimized by applying the ‘windowing’ process.

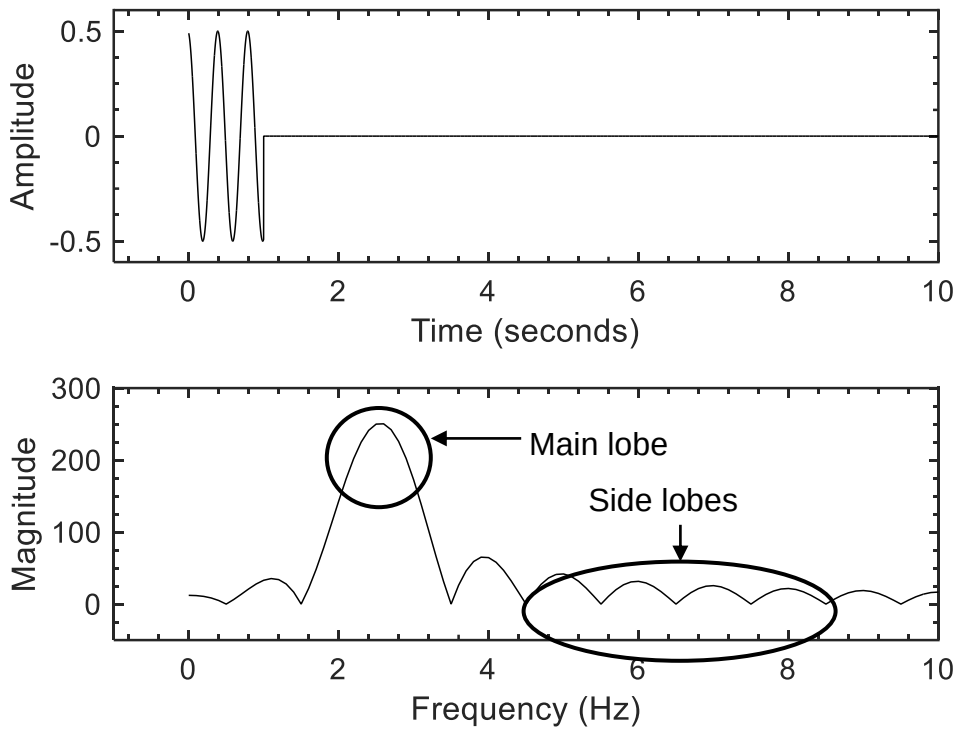

Fig. 8-9: Zero-padded time signal with its FFT magnitude spectrum

Windowing

Windowing process is another signal processing technique used for reducing the effects of the problem of energy leakage as shown in the previous section. This process is also a simple process where the time signal is multiplied by a function which starts and ends with zeros to remove the extraneous parts of a time signal. Fig. 8-10 shows the windowed time signal compared to the original time signal along with its FFT magnitude spectrum; a windowing type called 'Hanning' window is also shown. Different types of windows have been proposed in the signal processing literature; all of them with advantages and disadvantages; discussion of the types of windows is not in the scope of the study.

Note that the energy in the side lobes has been minimized and the peak magnitude is now equal to 125. The peak magnitude has also been reduced by almost half; the amplitude of the sinusoid in the time signal is therefore estimated as 125 / 500 / 2 = 0.5 where 500 is again f_s / 2 and '2' is a factor associated with the 'Hanning' window. Different windows would have different factors for the amplitude estimation.

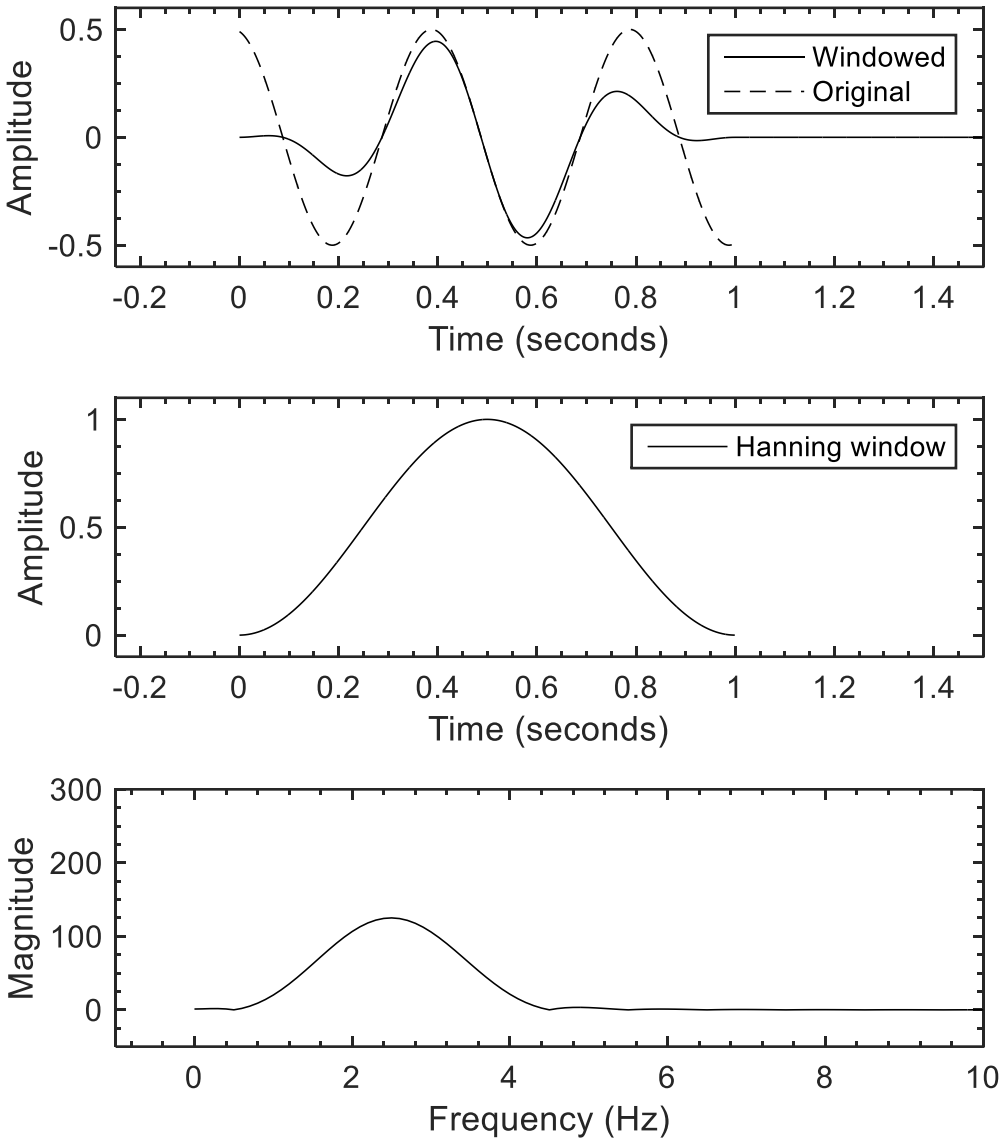

Fig. 8-10: Original and windowed time signal with the hanning window and the FFT magnitude spectrum after windowing